



**Micropattern Transfer Without Photolithography of
Substrate: Ni Electrodeposition using Enface Technology**

A Thesis Submitted by

Tri Widayatno

For the Degree of Doctor of Philosophy

School of Chemical Engineering and Advanced Materials

Newcastle University

November 2013

ABSTRACT

Since the standard photolithographic patterning technology possesses a number of sustainable issues, a “maskless” technology, Enface, has been proposed. Here, a patterned ‘tool’ placed opposite to the substrate within micrometre range is required. Etching or plating occurs by passing tailored current or voltage waveforms, provided that the electrolyte resistance is high. Enface is a resource efficient process as the use of chemicals is greatly reduced. This research project aimed to investigate the feasibility of Ni pattern transfer using Enface under stagnant conditions. It would be advantageous if Enface could be used for nickel deposition as it is a slow kinetic system and controlled by mixed mass transfer and kinetics which is a system where Enface has never been used before.

An electrochemical cell has been specifically designed and an electrolyte was systemically developed as required by Enface. Polarisation experiments were carried out to determine applied current densities that would be used in galvanostatic plating experiments for pattern transfer of millimetre and micron scale features. Deposited features were comprehensively characterised to see the performance of the patterning process. Current distribution during the pattern transfer experiments was investigated by simulation and modelling using Elsy software.

An electrolyte of 0.19 M nickel sulfamate was selected and shown to be capable of depositing nickel. Polarisation data from experiments in Enface system showed that each feature size requires a different applied current density. As expected, pattern transfers of metallic nickel were achieved for millimetre and micron scale features at a current efficiency of around 90 % with current spreading were observed. The deposited feature width broadens with increasing time and decreasing feature size. In addition, maximum thickness that could be achieved was around 0.5 μm due to entrapped gas bubbles leading to process termination. The gas bubbles were detrimental to the deposits resulting in a rough and inhomogeneous surface as well as photoresist degradation. Ultrasound agitation was shown to be capable of diminishing the effect of gas bubbles. However it requires an optimisation of applied power density to avoid negative effects of cavitation bubbles. The result of simulation showed a non-uniform current distribution across the feature width with the highest current density at the centre resulting in a bell-shaped surface profile which is in agreement with the experiments. However, the deposited shape evolution obtained from the experiments is consistently much better than those obtained from the simulation.

AKNOWLEDGEMENT

I would like to sincerely thank:

- Prof. Sudipta Roy for her invaluable guidance, advice, and support throughout the years during my studies.
- Dr. Todd Green for his useful advice on particular topics in this project
- Simon Coleman for help with making photolithographed stuffs and surface profile measurement.
- All members of Prof. Roy's research group – Electrochemical Nanomaterials: Peter, Jeet, Naray, Swati, Mosaad, Susana, and Simon for the friendship, good discussions, and friendly environment in the Lab.
- Newcastle University's Advanced Chemical and Materials Analysis (ACMA) unit, especially Pauline for SEM and EDX measurement, Maggie for XRD analysis, and Dave Dunbar for ICP analysis.
- National EPSRC XPS User's Service (NEXUS) hosted by nanoLAB Newcastle University, especially Prof. Peter Cumpson, Dr. Naoko SANO, and Dr. Jose Portoles for help with XPS measurements.
- Sanggar Dewanto for help with optical profilometry measurements.
- Vince Scott, Iain Strong, Iain Ditchburn, Rob Dixon, Paul Sterling, Stuart Latimer, Simon, Jimmy, and Brian for their advice and assistance.
- My parents, Suradi and Sumi, for constant support, encouragement, and prayer
- Special thanks to my family. My beloved wife, Hana, for your love, patience, inspiration, and prayer. To my little girl, Hanin, and my boys, Haidar, Hafi, and Hamza who missed out a lot of daddy time during my study, I would say thank you and love you all.
- Finally I would like to thank the Ministry of Education and Culture through Directorate General for Higher Education, Government of Republic of Indonesia for funding my PhD study, Poc-Enface for research studentship, Newcastle University International Postgraduate Scholarship, and Universitas Muhammadiyah Surakarta for fully supporting my study.

LIST OF CONTENTS

ABSTRACT	i
ACKNOWLEDGEMENT	ii
LIST OF FIGURES	viii
LIST OF TABLES	xv
LIST OF SYMBOLS	xviii
LIST OF ABBREVIATIONS	xxi
Chapter 1 Introduction	1
1.1 Background	1
1.2 Photolithography	2
1.2.1 Substrate cleaning.....	3
1.2.2 Photoresist coating.....	3
1.2.3 Soft Bake.....	3
1.2.4 Exposure.....	3
1.2.5 Development.....	4
1.2.6 Hard bake.....	5
1.2.7 Photolithography challenge.....	5
1.3 Patterning Process	5
1.3.1 Pattern Transfer with Additive Method.....	5
1.3.2 Pattern Transfer with Subtractive Method.....	8
1.4 Disadvantages of Photolithographic Patterning Process	10
1.5 Maskless Patterning Process	11
1.5.1 Direct Imaging.....	11
1.5.2 Inkjet Technique.....	11
1.5.3 Electro-hydrodynamic Atomisation (EHDA)	12
1.5.4 Electrochemical Microfabrication	12
1.6 Enface	14
1.7 Outstanding Issues	18
1.8 Current Work	19
1.9 Aim and Objectives	20

Chapter 2 State of The Art Electrodeposition Of Nickel	21
2.1 Electrolyte formulation	21
2.2 Electrodes	26
2.3 Kinetics and mechanism	27
2.4 Summary	29
Chapter 3 Fundamental Aspects.....	31
3.1 Physicochemical properties of metals in solution	31
3.1.1 <i>Conductivity.....</i>	31
3.1.2 <i>pH.....</i>	32
3.2 Chemistry of metal ions and complexes	33
3.3 Thermodynamics of metals in aqueous solution.....	34
3.3.1 <i>Standard potential.....</i>	34
3.3.2 <i>Equilibrium Potential.....</i>	34
3.3.3 <i>Pourbaix Diagram.....</i>	36
3.4 Electrodeposition from aqueous solution.....	38
3.4.1 <i>Kinetic of Charge Transfer Process.....</i>	40
3.4.2 <i>Tafel Plot.....</i>	42
3.4.3 <i>Mass Transfer Process.....</i>	43
3.5 Mixed Potential System.....	44
3.6 Kinetics of Multistep Electrode Reaction.....	45
3.7 Performance of Electrochemical Deposition Process.....	47
3.7.1 <i>Electrodeposition rate.....</i>	47
3.7.2 <i>Current efficiency.....</i>	48
3.7.3 <i>Energy Consumption of the Electrochemical Deposition.....</i>	48
	50
Chapter 4 Experimental	
4.1 Electrolyte Development.....	50
4.2 Electrochemical Apparatus.....	52
4.2.1 <i>Standard Three-Electrode System.....</i>	52
4.2.1.1 <i>Electrochemical Cell.....</i>	52
4.2.1.2 <i>Rotating Disk Electrode (RDE)</i>	53
4.2.1.3 <i>Electrode Preparation.....</i>	55
4.2.2 <i>Enface System.....</i>	56

4.2.2.1	<i>Electrochemical Cell</i>	56
4.2.2.2	<i>Electrode Preparation</i>	57
4.2.2.3	<i>Pattern Feature</i>	59
4.2.3	<i>Ultrasound Unit</i>	64
4.3	Instrumentation	65
4.3.1	<i>Potentiostat</i>	65
4.3.2	<i>Conductivity and pH Meter</i>	65
4.4	Procedures	66
4.4.1	<i>Polarisation Measurement in a Three-electrode Cell and RDE System</i>	66
4.4.2	<i>Electrochemical characterisation of nickel electrodeposition in Enface system under stagnant condition</i>	68
4.4.3	<i>Electrochemical characterisation of nickel electrodeposition in Enface system under ultrasound agitation</i>	69
4.4.4	<i>Nickel Pattern Transfer Experiments under Stagnant Condition..</i>	70
4.4.5	<i>Nickel Pattern Transfer under Ultrasonic Agitation</i>	71
4.5	Structure Characterisation	71
4.5.1	<i>Feature size and shape determination</i>	71
4.5.2	<i>Deposit Characterisation</i>	72
4.5.2.1	<i>Optical Microscopy</i>	72
4.5.2.2	<i>Scanning Electron Microscopy (SEM)</i>	72
4.5.2.3	<i>X-ray Photoelectron Spectroscopy (XPS)</i>	73
4.5.2.4	<i>XRD analysis</i>	73
4.5.2	<i>Current Efficiency of Nickel Deposition</i>	74
Chapter 5	Experimental Results and Discussion:	75
	Electrochemical Characterisation	
5.1	Electrochemical characterisation of the electrolyte in three-electrode cell using rotating disc electrode (RDE)	76
5.2	Electrochemical characterisation of nickel electrodeposition in Enface reaction system under stagnant and moderate agitation..	80
5.3	Kinetic Analysis	82
5.4	Experimental $\eta - j$ Data Analysis using graphical method	86
5.5	Measurement of Current Density	87

5.6 Electrochemical Characterisation of the Nickel electrolyte under ultrasound agitation	90
Chapter 6 Experimental Results: Pattern Transfer.....	92
6.1 Cell Monitoring Potential during Nickel Pattern Transfer process	93
6.2 Hydrogen Evolution	95
6.3 Pattern Transfer on Millimetre scale Feature of 1 mm x 5 mm....	96
6.4 Pattern Transfer on Manually Fabricated Micron Scale Feature	99
6.4.1 <i>Manually fabricated micropattern structure 1</i>	99
6.4.2 <i>Manually fabricated micropattern structure 2.....</i>	103
6.5 Microscale Pattern Transfer using Photoresist.....	108
6.5.1 <i>Photolithographed micropattern structure 1</i>	108
6.5.2 <i>Manually fabricated micropattern structure 2.....</i>	112
6.6 General comparison of deposited features.....	108
6.7 Surface Analysis.....	115
6.8 Verification of Thickness and Surface Profile measurements	117
6.9 Material Analysis.....	119
6.9.1 <i>EDX Analysis</i>	119
6.9.2 <i>Scanning Electron Microscopy (SEM)</i>	120
6.9.3 <i>X-ray Photo electron Spectroscopy (XPS) Analysis.....</i>	121
6.10 Effect of increasing mass transfer	129
6.11 Analysis of Electrolyte Stability and Enface Process Sustainability	131
Chapter 7 Simulation And Modelling Of Current Distribution	133
7.1 Background.....	133
7.2 Basic Principle of the Numerical Calculation using Elsy.....	134
7.2.1 <i>General Transport Equations for Multi-ion System in Dilute Solution.....</i>	135
7.2.1.1 <i>The flux of an ionised species.....</i>	135
7.2.1.2 <i>Mass Balance for a small volume increment.....</i>	135
7.2.1.3 <i>Electro-neutrality.....</i>	136
7.2.1.4 <i>The Current Density.....</i>	136
7.2.1.5 <i>The continuity Equation.....</i>	136

7.2.2	<i>Derivative equations for the ions transport in dilute solution.....</i>	137
7.2.3	<i>Applications of Potential-Theory Model.....</i>	138
7.2.4	<i>Boundary Conditions.....</i>	138
7.2.4.1	<i>Electrodes.....</i>	138
7.2.4.2	<i>Deposition at Electrodes.....</i>	139
7.2.4.3	<i>Insulating wall.....</i>	139
7.3	Method of Solution.....	139
7.4	Kinetic Parameters.....	140
7.5	Reactor Configuration.....	141
7.6	Pattern Transfer Modelling.....	145
7.6.1	<i>Simulation on a single feature</i>	146
7.6.2	<i>Simulation on 2 pattern features</i>	147
7.6.3	<i>Simulation on 3 pattern features</i>	149
7.6.4	<i>Comparison between Experimental and Simulated Results..</i>	151
7.7	Effect of Current Distribution	154
Chapter 8	Conclusions.....	155
Chapter 9	Future Work.....	161
References.....		163
Appendices		185

LIST OF FIGURES

Figure 1.1 Schematic illustration of (a) Optical Lithography System, (b) Photolithographic Patterning Process	2
Figure 1.2 (a) contact printing, (b) proximity printing, and (c) projection printing.....	4
Figure 1.3 Typical physical vapour deposition (PVD) adapted from literature	6
Figure 1.4 Schematic of typical Chemical vapour deposition (CVD) process	7
Figure 1.5 Diagram of Electrochemical Printing (EcP)	13
Figure 1.6 Basic principle of Electrochemical Micromachining: (a) without mask and (b)with mask	13
Figure 1.7 Principle of Enface Patterning Process	15
Figure 3.1 Pourbaix diagram for the system nickel-water, at 25°C	38
Figure 3.2 A simple three-electrode electrochemical deposition systems	39
Figure 3.3 Steps Involved in the process of electrodeposition	40
Figure 3.4 Tafel plots for anodic and cathodic regions of the current density - overpotential curve for $O + e^- \rightarrow R$ with $\alpha = 0.5$, $T = 298$ K, and $j_0 = 10^{-6}$ A/cm ²	42
Figure 3.5 Mixed Potential Diagram of binary metal system, with metal M_1 nobler than metal M_2 , J_{M_1} is a measured current density of pure M_1 and J_{M_2} is a current density response of pure M_2 , J_M will be the measured current density of mixed M_1/M_2 system, and E_M is a mixed potential	45
Figure 4.1 Diagram of three-electrode cell for initial electrochemical characterisation of the chosen electrolyte (0.19 M nickel sulfamate)	52
Figure 4.2 Pattern of Flow at surface of RDE	53
Figure 4.3 Schematic diagram of rotating disk electrode (RDE) a) typical RDE tool, b) electrode tip with diameter d (5 or 2 mm)	54
Figure 4.4 Schematic diagram of vertical-cylindrical cell with dimensions in millimetre (a) side view, (b) electrode holders, (c) top view	56
Figure 4.5 The polished copper disk (cathode) appearance with a roughness of 10 -20 nm	57

<u>Figure 4.6</u> The polished nickel disk (anode) appearance with a roughness of 10 – 20 nm	58
<u>Figure 4.7</u> Optical images of pattern feature using kapton tape a) the profile of the feature edge b) the thickness measurement.	59
<u>Figure 4.8</u> Designed millimetre scale pattern with feature sizes of a) 8 mm x 4 mm, b) 8 mm x 2 mm, c) 5 mm x 2 mm, d) 5 mm x 1mm	59
<u>Figure 4.9</u> Micro-pattern manually prepared by using a kapton tape a) structure 1, b) structure 2	60
<u>Figure 4.10</u> Optical micrograph of micropattern prepared using Kapton tape (a) line, (b) small rectangle	61
<u>Figure 4.11</u> Micro-pattern features prepared using photolithography (structure 1)	62
<u>Figure 4.12</u> Micro-pattern features prepared using photolithography (structure 2)	62
<u>Figure 4.13</u> Ultrasound Units used to agitate the nickel pattern transfer	64
<u>Figure 4.14</u> Potentiostat of Autolab PGSTAT30 used in the polarisation and pattern transfer experiments	65
<u>Figure 4.15</u> Dual pH and conductivity meter used to measure physicochemical properties of the electrolytes	66
<u>Figure 4.16</u> Typical potential-time waveform in linear sweep voltammetry	67
<u>Figure 4.17</u> Schematic for set-up for nickel pattern transfer under ultrasound agitation	69
<u>Figure 4.18</u> Travelling microscope for measuring deposited feature size	72
<u>Figure 4.19</u> An ellipsoidal model for estimating the nickel deposits volume	74
<u>Figure 5.1</u> (a) Cathodic Polarisation Curves for 0.19 M nickel sulfamate at various scan rates, the RDE rotation speed was 0 rpm, (b) zoom of the low current density region to show the steady state condition (c) zoom of nickel deposition region for 0.5 mV/s scan rate	76
<u>Figure 5.2</u> Comparison between cathodic polarisation Curves for 0.19 M nickel sulfamate with and without ohmic drop correction at 0.5 mV/s scan rate. The RDE rotation speed was 0 rpm	77
<u>Figure 5.3</u> Cathodic Polarisation Curves for 0.19 M nickel sulfamate at 0.5 mV/s scan rate, the RDE rotation speed varied between 0 and 3500 rpm	78

- Figure 5.4** Cathodic and anodic Polarisation Curves for 0.19 M nickel sulfamate on copper substrate at 0.5 mV/s scan rate, the RDE rotation speed was 0 rpm. 80
- Figure 5.5** Comparison of Cathodic Polarisation Curves for 0.19 M nickel sulfamate on copper substrate at 2 mV/s scan rate in non-agitated Enface system with fully exposed anode and RDE system at room temperature 20 ± 2 °C. 81
- Figure 5.6** A schematic illustration of the mechanism of nickel electrodeposition in Enface system 84
- Figure 5.7** (a) Three-electrode cell polarisation of a copper disk electrode in a 0.19 M nickel sulfamate electrolyte, at 0.5 mV/s scan rate (b) Tafel analysis performed on the j - η data, (c) shows the fit of the line. 87
- Figure 5.8** (a) Cathodic Polarisation Curves for 0.19 M nickel sulfamate in non-agitated Enface system on various pattern feature sizes at 2 mV/s scan rate under no agitation (b) zoom of nickel deposition region for 5 mm x 1 mm and 8 mm x 2 mm features. 88
- Figure 5.9** polarisation curves for 0.19 M nickel sulfamate carried out in Enface system at 1 mV/s scan rate showing the effect of ultrasound agitation, (—) with no US probe, (---) with silent US probe, and (- - -) with US of 35 % max amplitude (a) on fully exposed anode (b) on a feature of 1 mm x 5 mm. 90
- Figure 6.1** (a) Cell potential profiles against deposition time of nickel pattern transfer using Enface on various pattern feature sizes and structures, (b) zoom in of potential range between -2.0 and -2.6 V showing the potential and time threshold. 93
- Figure 6.2** (a) Cell potential profiles against deposition time of nickel pattern transfer using Enface on photolithographed micropattern features structure 1 and 2, (b) inset: zoom in of potential range between -2.09 and -2.33 V showing potential threshold. 94
- Figure 6.3** (a) Profilometer scans showing the thickness, roughness and width of plated nickel pattern obtained at -4.53 ± 0.55 mA/cm² for various plating times, (b) Deposit thickness growth rate. 97
- Figure 6.4** Cathodic current efficiency of nickel pattern transfer on 1 mm x 5 mm feature size for different deposition times at applied current density of -4.53 ± 0.55 mA/cm². 98
- Figure 6.5** Profilometer measurement showing the thickness, roughness, and width of deposited nickel feature obtained at -7.17 ± 0.92 mA/cm² for 300 s on the feature of parallel three lines with M - middle line with 377 μ m width, CE – linear feature 1.5 mm gap from middle line with 373 μ m width, FE – linear feature 2 mm gap from middle line with 317 μ m width. 101
- Figure 6.6** Optical micrograph of deposit features obtained from 0.19 M nickel sulfamate at room temperature (20 ± 2 °C) and stagnant condition using patterned anode with Kapton tape feature of structure 1 for 300 s, (a) original structure 1 (b) original feature 102

(M), and (c) deposited feature (M), yellow straight lines show the original size.

- Figure 6.7** Profilometer measurement showing the thickness, roughness, and width of deposited nickel obtained at -7.59 ± 0.92 mA/cm² on manually patterned anode structure 2 for 125 s, with LM-middle linear feature of 215 μ m width, SRL-small rectangular feature 2 mm gap from middle line with 212 μ m width, SRR- small rectangle 1.5 gap from middle line with 165 μ m width. 105
- Figure 6.8** Optical micrograph of deposit features obtained from 0.19 M nickel sulfamate at room temperature (20 ± 2 °C), for 125 s, and stagnant condition for Kapton tape-fabricated feature of structure 2, (a) arrangement of structure 2 (b) original feature (LM), and (c) original feature (SRR), (d) deposited feature (LM), yellow straight lines show the original size, and (e) deposited feature (SRR), yellow rectangle shows the original size. 107
- Figure 6.9** Profilometer measurement showing the thickness, roughness, and width of deposited nickel obtained at -0.91 ± 0.07 mA/cm² on photolithographically patterned anode structure 1 for 300 s and 600 s. the features were large square of 793.65 μ m x 793.65 μ m. 110
- Figure 6.10** (a) Photolithographed pattern feature structure 1 on the anode, (b) original large square pattern feature, and Optical Image of plated cathodes at -0.91 ± 0.07 mA/cm² on photo-lithographically patterned anode structure 1 large square feature of 793.65 μ m x 793.65 μ m for (c) 300 s and (d) 600 s, yellow square shows the original feature. 111
- Figure 6.11** (a) Photolithographed micropattern structure 2, (b) Original large square feature, (c) original linear feature, and Optical micrograph images of plated nickel pattern on the cathode, (d) large square, yellow square shows the original feature (e) linear feature, yellow lines show the original feature, obtained by DC plating at 1.93 ± 0.46 mA/cm² for 300 s. 114
- Figure 6.12** Original pattern features showing the dimension (a) manually fabricated linear micron scale pattern structure 1, (b) small rectangular feature micron scale pattern structure 2, Deposited feature appearance in 3D, red colour shows the nickel deposit, obtained from galvanostatic plating (a) at -7.17 ± 0.92 mA/cm² for 300 s from the linear feature, (b) at -7.59 ± 0.92 mA/cm² for 300 s from the rectangular feature. 116
- Figure 6.13** Elemental map analysis of nickel deposits on copper substrate, red represents the copper and green colour shows the nickel deposit, obtained from galvanostatic plating (a) at -7.17 ± 0.92 mA/cm² for 300 s on manually fabricated micron scale pattern structure 1, linear feature with 260 μ m width, (b) at -7.59 ± 0.92 mA/cm² for 300 s on micron scale pattern structure 2, small rectangular feature (587.22 μ m x 1020 μ m) 117

- Figure 6.14** Comparison of surface profile measurement between (—) Zygo optical profilometer and (—) Tencor long scan profiler for kapton tape-fabricated micropatterned anode structure 2, (a) SRR- small rectangle 1.5 gap from middle line with 165 μm width (b) LM- middle linear feature of 215 μm width, (c) SRL-small rectangular feature 2 mm gap from middle line with 212 μm width. 118
- Figure 6.15** EDX spectra of deposited feature of 1 mm x 5 mm obtained from 0.19 M nickel sulfamate at room temperature (20 ± 2 $^{\circ}\text{C}$), stagnant condition, and for 600 s (a) at the middle part (b) at the edge of the feature. 120
- Figure 6.16** SEM images images of deposited feature of obtained from galvanostatic plating (a) at -7.17 ± 0.92 mA/cm^2 for 300 s on manually fabricated micron scale pattern structure 1, linear feature with 260 μm width, (b) at -7.59 ± 0.92 mA/cm^2 for 300 s on micron scale pattern structure 2, small rectangular feature (587.22 μm x 1020 μm) at 50 x magnification, (c) 500 x, and (d) 2000 x magnification 121
- Figure 6.17** XPS spectra of a fresh deposited nickel feature of 1 mm x 5 mm on copper substrate (a) survey scan, (b) high resolution scan for specific area of nickel (Ni 2p), and (c) high resolution scan for copper (Cu 2p). 122
- Figure 6.18** XPS spectra of the deposited nickel feature of 1 mm x 5 mm on copper substrate left in room temperature for ± 2 months (a) survey scan, (b) high resolution scan for specific area of nickel (Ni 2p), and (c) high resolution scan for copper (Cu 2p). 123
- Figure 6.19** XPS spectra of the deposited nickel feature of 1 mm x 5 mm on copper substrate treated by applying temperature of 90 – 100 $^{\circ}\text{C}$ for ± 100 hours (a) survey scan, (b) high resolution scan for specific area of nickel (Ni 2p), and (c) high resolution scan for copper (Cu 2p). 124
- Figure 6.20** XPS spectra of the deposited nickel feature of 1 mm x 5 mm on copper substrate annealed at temperature of 180 - 200 $^{\circ}\text{C}$ for 5 – 10 mins (a) survey scan, (b) high resolution scan for specific area of nickel (Ni 2p), and (c) high resolution scan for copper (Cu 2p). 125
- Figure 6.21** Cell potential profile of nickel pattern transfer using Enface under stagnant condition and ultrasound agitation on 1 mm x 5 mm feature. 128
- Figure 6.22** Optical profilometer measurements showing the deposit thickness, surface profile and the roughness of the deposited features (— -) 26 W/m^2 ultrasound power density for 1500 s and (— -) 18 W/m^2 power density for 1200 s, with power densities of 18 and 26 W/cm^2 respectively. 129
- Figure 6.23** optical micrograph of deposited nickel feature obtained from pattern transfer on the 1 mm x 5 mm feature at 4.2 – 5.5 mA/cm^2 for 1200 s under ultrasonic agitation power density of (a) 18 W/m^2 and (b) 26 W/m^2 . 130

Figure 7.1	Typical electrochemical cell used in simulation using Elsy with constant electrolyte conductivity and uniform ionic species gradient	134
Figure 7.2	(a) Cross-sectional view of the electrochemical reactor, with 10 mm electrode diameter, 0.3 mm interelectrode spacing, 100 mm reactor diameter, and 63 mm solution heights (red dash-line shows the Elsy system). (b) 2D reactor model and its shape (b'), (c) Axy-Symmetrical reactor geometry created by rotating the original cell orientation by 90° clockwise and its shape (c') with r_E : electrode radii, r_H : holder radii, and r_R reactor radii.	142
Figure 7.3	Current distributions across the cathode for 2D and axy-symmetrical configuration (a) $d_E=20$, $r_E = 10$, (b) $d_E=10$, $r_E = 5$, (c) $d_E=8$, $r_E = 4$, (d) $d_E=4$, $r_E = 2$.	144
Figure 7.4	Pattern feature geometries (a) fully exposed anode, (b) a single feature, (c) two features, (d) three features with feature width (exposed anode, A), feature spacing (resist, unexposed (B)), and the feature height (resist thickness, C)	145
Figure 7.5	j/j_{avg} across the cathode vs. normalised electrode length (x/L), on a single feature, at 600 s deposition time, various feature size (no patterned, 1 – 5 mm) with different applied current densities corresponding to the feature sizes.	146
Figure 7.6	Normalised thicknesses (Thickness/average thickness) along the cathode vs. normalised electrode length (x/L), on a single feature, at 600 s deposition time, with different applied current densities corresponding to the feature size.	147
Figure 7.7	Current densities across the cathode vs. normalised electrode length (x/L), on two features (0.3 mm width) with feature spacing 1 – 5 mm, at 600 s deposition time and applied current density of -8.18 mA/cm^2 (anode area).	147
Figure 7.8	Deposit growth across the cathode vs. normalised electrode length (x/L), on two features (0.3 mm width) with feature spacing (a) 2 mm and (b) 5 mm at various deposition times and applied current density of -8.18 mA/cm^2 (anode area).	149
Figure 7.9	Current densities across the cathode vs. normalised electrode length (x/L), on three features (0.3 mm width) with feature spacing 2 and 1.5 mm, at 100 - 300 s deposition time and applied current density of -7.17 mA/cm^2 (anode area).	150
Figure 7.10	Deposit growth across the cathode vs. normalised electrode length (x/L), on three features (0.3 mm width) with feature spacing 2 and 1.5 mm, at various deposition times (100 – 300 s) and applied current density of -7.17 mA/cm^2 (anode area).	151
Figure 7.11	Comparison of simulated and experimental deposit shape development in the nickel pattern transfer on 1 mm x 5 mm feature, for 600 s deposition time, and applied current density of -4.53 mA/cm^2 (anode area) (— —) simulated data secondary current distribution, (- - -) Simulated data primary current distribution (■) Experimental data points, (———) polynomial approximation of experimental data).	152

-
- Figure 7.12** Comparison of experimental and simulated shape evolution for a three-feature configuration at current density of -7.17 mA/cm^2 for processing time of 300 s, (—) simulated data secondary current distribution, (---) Simulated data primary current distribution, (•) Experimental data points, (—) polynomial approximation of experimental data, and (---) simulated data at higher electrolyte. 152
- Figure 7.13** Comparison of experimental and simulated shape evolution for a three-feature configuration at current density of -7.17 mA/cm^2 for processing time of 600 s, (—) simulated data secondary current distribution, (---) Simulated data primary current distribution, (•) Experimental data points, (—) polynomial approximation of experimental data, and (---) simulated data at higher electrolyte. 153
- Figure 7.14** Comparison of secondary and primary current density distribution vs. normalised electrode length (x/L), on three features (0.3 mm width) with feature spacing 2 and 1.5 mm, at 300 s deposition time and applied current density of -8.15 mA/cm^2 (anode area). 150

LIST OF TABLES

<u>Table 2.1</u> Technical data of commercially available and commonly developed electrolytes for nickel electrodeposition available in the market and publications.....	24
<u>Table 3.1</u> Ionic conductivity of cations and anions involved in the electrolytes	31
<u>Table 3.2</u> Ionic mobility (u) of several components involving in the process	32
<u>Table 3.3</u> Reactions and Equilibrium Formulae of nickel in water	37
<u>Table 4.1</u> Calculated conductivities for nickel solutions containing different concentrations of Ni ²⁺	50
<u>Table 4.2</u> Conductivities (calculated and measured) and pH for the selected nickel solutions	51
<u>Table 4.3</u> Characteristic of manually fabricated pattern features in millimetre scale.	60
<u>Table 4.4</u> Characteristic of micropattern manually prepared using kapton tape	61
<u>Table 4.5</u> A summary of feature sizes and area of micropattern prepared by photolithography structure 1	63
<u>Table 4.6</u> A summary of feature sizes and area of micropattern prepared by photolithography structure 2	63
<u>Table 4.7</u> Temperatures and Conductivities of standard solution for the pH meter calibration.	66
<u>Table 4.8</u> Ultrasound amplitudes with their corresponding power densities	70
<u>Table 4.9</u> the applied current densities and deposition times for each pattern structures.	70
<u>Table 4.10</u> Samples conditioning and treatment for copper diffusion investigation	73
<u>Table 5.1</u> Comparison of Commercial and commonly developed nickel electrolyte and nickel electrodeposition solutions for EnFACE process	75
<u>Table 5.2</u> Comparison of cathodic polarisation data for 0.19 M nickel sulfamate at 2 mV/s scan rate between non-agitated Enface system with fully exposed anode and RDE system	81
<u>Table 5.3</u> A summary of the kinetic data and the results of the analytical calculation of the kinetic of nickel electrodeposition in the electrolyte of 0.19 M nickel sulfamate.	85

Table 5.4 Physicochemical properties and kinetic parameters of the electrolyte used in micropattern transfer process simulations. κ is the measured electrolyte conductivity, j_0 is the calculated exchange current density, and α is the calculated cathodic transfer coefficient, for comparison other data in literature are also listed.	87
Table 6.1 The applied current densities value for each pattern feature size and structure.	92
Table 6.2 Feature spread of nickel pattern transfer on 1 mm x 5 mm feature size at different deposition time at applied current density of -4.53 ± 0.55 mA/cm ² presented as ratio of deposited feature width (D) and original feature (O).	96
Table 6.3 Current efficiency of nickel pattern transfer on 1 mm x 5 mm feature size at various deposition times at applied current density of -4.53 ± 0.55 mA/cm ² .	98
Table 6.4 Feature spread of nickel pattern transfer on micropattern feature (parallel three lines structure 1) via galvanostatic plating at -7.17 ± 0.92 mA/cm ² for 300, with M - middle line, CE - feature with 1.5 mm gap from middle line, FE - feature with 2 mm gap from middle line, presented as ratio of deposit width (D) and the original feature (O).	100
Table 6.5 Current efficiency of nickel pattern transfer on micropattern feature (parallel three lines structure 1) via galvanostatic plating at -7.17 ± 0.92 mA/cm ² for 300 s, with M- middle line, CE- feature with 1.5 mm gap from middle line, FE- feature with 2 mm gap from middle line.	101
Table 6.6 Feature spread of nickel pattern transfer on micropattern feature (structure 2) via galvanostatic plating at -7.59 ± 0.92 mA/cm ² for 125 s, with LM-middle line, SRL-small rectangle 2 mm gap from middle line, SRR- small rectangle 1.5 gap from middle line, D = deposited feature width and O=original feature width.	104
Table 6.7 Current efficiency of nickel pattern transfer on micropattern feature (structure 2) via galvanostatic plating at -7.59 ± 0.92 mA/cm ² for 125 s, with LM-middle line, SRL-small rectangle 2 mm gap from middle line, SRR- small rectangle 1.5 gap from middle line.	104
Table 6.8 Large square shrinkage and thickness of deposited nickel obtained from photolith micropattern feature structure 1 at current density of -0.91 ± 0.07 mA/cm ² for 300 s and 600 s.	109
Table 6.9 Feature spread of nickel pattern transfer on photolithographed micropattern feature structure 2 at 1.93 ± 0.46 mA/cm ² for 300 s.	112
Table 6.10 A summary of identification of nickel chemistry based on the peaks and binding energy observed from the XPS scan in Figure 6.17 – 6.19 for a deposited nickel feature of 1 mm x 5 mm on copper substrate.	126

Table 6.11 Identification of nickel chemistry based on the peaks and binding energy observed from the XPS scan in Figure 6.20 for a deposited nickel feature of 1 mm x 5 mm on copper substrate annealed at temperature of 180 - 200 °C for 5 – 10 min	126
Table 6.12 A summary of feature broadening measurements of the nickel deposit obtained under ultrasound wave of 18 and 26 W/m ² power densities.	129
Table 6.13 Comparison between photolithographic patterning and Enface process on the assessment of energy consumption, chemical usage, and labour cost	132
Table 7.1 Physicochemical properties and kinetic parameters of the electrolyte used in micropattern transfer process simulations. κ is the measured electrolyte conductivity, $D_{Ni^{2+}}$ is Diffusion coefficient of Ni^{2+} , j_0 is the calculated exchange current density, and α is the calculated cathodic transfer coefficient.	140
Table 7.2 Electrodes and holders size of electrochemical cell used in the simulation	143

LIST OF SYMBOLS

∇p	Hydrostatic pressure gradient	$\text{kg m}^{-2}\text{s}^{-2}$
$\nabla\phi$	potential gradient	Volt
a	activity of ion	
A_{wt}	Atomic weight of deposited metal	gram mol^{-1}
α_A	Anodic charge transfer coefficient	
α_C	Cathodic charge transfer coefficient	
β	instrumental line broadening	
β_x	stability constant of metal complex	
C	Molar concentration	mol m^{-3}
D	the diffusion coefficient	$\text{m}^2 \text{s}^{-1}$
E	Applied potential	V
E^0	standard potential	V
E_e	equilibrium potential for a single electrode	V
$E^{0'}$	formal potential	V
E_{cell}	The cell potential	V
ϵ	dielectric constant of the solution	Farad m^{-1}
η	overpotential	V
F	Faraday's constant	C mol^{-1}
g	Gravity constant	m s^{-2}
γ_i	activity coefficient of species i	
h	thickness of the deposit	cm
I	Applied current	A
j	Current density	mA cm^{-2}
j_0	the exchange current density	mA cm^{-2}
K	shape factor	

k	Kinetic constant	s^{-1}
κ	molar conductivity	$S\ m^{-1}$
l	Length of the feature	cm
λ_{\pm}	ionic conductivity	$S\ m^2\ mol^{-1}$
λ	x-ray wavelength	nm
m	Quantity of the deposit	mol
M	molarity	$mol\ L^{-1}$
μ	Dynamic viscosity	centipoise (cP).
n	number of transferred electrons	
N_i	the flux of mass transport	$mol\ m^{-2}s$
ω	Angular velocity	$rad\ s^{-1}$
ϕ	Cathodic current efficiency	
Q	Applied electrical charge	C
Q_j	the charge required for the reaction of interest	C
Q_{tot}	the total applied charge	C
r_R	Rate of reactions	$mol\ l^{-1}\ s^{-1}$
r	Radius of the RDE	cm
R	universal gas constant	$J\ K^{-1}\ mol^{-1}$
ρ	density of the deposit	$g\ cm^{-3}$
Re	the Reynolds number	
R_i	the production rate of species i	$mol\ m^{-2}\ s$
S	surface area of the deposit	cm^2
Sc	Schmidt Number	
Sh	Sherwood number	
t	Processing time	s
T	absolute temperature	K
Θ	A projection exposure angle	rad
θ	Bragg angle	rad

τ	crystallite size	nm
u_{\pm}	ionic mobility	$\text{m}^2\text{s}^{-1}\text{V}^{-1}$
u_i	the mechanical mobility of the species	$\text{m}^2 \text{mol J}^{-1} \text{s}^{-1}$
ν (<i>upsilon</i>)	Kinematic viscosity	$\text{cm}^2 \text{s}^{-1}$
v	Linear velocity (solvent)	m s^{-1}
V	volume of the deposit	cm^3
ν^{+}/ν^{-}	numbers of moles of cations / anions from one mole dissolved electrolyte	
w	weight of the deposit	g
W	The energy used in the electrodeposition	joule
w_d	a half of the deposit width	cm
x	Distance between two points	cm
x/L	Normalised electrode length	
X, Y, Z	Cartesian Coordinates system	
z	number of electrons/charge in electrode process	

LIST OF ABBREVIATIONS

ALD	atomic layer deposition
CCD	continuous charge and deflect
CE	counter electrode
CVD	chemical vapour deposition
DC	direct current
DOD	dot on demand
EBM	electron beam machining
EcM	electrochemical micromachining
EcP	electrochemical printing
ECR	electron cyclotron resonance
EDHA	electro-hydrodynamic atomisation
EDM	electrical discharge machining
EDX	energy dispersive X-ray
EnFACE	electrochemical nano-micro-fabrication by flow and chemistry
FIB	focus ion beam
GPES	General Purpose Electrochemical System
IC	Integrated circuit
ICDD	International Centre for Diffraction Data
ICP	inductively coupled plasma
ITO	indium tin oxide
LBM	laser beam machining
LDI	laser direct imaging
LSV	linear sweep voltammetry
MEMS	micro-electromechanical system
MITRe	multi ion transport and reaction

NHE	normal hydrogen electrode
NEMS	Nano-electromechanical system
OCP	open circuit process/potential
PVD	Physical vapour deposition
PTFE	Polytetrafluoroethylene
PVC	polyvinyl chloride
PZT	Lead Zirconate Titanate
RDE	rotating disc electrode
SHE	standard hydrogen electrode
SCE	saturated calomel reference electrode
SEM	scanning electron microscope
US	ultrasound
UV	ultraviolet
UV-Vis	ultraviolet-visible
WE	working electrode
XPS	X-ray Photoelectron Spectroscopy
XRD	X-ray diffraction

Chapter 1

Introduction

1.1. Background

Microdevices refer to microfabricated devices with typical dimensions between 0.02 and 100 μm . Owing to a progressive miniaturisation, the devices have shrunk from an initial dimension of millimetre down to nanometre range ^[1-4]. The miniaturisation gains advantages of smaller size which results in reducing raw material usage ^[5, 6], minimising waste ^[7, 8], and less production cost ^[6, 9] as well as improving the device performance and flexibility to integrate with other devices ^[3, 4, 6, 8].

The continuing advancement of the microscopic devices plays a key role in the rapid growth of modern technologies in various research areas such as microelectronics ^[10, 11], microfluidics ^[5, 7], optoelectronics ^[12, 13], microsensor ^[9, 14, 15], medical ^[16] biomechanics ^[17] and micro-electromechanical system (MEMS) ^[18, 19]. Such attractive market opportunities in business sector has become one of the major driving forces for the development of microdevices as it has become a multibillion dollar global industry in recent years ^[20, 21]

The technologies used in manufacturing such small devices for a wide range of applications are known as microfabrication. A standard process for microfabrication is conceived over decades and has been developed since the invention of transistor in 1947 ^[1, 2]. The process consists of several stages ^[1, 2, 22] including the most crucial step of patterning process. The quality and reliability of the generated pattern on the devices are essential in imparting their functionality ^[1, 2, 7, 23]. Therefore, various approaches have been developed to achieve such pattern transfer that is technologically viable and economically feasible ^[1, 2, 24].

Even though a number of technologies are available for pattern transfer, currently lithography is the most popular method ^[2]. Several lithography techniques are available for aligning pattern onto substrate i.e. ion-beam lithography ^[25, 26, 27, 28], electron-beam lithography ^[29, 30, 31], and photolithography ^[32-35]. Photolithography, by far, is the most extensively used method in the industries ^[1, 2, 36]. The technique is a less expensive and capable of achieving a relatively good resolution of submicron. Moreover, the chemistry and the technology of photolithography have been well established over long period ^[36-39], which have allowed it to be a platform and standard technology to achieve the pattern replication ^[1, 2, 36]. Consequently, this technology is extensively used to manufacture a wide range of microdevices, for instance integrated circuit, printed circuit board, sensors and actuators ^[36, 37]

1.2 Photolithography

Photolithography is capable of defining a pattern feature down to 37 nm wide with a resolution of 90 nm^[40]. If the microdevices require a pattern feature below 37 nm, advanced lithography methods i.e. ion-beam or electron beam is used^[2, 40].

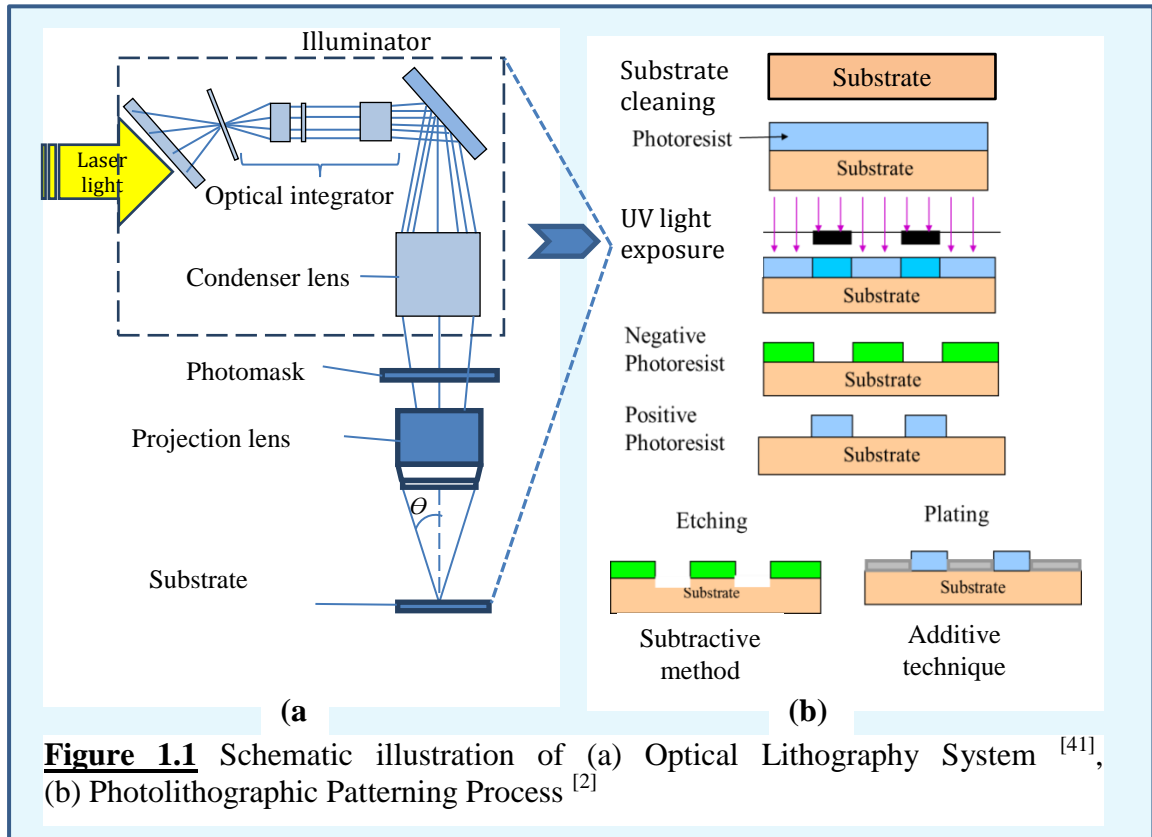


Figure 1.1 Schematic illustration of (a) Optical Lithography System^[41], (b) Photolithographic Patterning Process^[2]

The technology utilises optical means and a specific wavelength of ultraviolet (UV) light. A desired pattern is obtained by exposing a photoresist-covered substrate to UV light through a predesigned photomask. The more soluble resist due to exposure is removed using a developer solution to align the pattern onto to the substrate. The photolithography system is illustrated in Figure 1.1 (a)^[2, 41].

Photolithography patterning process is a multistage route involving a set of processes summarised in Figure 1.1 (b). The process is initially begun with cleaning the substrate from any possible contaminants and covering each individual substrate by using a photoresist. A photoresist pattern is created by subsequent steps including soft bake, ultraviolet (UV) light exposure, development, and hard bake^[2]. The resist pattern is used as a mask in the subsequent step through which a functional pattern on the substrate is defined by using either an additive or a subtractive method. Finally, when the remaining resist is stripped off, the desired functional pattern is left behind^[2].

1.2.1 Substrate cleaning

Cleaning the substrate from any contaminants prior to lithography is an essential step as the contamination can cause undesirable defects on the photoresist pattern^[2] that may lead to the microdevice faulty^[42]. To avoid any further contamination that possibly causes severe defects to the micropattern^[42], the whole process of photolithography takes place in a specifically designed and thoroughly controlled area named a clean room with respect to contaminants, temperatures, air pressure, humidity, and lighting^[2, 41].

1.2.2 Photoresist coating

The contaminant-free substrate is ready to be coated with a photoresist. Photoresist is a light-sensitive polymer resin that chemically changes when exposed to UV-light. The photoresist may become more soluble or insoluble to a particular chemical solvent^[2, 43]. Photoresist mainly comprises a polymer (base resin), a sensitizer, and a solvent. The UV-light exposure triggers a photochemical reaction that changes the structure of the polymer either by breaking the polymer chain down (positive type) or cross linking polymer side chains (negative type)^[2]. The sensitizer additive has a function of controlling the reaction. The viscosity of the photoresist adjusted by the solvent allows coating application on the substrate^[2]. The coating process is carried out either by a typical method, spinning, or by alternative techniques i.e. spraying, printing, and electrophoresis^[2].

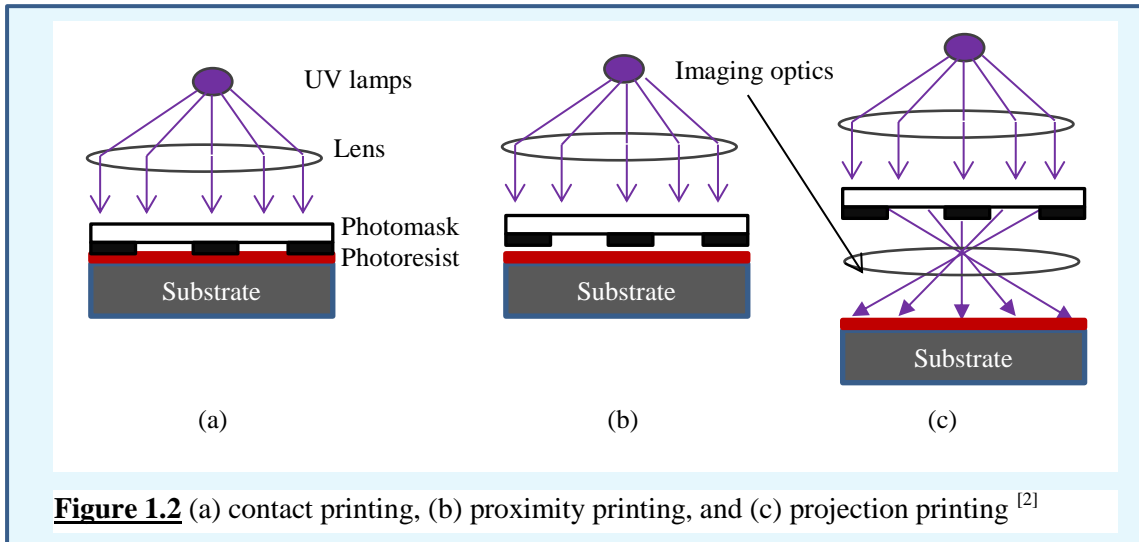
1.2.3 Soft Bake

After coating process, about 15% solvent still remains in the freshly resist-coated substrate. An internal stress due to the spinning may also be left behind. A soft bake is necessary to eliminate the solvent and the stress as well as to increase the photoresist-substrate adherence. Appropriate temperature, baking time, and procedure are required to ensure the solvent being sufficiently removed. Over baking due to inappropriate time or temperature causes damage in photo-reactive component of photoresist reducing its sensitivity^[2].

1.2.4 Exposure

The resin-coated substrate is exposed to ultraviolet (UV) light through a patterned photomask. The current UV used is in the range of 193-436 nm^[44] generated from ArF lasers^[2]. To achieve a pattern with good resolution, the level of light intensity is determined based on the lithographic sensitivity and light absorbency of the resist.^[2] Photomask is a pre-designed patterned tool utilised in repetitively duplicating a desired

feature on photoresist-coated substrate. The mask is typically a rigid material such as flat glass (transparent to near UV) or quartz plate (transparent to deep UV), covered with a patterned opaque material (about 100 nm thick ^[1]) i.e. chrome ^[2, 45]. The feature of the pattern is defined by the transparent parts of the mask, as the opaque material absorbs and blocks the incident light to pass through ^[2, 45].



The mask fabrication process has to be carefully inspected to ensure the photomask is defect free. As a consequence, the photomask manufacturing process is expensive and time consuming.

According to the position of the mask, there are three different approaches to carry out the UV light exposure including contact printing, proximity printing, and projection printing (Figure 1.2). At present, photolithography process mainly utilises the projection printing method due to its reliability ^[2].

1.2.5 Development

The selective removal of the photoresist due to the different resist solubility creates a relief pattern that is subsequently used as a mask for patterning process. The exposed area of a positive photoresist becomes more soluble to a developing solvent. Hence, a similar pattern with the mask will be formed on the substrate. Whereas the exposed area of negative photoresist will be less soluble, accordingly the unexposed area is removed by a developer solution to form a reverse pattern compared to the mask ^[32]. To ensure the development process is optimally achieved, the developer solution should be (1) properly selected according to the type of photoresist, (2) appropriately diluted, and (3) operated at a sufficient processing time ^[2].

1.2.6 Hard bake

After development, an undesirable resist, a residual coating solvent, and a developer solution residue are commonly left behind. In some cases, the adhesion of photoresist also decreases due to penetration of developing solvent underneath the photoresist or due to swelling of the photoresist. Post baking or also known as hard baking is crucial step to eliminate the residual resist, solvent, and developer as well as to regain the adherence and the hardness of the photoresist. The resist-coated substrate is hard baked at slightly higher temperature than the soft baking which is around 120 – 180 °C for 20 – 30 minutes^[46]. As hard bake is a final step of photolithography, a resist-patterned substrate after this stage is ready to use in subsequent process i.e. pattern transfer.

1.2.7 Photolithography challenge

In practical aspects, photolithography encounters two main challenges particularly in a photoresist technology and pattern imaging process^[47]. Uniform, well adhering and high reliability resist coatings are required for the subsequent patterning process^[47]. Photolithography on a non-planar or complex topography often raises several issues i.e. a lack of step coverage and photoresist adherence as well as thickness homogeneity^[47]. In addition, pattern imaging on extreme topographies has challenges in image quality i.e. a low depth focus and fidelity^[2, 47]. Recent development on the technology of photolithography have focused on increasing performance of the process for a wider range of topography, a better resolution and registration, as well as a higher productivity^[2].

1.3. Patterning Process

Pattern transfer is a process to generate a functional pattern on the substrate. The pattern generation is one of essential steps in microfabrication technology^[1, 2, 23], hence it is important to critically review the process. The pattern transfer can be attained by either additive or subtractive technique^[1, 2]. This patterning through the lithographed resist pattern is also well known as a process of pattern transfer through a mask^[36, 48]. Some popular methods of additive and subtractive pattern transfer technology will be briefly described in the following sub-chapters.

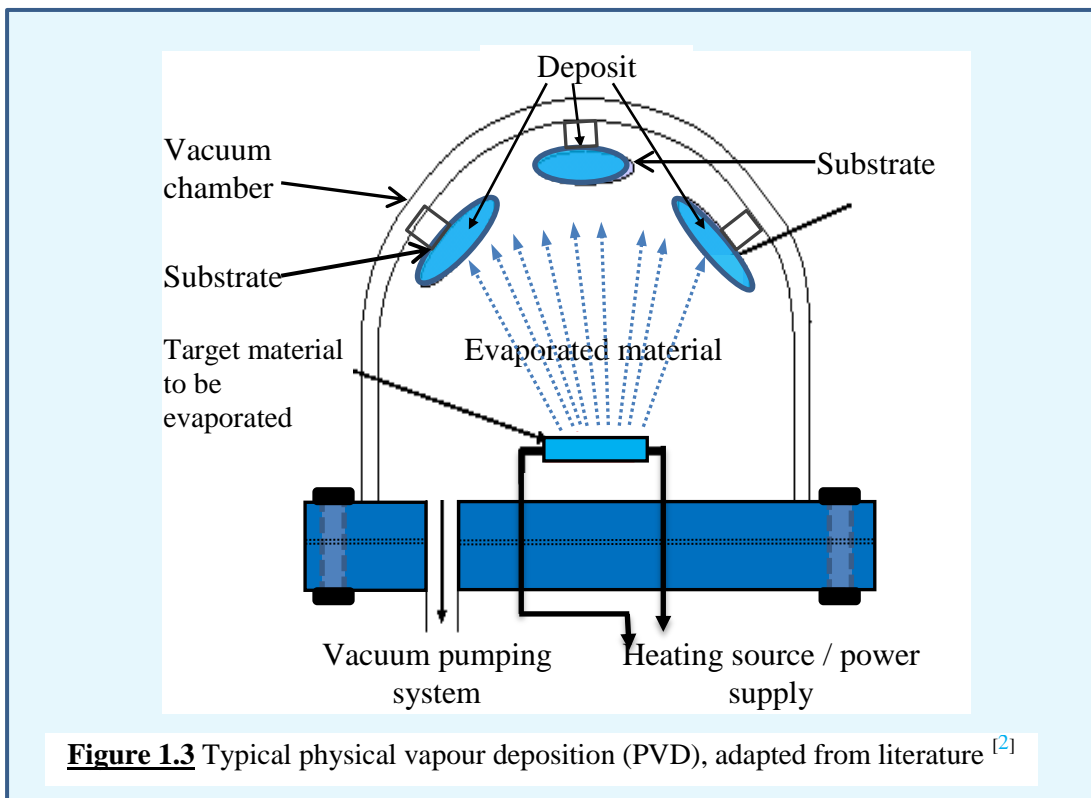
1.3.1 Pattern Transfer with Additive Method

Additive methods for pattern alignment which are also known as deposition techniques involve a process of selectively adding materials to a work piece to construct

a microstructure ^[2, 49]. The procedures for additive process can be categorised according to energy or method used in the process to obtain the thin film i.e. mechanical, thermal, chemical, or electrochemical. Physical vapour deposition (PVD), chemical vapour deposition (CVD), and electrochemical deposition techniques are amongst the most popular techniques ^[1, 2].

Physical Vapour Deposition

Basic concept of physical vapour deposition (PVD) is obtaining a film deposit from evaporated atoms of desired material by condensation onto a substrate in a vacuum. There are various methods for emitting the material atoms applicable in the PVD which mainly can be categorised into vacuum evaporation ^[1, 2], sputtering ^[1, 2, 50], laser ablation ^[2], and ion plating techniques ^[1, 2, 50 - 52]. The principle of PVD is illustrated in Figure 1.3.



The PVD technique is extensively used in fabrication of single and multilayer thin films ^[53]. PVD is also applicable for deposition of high melting point metals and metal alloys such as TiW, TiN, and ZnO ^[1]. The rate of deposition using PVD is typically 0.1 – 10 nm/s. However, PVD technology suffers from shortcomings of a relatively low deposition rate, a line-of-sight deposition, inefficient desired material usage, sophisticated and expensive equipment cost ^[1, 2, 54].

Chemical Vapour Deposition

Chemical vapour deposition (CVD) is a technology to obtain thin layer of solid deposit on a substrate involving a chemical reaction and/or a dissociation of reactants in an activated gaseous phase by heating, plasma, or light ^[55]. The deposition process requires a relatively high temperature and a chemical precursor. When the reactant gas or precursor gas is admitted into a reaction chamber at an appropriate temperature, the reaction takes place to form solid layer deposit on the substrate ^[56]. Figure 1.4 shows the schematic illustration of a CVD process.

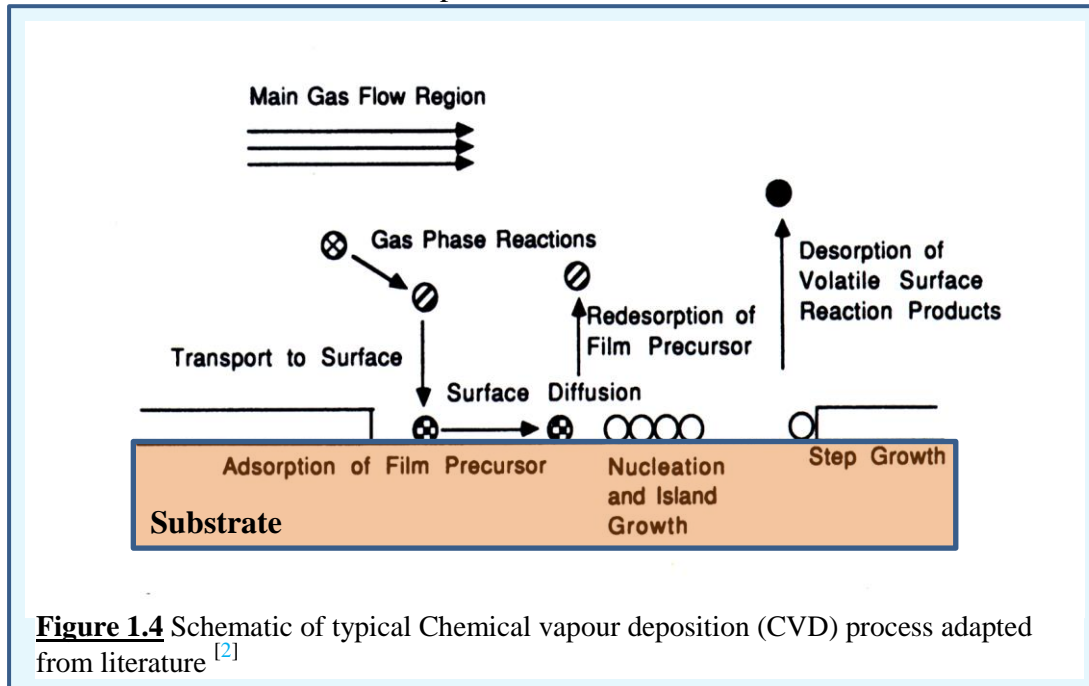


Figure 1.4 Schematic of typical Chemical vapour deposition (CVD) process adapted from literature ^[2]

Several variants of CVD are available for industrial application including low-pressure CVD, very-low-pressure CVD, plasma-enhanced CVD, high-density plasma CVD, atomic layer deposition (ALD), and the most advanced technique in CVD - namely, atmospheric pressure CVD, metal-organic CVD, and vapour phase epitaxy ^[2, 55, 56].

CVD technology is relatively well established and broadly used in many commercial applications such as electronics, optoelectronics, surface thin film coating, extraction-pyro-metallurgy, and fibre or composites materials ^[55, 57]. A wide range of materials as a pure element or mostly in the form of material compounds can be deposited by this technology ^[57]. The CVD method provides several advantages compared to PVD technique i.e. it produces uniform, pure, and homogeneous deposit films. Orientation of the product, surface morphology, crystal structure, and deposition rate can be controlled by adjusting appropriate parameters such as surface chemical reaction and mass transfer ^[1]. In addition, the CVD process takes place at a relatively low temperature. However, the main issues of CVD technology are the degree of

selectivity^[58], limited thickness of film (only 10 – 1000 nm)^[1], complex reaction process, sophisticated equipment, high processing cost, and less environmentally friendly due to the generation of hazardous chemical waste^[55].

Electrochemical Deposition

Electrochemical deposition refers to a process of material deposition on to a work piece involving electrochemical reaction. Electrolytic deposition and electroless deposition are two common types of electrochemical deposition technology^[59]. The former requires an external power supply to drive the electrochemical reaction^[1, 2, 60], whereas no external current is required for the latter^[2, 61]. The quality of the deposit depends upon several fundamental factors i.e. kinetics, mass transfer, and electrochemical parameters^[62, 63].

The application of electrochemical deposition in microfabrication industries ranges from fabrication of photo-circuit board, IC chip, MEMS, NEMS to chip carrier and packages. This is due to several distinctive advantages that are unachievable by other means such as cost effectiveness, simplicity, controllability, selectivity, and flexibility^[2, 64 - 67]. Nevertheless, the electrodeposition method also has some drawbacks such as difficulty in alloy deposition of two metals with very different reduction potentials from a single bath and issues of electrolyte stability^[67],

1.3.2 Pattern Transfer with Subtractive Method

Subtractive fabrication methods employ a process of removing materials from substrate to form microstructure. The microstructure construction can be attained by a number of techniques^[68] categorised into several types based on the media of the process such as dry etching or wet etching and the energy used namely, thermal processes or mechanical techniques^[2].

Dry Etching

Dry etching represents a process of solid surface removal in a vapour or gas environment by either physical process (inert-ion bombardment/sputtering), or chemical mechanism (chemical reaction on the surface), or combination of physical and chemical process. Some popular dry etching mechanisms are sputtering or ion beam, chemical, plasma, reactive ion, high density plasma (electron cyclotron resonance, ECR or inductively coupled plasma, ICP), reactive-ion-beam, and chemically-assisted ion-beam etching^[1, 2, 69].

Even though dry processes have a number of advantages i.e. minimum or even zero waste disposal^[2], better resolution etching, good controllability^[70], and prevention

of underlying metal roughening^[71], issues related to high equipment cost, hazardous reactant gases, limited etch depth due to resist erosion, surface damage due to energetic ion bombardment, and limited choice of chemistries can cause problems^[70].

Wet Etching

Wet etching involves a removal of material in liquid environment using an etchant which is usually a chemical solution^[72]. To achieve a desired feature profile of the etch, several steps of wet etching mechanism are available. Wet etching process can be classified into chemical etching, photochemical etching, electrochemical etching, and combined techniques^[2].

Wet etching is preferred in manufacturing a device requiring great surface electronic properties as the method causes nearly no surface electronic damage on the substrate. This technique is also advantageous in a wide range of reactant choices, simplicity, cost effectiveness, and capability to perform crystallographic etching. There are, however, disadvantages in using wet process such as undercut of an overlying resist mask, environmental issues regarding disposal of used solution, difficulty in obtaining vertical feature profile, and less control on dimension of etch profile^[69].

Thermal etching process

A process of material removal from a target feature on substrate is performed by heating. A portion of the work piece is melted or vaporised in order to be subtracted away to form a desired microstructure. In general, there are three types of thermal energy based etching: electrical discharge machining (EDM)^[2, 73, 74], electron beam machining (EBM)^[75], laser beam machining (LBM)^[76, 77], and plasma arc etching^[2]. The requirement of the high energy is the main drawback and sustainable issue of this process. Along with its benefits and drawbacks, the thermal process has been widely utilised in manufacturing microstructure of various substrate materials through etching process for many industries^[2, 77].

Mechanical process

In mechanical etching process, microstructure pattern is physically engraved by a mechanical energy from the collision of highly energised particles with a substrate^[2, 78]. When the highly energetic particles strike the work piece, a plastic deformation zone and micro-scratches are generated to form the desired feature^[2, 78-80]. Typical properties of the particles that can be used in this method are small (several microns in diameter)^[79], angular, hard^[80], non-metallic, and sharp^[2]. The mechanical etching process is applicable for manufacturing microstructure onto a hard and brittle substrate

material ^[78, 80] i.e. glass, ceramic, and silicon wafer coating ^[78, 79], as well as flexible substrates of indium tin oxide (ITO) ^[79]. However, sustainable issues are excessive energy use due to the requirement of a compressed gas ^[2] and it is applicable only for limited number of materials ^[78-80]

1.4 Disadvantages of Photolithographic Patterning Process

Despite the popularity and the continuing development of the photolithographic microfabrication technology ^[1, 2, 81], a number of drawbacks associated to the technique has been identified ^[82 - 85]. The technology has been dynamically advanced to adjust with economic ^[24], environment ^[82, 86, 87], and social demands ^[88, 89].

The drawbacks concerning the process can be listed as follows:

1. Parallel interdependent developments of lithography and the pattern transfer technology are required ^[66, 68].
2. Multistage process possibly leads to an increase in error occurring in each step i.e. lack of UV exposure ^[90].
3. An extensive use of water, a production of copious amount of waste ^[83, 84], and a time consuming process ^[83, 84, 90, 91].
4. Photolithograph on every single work piece requires a huge amount of chemical and processing time ^[83, 84].
5. Pattern feature size obtained in multidevices fabrication may potentially vary due to the degradation of the chemicals as a result of multiple uses ^[90].
6. The use of clean room is unavoidably required which results in expensive operational cost ^[83, 84].
7. A slow and expensive process that hinders alteration to developed technologies and industrial demands ^[90].
8. Considerable efforts including a mask design, digitation, and fabrication that increase inefficiency. In addition, a documentation of unused mask increases maintenance expenses and storage space ^[81].

Recent development in the microfabrication technology is mainly aimed to simplify the manufacturing process in order to achieve more sustainable technique ^[6, 87, 89, 92, 93, 94]. Various approaches have been carried out to develop a more sustainable and to obtain less expensive patterning process ^[95, 96, 97]. An alternative option to develop more environmentally friendly pattern transfer process is by achieving pattern transfer without relying on photolithography of each individual work piece ^[83, 84, 90] or mask-less pattern transfer.

1.5 Maskless Patterning Process

Maskless pattern transfer means a process of obtaining functional pattern on a work piece without requiring a physical rigid mask. At present, available maskless methods are capable to fabricate nanoscale devices, whenever photolithography is inappropriate^[37]. The maskless method can be classified into four major categories i.e. direct imaging, inkjet, electro-hydrodynamic atomisation (EDHA), and electrochemical methods^[37]. The most popular and widely utilised technique is direct imaging^[37], but the inkjet technique also gained more attention in the last decade^[37]. Electrochemical patterning methods have been utilised in a wide range of application as they proposed a number of advantages, however it has a less attention and publication^[9].

1.5.1 Direct Imaging

To align pattern onto a substrate, initially a digitally developed image is transformed into a pixelated image. The pixelated digital image is then defined onto a substrate to form microstructure by specifically designed apparatus such as laser device, focus ion beam (FIB), or inkjet printer^[37].

The best known direct imaging technique is laser direct imaging (LDI). This method uses a focused laser directed to a substrate to create micropattern by deposition or etching^[37, 98]. A chemical or physical reaction could be the reason behind the development of pattern on the substrate. The reaction drives the process of deposition, ablation, sensitization or chemical activation of the substrate material to obtain microstructure^[37].

LDI technique offers a possibility to manufacture a 2D^[99] or 3D pattern^[100]. The 2D and 3D structures can be gained by externally controlling the dimension and the beam through digital instrumentation^[37]. The process of pattern development on the substrate are well explained in a number of publications^[37, 100 – 108] including the variant of LDI^[37, 109]

1.5.2 Inkjet Technique

A pattern on a work piece as an active layer or a pattern mask for later process step can also be created by inkjet method. In this method, multiple material droplets are emitted from an inkjet head device toward a particular area of the substrate to form the desired pattern. The formation of the target microstructure is digitally controlled by a computer system^[37, 110]. There are two categories of inkjet technique, namely continuous charge and deflect (CCD) and dot on demand (DOD). The former produces larger droplets (50 – 500 μm) and a higher frequency of 1 MHz, hence is suitable to

cover relatively large area of substrate. For the latter, the droplets with smaller size (20 – 100 μm) and less frequency are ejected from the nozzle according to a digital input [37, 111].

Several advantages are offered by the inkjet technique, as it is a versatile [112], low cost, low temperature, and environmentally friendly process [110, 111]. However, the method is considered as a sophisticated and complicated, therefore it requires optimisation of the process and the material used [37]. Above all, the technology has been utilised to fabricate micro-sensing components, nano-tubes, nano-wires and other polymer compounds [112] such as bio-adhesive [113].

1.5.3 Electrohydrodynamic Atomisation (EHDA)

The EHDA technique which is also called the electrospray method is a variant of inkjet technology. It differs from other inkjet techniques as the liquid ejected from a nozzle in the form of a thin jet. The thin jet is subsequently broken up into droplets due to the effect of electrical field [37]. The jet dimension which is smaller than the diameter of inkjet nozzle produces smaller droplets which are advantageous of offering a wider range of resolution without being impeded by the diameter of nozzle [37]. The technique also offers a possibility to produce well defined droplets with dimensions ranging between nanometre scale and several micrometres [114].

The electrospray technique has been utilised to fabricate biodegradable alginate microparticles [115], polyetherimide nanoparticles [114] and micromoulding of PZT [116]. However, since EHDA is comparatively new method in inkjet technology, its potential and advantages have not been fully exploited [37].

1.5.4 Electrochemical Microfabrication

A basic principle of maskless electrochemical microfabrication technique is to utilise a localised electrochemical reaction leading to a formation of a small scale structure on a substrate. The localised reaction has been capable of generating the microstructure on the work piece [37, 117-122]. Currently, maskless electrochemical patterning has been achieved by several different methods: electrochemical printing (EcP) [123-126], electrochemical micromachining (EcM) [127-132], nanosecond current pulse method [133], laser-enhanced electroplating [134], and electrochemical nano-micro-fabrication by flow and chemistry (EnFACE) [23, 36, 37, 81, 83, 84, 91, 135].

EcP, shown in Figure 1.5, as an alternative process for microstructure fabrication, provides a number of advantages: (1) EcP is easily scalable [37],

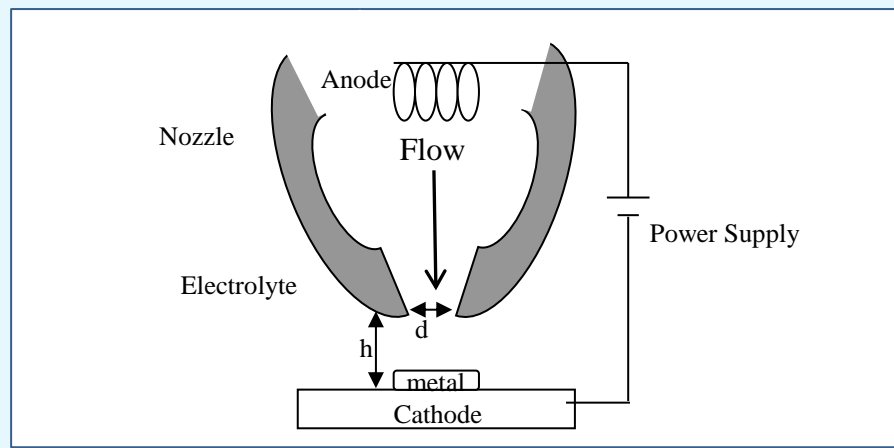


Figure 1.5 Diagram of Electrochemical Printing (EcP)^[37, 123].

(2) requires less cost and processing time^[136], (3) Applicable for many materials of substrate and deposit^[37, 117, 123, 124, 136, 137] and it is capable to manufacture 2D and 3D microstructure^[123]. However, several issues concerning the EcP process has been identified. A small size nozzle of microjet results in a high fabrication cost. In addition, corrosion reaction on the work piece may occur^[37].

Another maskless electrochemical technique, electrochemical micromachining (EcM), exploits a local electrochemical dissolution reaction to form a micropattern on a substrate.

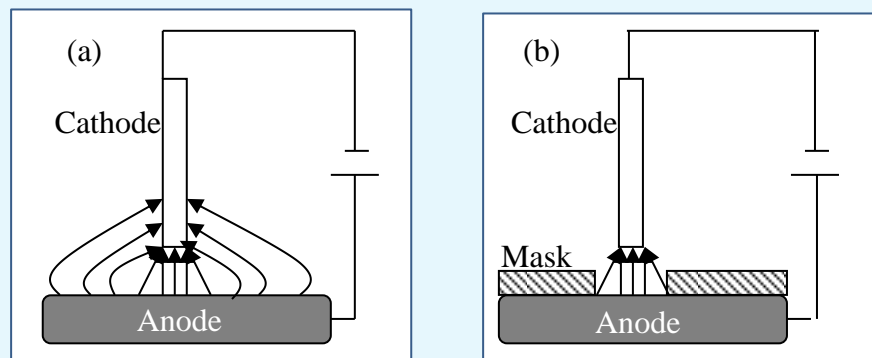


Figure 1.6 Basic principle of Electrochemical Micromachining: (a) without mask and (b) with mask^[37]

The localised electrochemical etching can be gained by means of an insulating mask such as a photo mask on the substrate or a tool (counter electrode), or by placing the counter electrode at a close proximity with the substrate^[127-132]. In later development of the EcM method, a utilisation of nanosecond current pulse and laser are applied to enhance the process^[133, 134]. Basic apparatus of the EcM technique can be seen in figure 1.6^[37].

1.6 EnFACE

A review on microfabrication technology by Roy (2007)^[37] led to a conclusion that an alteration of standard photolithographic process to unconventional method without a physical mask is necessary. Therefore, a novel approach to develop a more efficient microfabrication technology is crucial.

A new concept of mask-less microfabrication technique based on selective electrochemical process without involving photolithography of substrate has been proposed and developed by Roy and co-workers^[23, 36, 37, 81, 83, 84, 91, 135]. The method was named Electrochemical nano and micro-fabrication by Flow and ChEmistry (EnFACE). In Enface system, as shown in Figure 1.7, a desired pattern is defined on an electrochemical tool which serves as anode and placed at a narrow gap opposite to substrate which is cathode.

Here, the two electrodes are located facing each other in an electrochemical reactor. Pattern transfer is achieved by imposing direct or pulse current from external power supply across the two electrodes, provided that the electrolyte resistance is high^[23, 36]. A metal deposit of an exposed area of patterned anode is selectively formed on the cathode via electrodeposition. A successful pattern transfer is achieved by optimisation of electrolyte flow and electrochemistry.

A number of advantages in obtaining metallic pattern generation could be:

1. Multiple substrates can be patterned using a single patterned tool reducing photolithography usage and clean room access. So the process time and capital cost will be significantly minimised^[23, 37, 81].
2. A low concentration of metallic salt in the electrolyte minimises chemical usage and operational cost. This also calls to an efficient, less hazardous, environmentally friendly, and sustainable process^[81].
3. Enface pattern transfer runs at low temperature and low operational pressure. Hence the energy consumption can be minimised^[23, 81]

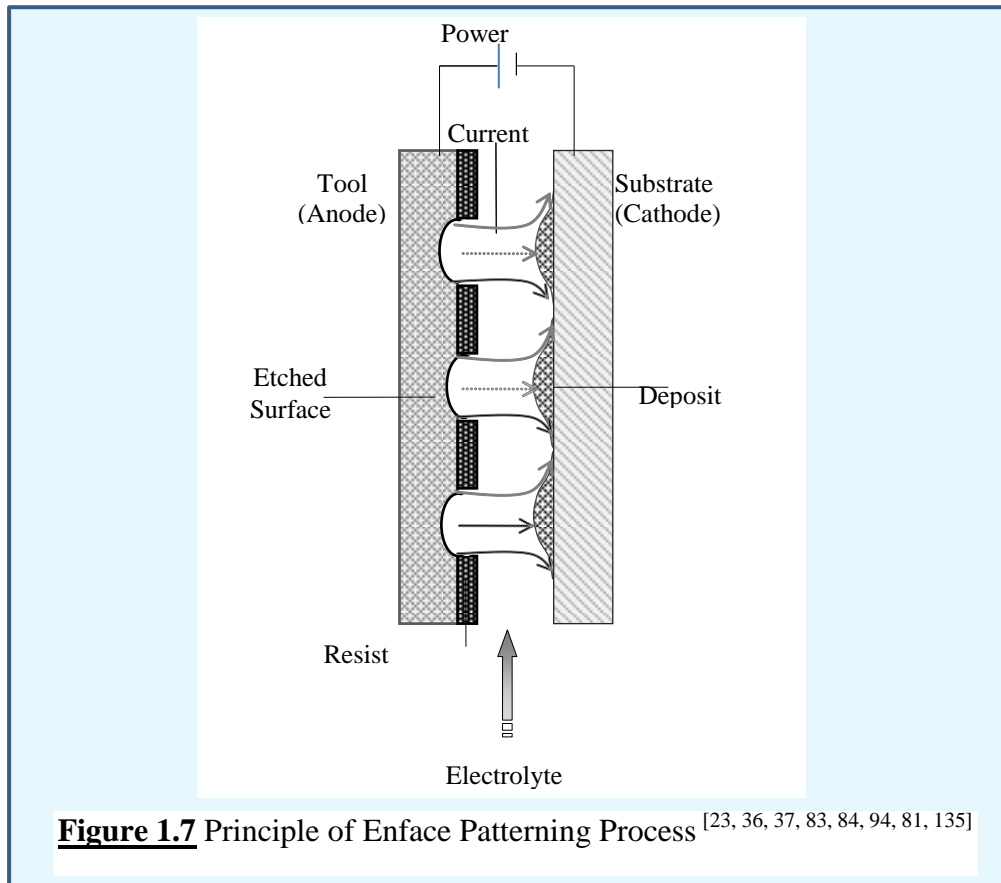
Henceforth, the Enface technology has been utilised to transfer metallic patterns (e.g. copper) that would be useful for fabrication of microdevices i.e. the technology has been proposed to fabricate circuit board^[81].

Despite the apparent advantages, the Enface technology is still facing several challenges. The main concern of this maskless technique is current spreading. As illustrated in Figure 1.7, the current lines spread out into the electrolyte reducing the possibility to transfer the pattern. To minimise the current divergence, the EnFACE technique requires low electrolyte conductivity of very dilute solution and coupled with

a narrow interelectrode gap ^[23, 36, 37, 81, 83, 84, 91, 135]. However, the narrow interelectrode gap causes another significant hindrance i.e. trapped gas due to an excessive gas evolution ^[23, 83] which can severely affect the process. Moreover the electrodes surface may completely be blocked preventing current to pass through.

A number of practical limitations of Enface method have also been identified:

1. Maintain the interelectrode spacing at a tolerable uncertainty, as fixed electrode separation distance ensures reproducibility of the result ^[23, 83].



2. Place the two electrodes parallel vertically facing each other to ensure homogeneous depth/thickness of the pattern ^[23, 83].
3. Electrode preparation i.e. polishing and cleaning is also crucial to obtain a flat and uncontaminated surface, which is also useful for achieving homogeneous pattern thickness ^[23, 83].
4. Hydrodynamic of the solution also play important role on overcoming gas evolution and mass transfer limitation due to high pressure drop at the narrow gap. Circulated solution by flow reactor was observed to improve the process and to some extent could remove trapped bubbles. However, typical industrial

pattern transfers are carried out in a tank based reactor. Hence, finding a method of agitation to improve tank-based process is necessary^[91].

5. Demonstrate the ability of Enface to reproduce acceptable micropattern is necessary in order to achieve a full application of Enface technology into industrial and commercial sector^[91].

Overcoming those limitations is crucial to ensure a practical applicability of Enface technology can be achieved.

Several studies to explore the feasibility of EnFACE patterning technique have been carried out. An initial experimental work on copper pattern transfer through etching has been demonstrated by Scönerberger and Roy (2005)^[23, 83]. The patterning works were carried out in a vertical flow reactor with a copper disc served as an anode, a patterned gold coated glass disc as a cathode and at interelectrode gap of 500 μm . Electrolytes containing copper sulphate (0.1 – 0.5 M), sodium sulphate (0.1 M), and sulphuric acid (0.5 M) with corresponding conductivities range between 2.7 – 56 S/m were employed. Electrolyte flow rates were varied between stagnant and 150 cm^3/s (7.5 m/s). Micropattern features used in this investigation consisted of lines of 100 μm width, 3 mm length and 81 small squares with 100 μm sides with distance of 200 μm each other^[23, 83]. The experiments were carried out using DC galvanostatic, DC potentiostatic, pulsed current and pulsed voltage^[23, 83].

Acceptable pattern transfer were obtained from non-acidified electrolyte purely containing copper sulphate (CuSO_4) as well as $\text{CuSO}_4 + \text{Na}_2\text{SO}_4$ at the solution flow rate of 70 cm^3/s (for current density $\leq 6 \text{ A}/\text{cm}^2$), with the best result at conductivity of 2.7 S/m. A sinusoidal shape was obtained in the acidified solution, whereas a rectangular pattern was produced from non-acidified electrolyte^[23, 83]. Higher current density tended to improve the result with an approximately 1.5 μm etch depth was obtained at 1 A/cm^2 for 180 s. A deeper etch was not observed when the processing time exceeded 180 s. In addition, Potentiostatic pattern transfer was not feasible at potential greater than 2 V due to the excessive oxygen evolution. At voltage of 1 V, the corresponding current density rose and the etched area was relatively rougher^[23, 83].

Pulsed current pattern transfer was found to be unviable because of the excessive oxygen generation on the electrodes. Conversely, best pattern transfer was achieved by pulsed voltage from the electrolyte of 0.1 M CuSO_4 , with peak potential of 20 V, 1 ms pulsed-on time, and 0.02 duty cycle. The depth of etch increased with increase in number of cycles, and the etch depth of 3.3 μm was obtained by 20,000 cycles. In addition, by using pulse potential a better precision and resolution of pattern were

achieved. Along with the achievement, however, two main issues of Enface process were identified: trapped gas bubbles in the electrode gap and difficulty in maintenance of parallel electrode placement ^[23, 83].

A theoretical investigation of pattern transfer by etching process using Enface method has been performed by Nouraei and Roy (2008) ^[84] by simulating the process using ElsyCa-2D software ^[84] as the software is capable of determining potential distribution at micro and macro scale. Physicochemical and electrochemical kinetic data used were from a similar electrolyte of previous work ^[23, 83]. The kinetic data were experimentally determined prior to the simulation. Comparing the outcome of the simulation to the previous experimental result ^[23, 83], a similar physical characteristic of pattern replication was obtained. Different shapes of transferred features were obtained from two different electrolytes. A non-acidified electrolyte produced a rectangular shape, whilst a sinusoidal shape was obtained from more acidic media ^[84].

A further investigation on the phenomena revealed that the change of pattern profile was determined by interfacial reactions during copper dissolution process. The etching process in an acidified solution was controlled by electrolyte conductivity leading to the formation of sinusoidal shape. The analysis also showed that the formation of a rectangular shape of the etch in non-acidified media was caused by surface passivation of the substrate due to an oxidation reaction of copper to cuprous oxide ^[84, 81]. The absence of acid in the electrolyte was found to be the cause of the metal passivation process. Since the rate of passivation is determined by electrochemical and engineering parameters, this analysis revealed how crucial it was to optimise such parameters ^[84, 81].

As pattern transfer is complex process involving engineering and electrochemical parameters, a statistical analysis to identify factors affecting the process and to investigate their interdependency was performed by Nouraei and Roy (2009) ^[138]. The analysis was carried out using commercial software of Stat-Ease Design. This study utilised “a factorial design of experiment” approach to identify the variability and the interaction between factors including the level of the effect of the parameter. This design analysis showed that determining the effects of controllable parameters of the etching process was essential as a small inappropriate parameter setting could significantly affect the result.

The pattern transfer data investigated in this study were collected from the system that was similar to previous study on copper etching ^[23, 83]. Quantification of the effect of the parameters was carried out using 2⁴ factorial method. In this technique, a

set of 16 experiments was performed at lower and upper level of experimentation with an addition of 3 experiments in the mid-level of factorial design. The overall result suggested that the most influential parameters of etching process using Enface technique were current density and etching time. However, the interaction between the two parameters was observed to have more significant effect ^[138].

Following the successful pattern transfer of copper through etching process, Qi-Bai Wu *et al.* (2011) ^[36] investigated a patterning process by means of electrochemical deposition using Enface technique. The experiments were conducted in a flow reactor that was similar to the cell used in etching experiments. In this study, polished copper discs were used as the anodes which were patterned with a photoresist to form a feature of parallel 100 μm lines separated by 500 μm resist gap. Fully exposed nickel discs served as the cathode. The patterned anode and the cathode were specifically placed in the flow cell to achieve a minimum interelectrode spacing of 300 μm . A 0.1 M copper sulphate (CuSO_4) solution was used in the experiment with a rate of circulation was 40 ml/s. A galvanostatic method was used to carry out the copper electrodeposition process using a direct current (DC) power supply or pulse rectifier. A limiting current of 78 mA/cm^2 was initially determined for copper electrodeposition in the electrolyte ^[36].

The overall results of the study suggested that a metallic pattern transfer can be achieved by electrodeposition process. Sharp and bright copper deposits were obtained at applied current densities ranging between 30 and 90 % of limiting current density. Pattern deposit of 120 – 200 μm linewidths greater than original feature of 100 μm have been replicated on the nickel substrates. A maximum thickness of good deposit achieved was 0.8 μm obtained at deposition time of 30 s and at 90% limiting current. In addition, the deposit growth rate achieved by DC plating was about 1.2 $\mu\text{m}/\text{min}$. The pulse plating study was carried out at an average current density of 46 mA/cm^2 and a current on/off time of 10/50 ms corresponding to 0.17 duty cycle. Sharp and relatively smoother deposits were obtained with a total thickness of 2.6 μm for deposition time of 240 s. However, the pulse plating did not reduce the current dispersion. Moreover, the deposition rate for direct current plating was twice as fast as that achieved by pulse plating ^[36], and therefore preferable.

1.7 Outstanding Issues

As previously reviewed, earlier studies of Enface have focused on the etching ^[23, 83] and deposition ^[36] of copper, its usefulness for etching and plating other metals has not been examined. In order to fully utilise Enface in broader industrial application, it is

necessary to demonstrate the capability of Enface to transfer a pattern of various metal on wide range of work piece.

In addition, in those studies, copper was etched and deposited in electrochemical cells under forced convection flow ^[23, 36, 83]. However, typical industrial process of pattern transfer is performed in a tank-based electrochemical cell, where agitation is much slower. The performance of Enface in the typical industrial conditions is unknown.

Finally, the previous studies of Enface were concentrated on electro-etching and electrodeposition of copper that has fast kinetics of reduction-oxidation reaction ^[139]. In other word, electrochemical processes in the copper system are controlled by mass transfer indicated by limiting current densities being observed. Since Enface has never been applied to a system of slow kinetics, its applicability to such systems is unknown.

1.8 Current Work

In this work, a pattern transfer of nickel using EnFACE technology was investigated. Nickel reaction kinetics is relatively slow ^[140, 141], therefore it would be useful to investigate the applicability and the performance of Enface in such system. The pattern transfer experiments were carried out in a typical industrial condition of tank-based cell. As no agitation was applied to the system, the solution remained stagnant without a forced convection mass transfer. Since the technology has never been used in such system, a new approach was developed to study the micropattern electrodeposition of nickel.

Nickel deposit is conventionally obtained from electrolytes containing relatively high concentration of nickel salts i.e. 200.9 – 982.8 g/l (0.8 M – 1.4 M). It would be advantageous if Enface technique could be used to electrodeposit nickel patterns from electrolytes containing much lower concentrations of nickel ions, which could establish if Enface was a resource efficient process.

Another practical reason for the choice of these metals was due to use of nickel in microelectronics ^[142-144, 145]. Nickel with its unique properties is commonly used in various applications as a diffusion barrier, wear and corrosion resistance in a wide range of industries ^[142, 143]. In the last two decades, nickel as an under layer of palladium has gained increasing attention for industrial application, particularly in microelectronic packaging ^[146, 147, 148]. As an under layer of palladium deposit in a Ni/Pd leadframe packaging ^[142, 144, 145] nickel plays a role of preventing diffusion of the substrate (copper or copper alloy) ^[142, 144], protecting the copper leadframe from oxidation and corrosion, and providing solderable and wire bondable surfaces ^[142, 144, 145, 148, 149, 150].

The protecting finish firstly used was two metal layers Ni/Pd plating with nominal thickness 1.27/0.075 μm , and then due to a significant increase of palladium price, the thickness of palladium was reduced and replaced by a gold flash over the palladium ^[145]. The latest leadframe coating which is a metal multilayer of Ni/Pd/Au with a thickness of approximately 0.5/0.013 - 0.02/0.003 - 0.005 μm respectively ^[145, 147] has become the mainstream type of leadframe, because it has a stable wire bondability and solderability ^[149]. So the thickness of nickel layer in the coating is 0.5 μm that would be achieved in the nickel pattern transfer experiments.

Here, it is proposed to use EnFACE technology to selectively electrodeposit nickel pattern onto a copper substrate. A preliminary study reported that the application of Enface in the fabrication of Ni/Pd leadframe would reduce the use of photolithography and minimise the precious metal usage by 18% ^[147]. A systematic approach has been developed in order to achieve nickel pattern transfer.

1.9 Aims and Objectives

The overall project aimed to study the feasibility of the EnFACE process in electrodeposition of nickel layer pattern. This would assist to fully understand the technology in order to open a possibility of exploiting the technique in microelectronics fabrication particularly in leadframe packaging. A success in the fabrication of nickel coating on electronic contact would attract wide range applications of EnFACE in other micro-manufacturing processes, for example, circuit board fabrication.

In order to achieve the ultimate aim of the project, the following objectives have to be performed:

1. Develop nickel electrolytes for pattern transfer process in Enface system based on physicochemical properties data including: metallic ion concentration, pH, and conductivity
2. Design and build up an electrochemical cell for the Enface purpose
3. Perform electrochemical study on the selected electrolytes to identify potential and optimal current density for nickel electrodeposition.
4. Perform pattern transfer of nickel through electrodeposition onto copper substrate on different pattern feature sizes and structures.
5. Initiate study on nickel pattern transfer under ultrasound agitation.
6. Modelling and simulation of nickel pattern transfer process using Elsy are.

Chapter 2

State of The Art Electrodeposition of Nickel

Nickel electrodeposition can be achieved simply by a process of immersing two conductive electrodes (an anode and a cathode) in a conductive solution containing nickel salts. The two electrodes are externally connected to an electrical power supply. When DC or pulse current is imposed to the system, nickel will be electrodeposited on to the cathode. This process occurs because of the presence of positively charged nickel ions in the form of divalent (Ni^{2+}) in the electrolyte solution. The electrical current supplies electrons that react with the positive nickel ions (Ni^{2+}) to produce metallic nickel (Ni^0) deposited on to the cathode surface.

A wide range of industries has been utilising nickel deposit in various applications such as diffusion barrier and corrosion protection^[142, 143]. The performance and the functionality of the deposited nickel relate to its properties and microstructures^[86]. In general, the deposit characteristics and surface structure are primarily determined by the chemistry^[151], electrolyte composition^[152], physicochemical properties^[153], and electrodeposition parameters^[60, 154]. Therefore, understanding all factors affecting the nickel deposition process in non-agitated cell using Enface technique is essential.

2.1 Electrolyte formulation

Electrolyte formulation is important in order to optimally obtain desirable nickel deposit properties^[155]. The development of nickel electrolyte has a long history since it was firstly introduced. Initial formula of nickel electrolyte was developed by Bird (1837), Shore (1840), and Bottger (1843)^[154]. Bird and Shore developed the electrolyte from nickel chloride or sulphate, whereas Bottger practically deposited nickel from nickel and ammonium sulphate solution^[154]. In later development, Isaac Adams^[154] commercialised a nickel solution that was similar to Bottger's but could be operated at neutral pH^[154]. A high pH value indicated by high concentration of ammonia had a tendency to cause a decrease in efficiency and an increase in deposit embrittlement. An addition of boric acid and chlorides in nickel electrodeposition was firstly introduced by Weston and Bancroft respectively^[154]. It was realised that the presence of chlorides in the solution increases the efficiency of nickel anode dissolution^[154].

However, in modern nickel electrodeposition process, the most commonly used electrolyte solutions are Watts-type and sulfamate based baths. The Watts bath, initially formulated by Watts (1916), comprises a combination of nickel sulphate, nickel

chloride, and boric acid in an optimised composition, ^[154]. The sulfamate based electrolyte, firstly commercialised by Cambi and Piontelli (1939), primarily contains nickel sulfamate with an addition of nickel chloride and boric acid. Boric acid is added to the electrolytes as a buffering agent for stabilising the pH on near electrode surface to minimise hydrogen evolution ^[151, 154].

In practical nickel electrodeposition, the two types of electrolytes in a variety of compositions exhibit different characteristics for deposited nickel ^[154]. The properties of the deposit are also affected by operating conditions of the electrodeposition process such as pH, applied current density, and temperature ^[156]. Recent Watts bath formulated based on the initially developed composition is extensively used in many industrial applications due to its advantages. The Watts bath is relatively inexpensive ^[156], simply and easily formulated and used, eliminates use of ammonia, and can be operated at pH of 2 – 5 ^[157]. The electrolyte produces a nickel deposit with good properties in term of hardness ^[157] which are comparatively less brittle ^[158] and have relatively low internal stress (125 to 210 MPa) ^[158]. However, the Watts bath runs at relatively low current efficiency ^[154]

The nickel deposit obtained from sulfamate based baths exhibit distinctive properties such as low internal stress, high ductility, low sulphur contamination, and relatively good mechanical properties ^[60, 153]. They also have high purity, less porosity, and good heat-resistance ^[60, 158] in comparison with Watts bath. The sulfamate solution is also capable of electrodepositing nickel at high current density ^[60], high growth rate ^[153], high current efficiency ^[159], and higher throwing power than sulphate based electrolyte by 16 – 21% ^[60]. Owing to the advantages of sulfamate based baths, nickel for microelectronic applications is usually deposited from sulfamate ^[151-154] or sulfamate-chloride ^[60, 151, 154] electrolytes, where nickel concentration ranges between 0.8 M to 1.4 M ^[60, 154].

To obtain better nickel deposits, chemical additives are usually added to the standard electrolyte. The additives can be categorised to into (1) carrier, (2) brightener, and (3) auxiliary brightener. The carrier additives from aromatic compounds are introduced to the electrolytes for refining grain size. The brighteners such as formaldehyde, coumarin, thiourea are required to obtain bright deposit, but they increase the brittleness of the deposit. In addition, butyne-diol and pyridinium serve as auxiliary brighteners are often needed to promote levelling process ^[60].

Physicochemical properties of the electrolytes are also essential factor in obtaining pure, high conductive, and oxygen free metallic nickel deposit. An available

thermodynamics of nickel-water system i.e. Pourbaix diagram ^[160] suggested that electrodeposition of nickel is significantly affected by the solution pH ^[160]. On the one hand, at low pH (pH<4), hydrogen evolution is facile leading to low current efficiency, rise of pH near the electrode surface ^[60] leading to poor deposit properties (i.e. hydrogenated deposit) ^[60, 161]. Moreover, low solution pH results in higher concentration of proton that could increase the conductivity of the solution. On the other hand, if the pH of the solution greater than 7.5 increases the possibility to form nickel hydroxide (Ni(OH)). Hence In order to deposit nickel a solution pH between 4 and 7.5 is required ^[160, 162].

Compositions of commercially available and commonly developed electrolytes for nickel electrodeposition observed from suppliers, handbooks, and journal papers are presented in Table 2.1. The source references are also listed in the Table.

Table 2.1 Technical data of commercially available and commonly developed electrolytes for nickel electrodeposition available in the market and publications

No	References	Nickel Sulfamate (NiSm)				Nickel Sulfate (NiS)			
		Composition (g/l)	Rate ($\mu\text{m}/\text{min}$)	i (ASD)	η (%)	Composition (g/l)	Rate ($\mu\text{m}/\text{min}$)	i (ASD)	η (%)
1	[154]	NiSm 300-450, NiCl ₂ 0 – 30, BA 30 - 45		.5-30		NiS 225 – 400, NiCl ₂ 30 – 60 BA 30 - 45		3-11	
2	[60]	NiSm 300-360, NiCl ₂ 12-15, BA 30-35		5-12		NiS 250-300, NiCl ₂ 40-60, BA 30-35		2 - 8	
3	[163]	NiSm 300, NiCl ₂ 6, BA 30		2-25		NiS 350, NiCl ₂ 45, BA 37		5	95
4	[148]	NiSm 600, NiBr 40, BA 40		4-40					
5	Supplier: Transene	NiSm 272, BA 40.05		.5-22		NiS 110-275, NiCl ₂ 55-110, BA 11-55		1.1- 4.3	
6	Supplier: Texas Instrument	NiSm 982.8, BA 51.48							
7	Supplier: Riko Chemicals					NiS 225-300, NiCl ₂ 40- 70 BA 35- 45		2 - 8	
8	Supplier: PMD UK	NiSm 467.5–523, NiCl ₂ 8 – 12 BA 25 - 35	1 (at 5ASD)	.2-35		NiS 264, NiCl ₂ 55, BA 40	1 (at 5ASD)	2 - 4	
9	Supplier: Accu Labs Inc	NiSm 271.9, BA 25		.5-54					
10	Supplier: Growel.com	NiSm 412.5, NiCl ₂ 15, BA 30	1.06 (at 5.4 ASD)	2 - 8					
11	Supplier: Luster-on					NiS 205, NiCl ₂ 62, BA 43		4.3	
12	Supplier: A Brite Co.					NiS 240, NiCl ₂ 75, BA 52		4.32	
13	[164]					NiS 350, NiCl ₂ 45, BA 35 Na ₃ Citrate 30, 55°C		2	98
14	[165]					NiS 40, NiCl ₂ 15, BA 10, Sacc 2, 60 °C	0.68	2	95
16	[166]					NiS 7.74, BA 30.91,	0.006	2.78e-5	

18	[167]	NiSm 450, BA 30, Sacc 5, 30 -50 °C	0.3, 945µm at 52 h	2.3					
19	[168]					NiS 158.16, NA2S 11.93, BA 12, +organic extractant		7.5e-4 -0.84 V	96
20	[169]					NiS 262.85, NiCl ₂ 47.54, BA 43.28 2Buthyne-1, 4diol, 50°C	0.0625	3	
21	[170]					NiS 21.03, NH ₂ CH ₂ COOH 15 NaCl 104		0.5	71.4
22	[171]	NiSm 250.85	0.125	1					
23	[172]					NiS 336, NiCl ₂ 16.5, BA 30	1.245 0.49	10.8 5.4	99.2
25	[173]	NiSm 300, NiCl ₂ 15, BA 30		0.1 5	84 98				
27	[151]	NiSm 388.85, BA 50, NiCl ₂ 0, 6.25, 6.5, pH 4, 50 °C		18	95 - 99.9				
30	[159]	NiSm 600, NiCl ₂ 5, BA 40, pH 4, 22-60 °C	0.4 at 2ASD	0.1 – 6.4	96				
31	[174]	NiSm 388.85, BA 50, pH 4		3 - 60	96.2 99.9				
32	[152]	NiSm 300, NiCl ₂ 10, BA 40, At 60 °C and pH 3.8	0.260 0.525	1.5 3					
33	[153]	NiSm 338.67, BA 30, SDS 0.2		1.5	96.8				
34	[175]	NiSm 450, NiCl ₂ 4, BA 40, pH 4.2	0.05 (0°C) 0.09 (5°C)	1.6 3.6					
35	[176]	NiSm 200.86, BA 12.37, 30 °C		1	83				
36	[177]					NiS 240, NiCl ₂ 45, Malic acid 6 pH 4 at 50 °C		6	99.3
37	[178]					NiS 250, NiCl ₂ 55, BA 45 pH 3.5 – 4, at 20°C		0.805	

Remarks: NiSm = Nickel Sulfamate

NiS = Nickel Sulphate

NiCl₂ = Nickel Chloride

BA = Boric Acid

2.2 Electrodes

Nickel can be electrodeposited on a wide range of metallic cathodes such as platinum^[154], copper^[176, 159], nickel^[170], silicon^[179], steel^[180], etc. and metallic alloys including chromium/copper^[178], brass^[171], stainless steel^[168], carbon–polythene^[165], carbon steel^[169], and so on. The selection of the cathode is dependent on the application of the deposited nickel. For example, if the deposited nickel is for a diffusion barrier of an electronic contact, the substrate is copper or copper alloy since they are base metals for the electronic contact.

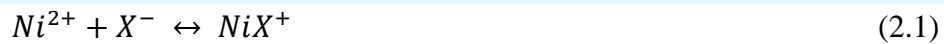
In general, the process of nickel electrodeposition utilises soluble or non-soluble anode^[154, 60, 156]. High purity nickel (99.99%) is often used as a soluble anode in industrial nickel electrodeposition processes to avoid a contamination. Dissolution of the nickel anode generating nickel ions is advantageous in replenishing discharged nickel ion at the cathode. However, the nickel anode may be passivated due to the formation of a resistive layer nickel oxide (NiO and NiO₂). This can occur at high anodic potential^[60] particularly in an electrolyte without addition of chloride, and is indicated by a significant decrease of current density^[60]. In some cases, chloride may be required in order to increase the solubility of the nickel anode and to prevent the passivation^[60, 154].

An alternative soluble anode commonly used in commercial process is a depolarised nickel^[60, 154]. The depolarised nickel comprises 99% nickel or greater, approximately 0.5% nickel oxide, and a trace amount of sulphur. The presence of nickel oxide and sulphur in the depolarised nickel provides uniform dissolution and enhances anodic activity that benefits to maintain nickel ion concentration in the solution. This soluble anode generates slurry; hence it requires vinyon, polypropylene, or orlon anode bags to hold it, in order to prevent electrolyte contamination. The contaminants from the residue may cause the deposit to roughen^[60, 154, 156]. However, the active area of the anode and current densities changes gradually during the process reaching a point when the anode has to be replaced causing interruption of electrodeposition^[60, 154].

Insoluble anodes are also frequently utilised in nickel electrodeposition to avoid unexpected passivation. Insoluble anodes that may be used in all-sulphate solutions are lead, carbon, graphite, or platinum^[154, 156]. Passivation may be avoided by using the non-soluble anodes, however oxygen evolution or other oxidation reaction may occur^[60]. In addition, nickel concentration and pH in the electrolyte gradually decrease that requires periodic maintenance by adding make-up solution and controlling the pH^[60, 156]. This raises the cost of process monitoring and may lower the overall production rate.

2.3 Kinetics and mechanism

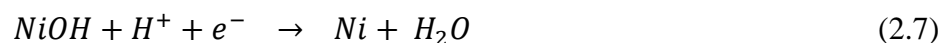
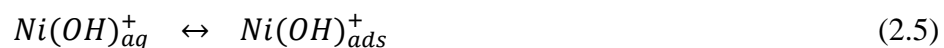
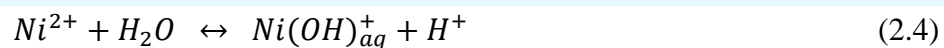
Numerous studies on kinetics and mechanism of nickel electrodeposition from various electrolytes have been carried out by many researchers^[181 - 193]. The investigations suggested that in general the process of nickel deposition involves reactions of two consecutive single-electron transfer steps. An occurrence of adsorbed species onto cathode surface as a part of the mechanism was also observed. The reaction mechanism was also found to be dependent on the electrolyte composition^[181] and pH^[140]. The general proposed mechanism of nickel deposition reactions^[141]:



The anion X^{-} was expected to be representing OH^{-} , SO_4^{2-} , or Cl^{-} , depending on the composition of the electrolytes^[181]. For example, if the electrodeposition is carried out in a Watts bath containing nickel sulphate, nickel chloride, and boric acid, it has been inferred that the anion X^{-} expected to be Cl^{-} and the rate determining step is reaction (2), the first electron transfer reaction^[141, 181].

A further study on electrodeposition of nickel from Watts electrolyte carried out by Oriňáková, R., L. Trnková, et al^[181, 182] suggested that in general the reaction of nickel deposition takes place through three main steps. (i) A chemical reaction for the initiation of deposition, (ii) an adsorption of intermediates on to the electrode surface, and (iii) a reaction of electroactive species involving electron transfer^[181, 182].

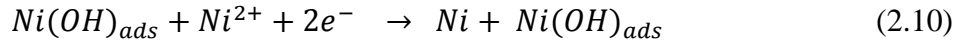
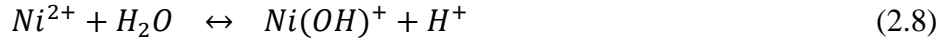
A pathway of sequential reactions proposed by Bockris^[183] tends to be the most relevant mechanism for nickel deposition. The mechanism of nickel electrodeposition in the Watts bath as described by Bockris^[181, 182] is as follows:



Steps 2.4 and 2.5 describe a homogeneous chemical reaction leading to the formation of an intermediate and its adsorption on the electrode surface, Steps 2.6 and 2.7 correspond to slow and fast electron transfer steps

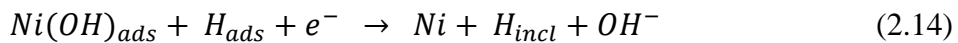
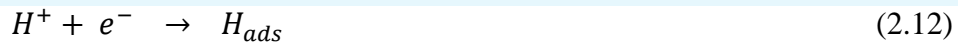
A different mechanism of nickel reactions was introduced by some researchers using un-buffered electrolytes^[181, 183-186]. They identified nickel monohydroxide ion

($Ni(OH)^+$) to be a key species in the charge transfer reaction steps. The first electron transfer reaction (2.9) takes place leading to an adsorbed product. The adsorbed species can follow two parallel electron transfer reactions (equation 2.10 and 2.11) leading to a metallic nickel deposit. The proposed mechanism was presented as follows:



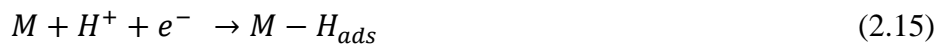
According to Grujicic, *et al* (2004)^[140], the rate determining step for nickel electrodeposition in an electrolyte with lower nickel concentration was the first electron transfer reaction (2.9). Referring to equation (2.8), a lower amount of the active intermediate ($Ni(OH)^+$) is produced as result of the lower nickel content. As a consequence, the rate of the first electron transfer reaction is controlled by the concentration of active intermediate ($Ni(OH)^+$) equation (2.9)) so that it becomes the rate determining step. On the other hand, in a solution with high nickel concentration, there is plentiful supply of $Ni(OH)^+$ which can readily combine with electrons to form $Ni(OH)$. The reaction rate is then controlled by the concentration of adsorbed species as saturation of the electrode surface has been reached. Therefore, in this case, the nickel deposition is controlled by the adsorption step^[140].

All the above sequence of reactions shows that nickel oxides or hydroxides may be co-deposited or form a film on the surface^[187, 188]. In addition, hydrogen evolution reaction tends to occur simultaneously with nickel electrodeposition process. The reaction mechanism of hydrogen evolution was expressed as follows:

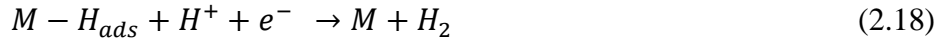


A further study on the mechanism of hydrogen evolution reaction revealed two possible steps of overall reactions described as follows^[181, 182]:

i. A mixture of Volmer reaction (discharge) with Tafel recombination



ii. A combination of discharge and electrochemical desorption

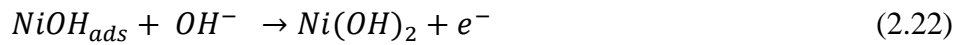


Reactions (2.12) and (2.13) evolve hydrogen, which may affect the morphology of nickel deposit i.e. porous and pitted surface ^[161]. Reaction (2.14) shows that hydrogen may be included (H_{incl}) in the nickel deposit causing high internal stress and embrittlement ^[151]. Therefore, nickel oxides or hydroxides, as well as hydrogen may be co-deposited along with nickel, which would be detrimental to the deposit ^[187, 188].

In the case of nickel anode, nickel dissolves through a sequence of reactions involving hydroxyl ions as follows ^[154]:



Passivation process of the nickel anode takes place through the following reactions ^[154].



2.4 Conclusion

The literature review shows that the type of electrolyte significantly influences the properties of deposited nickel. Deposited Nickel obtained from a sulfamate based electrolytic bath exhibits distinctive characteristics that are appropriate for microelectronic application. Therefore, the sulfamate based electrolyte would be preferable for use in the current project.

According to Table 2.1, nickel electrodeposition is typically carried out in concentrated nickel solutions (i.e. 0.8 -1.4 M) containing nickel salts, pH buffer, and other additives. On the other hand, the Enface process requires an electrolyte with specific physicochemical properties i.e. conductivity of around 2.7 S/m and pH of 4 – 7.5 which requires a dilute concentration and a composition that is different to the commercially and commonly available electrolytes. Therefore, a development of a new electrolyte that is appropriate for use in the Enface system is essential. The composition and the concentration of the electrolyte are determined based on its pH and conductivity.

A soluble anode made of high purity nickel would be a choice to be used in this current work to avoid any contamination due to a stringent requirement of microelectronic devices. The nickel anode is also advantageous in replenishing discharged nickel ions so that a periodic solution make-up is not required. In addition, referring to the mechanism of nickel electrodeposition from an un-buffered solution (Equation 2.8 – 2.11), the first electron transfer reaction (2.9) will be the rate determining step. This is due to the low concentration of nickel electrolyte for Enface process corresponding to the low conductivity.

Chapter 3

Fundamental Aspects

The overall project was to study the feasibility of Ni pattern transfer using Enface technique. In order to achieve this, a systematic approach had to be developed i.e. electrolytes development based on physicochemical properties, chemistry of ions and complexes, and thermodynamics of metal in aqueous solution. In addition, fundamental aspects of the process had to be understood including the basic concept of electrochemistry, mixed potential system, kinetics, and the performance of the process. The development of electrolytes and the fundamental aspects of the process will be thoroughly elucidated in this chapter.

3.1 Physicochemical properties of metals in solution

3.1.1 Conductivity

Earlier experiments and analysis have shown that pattern transfer was achievable at an electrolyte conductivity of around ≈ 2.7 S/m^[23]. As nickel salts are nearly fully ionised in solution^[194-196], the concentration of the salts to be dissolved was calculated using the standard conductance equation^[197, 198].

$$\kappa = \sum c_+ \nu_+ \lambda_+ + c_- \nu_- \lambda_- \quad (3.1)$$

In equation 1, κ is molar conductivity (S/m), λ is ionic conductivity ($\text{Sm}^2\text{mol}^{-1}$), c is molar concentration (mol/l), and the numbers of moles of cations ν^+ and anions ν^- are from one mole dissolved electrolyte. Ionic conductivities of cation and anion involved in the nickel electrolytes are presented in Table 3.1.

Table 3.1 Ionic conductivity of cations and anions involved in the electrolytes^[198, 199]

Cation	λ_+ ($\text{mSm}^2\text{mol}^{-1}$)	Anion	λ_- ($\text{mSm}^2\text{mol}^{-1}$)
Hydronium (H_3O^+)	34.97	Sulfamate ($\text{SO}_3\text{.NH}_2^-$)	4.83
Nickel (Ni^{2+})	4.96	chloride (Cl^-)	7.63

3.1.2 pH

A pH scale is commonly used to define an acidity of solutions. The strength of an acid corresponds to an equilibrium constant of acid dissolution. The dissociation constant of the acid is determined by hydrogen ions (H^+) concentration in the solution. However, due to relatively low concentration of hydrogen, a logarithmic reflection of the H^+ concentration is utilised to express the acidity of solutions which is known as pH. The value of pH is estimated by the following equation:

$$pH = -\log[H^+] \quad (3.2)$$

$$[H^+] = 10^{-(pH)} \quad (3.3)$$

Due to the fact that H^+ is present as H_3O^+ in aqueous solution, pH is also often expressed as:

$$pH = -\log[H_3O^+] \quad (3.4)$$

From the equation 3.2 or 3.4, the pH value depends on the concentration of H^+ in solution. The pH decreases as concentration H^+ increases^[200, 201]. The pH of a solution can be measured by either indicator method or using a pH meter^[201].

The presence of H^+ ions in the electrolyte is also important component in calculating conductivity of the solution due to its high ionic mobility^[197]. Ionic mobility of some cations and anions involved in a nickel sulfamate dissociation process is presented in Table 3.2.

Table 3.2 Ionic mobility (u) of several components involving in the process^[197]

Cation	u_+ ($10^{-8}m^2s^{-1}V^{-1}$)	Anion	u_- ($10^{-8}m^2s^{-1}V^{-1}$)
H^+	36.23	OH^-	20.64
Ni^{2+} [202]	4.99	Cl^-	7.91
		$NH_2SO_3^-$	8.29

An ionic and molar conductivity of the solution relate to the ionic mobility by equation 3.5

$$\lambda_{\pm} = zu_{\pm}F \quad (3.5)$$

$$\kappa = F \sum_i |z_i| u_i c_i \quad (3.6)$$

Where, z = charge, u_{\pm} = ionic mobility, and F = Faraday's constant

As z and F are constant for each material, the value of λ_{\pm} depends on its ionic mobility [198], and the molar conductivity is determined by the ionic mobility and the concentration of solution.

3.2 Chemistry of metal ions and complexes

To form complexed metals, ions or molecules are attached by coordination bond to the metals. The attached ions or molecules are commonly called ligands. In particular case, simple salt of noble metals often have poor stability, too high reduction potentials, and may not be easily dissolvable in solutions. In these unstable solutions, metals may easily precipitate. Furthermore, due to highly positive reduction potential, if a less noble metal is introduced to the solution e.g. as an electrode, a displacement reaction may occur leading to immersion deposition. The unexpected immersion plating tends to produce non-adherent and powdery deposits. A contamination of the electrolyte may also occur from less noble metal due to the displacement reaction. Hence, the complexation of the metals with suitable ligands is useful for increasing the stability and solubility as well as negatively shifting the reduction potential [203, 204]. However, too stable metal complexes cannot be discharged at the cathode leading to a practically impossible deposition process. Therefore, selecting suitable ligands is crucial to design a process that is theoretically and practically achievable [154].

The degree of ligand formation is commonly expressed by stability constant (β_x) defined according to equation (3.7) and (3.8)



$$\beta_x = \frac{[ML_x^{z+}]}{[M^{z+}][L]^x} \quad (3.8)$$

β_x represents a level of the stability of the corresponding metal complex. A low value of stability constant indicates a poorly stable metal complex, whereas a high stability of the complex specified by a large equilibrium constant [201].

3.3 Thermodynamics of metals in aqueous solution

Thermodynamics of electrochemical reaction concerns only the change in energy and entropy. The interrelationship between the two fundamental states drives the reaction to which direction should occur. The direction of the reaction is commonly described by equilibrium constant ^[205]. Parameters of thermodynamics can only be measured for systems at equilibrium ^[63, 205]. Several substantial parameters including electrode potential and its correlation with pH and thermodynamic equilibrium of metals in electrolyte is elucidated in this sub-chapter.

3.3.1 Standard potential

In an electrochemical system, reactions take place at an electrode. The electrode reaction is usually expressed as reversible reduction-oxidation.



An electrode potential of each electrode reaction measured at standard and at equilibrium condition is known as a standard potential. The standard condition represents a state of electrochemical system in which the activity of all components and partial pressures of gases are equal to unity. Equilibrium condition is achieved when the rate of forward reaction is equal to the rate of backward reactions; hence no net change takes place and no current passes on electrode reaction with respect to time. The standard electrode potential is usually measured against a reference electrode of standard hydrogen electrode (SHE). Data of standard electrode potential for various half-cell reactions are well published and can be found in literature ^[63]

3.3.2 Equilibrium Potential

In some cases the condition of the electrochemical system deviates from the standard. Nernst's formula is useful to calculate the electrode potential of non-standard system at equilibrium condition.

$$E_e = E^0 + \frac{RT}{nF} \ln \left(\frac{a_{Oxd}}{a_{Red}} \right) \quad (3.10)$$

Where, E_e = equilibrium potential, E^0 = standard potential, R = universal gas constant
 T = absolute temperature, n = number of transferred electrons,
 F = Faraday's constant, and a = activity of the ion

However, activities of ions (a) in equation 3.10 are not easily measured, leading to an introduction of an activity coefficient (γ_i). The activity coefficient relates the activity and the concentration of component i in a solution by

$$a_i = \gamma_i \frac{C_i}{C_0} \quad (3.11)$$

C_i is the concentration of component i and C_0 is standard concentration which is usually 1 M.

The Nernst's equation (3.10) simply becomes

$$E_e = E^0 + \frac{RT}{nF} \ln \left(\frac{a_{Oxd}}{a_{Red}} \right) = E^0 + \frac{RT}{nF} \ln \frac{\gamma_{Oxd} C_{Oxd}}{\gamma_{Red} C_{Red}} \quad (3.12)$$

$$E_e = E^0 + \frac{RT}{nF} \ln \left(\frac{\gamma_{Oxd}}{\gamma_{Red}} \right) + \frac{RT}{nF} \ln \frac{C_{Oxd}}{C_{Red}} \quad (3.13)$$

At this stage, the formal potential ($E^{0'}$) is introduced as an incorporation of the coefficient activity into the standard electrode potential.

$$E^{0'} = E^0 + \frac{RT}{nF} \ln \left(\frac{\gamma_{Oxd}}{\gamma_{Red}} \right) \quad (3.14)$$

Therefore, Its Nernst equation is given by

$$E_e = E^{0'} + \frac{RT}{nF} \ln \frac{C_{Oxd}}{C_{Red}} \quad (3.15)$$

However, an actual measurement of electrode potential in a real electrochemical system may not be the same as the potential calculated using Nernst's equation because a number of different species may coexist. Side reactions may occur and Interaction between all species in the system may lead to a mixed potential that results in a surface potential which is different ^[205].

3.3.3 Pourbaix Diagram

The effect of pH and electrode potential on thermodynamic equilibrium of metals in an electrolyte solution is represented by Pourbaix diagram. The Pourbaix diagrams which were firstly introduced by Marcel Pourbaix in 1945 for a corrosion study clearly show in what form the metal presents in the solution. For example, when the metal is in the form of metallic ion or being present as a solid or in other forms is displayed in the diagram. The diagrams are useful to predict potential and pH at which the metal electrodeposition is possible to occur ^[206]. However, due to the assumption of equilibrium condition, the diagrams do not involve kinetic considerations. Hence, the reactions may be thermodynamically possible but they may not occur in a real system due to the kinetics restriction ^[206, 207].

The construction of Pourbaix diagrams involves various equilibrium reactions of both chemical and electrochemical reactions. Prior to construct the Pourbaix diagram, reactions including chemical and electrochemical at equilibrium conditions have to be developed ^[160].

Nickel – water system

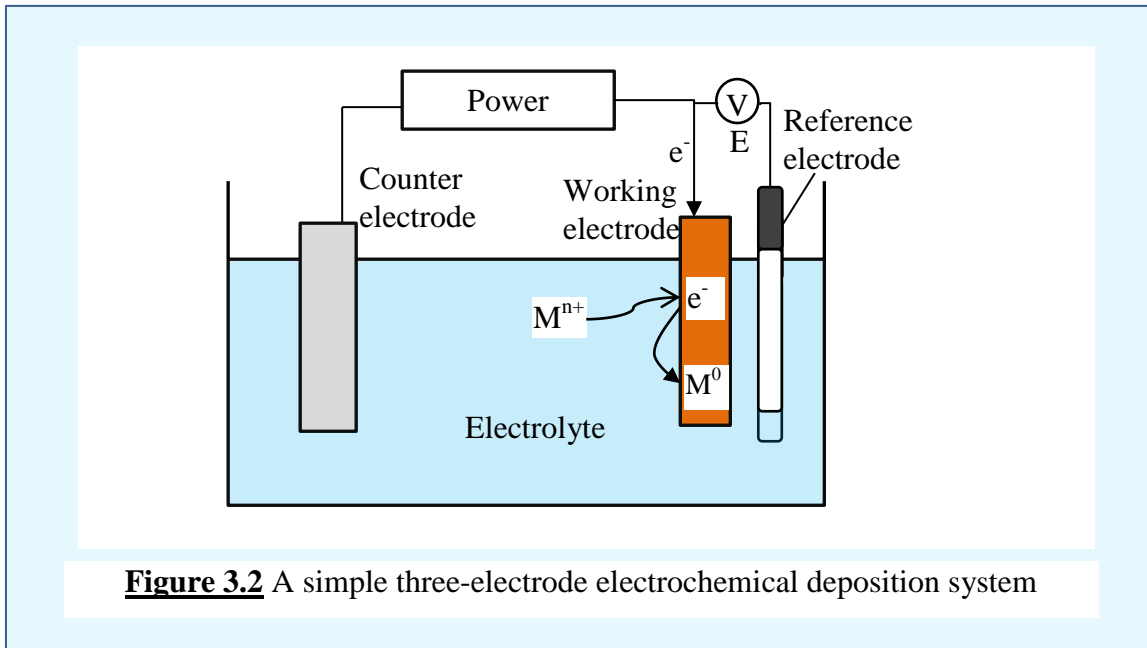
A Pourbaix diagrams for nickel-water system is constructed based on the developed equilibrium reaction equations listed in Table 3.3. The Pourbaix diagram is presented in Fig. 3.1

The pourbaix diagram of nickel-water system shown in Figure 3.1 indicates that in order to obtain pure, high conductive, and oxygen free nickel, a pH lower than 7.5 is required ^[60, 160]. Nickel will be in the form of Ni^{2+} in solution at pH less than 7.5. The Ni^{2+} can be deposited without a formation of hydroxide at pH no more than 7.5. As the hydroxide is highly resistive, the co-deposition of nickel hydroxide should be avoided.

Table 3.3 Reactions and Equilibrium Formulae of nickel in water at 25 °C^[160]

Reactions	Equilibrium Conditions
1. $\text{Ni}^{2+} + 2\text{H}_2\text{O} \rightarrow \text{HNiO}_2^- + 3\text{H}^+$	
1'. $\text{Ni}^{2+} / \text{HNiO}_2^-$	pH = 10.13
2. $\text{Ni} + \text{H}_2\text{O} \rightarrow \text{NiO} + 2\text{H}^+ + 2\text{e}^-$	a. $E_0 = 0.110 - 0.0591 \text{ pH}$ b. $= 0.116 - 0.0591 \text{ pH}$
3. $3\text{NiO} + \text{H}_2\text{O} \rightarrow \text{Ni}_3\text{O}_4 + 2\text{H}^+ + 2\text{e}^-$	a. $E_0 = 0.897 - 0.0591 \text{ pH}$ b. $= 0.876 - 0.0591 \text{ pH}$
4. $2\text{NiO} + \text{H}_2\text{O} \rightarrow \text{Ni}_2\text{O}_3 + 2\text{H}^+ + 2\text{e}^-$	a. $E_0 = 1.032 - 0.0591 \text{ pH}$ b. $= 1.020 - 0.0591 \text{ pH}$
5. $2\text{Ni}_3\text{O}_4 + \text{H}_2\text{O} \rightarrow 3\text{Ni}_2\text{O}_3 + 2\text{H}^+ + 2\text{e}^-$	$E_0 = 1.305 - 0.0591 \text{ pH}$
6. $\text{Ni}_2\text{O}_3 + \text{H}_2\text{O} \rightarrow 2\text{NiO}_2 + 2\text{H}^+ + 2\text{e}^-$	$E_0 = 1.434 - 0.0591 \text{ pH}$
7. $\text{Ni}^{2+} + \text{H}_2\text{O} \rightarrow \text{NiO} + 2\text{H}^+$	a. $\log(\text{Ni}^{2+}) = 12.18 - 2 \text{ pH}$ b. $= 12.41 - 2 \text{ pH}$
8. $\text{NiO} + \text{H}_2\text{O} \rightarrow \text{HNiO}_2^- + 3\text{H}^+$	a. $\log(\text{HNiO}_2^-) = -18.22 + \text{pH}$ b. $= -17.99 + \text{pH}$
9. $\text{Ni} \rightarrow \text{Ni}^{2+} + 2\text{e}^-$	$E_0 = -0.250 + 0.0295 \log(\text{Ni}^{2+})$
10. $\text{Ni} + 2\text{H}_2\text{O} \rightarrow \text{HNiO}_2^- + 3\text{H}^+ + 2\text{e}^-$	$E_0 = 0.648 - 0.0886 \text{ pH} + 0.0295 \log(\text{HNiO}_2^-)$
11. $3\text{Ni}^{2+} + 4\text{H}_2\text{O} \rightarrow \text{Ni}_3\text{O}_4 + 8\text{H}^+ + 2\text{e}^-$	$E_0 = 1.977 - 0.2364 \text{ pH} - 0.0886 \log(\text{Ni}^{2+})$
12. $3\text{HNiO}_2^- + \text{H}^+ \rightarrow \text{Ni}_3\text{O}_4 + 2\text{H}_2\text{O} + 2\text{e}^-$	$E_0 = -0.718 + 0.0295 \text{ pH} - 0.0886 \log(\text{HNiO}_2^-)$
13. $2\text{Ni}^{2+} + 3\text{H}_2\text{O} \rightarrow \text{Ni}_2\text{O}_3 + 6\text{H}^+ + 2\text{e}^-$	$E_0 = 1.753 - 0.1773 \text{ pH} - 0.0591 \log(\text{Ni}^{2+})$
14. $\text{Ni}^{2+} + 2\text{H}_2\text{O} \rightarrow \text{Ni}_2\text{O}_3 + 6\text{H}^+ + 2\text{e}^-$	$E_0 = 1.593 - 0.1182 \text{ pH} - 0.0295 \log(\text{Ni}^{2+})$

including the reference electrode are immersed into the electrolyte in an electrochemical cell (Fig. 3.2). The reference electrode is connected to working electrode through a high impedance voltmeter for measuring the electrode potential.



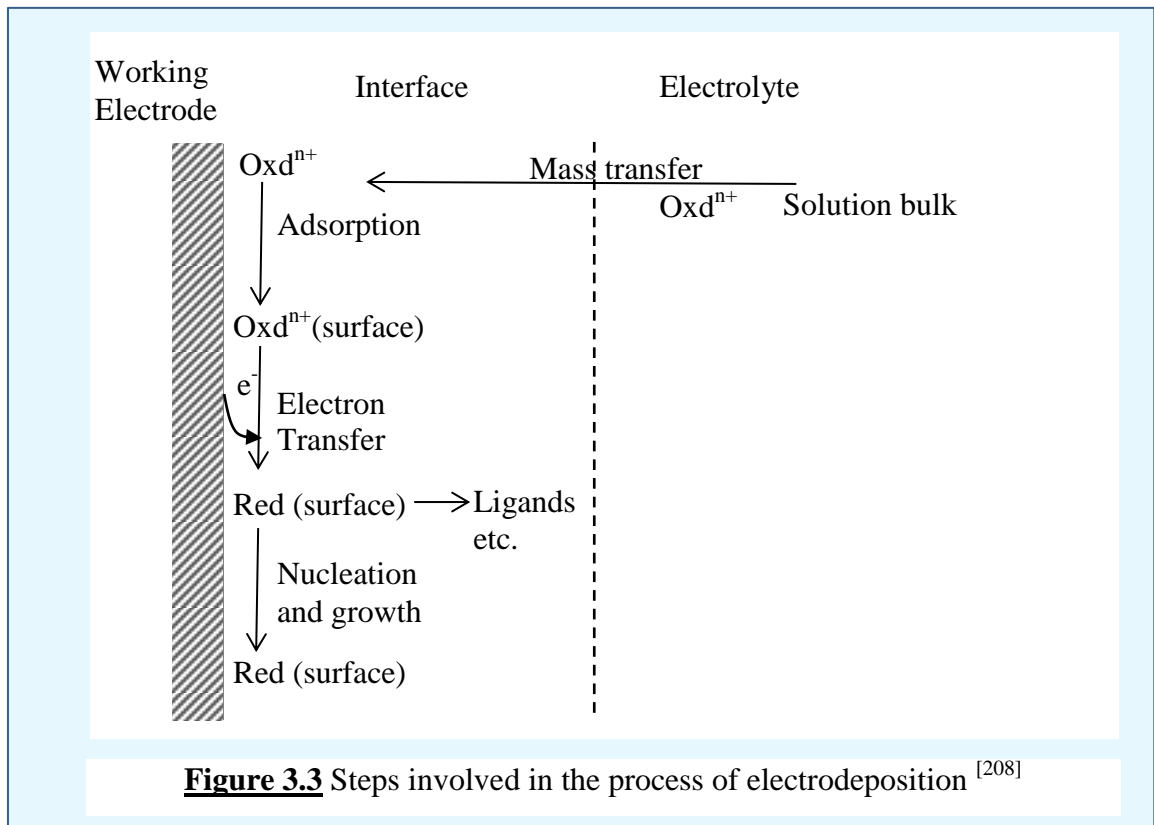
The deposition of metal is driven by a deviation of the electrode potential from its equilibrium value which is known as the overpotential (η). For example, when a negative charge supplied by external power supply is imposed to the working electrode, it drives the current to flow between working and counter electrodes. As a result, the metal ions e.g. M^{n+} is reduced to a solid state (M^0) and deposited on to the working electrode. The reaction on the electrode surface is often represented by a simple electron transfer reaction of ^[62]:



Apart from the charge transfer reaction, the electrochemical deposition actually takes place through several complex processes. The processes can be summarised as a sequent stages:

- Mass transfer of metallic ions from bulk electrolyte to the electrode/solution interface
- Adsorption of electroactive ions onto electrode surface
- Charge transfer reaction at the electrode surface
- Nucleation of the product (metal) and is incorporated into growing lattice at the electrode surface ^[62]

Overall steps involved in the electrodeposition process are illustrated in Fig 3.3.



The rate of the electrodeposition process is governed by the slowest step. In practice, the rate is determined by either the charge transfer or mass transfer process or the combination between the two.

3.4.1 Kinetics of Charge Transfer Process

As the potential is applied to the working electrode, the electrode potential is shifted from its equilibrium value and a current flows. The different potential which is called the overpotential (η) serves as the driving force for electrodeposition process to take place.

$$\eta = E - E_e \quad (3.17)$$

Where E is applied potential and E_e is equilibrium potential.

According to Nernst's equation (3.15), the reaction at the electrode surface depends on the value of the overpotential. If the overpotential is negative ($E < E_e$), to re-establish the equilibrium an electron transfer takes place from the electrode to the reactant governing a reduction reaction, hence the ratio of $\frac{C_{Oxd}}{C_{Red}}$ decreases. In this case, the cathodic current flows to supply the electron (ne^-). On the other hand, anodic current flows for oxidation reaction when more positive potential ($E > E_e$) imposed to the working electrode.

In some cases, the kinetics for the electron transfer is slow, controlling the overall rate of the electrodeposition process. To analyse the electrochemical process where the overall rate of deposition reaction is under kinetic control, some assumptions are taken into account to simplify the system:

- No other chemical or electrochemical reaction involves, only simple electron transfer reaction (equation 3.16) takes place
- The rate of mass transfer is significantly higher than the rate of the reaction, so mass transfer will never be a rate limiting step.
- The concentration of reactant (metallic ion) at the electrode surface is the same as that in the bulk of solution.

In a condition when any value of overpotential is applied to drive the electrochemical reaction, the measured net current density (i) can be defined as:

$$j = \vec{j} + \tilde{j} \quad (3.18)$$

Where, j is a current density which is a normalised form of current respect to an electrode area (a current flow per unit area of a respected electrode). \vec{j} and \tilde{j} are partial cathodic and anodic current density respectively. The overpotential relates to the current density by Butler-Volmer formula. The simplified equation is presented in eq (3.19).

$$j = j_0 \left[\exp\left(\frac{\alpha_A n F \eta}{RT}\right) - \exp\left(\frac{-\alpha_C n F \eta}{RT}\right) \right] \quad (3.19)$$

Where j_0 is the exchange current density, α_A and α_C are anodic and cathodic charge transfer coefficients respectively. The exchange current density refers to an equilibrium partial current density as the anodic and the cathodic partial current densities are equal. The value of the exchange current density depends on the electrochemical reaction and the electrode material and surface ^[62]. The relationship between α_A and α_C is as equation (3.20)

$$\alpha_A + \alpha_C = 1 \quad (3.20)$$

As can be seen from Butler-Volmer equation (3.19), the current density is affected by several parameters i.e. the overpotential, the charge transfer coefficient, the temperature, and the exchange current density. In particular, the current density increases with the increase in overpotential results in an increase in the rate of electrochemical reaction.

3.4.2 Tafel Plot

To evaluate and to determine kinetic parameters of electrochemical reactions using Butler-Volmer model, j - η equation can be approximated by several assumptions. For example, for large overpotentials, one of the partial current densities (either anodic or cathodic term) in (3.19) is insignificant and can be ignored. In the case of electrodeposition at a highly negative overpotential

$$\exp\left(\frac{-\alpha_c n F \eta}{RT}\right) \gg \exp\left(\frac{\alpha_A n F \eta}{RT}\right) \quad (3.21)$$

Equation (3.19) is shorten (3.22) and is often expressed in the Tafel form (3.23, 3.24)

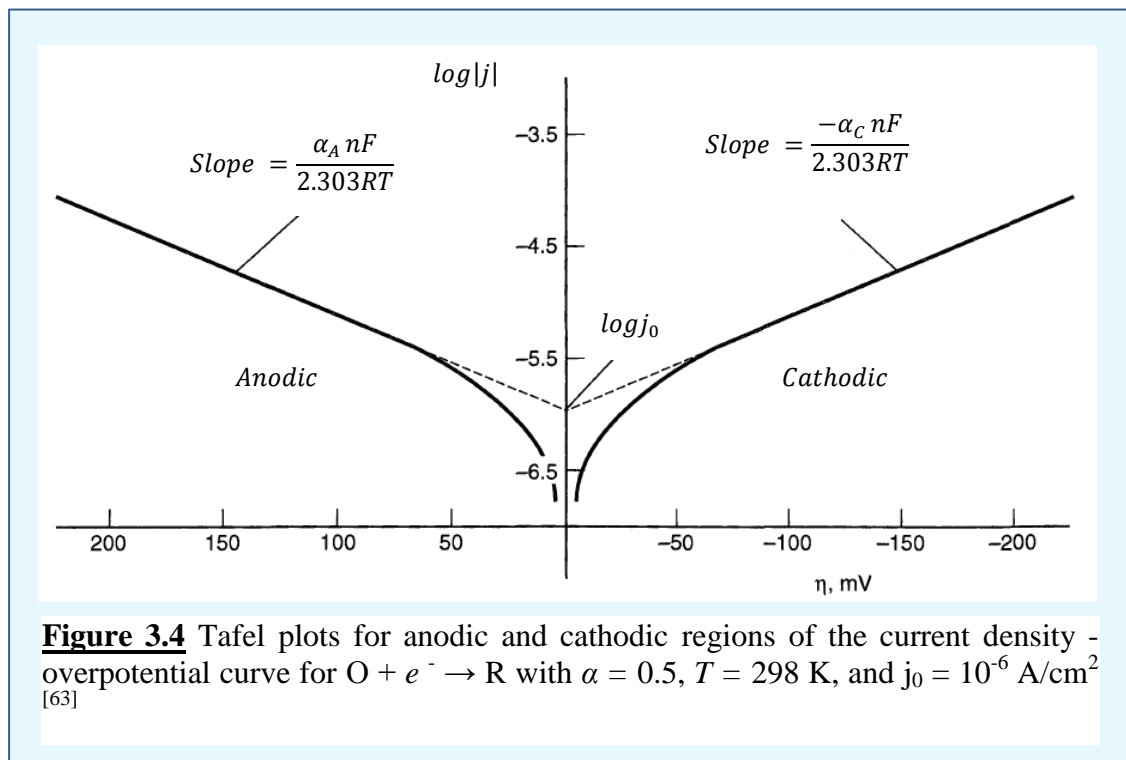
$$j = j_0 \left[-\exp\left(\frac{-\alpha_c n F \eta}{RT}\right) \right] \quad (3.22)$$

$$\ln \left| \frac{j}{j_0} \right| = -\frac{-\alpha_c n F}{RT} \eta \quad (3.23)$$

$$\eta = \frac{RT}{-\alpha_c n F} \ln j_0 - \frac{RT}{-\alpha_c n F} \ln j \quad (3.24)$$

$$\eta = \frac{2.303 RT}{-\alpha_c n F} \log j_0 - \frac{2.303 RT}{-\alpha_c n F} \log j \quad (3.25)$$

Kinetic parameters such as exchange current density j_0 and charge transfer coefficient can be determined using the plot of η vs. $\log|j|$ known as Tafel plot (Figure 3.4).



The charge transfer coefficient is calculated from the slope of the Tafel plot. The exchange current density (j_0) is obtained from the intercept of the Tafel plot at overpotential (η) of 0 mV.

3.4.3 Mass Transfer Process

As the charge transfer reaction takes place, the concentration of the metallic ion near the electrode surface decreases. To ensure the reaction proceeds, the depletion must be replenished by fresh metallic ions/reactants. Hence, mass transfer of the reactant from the bulk of the solution to the electrode surface is needed. The mass transfer of the metallic ion occurs through several mechanisms:

- The different concentration of the reactant at electrode surface and in the bulk drives mass transfer of metallic ion by diffusion.
- The potential gradient causes migration of the metallic ion
- Mass transfer of metallic ion also takes places by mechanical motion of the solution through natural convection i.e. due to difference in density and pressure or through forced convection by an artificial agitation.

At a point near the electrode surface, the metallic ions mainly transferred from the bulk of the solution by diffusion. In general, the relationship of the flux of metallic ion and concentration gradient between two points is described by Fick's first law of diffusion.

$$N_i = -D_i \frac{dC_i}{dx} \quad (3.26)$$

In equation (3.25), N_i is the flux, i indicates the material diffusing, D represents the diffusion coefficient, C is concentration of the substance in the solution, and x is the distance between two points.

At steady state condition, the rate of electron transfer reaction is equal to the rate of mass transfer. Therefore,

$$\frac{\bar{j}}{nF} = -D_i \frac{dC_i}{dx} \quad (3.27)$$

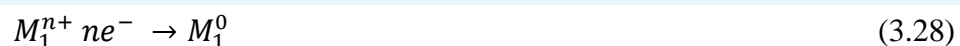
3.5 Mixed Potential System

In some cases, the electrodeposition process involves a complicated electrochemical system. Simultaneous reactions including several substances may occur. Theoretical approach based on mixed potential theory is used to understand the phenomena. The mixed potential theory was initially developed by Wagner and Traud^[209] for corrosion. The theory originally describes that the overall measured current density is a combination of partial cathodic and anodic current density^[209, 210].

In a multi-electrochemical system with more than one reaction, the mixed potential theory can be used to understand the contribution from each reaction. This can be performed if the current density of each single reaction is measured. According to the interaction between components involved in the process, three different mixed electrochemical systems are observed.

- Non interactive system: partial current density of each reaction is independent of each other. The overall current density can be estimated based on the current density of each reaction.
- Charge transfer coupled system: current density of pure component is not equal to its partial current density in the mixed system.
- Mass transfer coupled system: current density of one component depends on mass transfer rate of other component.

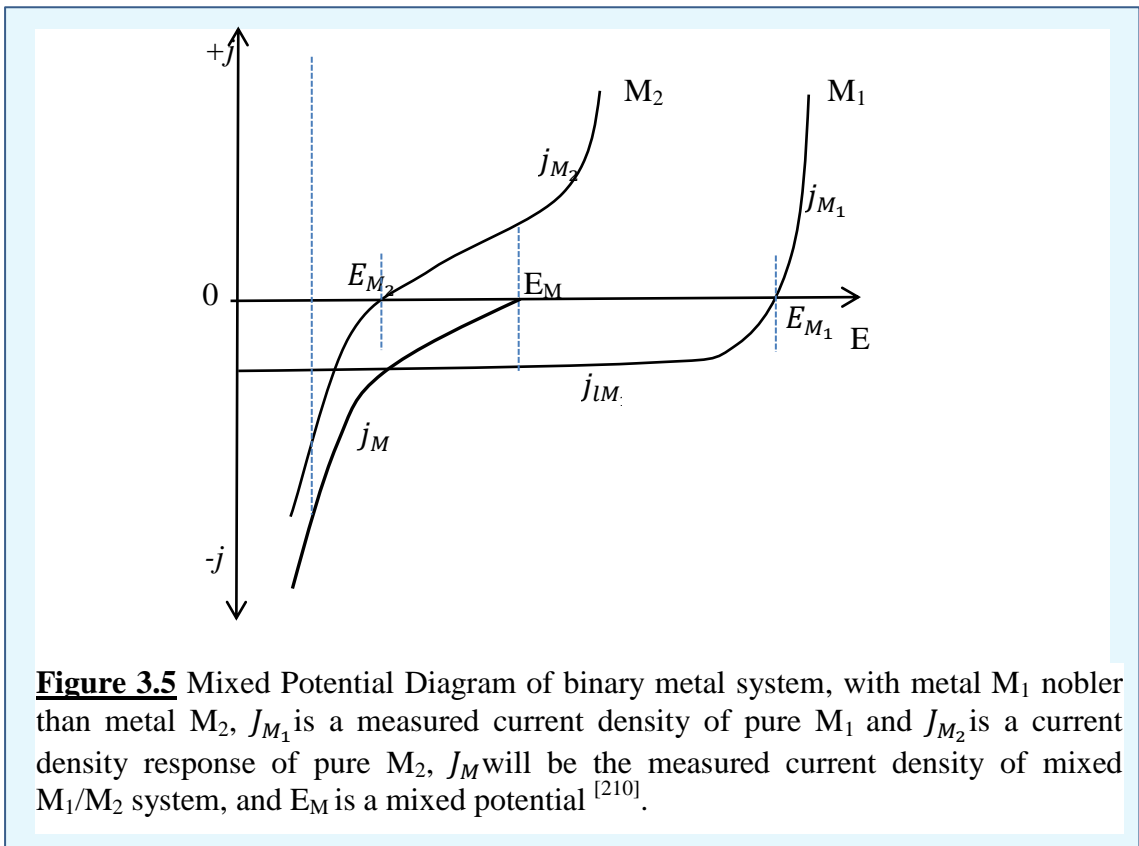
Binary system of two different metals (M_1 and M_2) is considered for an example of non-interactive system^[210]. In this case, metal M_1 is nobler than metal M_2 . Reduction reactions of the two metal systems are expressed as:



The first reduction reaction is assumed to be controlled by mass transfer i.e. copper system, whereas the second is under kinetic control i.e. nickel system. Fig 3.5 illustrates a potential – current profile for the M_1/M_2 system based on the mixed potential theory for the binary metal system.

As can be seen in Fig 3.5 J_{M_1} is a measured current density of pure M_1 system and J_{M_2} is a current density response of pure M_2 system. In non-interactive system, J_M will be the measured current density of mixed M_1/M_2 system which is the sum of their current densities. E_M is the mixed potential at which the current density of M_2

anodic reaction equal to the current density of cathodic reaction of M_1 . At this potential, if metal M_2 is immersed to a solution containing M_1^{n+} , there would be a displacement reaction. The M_1^{n+} would be reduced to M_1^0 , and the metal M_2 dissolve at the same rate.



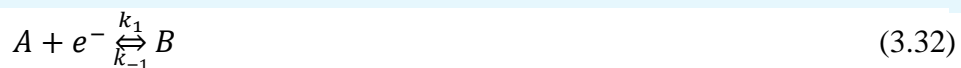
3.6 Kinetics of Multistep Electrode Reaction

Electrode reactions typically take place through more than one step. The multiple steps include electron transfer reactions that may occur consecutively. For example, two successive electron transfer reactions are observed in nickel electrodeposition process.



In electrochemical system, only a single electron transfer reaction should take place at a time and a step, therefore each charge transfer reaction occurs at a different potential region ^[211].

Considering general electrochemical reactions which sequentially occur in a steady state condition:



The rate of reaction of each component is given by

$$r_A = -k_1 C_A + k_{-1} C_B \quad (3.34)$$

$$r_B = k_1 C_A - k_{-1} C_B - k_2 C_B + k_{-2} C_D \quad (3.35)$$

$$r_C = k_2 C_B - k_{-2} C_D \quad (3.36)$$

Assuming the steady state to the intermediate (B) so that $r_B = 0$, the concentration of intermediate (C_B) can be expressed by

$$C_B = \frac{k_1 C_A + k_{-2} C_D}{k_{-1} + k_2} \quad (3.37)$$

At steady state, overall reaction rate (r_R) is equal to r_A and r_B which is given by:

$$r_R = r_A = r_D = \frac{k_1 k_2 C_A - k_{-1} k_{-2} C_D}{k_{-1} + k_2} \quad (3.38)$$

In the case of $k_{-1} \ll k_2$ and $k_1 \ll k_{-2}$, the rate of overall reactions (r_R) would be:

$$r_R = k_1 C_A - \frac{k_{-1} k_{-2}}{k_2} C_D \quad (3.39)$$

$$r_R = k_1 C_A - k_{-1} C_{B(D)}^0 \quad (3.40)$$

$$\text{Where } C_{B(D)}^0 = \frac{k_{-2}}{k_2} C_D = \frac{C_D}{K_{2 \text{ eq}}} \quad (3.41)$$

Equation (3.39) shows that, if $k_{-1} \ll k_2$ the kinetic parameter of the first reaction is the rate determining step of overall reactions ^[211, 212]. For this case, the cathodic current density at equilibrium condition is given by

$$j = n F k C_A \exp[\alpha F (E - E_e) / RT] \quad (3.42)$$

Where $k = k_1^0$, the standard rate constant of the forward reaction (3.32) at equilibrium.

In the case of $k_{-1} \gg k_2$, the rate of overall reactions (r) would be:

$$r_R = \frac{k_1 k_2}{k_{-1}} C_A - k_{-2} C_D \quad (3.43)$$

$$r_R = k_2 C_{B(A)}^0 - k_{-2} C_D \quad (3.44)$$

$$\text{Where } C_{B(A)}^0 = \frac{k_1}{k_{-1}} C_A = K_{1 \text{ eq}} C_A \quad (3.45)$$

The rate of the overall charge transfer reaction is determined by the kinetic parameters of the second step ^[211, 212, 213].

Accordingly, the cathodic current density becomes:

$$j = n F k C_A \exp[\alpha F (E - E_e) / RT] \quad (3.46)$$

Where $k = \frac{k_1^0 k_2^0}{k_{-1}^0}$, with k_{-1}^0 is the rate constant of the backward reaction (3.32) and k_2^0 is the standard rate constant of the forward reaction (3.33)

3.7 Performance of Electrochemical Deposition Process

A performance of electrodeposition process can be quantified through a number of electrochemical parameters such as deposition rate, current efficiency, and energy consumption. Thereafter, the feasibility of the electrodeposition of nickel in Enface system is evaluated based on the performance. The thermodynamic and kinetic parameters of the deposition reactions such as current density, potential, and deposition time are capable to be used to estimate the rate of electrodeposition, the current efficiency, and the energy consumption. .

3.7.1 Electrodeposition Rate

Faraday's law suggests that the molar deposit quantity on the working electrode is proportional to the quantity of applied electrical charge as given by equation (3.47).

$$m = \frac{Q}{nF} \quad (3.47)$$

At constant applied current, Q is defined as

$$Q = I dt \quad (3.48)$$

At a time of dt , the amount of metal deposited onto the electrode would be dm , therefore the equation will become

$$dm = \frac{I dt}{nF} \quad (3.49)$$

$$\frac{dm}{dt} = \frac{I}{nF} \quad (3.50)$$

Where, $\frac{dm}{dt}$ = molar deposition rate (g/s),

m = Quantity of the deposit (mol)

Q = Applied electrical charge (C),

n = number of transferred electron

F = Faraday's constant (C/mol),

I = Applied current (A)

t = time (s)

The growth rate of the deposit can also be estimated by the derivation of equation (3.49),

$$\frac{dw}{A_{wt} dt} = \frac{I}{nF} \quad (3.51)$$

$$\frac{\rho dV}{dt} = \frac{I A_{wt}}{nF} \quad (3.52)$$

$$\frac{\rho S dh}{dt} = \frac{I A_{wt}}{nF} \quad (3.53)$$

$$\frac{dh}{dt} = \frac{I A_{wt}}{\rho S n F} \quad (3.54)$$

Where, A_{wt} = Atomic weight of deposited metal (gram/mol)

w = weight of the deposit (g)

ρ = density of the deposit (g/cm^3)

V = volume of the deposit (cm^3)

S = surface area of the deposit (cm^2)

h = thickness of the deposit (cm)

$\frac{dh}{dt}$ = growth rate of the deposit (cm/s)

3.7.2 Current Efficiency

As previously described, most electrochemical systems involve more than one reaction. If the multiple electrochemical reactions take place simultaneously at the same potential, the applied charge are consumed not only by the desired reaction but also by the competing reaction. The percentage of the charge consumed by the desired reaction is called the current efficiency (ϕ). Hence, in general, if the efficiency is 100 %, the applied charge is all used by the reaction of interest, whereas the charge is partially used in competing process at a current efficiency under 100%.

The current efficiency of metal electrodeposition is defined as the charge required for the reaction of interest (Q_j), divided by the total applied charge (Q_{tot}).

$$\phi = \frac{Q_j}{Q_{tot}} \times 100 \quad (3.55)$$

The required charge (Q_j) is calculated based on the quantity of deposited metal using Faraday's law.

3.7.3 Energy Consumption of the Electrochemical Deposition

The energy (W) used in the electrodeposition of metal can be estimated using the cell potential and the applied charge.

$$W = Q \cdot E_{cell} \quad (3.56)$$

$$Q = \int I dt \quad (3.57)$$

At constant applied current,

$$Q = I \int dt \quad (3.58)$$

$$W = E_{cell} I \int dt \quad (3.59)$$

The cell potential (E_{cell}) is defined as the potential difference between two electrodes in the cell due to overpotential and ohmic drop across the cell.

$$E_{cell} = E_{e,C} - |\eta_A| - |\eta_C| - IR_{cell} - E_{e,A} \quad (3.60)$$

Where, $E_{e,C}$ and $E_{e,A}$ are equilibrium potentials of the cathode and the anode respectively. $|\eta_C|$, $|\eta_A|$ are activation concentration and resistance polarisation for the cathode and anode. IR_{cell} is the ohmic drop across the cell.

Chapter 4

Experimental

Experimental details of the electrodeposition of nickel pattern described in this chapter include (1) the development of electrolyte, (2) the apparatus, the instrumentation, and preparation as well as characterisation of electrodes (3) electrochemical characterisation of the nickel electrolyte: in three-electrode cell using rotating disc electrode (RDE), in a narrow inter-electrode gap of Enface system under stagnant conditions, and under ultrasound agitation (4) the nickel pattern transfer experiments including characterisation of the electrodeposited nickel,

4.1. Electrolyte Development

Earlier description stated that a successful pattern transfer using Enface method was driven by the electrolyte physicochemical properties i.e. conductivity of 2.7 S/m and pH of 4 -7.5. Initially, the equation (3.1) was used to estimate the concentration and composition of nickel sulfamate in the solution in which its conductivity value was around 2.7 S/m. In some of the electrolytes NiCl_2 was used to see whether dissolution of anode could be increased, hence passivation could be avoided.

Table 4.1 Calculated conductivities for nickel solutions containing different concentrations of Ni^{2+}

Composition		Calculated Conductivity (S/m)
Ni-Sulfamate (M)	Nickel Chloride (M)	
0.30	-	4.39
0.20	-	2.92
0.19	-	2.78
0.15	-	2.19
0.29	0.01	4.44
0.19	0.01	2.98
0.14	0.01	2.24

The calculated conductivity values for the nickel solutions containing different concentrations of Ni^{2+} are shown in Table 4.1. The Table shows that the concentration of nickel in solution needs to remain within 0.15 – 0.2 M for sulfamate and a mixture of sulfamate and chloride electrolytes. Accordingly, the electrolytes containing 0.19 M nickel sulfamate with and without addition of 0.01 M nickel chloride were selected for use in the experiments

The electrolyte solutions were prepared from analytical grade of nickel (II) sulfamate tetrahydrate ($\text{Ni}(\text{SO}_3\text{NH}_2)_2 \cdot 4\text{H}_2\text{O}$ 98 %, Sigma-Aldrich) and nickel (II) chloride hexahydrate ($\text{NiCl}_2 \cdot 6\text{H}_2\text{O}$ 99 %, Fisons Scientific) in a high purity deionised water i.e. 18 M Ω . Physicochemical property measurements were carried out to determine the actual pH and conductivity of the electrolyte. The conductivity and pH of the chosen electrolytes are presented in Table 4.2.

Table 4.2 Conductivities (calculated and measured) and pH for the selected nickel solutions

Electrolyte	Calculated* Conductivity (S/m)	Experimental Data (20±2 °C)	
		Conductivity (S/m)	pH
0.19 M $\text{Ni}(\text{SO}_3\text{NH}_2)_2$ + 0.01 M NiCl_2	2.98	2.37 ± 0.04	6.45 ± 0.14
0.19 M $\text{Ni}(\text{SO}_3\text{NH}_2)_2$	2.78	2.19 ± 0.06	6.70 ± 0.22

*detailed calculation is presented in Appendix A

As can be seen, the pH of the solutions had already been in the expected range; therefore no further pH adjustment was required. In addition, observing the physicochemical properties of the electrolytes shown in Table 4.2, the measured and the calculated values of the electrolyte conductivity are different. The discrepancy indicates that nickel sulfamate dissociation constant is less than 1.0 (around 0.78), despite the fact that nickel sulfamate is highly ionised in solution^[194 - 196]. Though, the standard conductance equation (3.1) for a fully ionised solution was useful to approximate the conductivity of the nickel sulfamate solution.

Electrolytes containing 0.19 M nickel sulfamate was chosen and an addition of nickel chloride (0.01 M) was initially preferred for promoting dissolution and preventing passivation of nickel anode^[154, 156]. However the presence of chloride in the solution had caused an instantaneous corrosion of the cathode disk leading to copper contamination. The contamination could possibly generate an unexpected dark nickel deposit^[214], and nickel coating failure^[215] i.e. a decrease in bondability. Furthermore, a copper oxide may also be formed in an exposed area of the contaminated nickel deposit surface as copper is easily oxidised^[215]. Therefore, the 0.19 M nickel sulfamate solution without nickel chloride additive was used in the entire experiments.

4.2 Electrochemical Apparatus

4.2.1 Standard Three-Electrode System

4.2.1.1 Electrochemical Cell

In the first stage of electrochemical characterisation of the chosen solutions, polarisation experiments were carried out in a standard system of three-electrode cell. The cell was made of a vertical-cylindrical glass with diameter of 6.5 cm and 8.5 cm height. The cell was featured with a side glass neck for inserting a luggin capillary tube. The glass cell was also equipped with a glass lid with three necks. The centre neck was used for introducing rotating disk electrode (RDE, EDI101 Radiometer Analytical), whereas the other two necks were smaller that can be used to mount a counter electrode and thermometer when required. An approximately 250 ml of nickel solution was used to sufficiently fill up the cell. The cell is described in Figure 4.1.

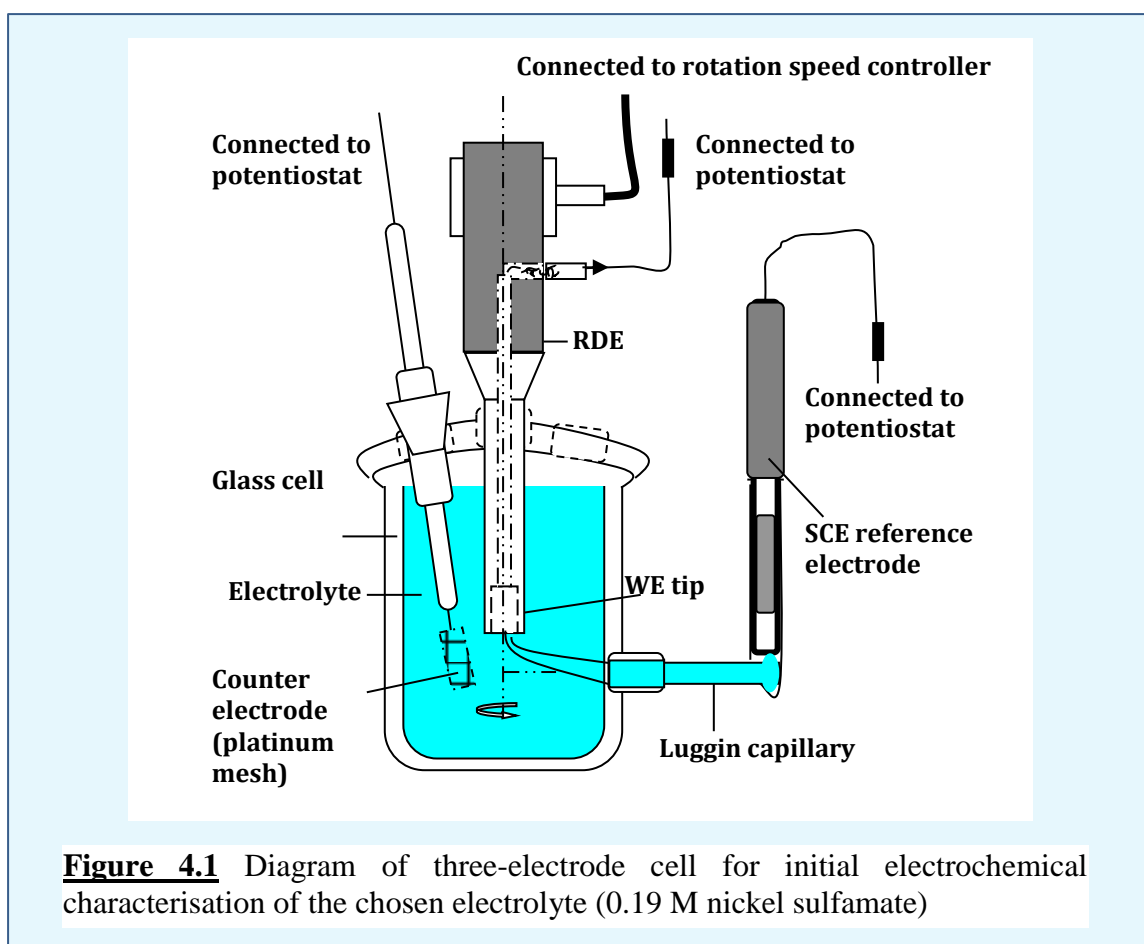
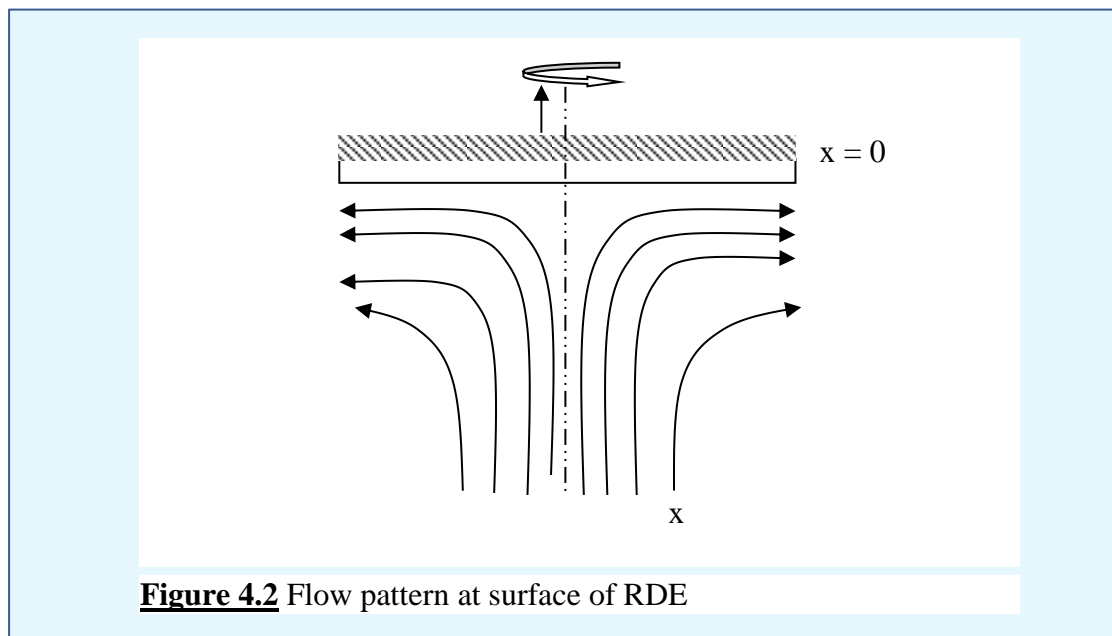


Figure 4.1 Diagram of three-electrode cell for initial electrochemical characterisation of the chosen electrolyte (0.19 M nickel sulfamate)

4.2.1.2 Rotating Disk Electrode (RDE)

Rotating Disk Electrode (RDE) is a hydrodynamic electrochemical apparatus that has been used to study behaviour of a variety of metal electrodeposition from an electrolyte solution including nickel. The electrode itself is mechanically rotated to give an agitation effect to the electrolyte. Due to a centrifugal effect, a uniform axial velocity and well defined fluid flow that is useful for mass transfer investigation is produced ^[216]. A mass transfer effect on electrochemical reaction particularly the effect of convection and diffusion can be measured using the RDE system ^[217]. In addition, by means of the RDE, several parameters of electrochemical system including a coefficient of diffusion and electrode reaction parameters (i.e. kinetics and reaction mechanism) can be estimated ^[216].

When the RDE is axially rotated, the centrifugal effect pulls electrolyte solution toward the surface of electrode where the reaction occurs. At the same time, the solution that has reacted was pushed away from the centre of the electrode surface to radial direction forming a uniform potential flow ^[218]. This condition results in a uniform mass transfer rate all over the disk ^[219]. Mass transfer of reactants from the solution bulk to the electrode surface is also enhanced with a magnitude of the rotation speed. The arrows in Figure 4.2 illustrate the flow of the electrolyte during disk rotation.



The parameters of the rotation i.e. the ratio of free stream velocity to the axial velocity as well as the Reynolds number determine the type of the flow ^[220].

$$Re = \frac{\omega r^2}{\nu} \quad (4.1)$$

The Sherwood dimensionless correlation for the RDE system is expressed by ^[221]

$$Sh = 0.621 Re^{\frac{1}{2}} Sc^{\frac{1}{3}} \quad (4.2)$$

$$Sc = \frac{\nu}{D} \quad (4.3)$$

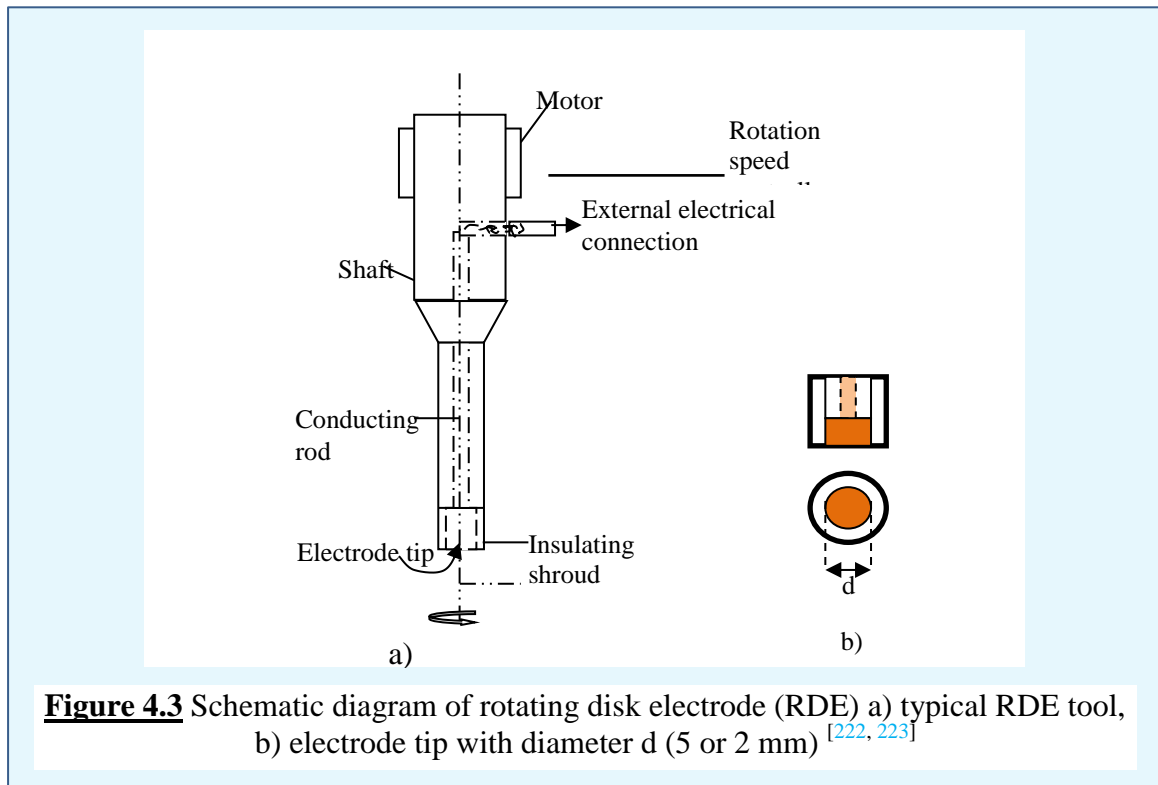
$$Re = \frac{\omega r^2}{\nu} \quad (4.4)$$

$$Re < 2.7 \times 10^5 \quad (4.5)$$

If a laminar flow profile of the solution is maintained by keeping the rotation speed below the limits, mass transfer equation is given by ^[216]

$$\frac{\partial[C]}{\partial t} = D \frac{\partial^2[C]}{\partial x^2} - v_x \frac{\partial[C]}{\partial x} \quad (4.6)$$

Where C is concentration of reactant, t is time, D is diffusion coefficient, v is velocity of the solution, and x is distance from the electrode surface. As can be seen in the equation (4.6), mass transfer is determined by diffusion and convection.



The RDE used in these experiments was constructed from a disk of copper or gold surrounded by PTFE shroud. The disk was mounted on to a metal rod (i.e. copper) in the core of a mechanical shaft. The RDE was set vertically in the electrochemical cell with surface of electrode disk was facing downward (Figure 4.1). A simple diagram of the RDE is shown in Figure 4.3.

The RDE was axially rotated by an externally controlled motor inside the shaft. The motor was connected to a CTV101 speed control unit from Radiometer Analytical that could be operated at a range of rotation speed between 0 and 5000 rpm.

4.2.1.3 Electrode Preparation

Working Electrode

The working electrode (WE) was a copper disk (5 mm diameter) for nickel deposition study experiments. The disk was surrounded by a PTFE shroud (10 mm diameter). Both nickel and gold tips were obtained from Radiometer Analytical.

Before each experiment, the copper disk surface was cleaned using a dilute nitric acid solution (5 %) and then gently polished by wet silicon carbide papers with fineness of #2400 and #4000 grit (Struers Ltd, UK) to obtain a mirror finish. The polishing process was carried out using a polishing machine (Struers Dap-7). After polishing, the electrodes were washed thoroughly using deionised water and acetone to remove impurities. The disk was mounted to a rotating disk electrode (RDE) shaft and immediately immersed to the electrolyte after being polished and cleaned.

Counter Electrode

A platinum mesh (99.9 % purity, Goodfellow) with a surface area greater than the working electrode (1 cm width and 2 cm length) was used as a counter electrode (CE). The counter electrode was always placed approximately 3 cm away from the working electrode throughout the experiments. Prior to each experiment, the counter electrode was cleaned up using a dilute nitric acid solution (5%). Thereafter the counter electrode was thoroughly washed using deionised water. This step was to ensure that the electrode surface was contaminant free. The counter electrode was immediately mounted to the cell and immersed in the electrolyte after being cleaned to avoid copper oxidation.

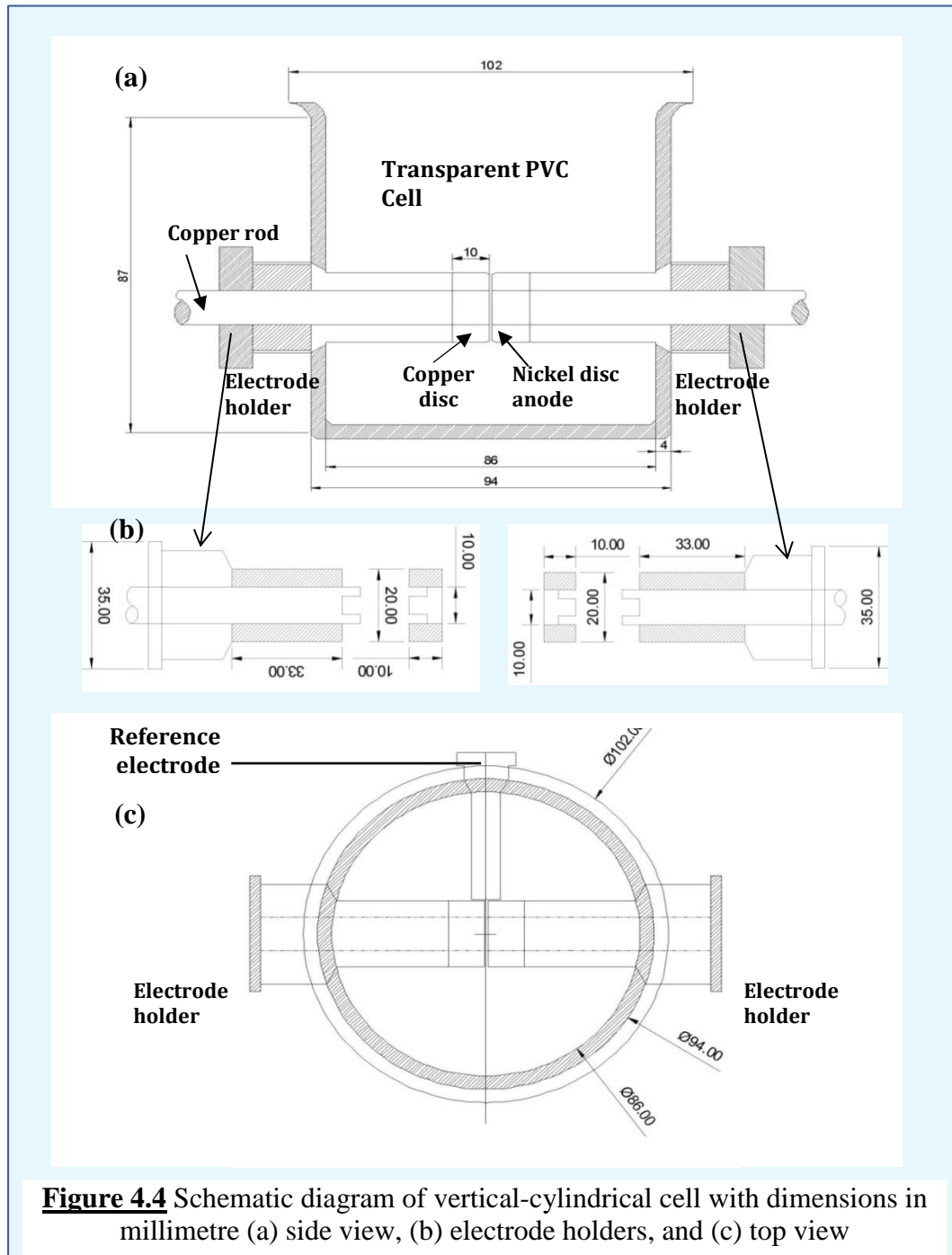
Reference Electrode

The potential was measured against a saturated calomel reference electrode (SCE) which was Hg/Hg₂Cl₂ in saturated KCl supplied by Thermo Scientific. The electrode potential of SCE is $E^0 = +0.241$ V vs (NHE) at 25 °C. The reference electrode was communicated to a point by approximately 3 mm away from the surface of working electrode using a luggin capillary glass probe. When it was not in use, the electrode was stored in saturated KCl solution and was ensured its tip was fully immersed.

4.2.2 Enface system

4.2.2.1 Electrochemical Cell

A cylindrical electrochemical cell was designed and built for the polarisation and the pattern transfer experiments using Enface method. The cell was mainly constructed of transparent polyvinyl chloride (PVC). The body of the cell was a PVC cylinder of 10 cm diameter and the height of the cell was 8 cm (Figure. 4.4 (a)).



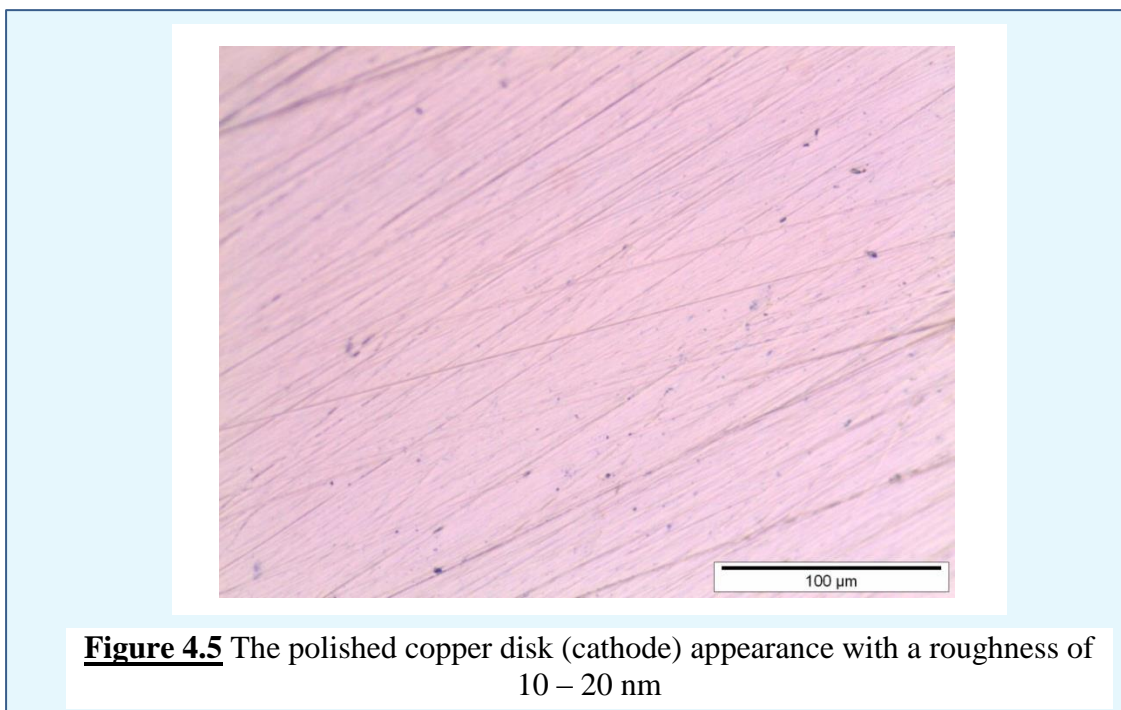
The cell had two polytetrafluoroethylene (PTFE) electrode holders on each side to locate the tool (anode) and the substrate (cathode) facing each other (Figure. 4.4 (b)). To achieve an electrode distance of approximately 300 μm , the electrode holders were

turned around in a clockwise direction by screw action. A stainless steel shim with a thickness of 250 μm (RS Components) was placed in between the electrodes to create the gap of approximately 300 μm . All experiments were carried out at this interelectrode gap. A copper rod in the core of the electrode holder connected the electrodes to a power supply, and the electrode discs are mounted to the electrode holder by a screw. About 500 ml of electrolyte was used to fill up cell, which ensured that the electrodes were fully immersed in solution. A reference electrode was fabricated by inserting it in PTFE holder located on the other side of this cell (Figure 4.4 (c)).

4.2.2.2 Electrode Preparation

Cathode

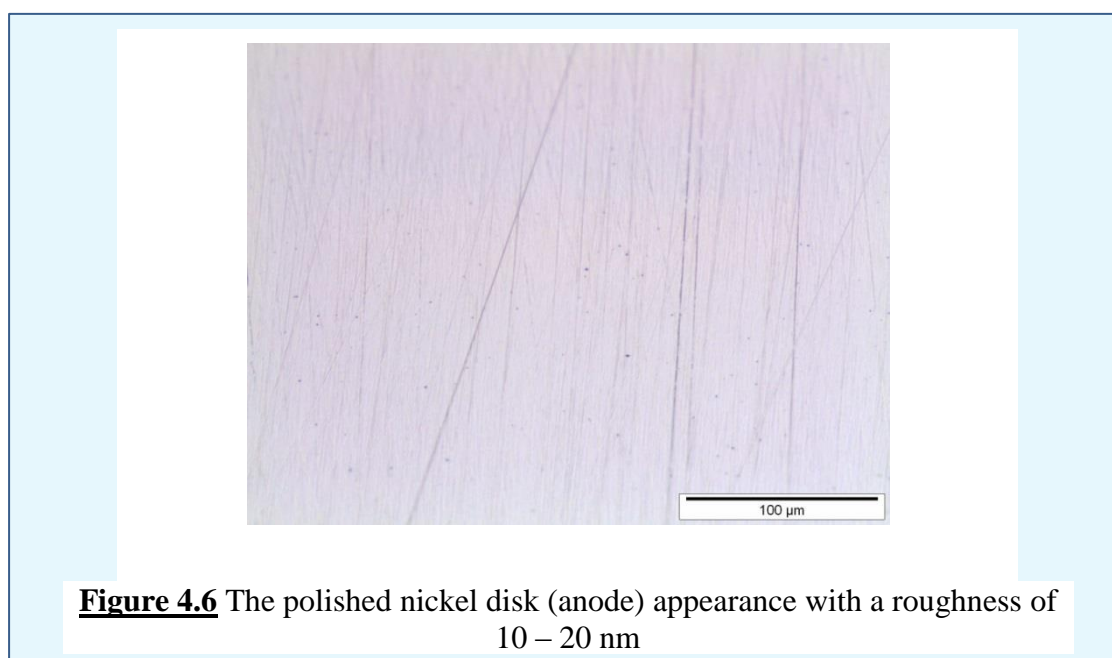
The cathodes or substrates were copper discs of 1.0 cm diameter. The copper disks were made by slicing copper rods (Goodfellow) with a purity of $> 99.99\%$. Prior to each experiment, each cathode disk was polished using the same procedure. A wet silicon carbide paper of #2400 and #4000 grit (Struers), along with the Struers Dap 7 polishing machine were used for the electrode polishing purpose. After a mirror finish had been achieved, the electrode disks were cleaned and washed using deionised water and acetone for impurities removal.



The appearance of polished copper disk is presented in Figure 4.5. Thereafter, the cathode disk was immediately mounted on to the electrode holder using a screw and directly immersed in the electrolyte to avoid the copper being oxidised.

Anode

The anodes, which served as the tool, were fabricated from 1 cm diameter nickel disk. The nickel disks were made of a sliced nickel rod with minimum purity of 99.99 % (Goodfellow). Each anode disk was gently polished using wet silicon carbide papers of grit #2400 and #4000 (Struers) until smooth and mirror finish surface was achieved. Thereafter, the polished nickel disks were thoroughly washed with deionised water and acetone. The polished nickel disk appearance is shown in Figure 4.6. In experiments on a fully exposed anode, the polished and cleaned nickel disk anode was mounted immediately on to the holder by a screw and subsequently immersed in the electrolyte. For experiments with patterned anode, pattern features were defined on to the anode using a resist material (i.e. kapton tape or photoresist).

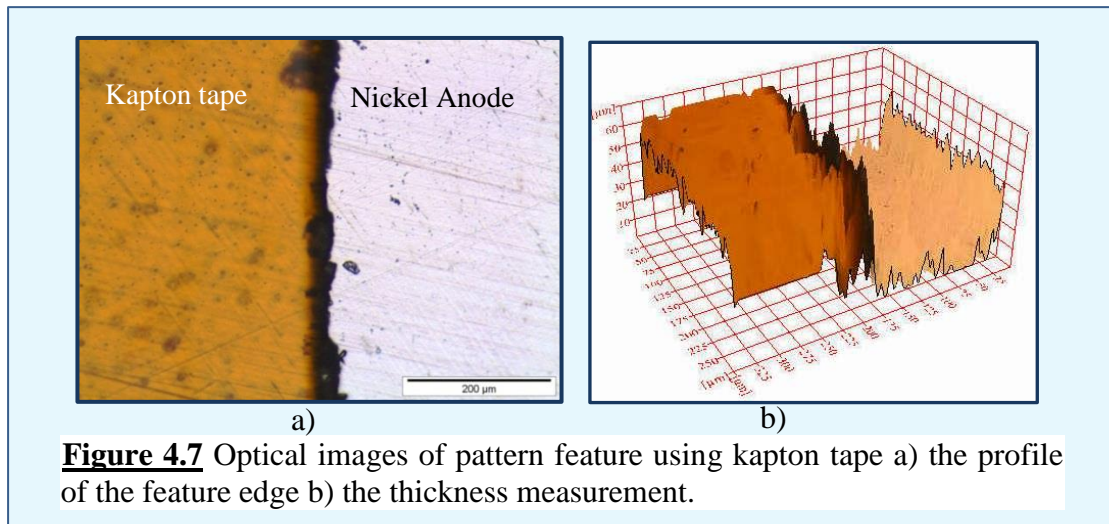


Reference Electrode

Due to the geometry of the cell that did not allow one to place a standard reference electrode at close proximity to the working electrode, a pseudo reference electrode of platinum wire with purity of 99.9 % (Goodfellow) was used and inserted into the PTFE holder. Pt has been shown to provide a constant potential in a variety of electrochemical systems such as aqueous and non-aqueous electrolytes including single or multi one-electron transfer reaction, under various conditions i.e. a wide range of temperatures and pressures^[224, 225]. This reference electrode was introduced into the system orthogonally to the working and counter electrodes. The

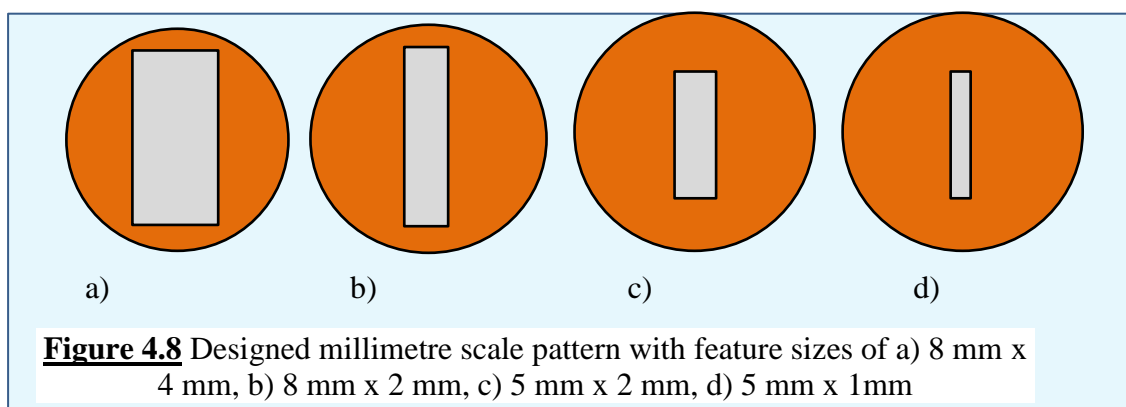
distance of the reference tip was adjusted to approximately 2 mm away from the cathode surface by turning it clockwise using a screw action. The potentials measured in polarisation experiments in Enface system were all against the platinum wire reference electrode.

4.2.2.3 Pattern Feature



In the first attempt of pattern transfer experiments, the anode was manually patterned by selectively covering the surface using a resistive material (kapton tape). Initially the surface of the anode was fully covered by the Kapton tape, and pattern features were cut into the tape using a surgical blade. The profile of the feature made of kapton tape is presented in Figure 4.7. As can be seen in Figure 4.7 (a), a rough and uneven profile of the feature edge was obtained due to the manual cutting process in creating the feature. In some cases, the manual cutting tool also caused a scratch on to the anode surface. Figure 4.7 (b) shows the kapton tape thickness measured by optical microscope (BX41, Olympus). The thickness of the resistive material was in the range of 60 - 65 μm . a significant roughness of the surface profile was possibly caused by the substrate roughness as a result of mechanical work (polishing).

Millimetre scale Features



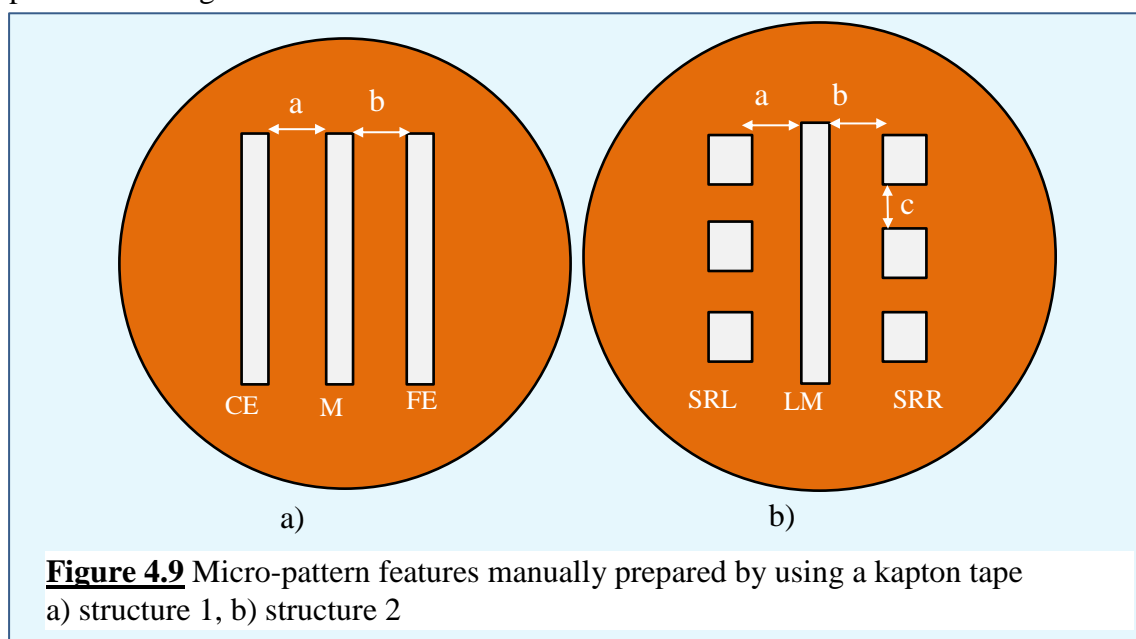
At first, a single pattern feature on the anode was used in the experiments. Rectangular pattern features of 8 mm x 4 mm, 8 mm x 2 mm, 5 mm x 2 mm, and 5 mm x 1 mm as shown in Figure. 4.8 were chosen. Each feature was defined on the centre of an anode disk. A summary of the pattern features characterisation is presented in Table 4.3.

Table 4.3 Characteristic of manually fabricated pattern features in millimetre scale.

Pattern Feature	Length (mm)	Width (mm)	Exposed Area (cm ²)	Percentage of exposed area (%)
Rectangle	8.11 ± 0.23	3.83 ± 0.17	0.31 ± 0.02	39.45 ± 2.04
Rectangle	7.47 ± 0.34	2.45 ± 0.16	0.18 ± 0.01	23.26 ± 1.83
Rectangle	5.14 ± 0.24	2.09 ± 0.10	0.11 ± 0.01	13.68 ± 0.96
Rectangle	4.98 ± 0.17	1.33 ± 0.15	0.07 ± 0.01	8.43 ± 0.99

Micrometre scale pattern using kapton tape

Initially micro-patterns were also manually prepared by using kapton tape. The anode surface was covered by kapton tape and then cut using a surgical blade to form desired features. Two micro-pattern structures consisting of several features of straight lines and rectangles with different width and spacing were designed. The structures are presented in Figure 4.9.



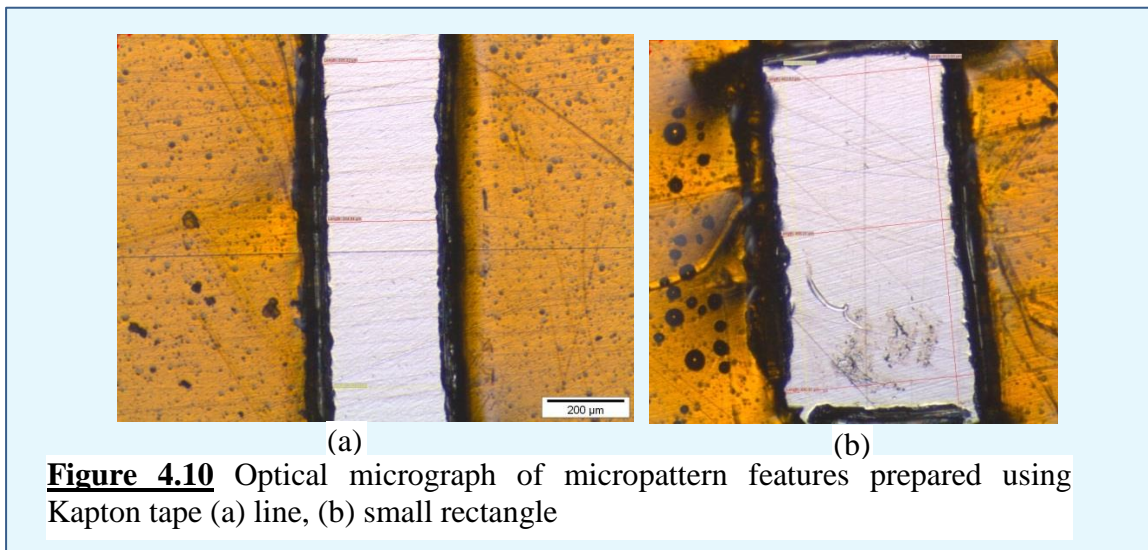
The feature dimensions including exposed area and spacing are summarised in Table 4.4. To approximate the total exposed area of each patterned anode, all area of the line

and the square were calculated and added up. Some errors in creating the micropattern were found due to the limitation of manual preparation with an accuracy of 97 %. Samples of optical images of the micro-pattern features are presented in Figure 4.10.

Table 4.4 Characteristic of micropattern features manually prepared using kapton tape

	Length (mm)	Width (μm)	Spacing (mm)	Exposed area (cm^2)	Percentage of the exposed to Total anode area (%)
Structure 1					
- lines	4.53 ± 0.25	276.67 ± 12.47	a 1.5 b 2.0	0.038 ± 0.003	4.79 ± 0.34
Structure 2					
- lines	7.53 ± 0.09	353.33 ± 54.37	a. 2.0 b. 1.5	0.055 ± 0.005	7.03 ± 0.64
- small rectangles	0.938 ± 0.009	502.72 ± 15.15	c. 1.5		

The manual cutting process also caused a rough and uneven edge of the features as can be seen in Figure 4.10.



Micrometre Scale Patterns using Photoresist

In the second part of the pattern transfer experiments, two structures of micropattern features were prepared using photolithography. The anode disks were patterned with a 0.8 -2.4 μm thick resist layer of AZ-5214E (AZ Electronic Materials). The micropattern structures 1 and 2 are shown in Figure 4.11 and 4.12 respectively. For

the structure 1 a negative photoresist was used so that it consists of the inverse of patterns would be transferred. The unexposed area of the micropattern comprised large squares (A), small squares (B), small circles (C), and some others complex features (D, E, F, G, H). The structure 2 was used a positive photoresist, so the micropattern that would be transferred contained large squares (A), small squares (B), small circles (C), and some others complex features (D, E, F, G, H) with an addition of vertical and horizontal linear feature (Figure 4.12). A summary of the features sizes and area is presented in Table 4.5 (structure 1) and Table 4.6 (structure 2).

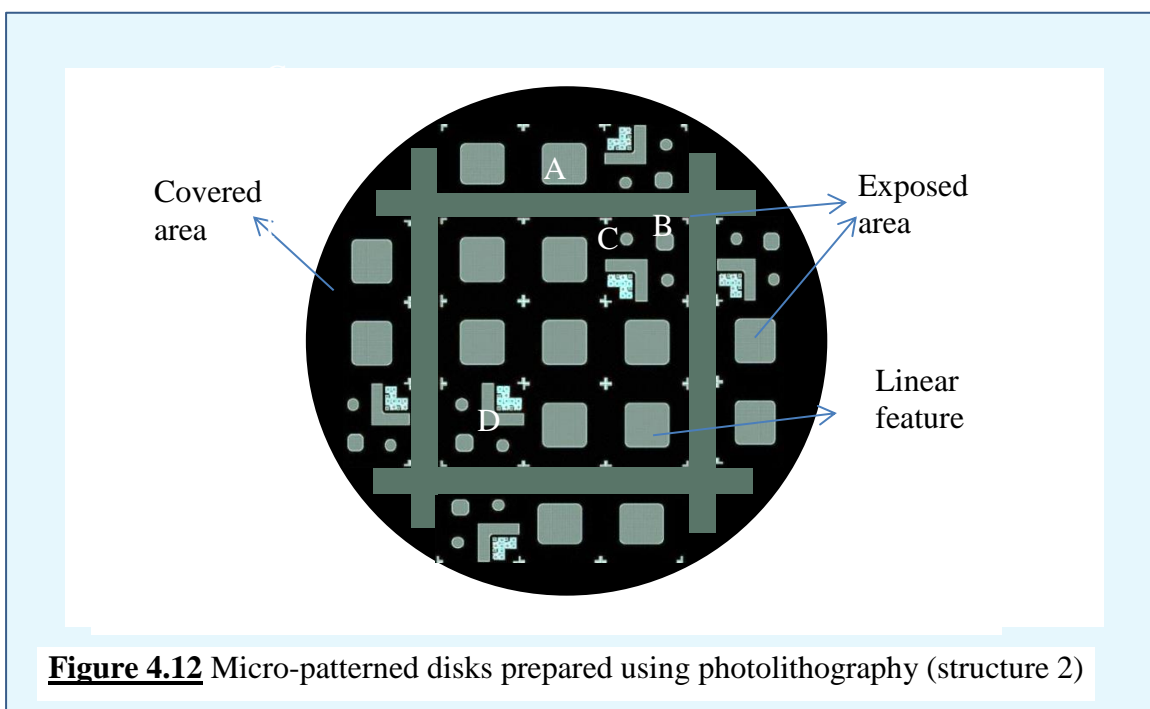
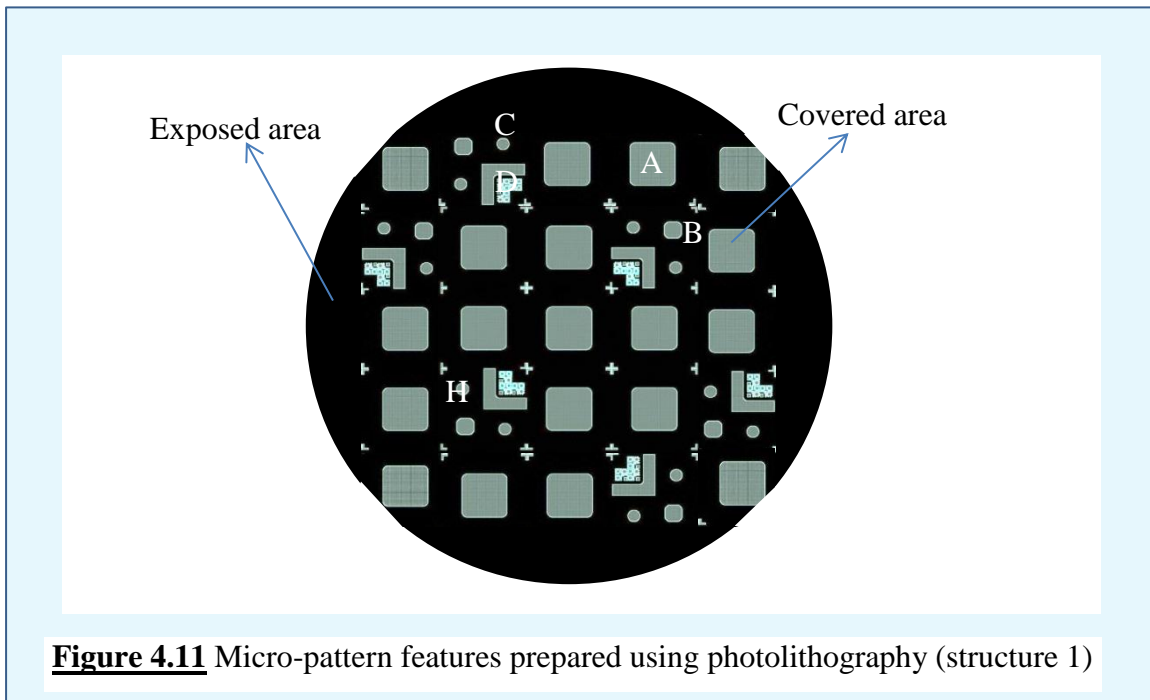


Table 4.5 a summary of feature sizes and area of micropattern prepared by photolithography for structure 1


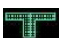






Features	Sizes (μm)	Number	Area (cm^2)	Percentage against Total anode area (%)
Large Squares (A)	793.65 x 793.65	22	0.13857	17.64
Small squares (B)	304.6 x 304.6	4	0.00371	0.47
Small circles (C)	D = 209.65	8	0.00276	0.35
Feature D		4	0.01358	1.72
Feature E 		8	0.00141	0.18
Feature F 		25	0.00207	0.26
Feature G 		12	0.00049	0.06
Feature H 		4	0.00053	0.07
A line in the edge		1	0.04338	5.52
Total covered area			0.20650	26.28
Total Anode area			0.78571	
Total exposed area			0.57922	73.72

Table 4.6 a summary of feature sizes and area of micropattern prepared by photolithography for structure 2

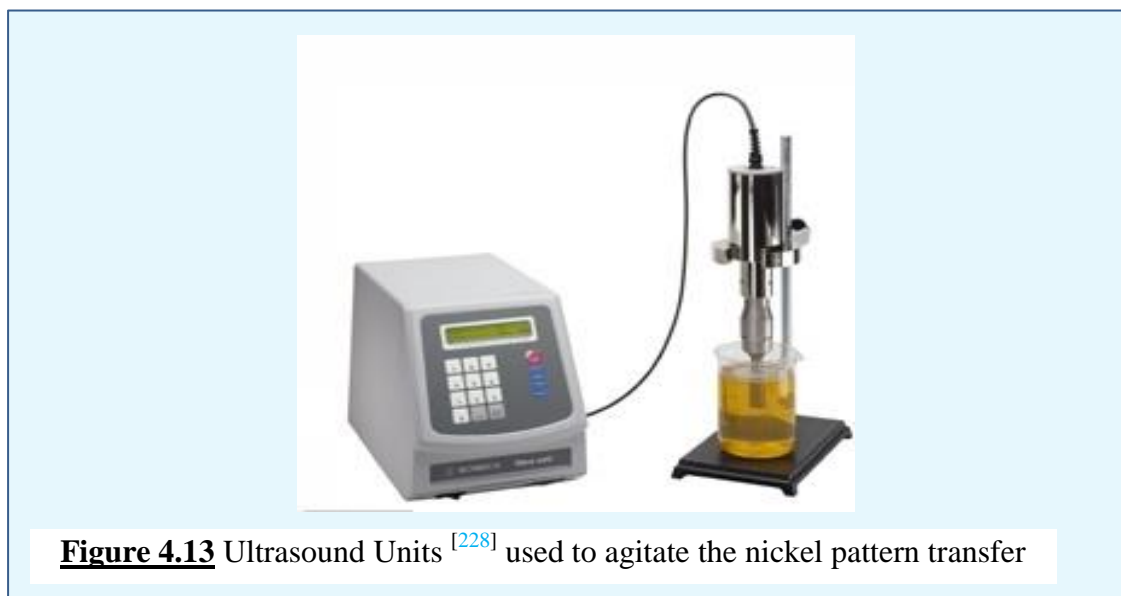
Features	Sizes (μm)	Number	Area (cm^2)	Percentage against the total anode area (%)
Large Squares (A)	802.63 x 802.63	18	0.11600	14.76
Small squares (B)	321.07 x 318.41	7	0.00716	0.91
Small circles (C)	D = 224.7	14	0.00555	0.71
Feature D		6	0.02040	2.60
Feature E 		4	0.00070	0.09
Feature F 		18	0.00149	0.19
Feature G 		12	0.00049	0.06
Feature H 		4	0.00053	0.07
A line in the edge		1	0.04338	5.52
Square line (L)		1	0.13600	17.31
Total exposed area			0.33114	42.15
Total Anode area			0.78571	

4.2.3 Ultrasound Unit

One of the main problems on the process of nickel pattern transfer using Enface method was gas bubbles trapped in the narrow interelectrode gap due to hydrogen evolution. In some cases, the electrodes surface was observed to be entirely blocked by the gas bubbles causing a sudden increase of cell potential as also reported in previous work ^[23]. This suggested that a sufficient agitation was required to overcome the gas bubbles issue. The agitation technique has to be appropriately chosen not only for eliminating the bubbles but also to achieve a good pattern transfer.

Ultrasound is well known as a fast agitation technique in an electrochemical system ^[227]. The ultrasonic agitation has the ability to enhance electrodeposition process by reducing crack formation ^[227] increasing the rate of mass transfer and the electrochemical reaction ^[227]. Therefore nickel electrodeposition of nickel under the ultrasonic agitation was carried out to improve nickel pattern transfer performance.

The experiments were carried out using an ultrasound horn of VC505 ultrasonic processor (Sonics, supplied by VWR) equipped with a standard probe with threaded end and replaceable tip (Figure 4.13). A titanium alloy tip (Ti-6Al-4V, 13 mm diameter) was fitted to the probe as a source of ultrasonic wave. A maximum power that can be supplied by the sonicator unit is 500 Watts at a constant frequency of 20 kHz.



4.3 Instrumentation

Instruments including potentiostat, pH/conductivity meter, and ultrasound unit mainly used throughout the experiments are described in this subchapter.

4.3.1 Potentiostat

All electrochemical experiments including polarisation experiments in the three-electrode cell and experiments in the Enface system were carried out using a PGSTAT30 potentiostat (Autolab) (Figure. 4.14). The potentiostat was connected to a laptop for data acquisition supported by General Purpose Electrochemical System (GPES) software version 4.9. The potentiostat was specified by potential range of ± 10 V and current ranges between 10 nA and 1A. The compliance voltage of the instrument was ± 30 V with maximum output current was ± 2 A. The data of potential-current collected from the experiments was interpreted using spreadsheet software (i.e. Microsoft excel).

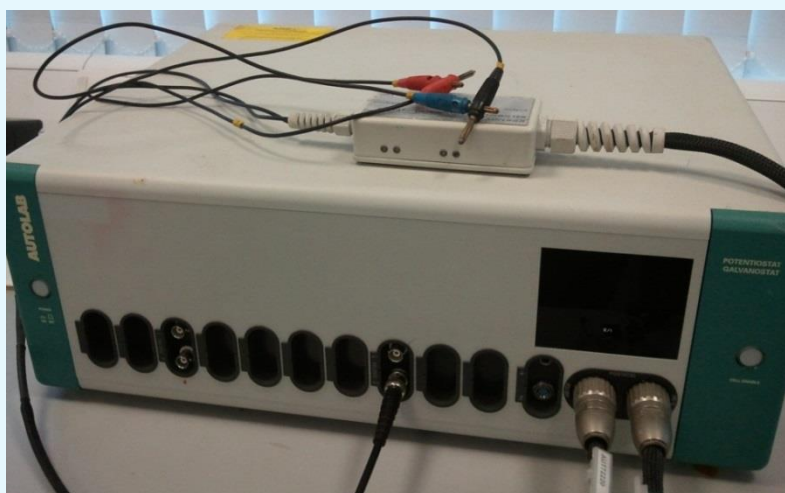


Figure 4.14 Potentiostat of Autolab PGSTAT30 used in the polarisation and pattern transfer experiments

4.3.2 Conductivity and pH Meter

An S47 SevenMulti™ dual pH and conductivity meter from Mettler-Toledo (Figure 4.15.) was employed in measuring pH and conductivity at room temperatures (18 – 22 °C). The pH measuring equipment is capable to measure a pH range between - 2.000 and 19.999 with an accuracy of ± 0.002 . A calibration of the pH meter using a customised buffer group of three (3) points against standard buffer solutions of pH 4.01, 7.00, and pH 10.01 (Mettler Toledo) was carried out prior to measurements.



Figure 4.15 Dual pH and conductivity meter used to measure physicochemical properties of the electrolytes

The conductivity measurement was accurate to $\pm 0.5\%$ with a resolution between $0.001\ \mu\text{S}/\text{cm}$ and $1000\ \text{mS}/\text{cm}$ ($1 \times 10^{-4}\ \text{S}/\text{m}$ and $100\ \text{S}/\text{m}$). Preceding the conductivity measurement, the conductivity measuring instrument was calibrated against a conductivity standard solution (Unidose, Radiometer Analytical). Five temperature points and their corresponding conductivity values of the standard solution, shown in Table 4.7, were used for the calibration.

Table 4.7 Temperatures and Conductivities of standard solution for the pH meter calibration.

Temperature, °C	20	25	30	35	40
Conductivity, $\mu\text{S}/\text{cm}$	900	1000	1104	1211	1320

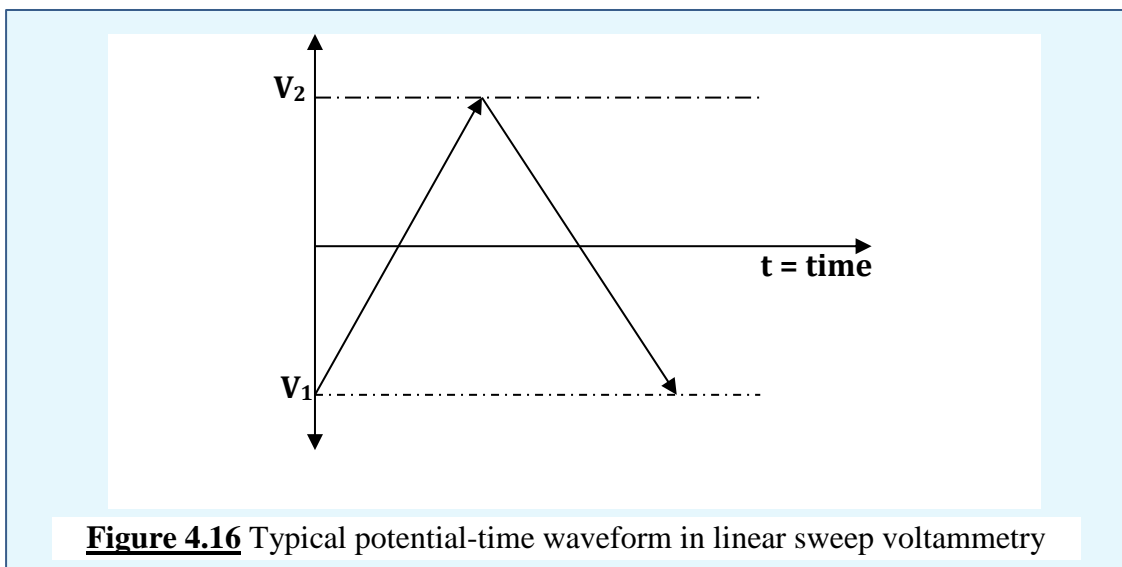
4.4 Procedures

4.4.1 Polarisation Measurement in a Three-electrode Cell and RDE System

The electrochemical deposition behaviour of nickel in the newly developed electrolyte was determined by polarisation experiments in a standard three-electrode cell using RDE system. Through these experiments, an onset potential for nickel electrodeposition was investigated. Linear sweep voltammetry (LSV) technique was employed to record polarisation data using the potentiostat of Autolab PGSTAT30 which was controlled by GPES software for data acquisition.

The principle of linear sweep voltammetry (LSV) technique is to linearly sweep electrode potential between two potential limits at a particular scan rate. Starting from an initial potential (V_1) toward negative direction until reach certain potential (V_2). At some cases the potential is reversely scanned back to the starting point (V_1).

During the potential sweep, current responses at working electrode are measured to produce a curve of voltammogram. Typical potential waveform as function of time is shown in Figure 4.16 ^[229]. Linear sweep voltammetry is often used to observe the potentials at which reduction or oxidation reactions take place.



If LSV is carried out at a slow scan rate (<5 mV/s) that allows the system to reach steady state prior to each measurement, a polarisation curve is obtained. The polarisation measurement is usually used in the initial stage of a metal electrodeposition process for investigating potential and applied current densities at which the metal deposition possibly to occur.

Preliminary polarisation experiments showed that an excessive hydrogen evolution was visible at an overpotential beyond -1.0 V. Henceforth, cathodic potentials were scanned from open circuit potential (OCP) to -1.0 V at different scan rates of 2, 5, and 10 mV/s to examine at which steady state condition was reached. To investigate the effect of convective-diffusion mass transfer, the RDE rotation speeds were varied between 0 and 3500 rpm.

A potential drop, known as I-R or Ohmic drop may occur as currents flow through the electrolyte with a relatively low conductivity. Since the potential was recorded between the reference electrode and the working electrode, the distance between the two electrodes has to be as close as possible to minimise the Ohmic drop. This can be achieved by a Luggin capillary tube. The tip of the Luggin capillary was

placed very close to the working electrode surface of about 3 mm, so that the uncompensated solution resistance was diminished due to the narrow distance [230, 231].

However, because the resistivity of the solution was very high, the uncompensated resistance of the solution might be significant even at the narrow gap [232]. Therefore, to ensure the measured potential was completely corrected, the uncompensated solution resistance was determined using the Autolab PGSTAT30 controlled by GPES software. I-interrupt method was used in the measurement [232, 233]. Once the resistance has been determined, potential value in the polarisation curves was corrected. I-R drop correction was carried out using GPES software.

4.4.2 Electrochemical characterisation of nickel electrodeposition in Enface system under stagnant condition

After electrochemical deposition behaviour of nickel in a standard system had been studied, polarisation experiments were carried out in the Enface system. The aim of the experiments was to investigate the effect of the cell geometry on the potential-current density profile. Linear sweep voltammetry (LSV) method was used to record polarisation data of the nickel deposition in the described cell (Figure. 4.4). The polarisation experiments were carried out in a stagnant solution at room temperature by using Autolab potentiostat (PGSTAT30) controlled by GPES 4.9 software for data acquisition. Potentials were scanned cathodically from open circuit potential (OCP) to -1.0 V at scan rate of 2 mV/s. The results from these experiments were used to determine optimal current densities for deposition of nickel features.

The experiments were initially carried out for the uncovered anode. However it was found that the polarisation data was affected by different feature sizes of the patterned anode. Therefore the polarisation experiments on several patterned anodes were performed to investigate the effect of feature sizes on the polarisation data. The polarisation experiments were carried out on pattern features of 8 x 4 mm, 8 x2 mm, 5x 2 mm, and 5x1 mm to observe how the potential-current profile changed.

The platinum wire reference electrode tip was arranged to be as close as possible (approximately 5 mm) to the working electrode to minimise a potential drop due to solution resistance. The uncompensated resistance between the working electrode and the reference electrode was also measured to correct the polarisation curves.

4.4.3 Electrochemical characterisation of nickel electrodeposition in Enface system under ultrasound agitation

The vertical-cylindrical cell described in Figure 4.4 was used with a 1 cm diameter copper disk as the substrate and the anode was a patterned nickel disk. A pattern feature of 5 mm x 1 mm was used throughout the experiments. The ultrasound probe was vertically placed in the cell facing to the narrow gap with a probe-electrode distance of approximately 1 cm. the set-up of the apparatus are shown in Figure 4.17.

Polarisation experiments were carried out in three electrode system. The potential was measured against the Pt wire reference electrode. The polarisation experiments were carried out under ultrasound agitation at two different amplitudes of 35% and 45% corresponding to power densities of 18 and 26 W/cm² respectively. Corresponding power densities to ultrasonic wave amplitudes are presented in Table 4.8. Polarisation data were recorded using the potentiostat of PGSTAT30 (Autolab) controlled by GPES software (version 4.9, as shown in Figure 4.14). An onset potential at which nickel deposition occurred was investigated and an optimal applied current density was determined.

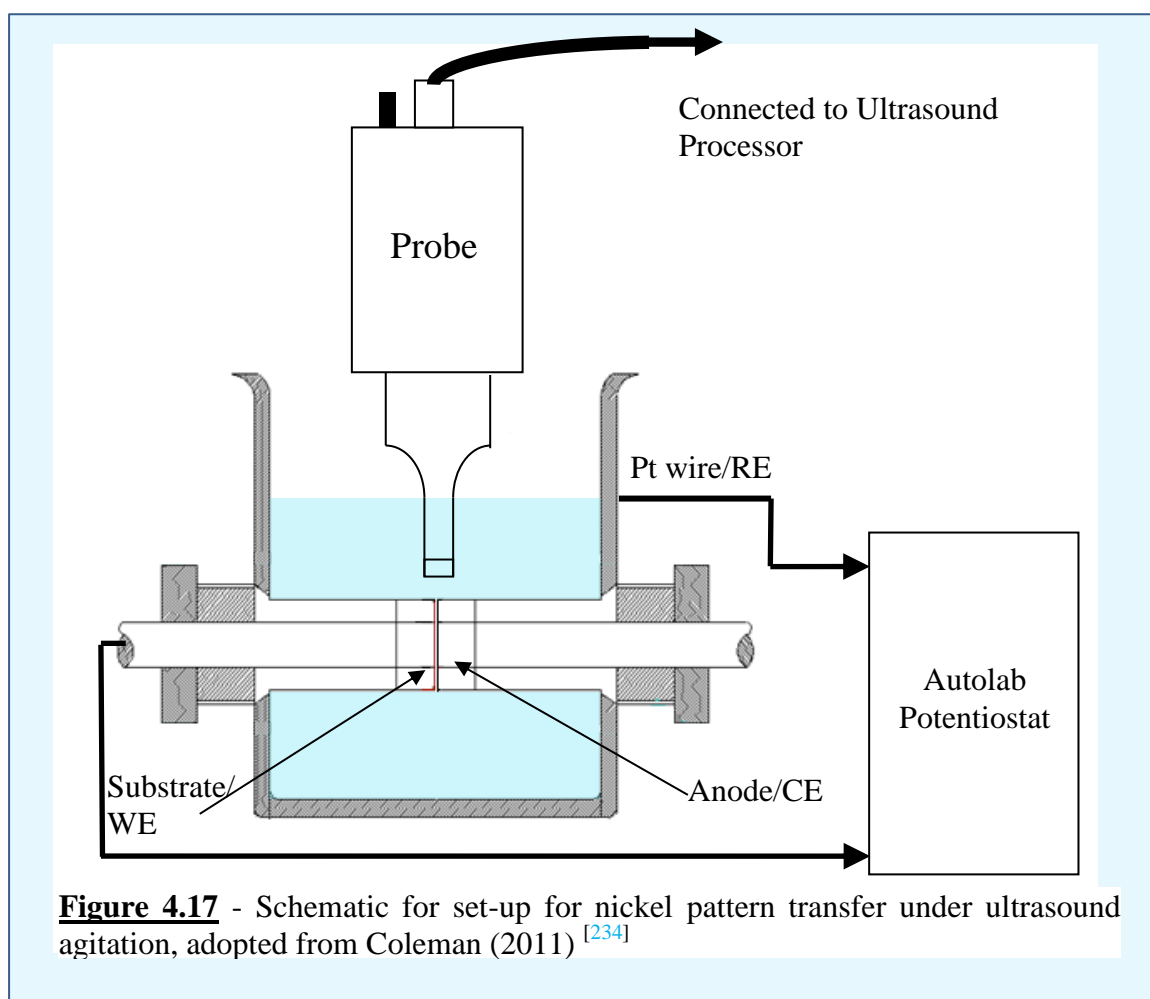


Table 4.8 Ultrasound amplitudes with corresponding power densities

Amplitude (%)	Power Density (W/cm ²)
30	16
35	18
40	21
45	26
50	29

4.4.4 Nickel Pattern Transfer Experiments under Stagnant Condition

Galvanostatic nickel deposition experiments were carried out for both millimetre and micrometre scale pattern features. Constant current densities corresponding to each feature size obtained from polarisation data were used to deposit nickel patterns.

Table 4.9 the applied current densities and deposition times for each pattern structures.

Pattern Features	Applied Current densities (mA/cm ²)	Deposition time (s)
Millimetre scale		
- 5 mm x 1 mm	-4.07 to -6.79	240 - 600
Micrometre scale (Kapton tape)		
- Structure 1	-6.46 to -8.29	180 – 300
- Structure 2	-6.67 to -8.50	125 - 190
Micrometre scale (photolithography)		
- Structure 1	-0.86 to -0.99	300 – 600
- Structure 2	-1.93 to -2.00	300

Deposition times varied between 240 s and 600 s in order to obtain different thicknesses. Deposition times were not possible to be longer than 600 s as there was profuse gas evolution beyond that period. Table 4.9 shows the applied current density ranges and deposition times for the patterned structures.

Conductivity and pH of the solution were measured before and after a number of pattern transfer experiments to determine if there was any significant difference in the properties of the electrolyte

4.4.5 Nickel Pattern Transfer under Ultrasonic Agitation

Nickel pattern transfer experiments under ultrasound agitation were carried out in Enface system. Galvanostatic pattern transfer experiments were carried out in a two-electrode system. Constant current density of 4.93 mA/cm^2 obtained from polarisation data were imposed to the system under ultrasound agitation at both amplitudes of 35 % and 45 % corresponding to power densities of 18 and 26 W/cm^2 respectively for 1200 s and 1500 s deposition times.. The effect of the agitation on the gas bubbles removal was visually observed. The shape and the size of the deposited nickel (feature) were measured using the travelling microscope. The deposit appearance was investigated using the optical microscope.

4.5 Structure Characterisation

4.5.1 Feature size and shape determination

To determine the shape of the electrodeposited nickel pattern, the thickness and the dimension of the deposit feature were measured. In the case of millimetre pattern features, the dimensions of the nickel deposits (i.e. features) were measured using a travelling microscope (J. Swift & Son series number 29371, Figure 4.18). The feature size of micrometre scale pattern was measured using optical microscope (BX41, Olympus). The measurements were carried out at 5x and 20x magnification depending on the features.

The thickness and the surface profile of the deposits were measured using a non-contact technique of an optical surface profiler (Zygo). The thickness across the entire feature was measured for the deposited nickel of the micron scale feature. In the case of millimetre scale features, the thickness across the entire width of the deposits could not be ascertained due to equipment limitation. In this case only the profile near the edges could be measured. This was carried out to investigate spread in the feature due to current distribution. A contact method for measuring surface profile of a deposited feature using Tencor P1 long scan profiler was also carried out to verify the results of previous measurements.

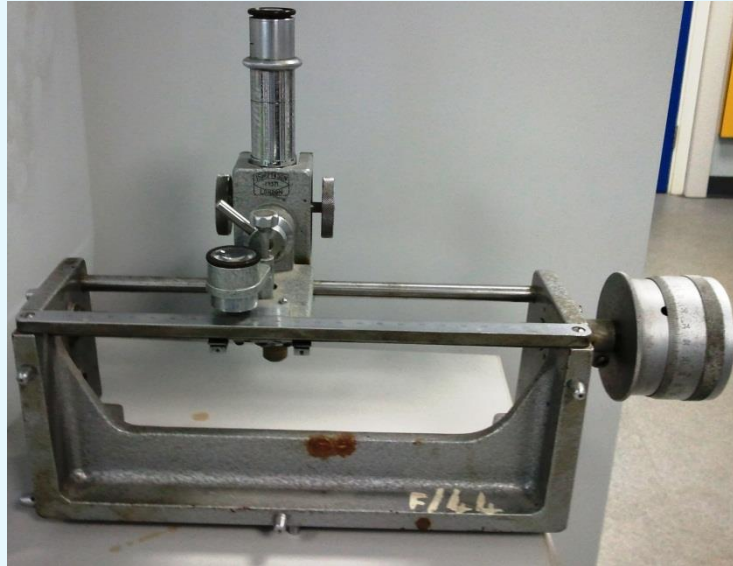


Figure 4.18 Travelling microscope for measuring deposited feature size

4.5.2 Deposit Characterisation

4.5.2.1 Optical Microscopy

Initial examination of surface morphology of the deposit was carried out using an optical microscope (BX41, Olympus) coupled with ALTRA 20 soft imaging system. The Olympus BX41 microscope was amplified with the Optiscan IITM motorised stage system (Prior Scientific) to accurately carry out a non-contact dimensional measurement. Supported by a computer system, the measurement could be directly taken from the PC monitor. This procedure was important for initial visual inspection of the deposit morphology as the experiments were repeatedly carried out. Digital images of the samples were usually taken at magnification of 5x and 20x depending on the target area. A further investigation on the surface morphology was carried out using a scanning electron microscope (SEM).

4.5.2.2 Scanning Electron Microscopy (SEM)

The microstructure of the nickel deposit was studied using a low vacuum SEM (Jeol JSM-5300LV). SEM was also used because it is more powerful than light microscope as the magnification of SEM is up to 200,000 times. The SEM inspection was aimed to examine if the deposit was dense.

An energy dispersive X-ray (EDX) analysis on the deposit was carried out to investigate if the deposits were metallic. The EDX spectroscopy is also useful to investigate how the deposit spread over the cathode surface through elemental mapping analysis. The measurements were accomplished using the SEM machine as it was equipped with EDX detector.

4.5.2.3 X-ray Photoelectron Spectroscopy (XPS)

A diffusion of copper from the substrate through the deposited nickel feature was investigated using X-ray Photoelectron Spectroscopy (XPS). The XPS analysis was carried out using K-Alpha instrument (Thermo Scientific). The analysis was carried out to investigate if the copper was detected on the surface of the nickel deposit indicating copper diffusion occurred along pores or grain boundaries.

To achieve this, several samples with different conditions and treatments were examined. At first, XPS analysis was carried out to investigate the presence of copper on the surface of freshly produced pattern feature as a base data. The investigation was carried out on pattern feature which was stored in a room temperature for 2 months representing storage period. To investigate the copper diffusion during operation of the device, a sample was treated by a temperature of 90 °C for 100 hours. Finally, a sample of pattern feature was annealed at temperature of 180 – 200 °C to analyse its performance during bonding process. A summary of all conditions is shown in Table 4.10.

Table 4.10 Samples conditioning and treatment for copper diffusion investigation

No.	Sample Id	Temperature	Time of analysis	Reason
1.	SR0H-T0	Room (18 – 20)	Fresh	Base data
2.	SR2M-T0	Room (18 – 20)	2 months	Storage
3.	S90C2M-T1	90 °C for 100 hours	1 month	Device operation
4.	S200C2M-T2	180 - 200 °C for 5 mins	1 month	Bonding process

4.5.2.4 XRD analysis

X-ray diffraction (XRD) analysis was carried out to investigate if there was any effect of heat treatment on the nickel crystal structure during the copper diffusion study. A Panalytical X'Pert Pro Multipurpose Diffractometer (Cu K α , 40 kV, 40 mA) was used in the analysis. An X'Celerator was built into the diffractometer to advance the detector technology as it is an ultra-fast X-ray detector with Real Time Multiple Strip (RTMS) technology. The diffractometer was also equipped with a secondary monochromator.

XRD measurements were carried out on samples with and without the heat treatment to investigate if there was any significant change in crystal structure or phase. Using the XRD data and Scherrer's formula (Equation 4.7), the average grain size of the deposited nickel can be estimated^[235].

$$\tau = \frac{K\lambda}{\beta \cos \theta} \quad (4.7)$$

In the equation (4.7), τ is crystallite size (nm), K is shape factor (0.9), λ is x-ray wavelength (nm), β instrumental line broadening at FWHM, and θ is Bragg angle (rad). To interpret XRD data, initially three XRD peaks with most intensity were identified. Thereafter, the average of the three peaks was used to calculate the average of crystal size. The phase on the samples was identified by observing an identical data in the database of International Centre for Diffraction Data (ICDD).

However, after several measurements have been carried out, nickel peak was not evident in XRD scan due to the submicron thickness of the deposit. Contribution from substrate to the diffraction probably overshadowed the contributions from thin film

4.5.3 Current Efficiency of Nickel Deposition

Current efficiency was calculated by dividing a theoretical charge that should have been applied to obtain the amount of deposited nickel at 100 % efficiency with the applied charge. The quantity of deposited nickel was estimated according to the shape and the thickness profile of the deposit. As in most cases the features were elliptical in shape, a half ellipsoid was used to approximate the deposit volume (Figure 4.18).

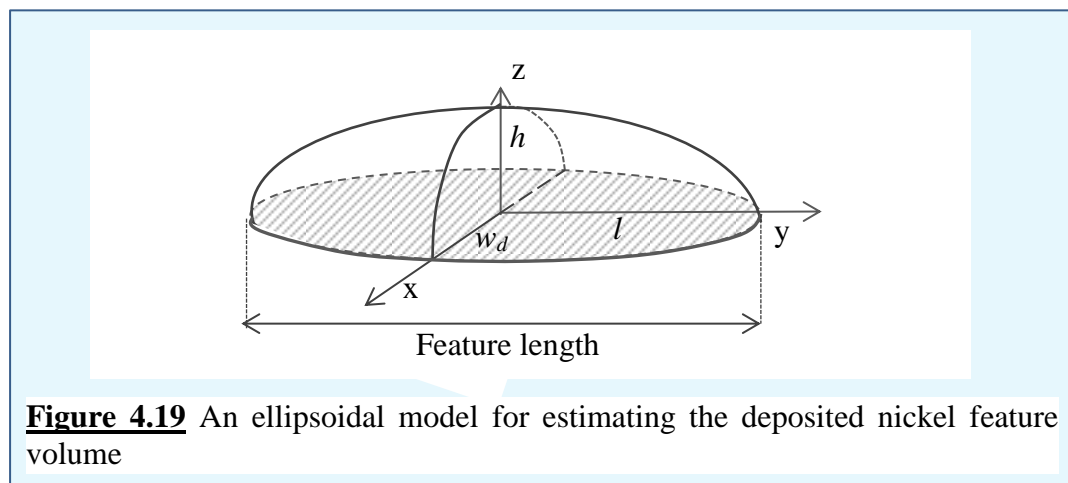


Figure 4.19 An ellipsoidal model for estimating the deposited nickel feature volume

A typical equation used to calculate the ellipsoidal volume was:

$$V = \frac{1}{2} \left(\frac{4}{3} \pi l \cdot w_d \cdot h \right) \quad (4.8)$$

In equation (2) h is the deposit thickness on the middle part, l is a half of the feature length, and w_d is a half of the deposit width. The weight of the nickel deposit was estimated using this volume and a nickel density from literature ^[156]. By means of faraday's formulae and electrochemical equivalent method, the theoretical charge was calculated. The cathodic current efficiency was calculated using equation (3.50).

Chapter 5

Experimental Results and Discussion:

Electrochemical Characterisation

The development of a nickel electrolyte for pattern transfer using Enface technique has been described in Chapter 4 section 4.1. Based on its physicochemical properties, the electrolyte solution of 0.19 M nickel sulfamate was selected for nickel pattern transfer process. Observing the composition and the properties of the chosen electrolyte by comparing to the commercially available and commonly developed nickel electrolytes (Table 2.1), a number of advantages could be gained. As shown in Table 5.1, the electrolyte has lower metal ion concentration, has no acidifying additive such as boric acid, is of neutral pH and can be operated at room temperature. This shows that the newly developed nickel electrolyte is advantageous to achieve environmentally friendly and less expensive process for pattern transfer. This also implies that Enface technology would demonstrate a sustainable process for nickel pattern deposition.

Table 5.1 Comparison of Commercial and commonly developed nickel electrolyte and nickel electrodeposition solutions for EnFACE process

	Electrolyte composition (g/l), Nickel Electrodeposition bath	
	Commercially available, commonly developed	For Enface process
Nickel Sulfamate	201 - 983	62.6
Nickel Chloride	0 – 30	-
Boric Acid	30 – 45	-
Temperature (°C)	32 – 60	Room temperature
pH	3.5 – 5	6 – 7
Conductivity	11.7 - 57.3 S/m	2.19 S/m

Therefore, this section will be focusing on electrochemical analysis of the electrolyte using voltammetry to gain a better understanding of the solution electrochemistry. The ultimate objective of these experiments was to determine whether it is possible to deposit nickel from the chosen electrolyte. In addition, through these experiments, the cathodic potential region where nickel deposition is feasible is identified.

5.1 Electrochemical characterisation of the electrolyte in three-electrode cell using rotating disc electrode (RDE)

A set of linear sweep voltammetry (LSV) experiments were carried out for the electrolyte containing 0.19 M nickel sulfamate in the three-electrode cell. The scan rate was varied between 0.5 and 10 mV/s at a rotation speed of 0 rpm to identify the condition where a near steady state condition was achieved. Each scan was repeated several times so that at least 5 identical polarisation data/curves were obtained to ensure its reproducibility. Even though the substrate changed from Cu to Cu/Ni during the experiment, the polarisation data was not significantly affected as the characteristic of Cu and Ni is relatively similar.

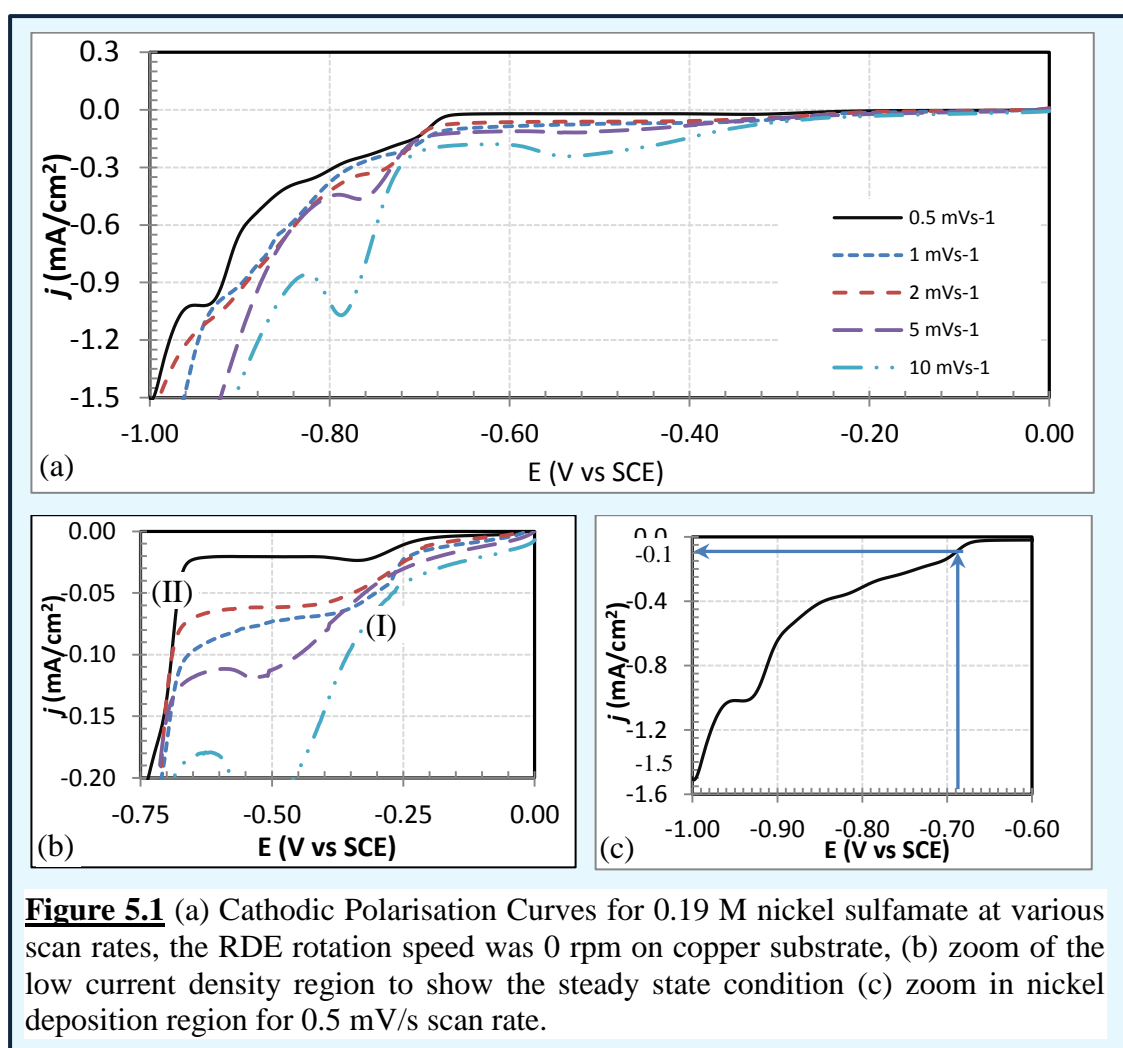
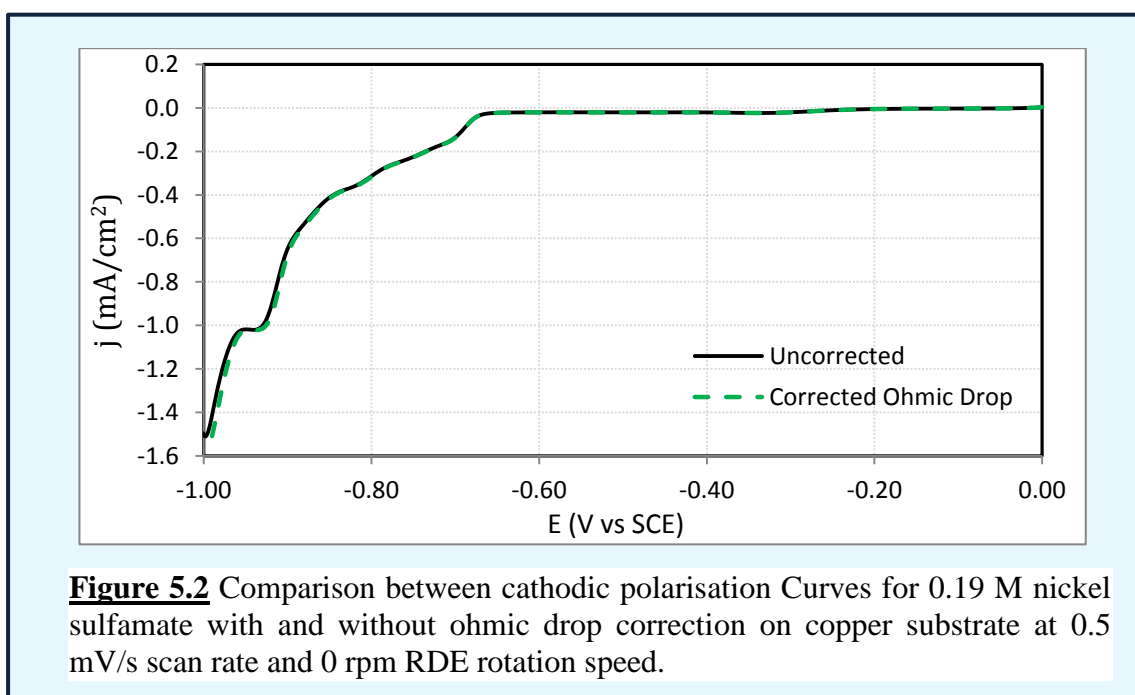


Figure 5.1 (a) shows linear sweep voltammograms for the reduction of 0.19 M nickel sulfamate at the different scan rates. It can be seen that at the higher scan rates, peaks corresponding to the inhibition effect of adsorbed species are observed. This indicates that the system has not reached equilibrium. Near steady state polarisation was achieved at a scan rate of 0.5 mV/s due to the absence of current density peaks. . The

slow scan rate provided a sufficient time for the electron transfer to take place and relax so that the response current was always measured at equilibrium. As a result, the difference between the system and its true steady state was negligible. True steady state polarisation data is normally recorded by either applying a constant potential for an indefinite period of time and observing the stable potential response, or *vice versa*.

As shown by the inset of Figure 5.1 (b), a cathodic current is observed commencing at an overpotential of around -0.015 V. However no deposit was observed at these potential. Two reduction waves, marked (I) and (II) are identifiable in the potential range from -0.2 to -0.4 V. An additional wave at overpotential of approximately -0.7 V, as shown in Figure 5.1 (c), indicated by a rapid increase in the current density and the appearance of a nickel deposit.

This suggests that nickel deposition is a multiple step. Based on the fact that nickel deposition was observed below -0.7 V, the reversible potential for nickel deposition was estimated to be in the potential region of -0.7 to -1.0 V. The corresponding current densities for nickel deposition were expected to be in the range of -0.1 to -1.5 mA/cm² as shown in Figure 5.1 (c). Hydrogen evolution was observed at overpotential greater than -1.0 V.

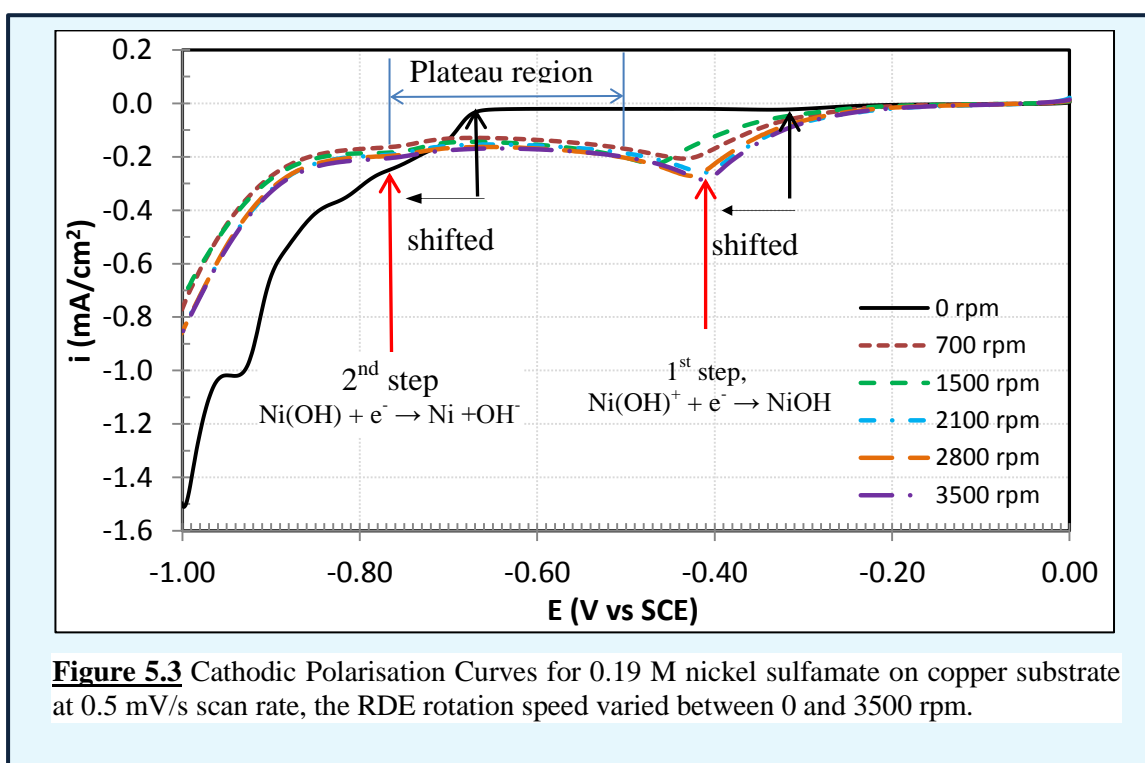


The uncompensated ohmic drop of the system was also measured in order to correct the data. Figure 5.2 shows a comparison between cathodic polarisation curves for 0.19 M nickel sulfamate with and without ohmic drop correction obtained at scan rate of 0.5 mV/s. As can be seen, the polarisation curves do not show a significant difference. This shows that the arrangement of placing the reference electrode at a close

proximity to the working electrode using the luggin capillary tube effectively minimised the potential drop.

Observing the polarisation curve for the electrolyte of 0.19 M nickel sulfamate obtained at 0.5 mV/s scan rate under no agitation as shown in Figure 5.1 - 5.3, it is characterised by two identifiable shoulders. First shoulder (I) lies at an overpotential between -0.2 V and -0.4 V, whereas the second (II) is from an overpotential around -0.7 V to a potential where hydrogen evolution becomes significant (-1.0 V). This suggests that nickel deposition took place through two consecutive one-electron transfer reactions as already discussed in Chapter 2 section 2.1.3. This is also in agreement with previous works ^[140, 236]. The shoulder (I) may relate to the first electron transfer (equation 2.6), and the second electron transfer process (equation 2.7) is represented by the shoulder (II).

Figure 5.3 shows the effect of RDE rotation speed on the polarisation data. A moderate increase in current density is observed for 700 rpm as compared to that for stagnant solution. This indicates that convective-diffusion improves the electrochemical reaction rate when the solution was agitated. However, a further increase in the RDE rotation speed up to 3500 rpm increased the current density only slightly, showing nickel deposition process is not mass transfer controlled ^[237]. The nickel deposition process tends to be controlled by mixed kinetics and mass transfer, as has been discussed in Chapter 2 Section 2.1.3. This finding is also in agreement with previous reports ^[165, 170, 238].



The plateau curve at potential range between -0.4 and -0.7 V shows that the first step is mass transfer dependant which is a transport of Ni^{2+} ions to the electrode surface. This is confirmed by the peak clearly identified when the system was agitated. The result is supported by previous study^[236]. It was also suggested that the active intermediate is being absorbed to the electrode surface simultaneously with the first reduction reaction^[236, 239] and in this work indicated by the decrease of current density after the peak. As a result, second step electron transfer depends on the adsorbed species which causes an inhibition effect^[240].

Figure 5.3 also shows that the agitation shifted the onset potential for nickel deposition and hydrogen evolution by approximately 0.10 V to more negative potential. This negative shift is thought to be caused by the enhancement of the inhibition effect of the adsorbed intermediate ($\text{Ni}(\text{OH})_{ads}$), as the rate of the first electron transfer increases with an increase in mass transfer of nickel ion (Ni^{2+}) resulting in more production of the adsorbed intermediate.

The polarisation curves for 0.19 M nickel sulfamate solution obtained from the standard three-electrode system at different RDE rotation speed (Figure 5.3) shows a small current density peak at a potential of around -0.4 to -0.44 V. This may be explained by the fact that under force-convective mass transfer due to disc rotation, nickel ion (Ni^{2+}) concentration at the cathode surface increases. This increases the rate of first reaction step, however with the increase in the production of $\text{Ni}(\text{OH})^+$ ions, the adsorption of excess intermediate inhibits the electron transfer process for the second step^[140, 241, 242]. This is shown by the extended plateau region under agitated conditions.

As already discussed in Chapter 2 section 2.13, nickel oxides or hydroxides, as well as hydrogen might be co-deposited along with nickel. In the case of an unbuffered neutral electrolyte in the presence of oxygen, the codeposition of hydroxides and hydrogen evolution more facile to occur as suggested by Cui (1995)^[236]. As shown in Figure 5.4, in the backward scan when the potential was swept to anodic direction, a single anodic peak is observed at an overpotential of -0.37 V prior to oxygen evolution representing oxidation of nickel. However, the intensity of the peak is much smaller than the nickel deposition. This shows that the deposited nickel oxidation was incomplete due to the formation of passivating species $\text{Ni}(\text{OH})_2$ ^[236].

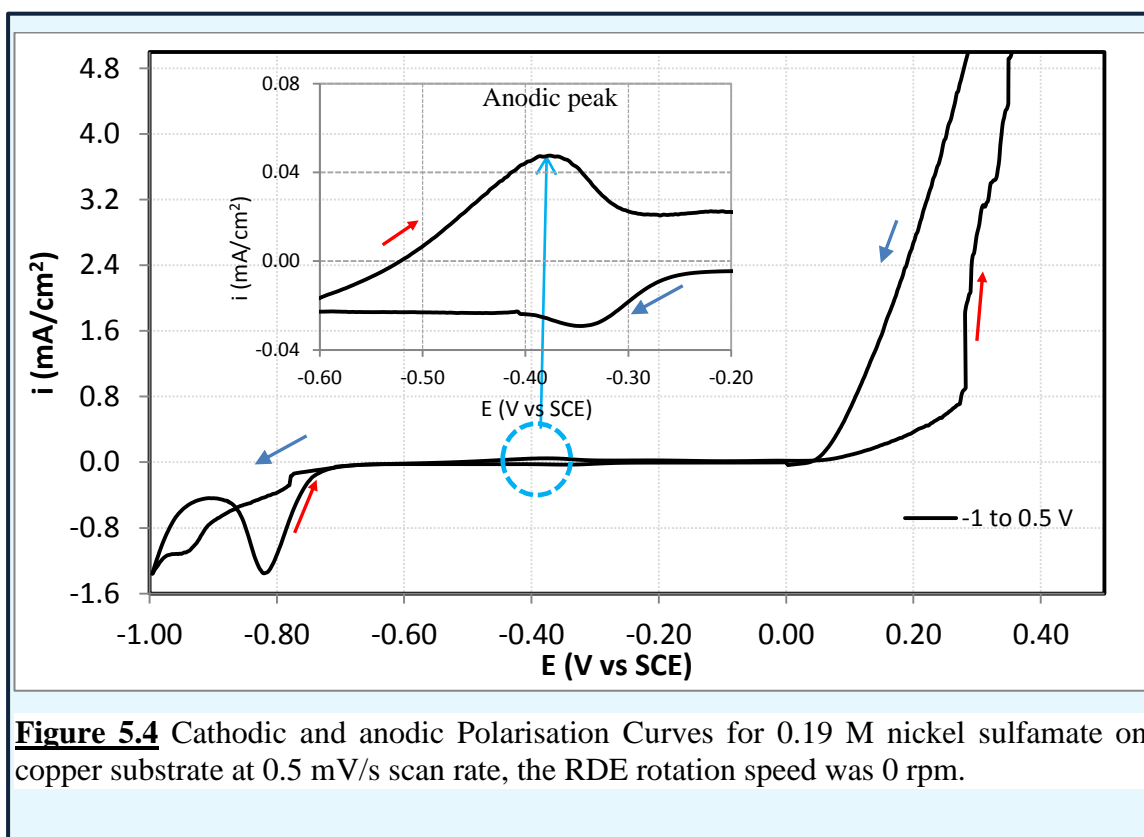


Figure 5.4 Cathodic and anodic Polarisation Curves for 0.19 M nickel sulfamate on copper substrate at 0.5 mV/s scan rate, the RDE rotation speed was 0 rpm.

5.2 Electrochemical characterisation of nickel electrodeposition in Enface reaction system under stagnant condition.

Linear sweep voltammetry (LSV) experiments were carried out to obtain polarisation data for the electrolyte containing 0.19 M nickel sulfamate in the Enface system at room temperature (20 ± 2 °C) under stagnant conditions. The overpotential was measured against Pt wire reference, while the current density was calculated based on the area of the feature on the anode. The reason to do so is mainly due to the fact that the pattern size on the cathode cannot be predicted prior to and as the deposit grows, the surface area continuously changes. In all experiments, the interelectrode gap was maintained at 300 μm and the scan rate was set to 2 mV/s with an assumption that near steady state polarisation conditions were achieved. Millimeter pattern features used in this polarisation experiments were manually fabricated by using kapton tape.

Figure 5.5 shows the cathodic polarisation data for 0.19 M nickel sulfamate carried out at scan rate of 2 mV/s in non-agitated Enface system compared to those obtained in standard three-electrode cell using RDE system at the same conditions. The comparison shows that the polarisation data is affected by the geometry of electrochemical cell for Enface system. Comparing the polarisation curves to those obtained in the standard three-electrode cell, the cathodic current density

commencement is shifted to more negative potential (at around -0.08 V, Figure 5.5 inset).

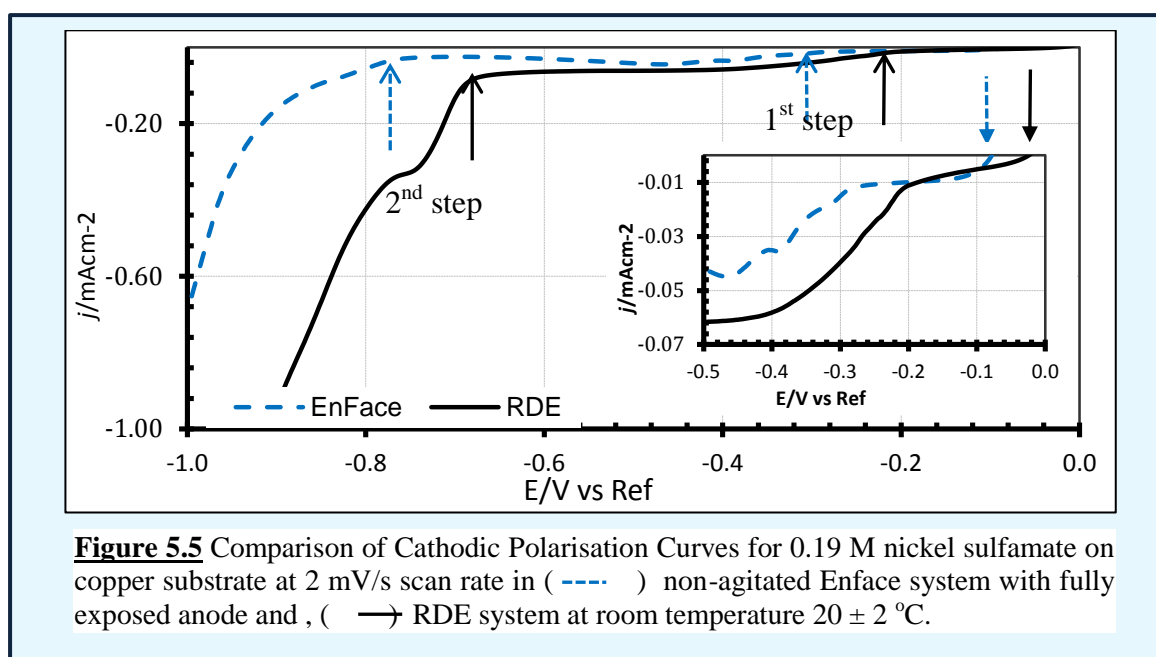


Figure 5.5 Comparison of Cathodic Polarisation Curves for 0.19 M nickel sulfamate on copper substrate at 2 mV/s scan rate in (- - -) non-agitated Enface system with fully exposed anode and , (—) RDE system at room temperature 20 ± 2 °C.

The potential region for nickel deposition is also shifted to approximately between -0.8 and -1.0 V with the significant hydrogen evolution occurred at a similar overpotential beyond -1.0 V. A summary of the comparison is presented in Table 5.2.

Table 5.2. Comparison of cathodic polarisation data for 0.19 M nickel sulfamate at 2 mV/s scan rate between non-agitated Enface system with fully exposed anode and RDE system.

System	Current density commencement	Ni deposition potential region	Hydrogen Evolution	Ni Deposition current densities
Enface	-0.08 V	-0.8 to -1.0 V	< -1.0	-0.05 to -0.7 mA/cm ²
RDE	-0.015 V	-0.7 to -1.0 V	< -1.0	-0.12 to -1.6 mA/cm ²

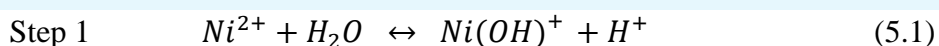
Polarisation curve of 0.19 M nickel sulfamate obtained in Enface system shown in Figure 5.5 is also characterised with two potentials where the current increase significantly i.e. -0.3 V and -0.8 V. The potentials correspond to nickel deposition mechanism involving two steps electron transfers which has been discussed in the previous section. In addition, current densities for nickel deposition obtained in the Enface system at the same conditions are lower than those obtained in the standard cell with RDE system. This might be due to sluggish transport of Ni^{2+} from the solution bulk outside the narrow gap towards the electrode surface within the gap. As a

consequence of the lower current densities, the rate of nickel deposition would be lower too.

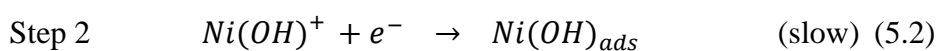
The narrow interelectrode gap might also affect the counter electrode reaction as one of the side product of nickel deposition reaction and hydrogen evolution is hydroxyl ions. As gas hydrogen bubbles and all side products including the hydroxyl ions remained within the narrow gap, the pH of the solution at the region near the electrode surface increased. Accordingly, the passivation of the nickel anode might be accelerated due to the excess of hydroxyl ions through the reactions (equation 2.22 -2.23). As a result, the polarisation data showed the lower current density.

5.3 Kinetic Analysis

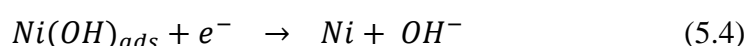
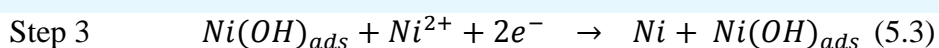
A kinetic analysis was carried out on polarisation data for 0.19 M nickel sulfamate obtained on copper substrate in non-agitated Enface system with fully exposed anode. As the polarisation data were obtained at a slow scan rate of 2 mV/s, it was assumed that the condition of near steady state has been achieved. As has been discussed, the potential-current data without agitation shows two current density waves indicating two reduction steps of nickel deposition. In an unbuffered neutral nickel electrolyte, as suggested by Cui and Lee (1995) ^[236], the mechanism of nickel deposition involves chemical reaction, adsorption, and two single-ion transfer. The process involves a formation of nickel monohydroxide ion ($Ni(OH)^+$) representing an active intermediate through a kinetically fast ^[140, 243] homogeneous chemical reaction in the first step. The chemical reaction (5.1) is led by the mass transfer of Ni^{2+} from the bulk to the electrode surface ^[165, 170, 238].



In the second step, the active intermediate is electrochemically reduced and simultaneously adsorbed onto cathode surface ^[243].



Two parallel electron transfer reactions (5.3 and 5.4) subsequently take place in the third step following the adsorption of the active intermediate. $Ni(OH)_{ads}$ is reduced through the reactions 5.3 and 5.4 to obtain metallic nickel deposit ^[236, 243].



Reaction (5.3) may predominantly occurs at overpotential above -0.7 V as the deposited nickel metal will not passivate but remained covered by the intermediate ($Ni(OH)_{ads}$). Reaction (5.4) becomes major pathway in the reduction of intermediate to metallic nickel at potentials below -0.7 V. However, the production of OH^- facilitates the formation of nickel hydroxide ($Ni(OH)_2$) so that the deposited nickel will passivate fast.

In a dilute solution with low nickel concentration, for step 2, the adsorption of intermediate ($Ni(OH)_{ads}$) is relatively fast, and the first electron transfer is slow so that it becomes a rate determining step, as has been confirmed by previous studies [140, 243]. Therefore, the rate of overall electrodeposition process is determined by the first electron transfer (5.2). Based on this, kinetic parameters of nickel electrodeposition including the charge transfer coefficient, the Tafel slope, and the exchange current density were calculated.

Referring to equation 3.37; the rate of the first electron transfer reaction (5.2) as the determining step is given by [211, 212]

$$\text{As } r_R = j, \quad j = nFAkC_A \exp[\alpha F \eta / RT] \quad (5.5)$$

$$j = nFkC_{Ni(OH)^+} \exp[\alpha F \eta / RT] \quad (5.6)$$

$$r_R = nFkC_{Ni(OH)^+} \exp[\alpha F \eta / RT] \quad (5.7)$$

Equations (5.5 – 5.7) are useful for calculating the charge transfer coefficient (α) at an overpotential and a current density where the first electron transfer is expected to occur. In order to be able to determine the charge transfer coefficient, the surface concentration of $Ni(OH)^+$ ($C_{Ni(OH)^+}$) has to be estimated. Since nickel electrodeposition takes place through multiple steps, a schematic illustration of the mechanism of mass transfer and reaction was developed so that the concentration of $Ni(OH)^+$ at the cathode surface could be estimated. The illustrative model is presented in Figure 5.6.

According to the mechanism shown in Figure 5.6, the surface concentration of $Ni(OH)^+$ depends on the reaction (5.1). Since equation (5.1) is a fast reaction, it can be considered to be at equilibrium.

$$K_e = \frac{[Ni(OH)^+][H^+]}{[Ni^{2+}][H_2O]} \quad (5.8)$$

Where K_e is the equilibrium constant.

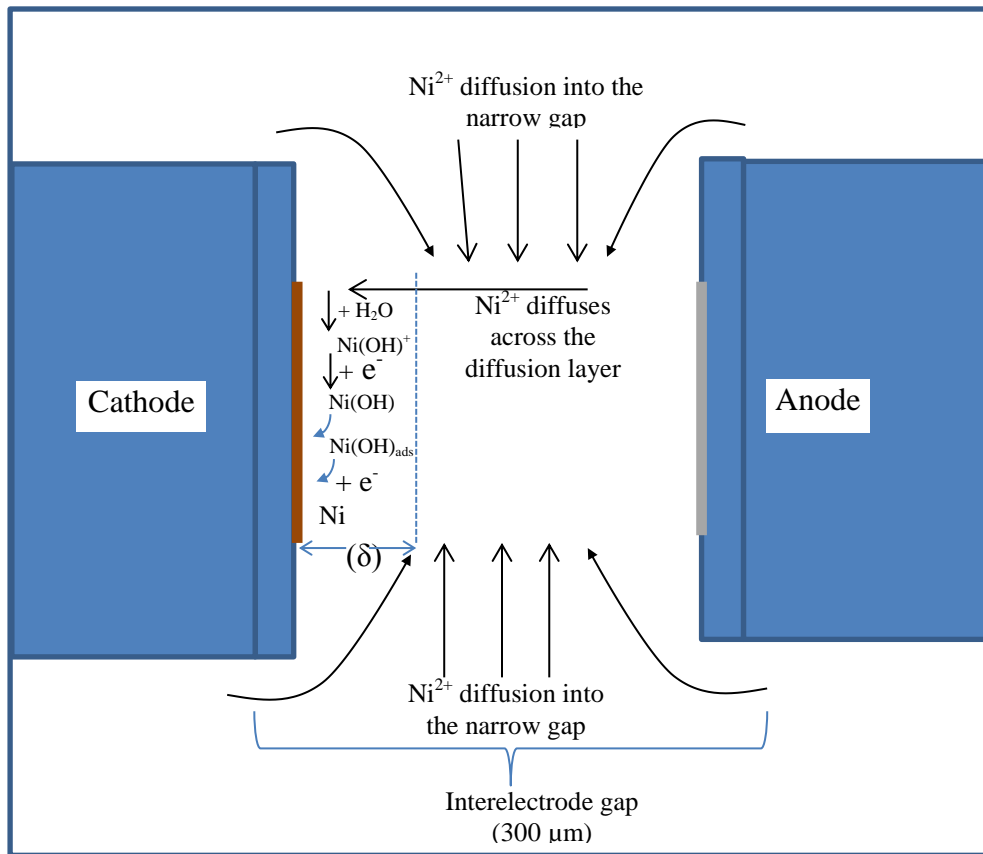


Figure 5.6 A schematic illustration of the mechanism of nickel electrodeposition in Enface system

The concentration of $Ni(OH)^+$ is given by:

$$[Ni(OH)^+] = \frac{K_e[H_2O][Ni^{2+}]}{[H^+]} \quad (5.9)$$

$$[Ni(OH)^+] = K'_e[Ni^{2+}] \quad (5.10)$$

When the concentration of H_2O is much higher than the concentration of Ni^{2+} (55.56 M vs. 0.19 M), therefore, it can be assumed that the initial concentration of $[Ni(OH)^+] \approx [Ni^{2+}] \approx 0.19$ M.

The surface concentration of $Ni(OH)^+$ at any time when the reaction takes place depends on the concentration depletion, due to sluggish transport within the narrow gap. The depletion is equal to the amount of $Ni(OH)^+$ that is consumed by reaction 5.1. This can be estimated by using Faraday's law for a fully exposed anode at a plating current of -0.035 mA/cm² for 200 s. The amount of consumed is $5.70E-08$ mol. The total Ni^{2+} within the solution in the electrode gap is $8.96E-06$ mol. Therefore the decrease in Ni^{2+} concentration is $5.70E-8$ mol (details in Appendix B). This shows that the depletion of Ni^{2+} is insignificant. The surface concentration of $Ni(OH)^+$ is therefore assumed to be

equal to its initial value of 0.19 M. This surface concentration was used to calculate the charge transfer coefficient (α) using Equation (5.6)

The Tafel slope for the electrochemical reaction is given by the following equation ^[211]

$$\left(\frac{dE}{d \log i}\right)_{C_{Ni(OH)^+}} = \frac{-2.303 RT}{\alpha F} \quad (5.11)$$

Referring to equation (3.22 and 3.23), the exchange current density is calculated by equation 5.13

$$\ln \left| \frac{j}{j_0} \right| = -\frac{-\alpha n F}{RT} \eta \quad (5.12)$$

$$j_0 = \frac{j}{\left[-\exp\left(\frac{-\alpha n F}{RT} \eta\right)\right]} \quad (5.13)$$

A summary of the kinetic data and the calculation results is presented in Table 5.3. A typical kinetic rate constant of nickel reduction reaction (k) and a diffusion coefficient of nickel (D) are obtained from literature ^[244].

Table 5.3 A summary of the kinetic data and the results of the analytical calculation of the kinetic of nickel electrodeposition in the electrolyte of 0.19 M nickel sulfamate.

Parameters of Nickel Electrodeposition	Data	Calculation Kinetic parameters
kinetic rate constant of nickel (k)	$8.75 \times 10^{-9} \text{ cm/s}$ ^[243]	
Diffusion coefficient (D)	$7.00\text{E-}06 \text{ cm}^2/\text{s}$ ^[243]	
Overpotential (η) for 1 st electron transfer reaction	-0.375 V	
Current density (j) for 1 st electron transfer reaction	-0.035 mA/cm ²	
Charge transfer coefficient (α)		0.36
Exchange current density (j_0)		$1.6 \times 10^{-4} \text{ mA/cm}^2$
Tafel Slope		160 mV/decade

5.4 Experimental $\eta - j$ Data Analysis using graphical method

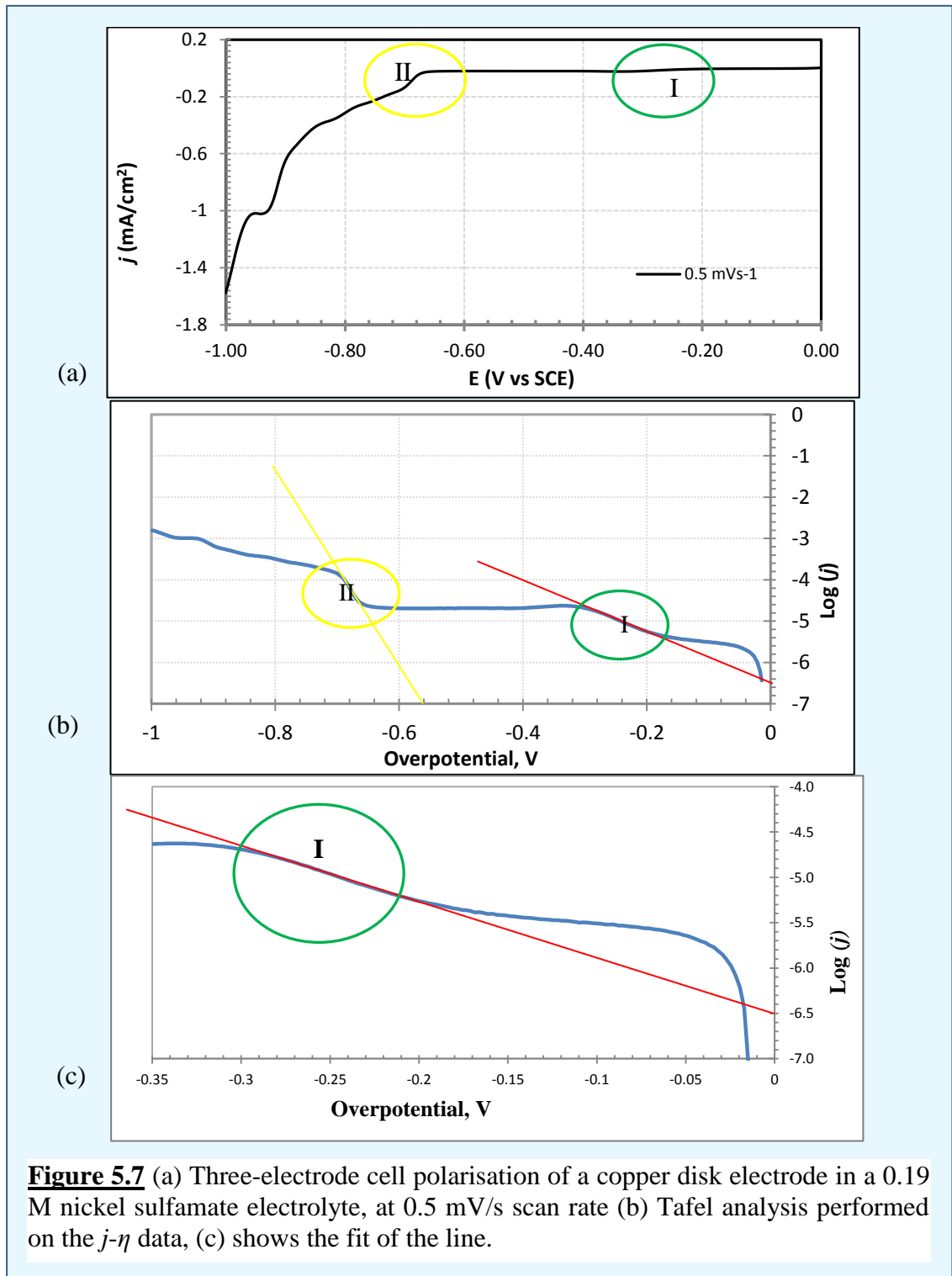
The polarisation data of nickel electrodeposition in an unstirred 0.19 M nickel sulfamate solution carried out at 0.5 mV/s scan rate using standard RDE system shown in Figure 5.7 (a) is used in this analysis. The kinetic parameters of the system were determined by plotting η vs $\log(j)$ which is known as Tafel plot (Figure 5.7 (b and c)). As the rate of nickel electrodeposition is controlled by the first electron transfer reaction, the Tafel slope at a region I is used to calculate the kinetic parameters.

From the Tafel plot (I) in Figure 5.7 (b and c), the kinetic parameters of the system were obtained and are presented in Table 5.4. The results of analytical and the graphical analysis of nickel electrodeposition kinetics are then compared with those obtained from literature. Table 5.4 also shows the kinetics parameters in this current study compared to those in literature. Some significant differences are observed which most probably caused by the difference in composition and concentration of the electrolytes, operating temperature, and pH which may lead to different reaction mechanism. However, the results obtained in this work are in the range of acceptable values.

Table 5.4 Physicochemical properties and kinetic parameters of the electrolyte used in micropattern transfer process simulations. κ is the measured electrolyte conductivity, j_0 is the calculated exchange current density, and α_c is the calculated cathodic transfer coefficient, for comparison other data in literature are also listed.

Electrolyte and Substrate	T (°C)	pH	κ (S/m)	Tafel Slope (mV/dec)	j_0 (mA/cm ²)	α_c
0.19 M Ni(SO ₃ .NH ₂) ₂ * copper, graphic	20 ± 2	6.70 ± 0.22	2.19 ± 0.06	159	3.16E-4	0.37
0.19 M Ni(SO ₃ .NH ₂) ₂ * copper, analytic	20 ± 2	6.70 ± 0.22	2.19 ± 0.06	160	1.60E-4	0.36
0.5 N NiSO ₄ [245]	room				1.00E-3	
0.85 M NiSO ₄ + 0.15 M NiCl ₂ , vitreous carbon [141]	25	5.18		143		
1.02 M NiSO ₄ , nickel [246]	25±1	2.5		110	5.80E-2	0.53
0.1 M Ni(SO ₃ .NH ₂) ₂ , mercury [247]	room	5 - 6		118		
0.63 M NiSO ₄ + 0.09 M NiCl ₂ , steel [248]	25	4.6		240		0.13
0.001 M Ni in molten fluoride, nickel rod [249]	497				7.30E-3	0.23
1.0 M Ni ²⁺ (citrate ligand) , copper substrate [243]	25±0.2	4 - 8		192	0.25E-5	0.15

* Results from this current work

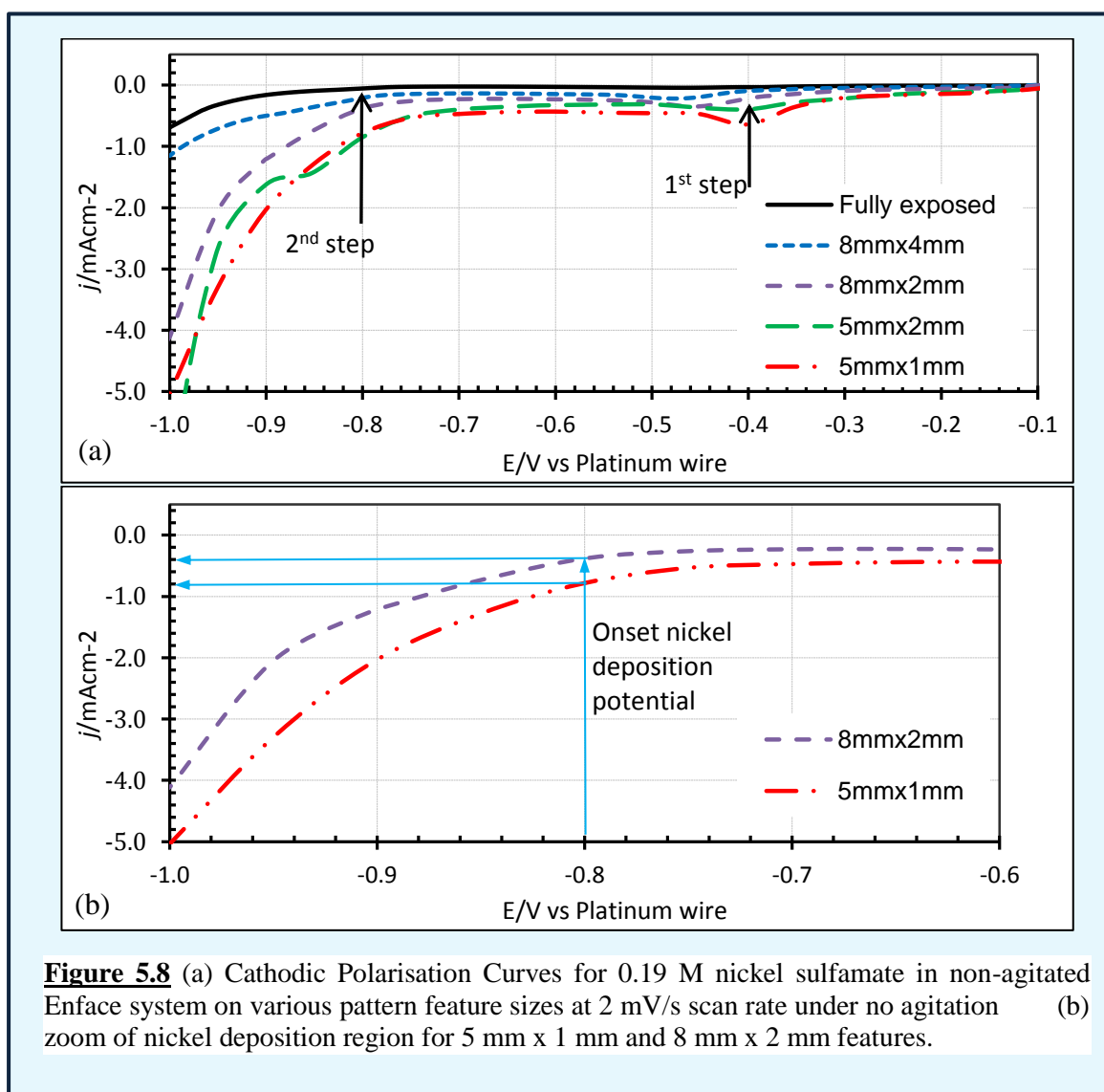


5.5 Measurement of Current Density

It was observed that potential-current densities behaviour for nickel pattern transfer was greatly affected by the pattern feature size. Figure 5.8 (a) shows the plot of potential vs. current density in Enface system for the anode with different feature sizes (i.e. fully exposed to 1 mm x 5 mm). The effect of varying feature sizes on current densities was also observed. As can be seen in Figure 5.8 (a), the current densities

increase as the feature size becomes smaller. The increase is possibly due to the decrease of the electro-active area on the anode as a result of smaller size of the feature as the current densities were calculated based on the active area. In addition, a diffusional mass transfer of Ni^{2+} through diffusion layer towards the electrode surface might be enhanced at smaller electroactive area due to a hemispherical diffusion. The enhancement of mass transfer led to an increase in the current densities. This finding is in agreement with literature [250- 252].

Therefore, polarisation experiments were carried out on each pattern feature size and structure to determine optimum current densities prior to pattern transfer experiments. In future work, the relationship of the applied current densities and the active area of anode may also be formulated in order to be able to simply estimate the current densities for new pattern features.



A closer examination of this variation is shown in Figure 5.8 (b), corresponding to the potential range for nickel deposition (-0.8 to -1.0 V). The applied current density

of nickel pattern transfer on the feature of 2 mm x 8 mm is expected to be in between -0.4 and -4.2 mA/cm². Whereas the current density for nickel deposition on the 1 mm x 5 mm feature is estimated to range between -1.0 and -5.0 mA/cm² (with respect to the exposed active area of the anode). Henceforward, these current density range (-1.0 to -5.0 mA/cm²) was used in the pattern transfer experiments on the feature of 1 mm x 5 mm.

The millimetre scale feature of 1 mm x 5 mm manually fabricated using kapton tape was initially used to study the possibility of nickel pattern transfer using Enface technology. The 1 mm x 5 mm feature size was adequate to be utilised in the experiments in order to understand the process of nickel pattern replication as it was the smallest millimetre scale that is easy to manually refabricate. Once the pattern transfer of millimetre scale was achieved and the process was fully understood, further investigation on pattern transfer with smaller feature dimensions, i.e. at the micron level, could be carried out based on the finding.

In Figure 5.8 (a), the peak is observed at potential of around -0.4 V in the polarisation curves for 0.19 M nickel sulfamate acquired in the Enface system. A narrow gap of the electrodes tended to affect the polarisation behaviour of nickel as the peak is not observed in typical polarisation curves for the RDE system. One possible explanation is that the small interelectrode gap and low nickel concentration hindered mass transfer of nickel from the bulk solution. It was thought that the current density decreasing after the peak was possibly caused by a lack of nickel ions in between the electrode due to a limited amount of nickel ions within the gap which were consumed by the first electron transfer.

However, a further investigation revealed that the amount of Ni²⁺ consumed by the first electrochemical reaction (after approximately 200 s) was estimated to be 5.70E-08 mol. The total Ni²⁺ in the solution within the electrode gap is 8.96E-06 mol. This means that there was only a 0.64 % decrease in the Ni²⁺ concentration in solution within the narrow gap. In conclusion, In conclusion, the current density drop after the first peak was not because of the lack of nickel ions within the electrode gap but most likely to be due to the adsorbed intermediate inhibiting further processes (i.e. the second electron transfer reaction) as has been previously discussed.

5.6 Electrochemical Characterisation of the Nickel electrolyte under ultrasound agitation.

Since nickel deposition is shown to be controlled by combined kinetics and mass transfer, further experiments were carried out using ultrasound agitation. Ultrasound is popular agitation technique in an electrochemical system as it is fast and capable of enhancing electrodeposition. Figure 5.9 shows cathodic polarisation curves for the reduction of 0.19 M nickel sulfamate without and with ultrasound (US) agitation for both fully exposed and patterned anode. The potential was swept from 0.0 V to -1.2 at scan rate of 1 mV/s. For fully exposed anode (Figure 5.9 (a)), in the absence of ultrasound probe, the reduction of nickel begins to occur at overpotential of approximately -0.85 V and the hydrogen evolution reaction occurred at overpotential greater than -1.0 V.

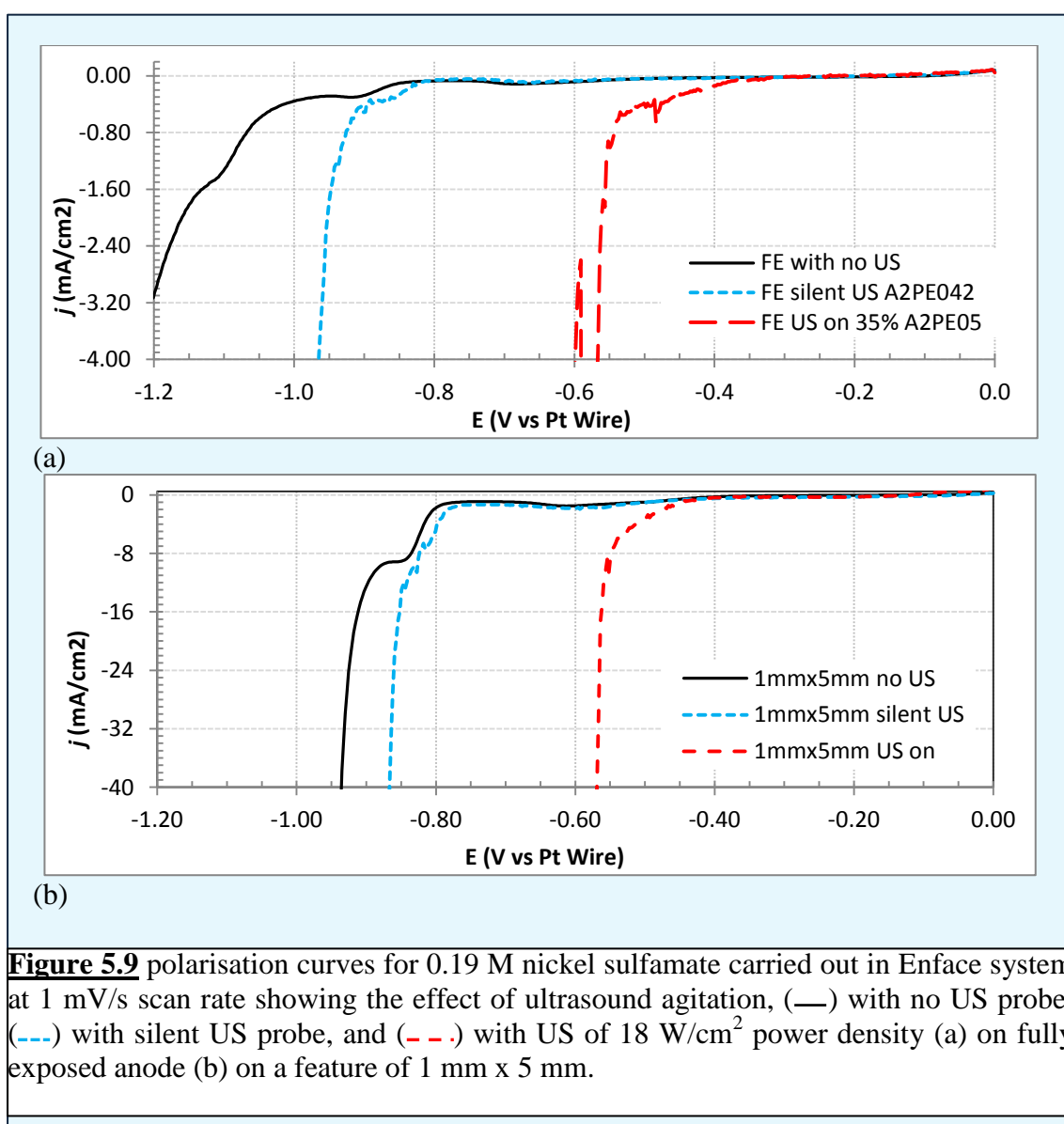


Figure 5.9 polarisation curves for 0.19 M nickel sulfamate carried out in Enface system at 1 mV/s scan rate showing the effect of ultrasound agitation, (—) with no US probe, (---) with silent US probe, and (- - .) with US of 18 W/cm² power density (a) on fully exposed anode (b) on a feature of 1 mm x 5 mm.

The effect of the ultrasound on the polarisation data of 0.19 M nickel sulfamate on the fully exposed anode was initially studied by introducing the US probe into the solution without ultrasonic wave being applied. The presence of the silent probe in the solution affected the potential-current density as the potential of hydrogen evolution occurred at lower cathodic overpotential of -0.97 V, whereas the nickel deposition potentials were shifted from -0.85 to a value of -0.8 V. In the case when ultrasound was applied to the system at a power density of 18 W/cm², a significant shift was observed. The potential of nickel reduction and hydrogen evolution were shifted to values of -0.4 V and -0.57 V respectively.

For the patterned anode with a 1 mm x 5 mm feature (Figure 5.9 (b)), without the introduction of ultrasound, the nickel deposition and hydrogen evolution begin at -0.9 V and -0.8 V respectively. When the ultrasound probe was introduced to the system, the potentials for nickel deposition and hydrogen evolution were -0.77 V and -0.87 V respectively, even when the probe was silent. This occurs probably due to the potential interaction between the probe and the electrodes in the electrochemical cell. As shown in Figure 4.18, the probe is located at a point of 1 cm away from the working electrode which is thought to be within the potential field causing potential interaction ^[234]. Therefore, further experimentation was abandoned.

Chapter 6

Experimental Results and Discussion: Pattern Transfer

Electrochemical characterisation presented in Chapter 5 has discussed potential and current density ranges at which the nickel pattern deposition occurs on millimetre scale features. The potential and current density ranges obtained from polarisation experiments were used as a guide to determine an appropriate current density that should be applied to achieve nickel pattern transfer. The previous polarisation data also suggested that within the potential region for nickel deposition, each pattern feature size exhibited different current density ranges. This led to a variation of current densities to be applied in the experiments according to the pattern feature dimension.

As has been described in chapter 4 section 4.4.4, the deposition experiments were carried out using anodes where each anode was patterned with different feature sizes including a manually fabricated millimetre feature of 1 mm x 5 mm, manually fabricated microscale features, and photolithographed micropattern features. Therefore, it was necessary to carry out polarisation experiments for each patterned anode so that the corresponding applied current density was determined. The applied current densities obtained from the previous polarisation data set at a constant value for each pattern feature size are presented in Table 6.1

Table 6.1 The applied current densities value for each pattern feature size and structure.

Pattern feature	Active area of anode (cm ²)	Applied current density (mA/cm ²)
Millimetre scale (4.98 ± 0.17 mm x 1.33 ± 0.1 mm)	0.067 ± 0.001	-4.53 ± 0.55
Manually fabricated micron scale feature with kapton tape		
Structure 1	0.038 ± 0.003	-7.17 ± 0.92
Structure 2	0.055 ± 0.005	-7.59 ± 0.92
Photolithographed micropattern feature		
Structure 1	0.579	-0.91 ± 0.07
Structure 2	0.331	-1.93 ± 0.46

In principle, electrodeposition of nickel pattern can be carried out by either galvanostatic method (fixed current) or potentiostatic technique (fixed potential). Since the galvanostatic is a typical method for use in commercial industrial plating processes, the nickel pattern transfer experiments were performed using the technique. Therefore,

this chapter aimed to investigate whether acceptable nickel pattern transfers could be achieved by galvanostatic technique through direct current electrodeposition using the applied current densities provided. The pattern transfer experiments were carried out by applying the set constant current density corresponding to the pattern feature area as shown in Table 6.1 for a particular time in between 100 and 600 s.

Since cell voltage is sensitive to physical changes such as anode passivation, degradation of solution concentration, and contamination of the electrode or the solution [154], monitoring the cell potential behaviour during pattern transfer experiments was necessary. The cell voltages were recorded against time for each experiment of nickel pattern transfer. The recorded cell potential profile could be used to investigate whether the physical changes occur during the process that could affect the pattern transfer performance.

6.1 Cell Potential Monitoring during Nickel Pattern Transfer process

Figure 6.1 shows cell potential profiles against deposition times for the nickel pattern transfer experiments using Enface on various pattern feature sizes and structures manually fabricated using kapton tape.

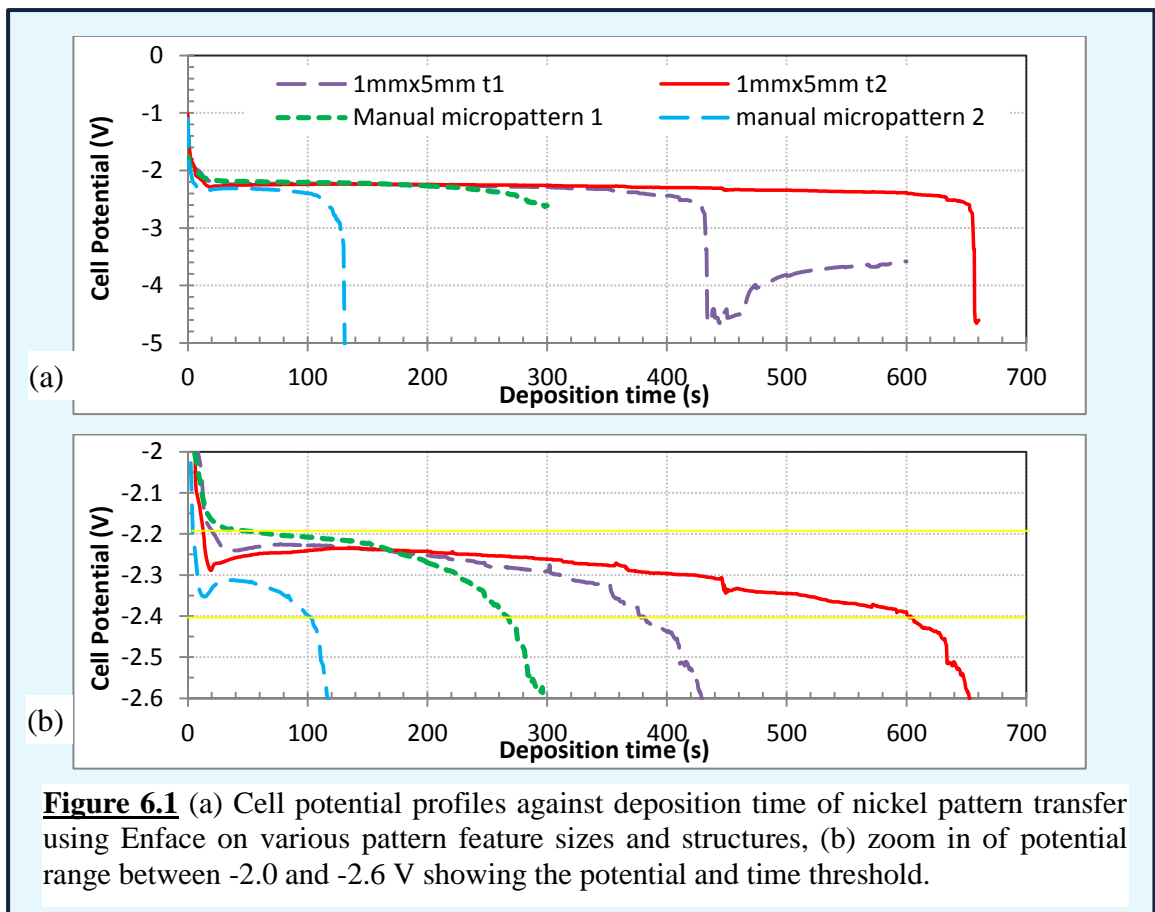


Figure 6.1 (a) Cell potential profiles against deposition time of nickel pattern transfer using Enface on various pattern feature sizes and structures, (b) zoom in of potential range between -2.0 and -2.6 V showing the potential and time threshold.

The cell voltages were recorded during the deposition experiments at the set values of applied current densities for each pattern feature size as shown in Table 6.1. Initially, the cell potentials significantly increased from a value of around -1.0 V, reaching a plateau at a value in between -2.2 and -2.4 V after approximately 20 s. The cell voltages remained in the range of -2.2 V - -2.4 V prior to the substantial increase.

Slightly different cell potential profiles were observed to occur in the pattern transfer experiments on micron scale features fabricated by using photolithography, as shown in Figure 6.2. The cell voltages were recorded to be plateau at a value between -2.15 and -2.4 V after deposition time of 20 s. However, the sudden significant increase of the cell potential during the experiments was not observed.

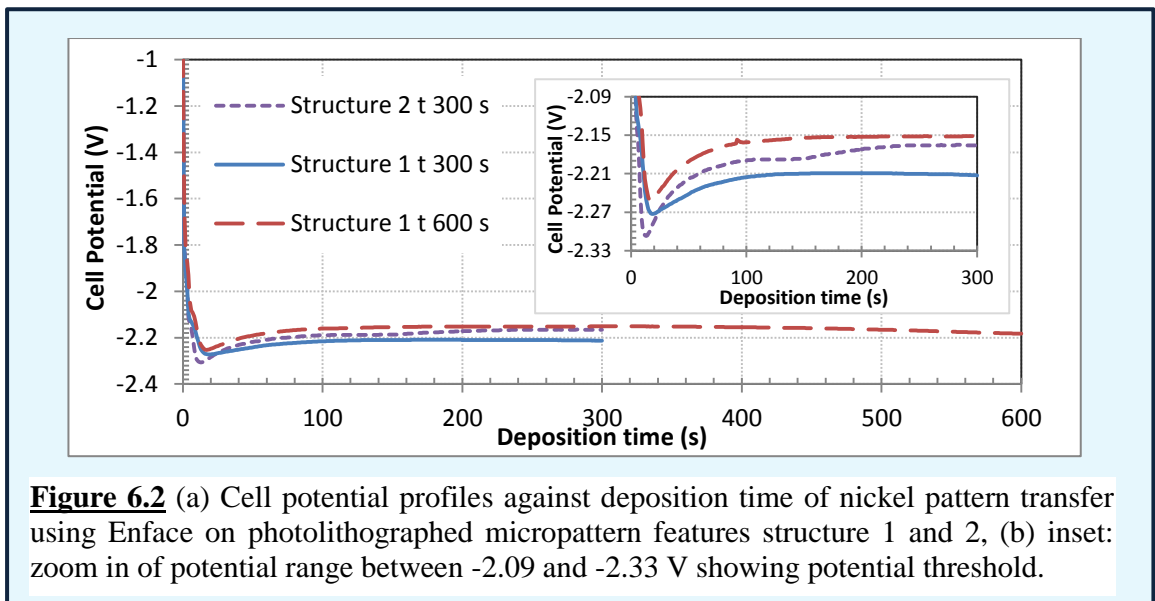


Figure 6.2 (a) Cell potential profiles against deposition time of nickel pattern transfer using Enface on photolithographed micropattern features structure 1 and 2, (b) inset: zoom in of potential range between -2.09 and -2.33 V showing potential threshold.

Deposited nickel features were obtained at the applied current densities set at a value as provided in Table 6.1. However, at lower applied current densities the cell potentials were recorded to be below -2.2 V, and the pattern transfer was not achieved. Whereas, burnt nickel deposits with black and grey colour were obtained at higher applied current density than those provided. At higher applied current densities, the cell potentials were observed to be greater than -2.4 V. This is a clear indication of a threshold cell potential which has to be fulfilled in order to achieve nickel pattern transfer.

In addition, at higher current densities leading to an increase of cell potentials to a value beyond -2.4 V, more excessive hydrogen was generated leading to the electrode surface being rapidly covered by entrapped gas bubbles. As the entire electrode surface was covered by the gas bubbles, the passage of the current was blocked causing the considerable increase in the cell potential leading to process termination. However, the potential increase in the end of the process did not occur in the pattern transfer on the

photolithographed micropatterns as shown in Figure 6.2 which might be due to the photoresist thickness. As the kapton tape was far thicker than the photoresist leading to more entrapped gas bubbles covering the active area of the anode during pattern transfer experiments.

6.2 Hydrogen Evolution

As previously stated in Chapter 2, hydrogen evolution reaction tends to occur during nickel deposition. In the process of electrodeposition of nickel pattern, as shown in Figure 6.1, hydrogen reduction reaction sets in after 30 – 50 s. This leads to formation of gas bubbles. This phenomenon may be explained by the fact that the narrow interelectrode gap impedes nickel mass transfer from the solution bulk so that Ni^{2+} ions near the electrode surface decreases. Thereafter, competing reactions, i.e., decomposition of water sets in leading to excessive hydrogen evolution.

The gas bubbles entrapped within the narrow interelectrode gap can block the electrode surface leading to inhomogeneous nickel deposition and low cathodic current efficiency. In the worst case, the entire surface of the electrode can be blocked in which no current can pass. This was indicated by a sudden significant increase of the cell potential as shown in Figure 6.1 under stagnant condition as has been observed during copper pattern transfer^[23, 36, 83]. In this case, deposition was terminated immediately after the increase of the cell potential was observed. As consequence, the deposition time was restricted to 125 - 600 s and the maximum thickness of the nickel deposit that could be achieved was constrained accordingly (around 0.54 μm).

Due to the gas bubbles issue, the electrochemical tools used to electrodeposit multiple substrates were inspected to verify that the nickel disk anodes did not deteriorate after being used for a number of pattern transfer experiments. In the case of pattern feature using kapton tape, the features were undercut which were most possibly due to the penetration of gas bubbles underneath the resist reducing its adhesion. However, the resist-covered area remained undamaged ensuring the current density distribution unchanged. However, in the case of photolithographed anodes, hydrogen evolution caused rapid degradation of the features. The pattern resists damaged and detached from the anodes surface resulted in the loss of the selective deposition. This could be due to the increase in pH due to H_2 evolution as positive photoresists are well known to be alkaline soluble.

6.3 Pattern Transfer on Millimetre scale Feature of 1 mm x 5 mm

At first, galvanostatic plating experiments for initial nickel pattern transfers were carried out in a stagnant solution of 0.19 M nickel sulfamate and at a room temperature (20 ± 2 °C) for a feature of 1 mm x 5 mm manually fabricated using kapton tape. The applied current density was -4.53 ± 0.55 mA/cm² as determined from polarisation experiments in Chapter 5 and the deposition time was varied between 240 s and 600 s. The experiments were performed in the electrochemical cell with a narrow interelectrode gap of approximately 300 μ m as described in Figure 4.4. During the experiments, physical changes within the electrode gap were visually observed and the cell voltages against time were recorded. Hydrogen generation within the gap was visibly commencing after 30 - 50 s of deposition process. Initially, a significant increase of the cell potential from -1.0 V to around -2.2 V was observed. Thereafter the cell voltages levelled off at a value between -2.2 and -2.4 V before the processes were terminated due to a considerable increase of the cell potential as has been illustrated in Figure 6.1.

Pattern replications were obtained from the experiments under these conditions. The deposited nickel feature widths were measured using a travelling microscope and compared to the original feature size to see whether there was a broadening of the deposited feature. The degree of broadening is presented as a ratio between the deposited feature width (D) and the original one (O).

Table 6.2 Feature spread of nickel pattern transfer on 1 mm x 5 mm feature size at different deposition time at applied current density of -4.53 ± 0.55 mA/cm² presented as ratio of deposited feature width (D) and original feature width (O).

Original Feature		Deposition Time	Deposit Feature Width (mm)	D/O (%)
Length (mm)	Width (mm)			
4.98 \pm 0.17	1.33 \pm 0.1	240	1.94 \pm 0.23	148.30 \pm 19.62
		300	2.34 \pm 0.01	179.18 \pm 38.93
		360	2.27 \pm 0.02	173.82 \pm 34.35
		480	2.59 \pm 0.01	198.07 \pm 56.25
		600	2.40 \pm 0.24	183.52 \pm 42.78

A summary of the measurement is presented in Table 6.2. Each data point is an average of at least 5 repetitions of the pattern transfer experiments to ensure its reproducibility. The variation represents a total error as a combination of systematic and random errors. The pattern feature on the anode was freshly fabricated for each deposition time to ensure that the results were comparable to each other. Due to the limitation of manual

fabrication, the original feature sizes were varied resulting in the variation of its dimension. The error bar was calculated and also presented in Table 6.2.

As can be seen in Table 6.2, a comparison between the deposited features dimension and the original feature shows that the widths of the deposited nickel features were greater by around 48 to 98 %. In this case, the deposited feature tended to broaden with increasing time.

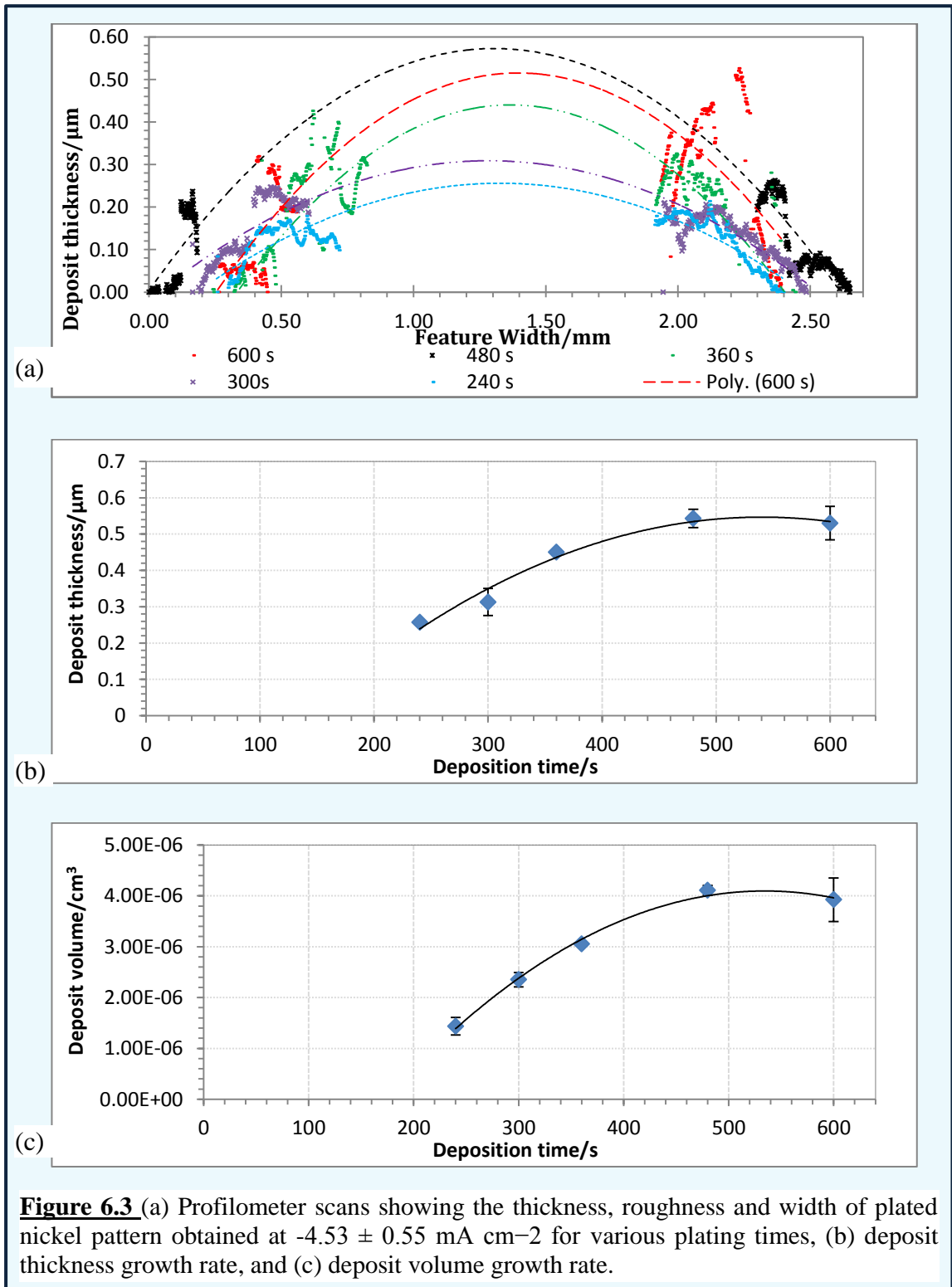


Figure 6.3 (a) Profilometer scans showing the thickness, roughness and width of plated nickel pattern obtained at $-4.53 \pm 0.55 \text{ mA cm}^{-2}$ for various plating times, (b) deposit thickness growth rate, and (c) deposit volume growth rate.

The thickness and the surface profile at the two edges of the deposited feature for different deposition times measured using optical profilometer are shown in Figure 6.3 (a). The entire surface profile could not be obtained due to equipment limitation. Therefore, the profile across the entire width was approximated using polynomial trend-line which is also included in the figure. As also shown in Figure 6.3 (a), the approximated surface profile of the deposited nickel surface across the width shows a bell-shaped with a peak is shown in the centre. The peak was considered as the deposited nickel thickness used in the further calculation. It can be seen that the peak of the bell-shaped profile representing the deposited nickel thickness increases over time.

The thickness data point was determined based on the peak value of the bell-shaped surface profile across the width of the deposited nickel for each deposition time. Figure 6.3 (b) indicates that the estimated thickness of the deposited nickel shows a second-degree polynomial growth as a function of time. Based upon the calculation, the thickness initially grows by approximately $0.072 \mu\text{m}/\text{min}$ to reach a maximum at 480 s. The growth rate subsequently decreased for deposition time beyond 480 s.

Table 6.3 Current efficiency of nickel pattern transfer on 1 mm x 5 mm feature size at various deposition times at applied current density of $-4.53 \pm 0.55 \text{ mA}/\text{cm}^2$.

Original Feature		Deposition Time (s)	Thickness (μm)	Current Efficiency (%)
Length (mm)	Width (mm)			
4.98 \pm 0.17	1.33 \pm 0.1	240	0.257 \pm 0.006	57.12 \pm 3.85
		300	0.313 \pm 0.037	69.86 \pm 15.00
		360	0.450 \pm 0.008	78.64 \pm 3.19
		480	0.543 \pm 0.025	83.79 \pm 6.31
		600	0.530 \pm 0.046	61.59 \pm 8.07

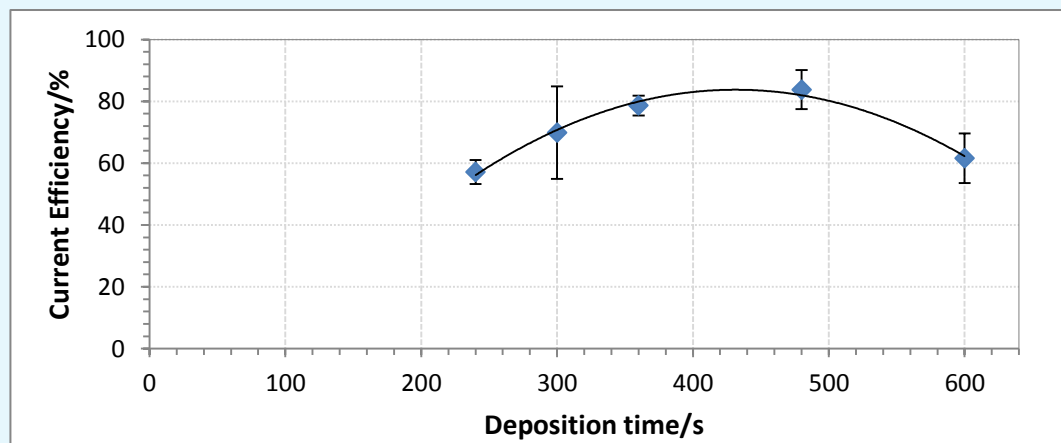


Figure 6.4 Cathodic current efficiency of nickel pattern transfer on 1 mm x 5 mm feature size for different deposition times at applied current density of $-4.53 \pm 0.55 \text{ mA}/\text{cm}^2$.

In most cases, the deposited nickel feature showed an elliptical shape. Considering this and the bell-shaped of the surface profile across the width, the volume and the quantity of the deposit was estimated by a half ellipsoid model (Figure 4.19). The deposit was assumed to be pore free as under SEM analysis it appears to be compact and dense with submicron thickness. The deposit growth rate was also investigated through an integral of the deposit volume as shown in Figure 6.3 (c). It can be seen that the second-degree polynomial trendline fits the data points. The volume of the deposited nickel initially increases over time until 480 s. Thereafter, it slightly decreased at a longer deposition times.

Using the estimated volume and amount of deposited nickel that have been determined, the theoretically required charge was calculated by Faraday formulae in order to determine the cathodic current efficiency. Table 6.3 shows the thickness of the deposited nickel on the centre part according to the peak value of the approximated surface profile and the cathodic current efficiency for the different deposition times, which is also presented in Figure 6.4.

As shown in Figure 6.4, the current efficiency of nickel pattern deposition for a 1 mm x 5 mm feature increases over time, but it tends to decrease after 480 s. This might be due to the fact that hydrogen evolution sets in after 30 -50 s and hydrogen bubbles become entrapped in the narrow gap blocking the electrode surface. The entrapped gas bubbles increased with time causing more competing reactions to occur, as has been discussed in section 6.2. As a result, the current efficiency reached a maximum value at approximately 480 s and it decreased afterward before the experiments were terminated. At the deposition time of 480 s and under the conditions provided, the deposit thickness of around 0.5 μm could be achieved with a relatively high cathodic current efficiency ($83.79 \pm 6.31 \%$). This indicates that the deposition time of around 480 s could be used in subsequent pattern transfer experiments.

6.4 Pattern Transfer on Manually Fabricated Micron Scale Feature

6.4.1 Manually fabricated micropattern structure 1

Since nickel pattern transfer on millimetre scale had been achieved, subsequent experiments were carried out to achieve pattern transfers on a micro-scale pattern. In the first attempt, microscale pattern features were manually fabricated. For this, the surface of the electrode was covered by kapton tape, and three linear features of approximately 300 μm width (Structure 1, Figure 4.9 (a)) were cut out. Galvanostatic electrodeposition experiments in the electrolyte of 0.19 M nickel sulfamate were carried

out at applied current density of $-7.17 \pm 0.92 \text{ mA/cm}^2$ previously determined by polarisation experiments for a deposition time of 300 s.

Pattern transfers were achieved through these procedures and under these conditions. The deposited nickel feature widths were measured by using optical microscope and compared to the original feature width. Table 6.4 shows a comparison between the deposited nickel linewidth and the original one. The deposited feature broadening is presented as a ratio between the deposited feature width (D) and the original one (O). Each data point is an average of at least 5 repetitions of the pattern transfer experiments to ensure its reproducibility. The variation represents a total error as a combination of systematic and random errors.

It can be seen in Table 6.4 that the deposited feature width is bigger than the original feature's by approximately 178 to 266 %. In comparison with the millimetre scale pattern transfer, this is initial indication that the level of feature broadening increases for the smaller feature width. The position of the feature on the anode also affected the degree of spreading. As also shown in the Table 6.4, the feature at the centre of the anode (M) has a greater broadening (366.67 %), whilst the feature FE located at near the edge has less spreading (278.57 %).

Table 6.4 Feature spread of nickel pattern transfer on micropattern feature (parallel three lines structure 1) via galvanostatic plating at $-7.17 \pm 0.92 \text{ mA/cm}^2$ for 300, with M - middle line, CE - feature with 1.5 mm gap from middle line, FE - feature with 2 mm gap from middle line, presented as ratio of deposit width (D) and the original feature (O).

Feature	Original Width (μm)	Deposition Time (s)	Feature Width (μm)	D/O (%)
M	222.2 ± 11.49	300	806.7 ± 20.6	366.67 ± 1.36
CE	293.3 ± 12.47		103.0 ± 40.8	350.42 ± 1.04
FE	281.2 ± 14.14		823.3 ± 55.6	278.57 ± 2.13

Surface profile measurements across the deposit feature width are shown in Figure 6.5. The surface profiles indicate the thickness and the width of the feature as have been presented in Table 6.4 and 6.5. In addition, the roughness of the deposited nickel is clearly visible across the surface profile as shown in Figure 6.5. The roughness on the deposit surface might be caused by the uneven substrate surface as result of polishing and inhomogeneous deposited nickel due to gas bubbles. The deposited nickel of the middle feature (M) seems to be rougher than those closer to the edge (CE and

FE). It was thought to be caused by the condition in which more entrapped gas bubbles in the centre of the cathode was observed.

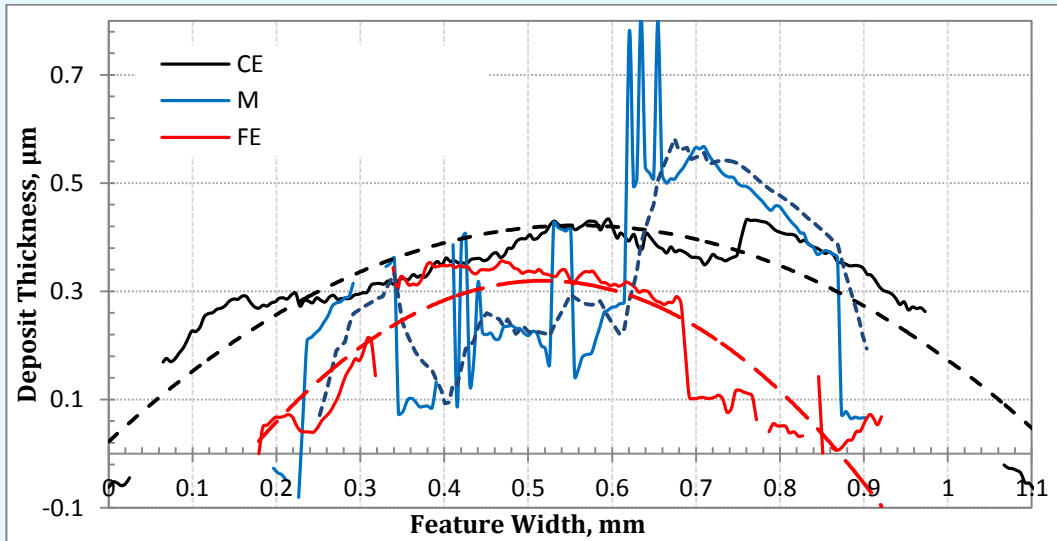


Figure 6.5 Profilometer measurement showing the thickness, roughness, and width of deposited nickel feature obtained at $-7.17 \pm 0.92 \text{ mA/cm}^2$ for 300 s on the feature of parallel three lines with M - middle line with 377 μm width, CE - linear feature 1.5 mm gap from middle line with 373 μm width, FE - linear feature 2 mm gap from middle line with 317 μm width. (---) trendline of CE feature profile, (—) trendline of M feature profile, and (—) trendline of FE feature profile.

The thickness of the deposited nickel estimated at the middle part along the length of each feature is presented in Table 6.5. Based on the feature surface profile across the width collected using optical profilometry as shown in Figure 6.5, the thickness was determined according to the peak value of each feature trendline. The amount of the deposited nickel was calculated by using the same assumption of feature shape which is a half ellipsoid. The overall cathodic current efficiency calculated using Faraday's formulae based on the estimated amount of deposited nickel is also shown in Table 6.5.

Table 6.5 Current efficiency of nickel pattern transfer on micropattern feature (parallel three lines structure 1) via galvanostatic plating at $-7.17 \pm 0.92 \text{ mA/cm}^2$ for 300 s, with M- middle line, CE- feature with 1.5 mm gap from middle line, FE- feature with 2 mm gap from middle line.

Feature ID	Deposition Time (s)	Deposit Thickness (μm)	Current Efficiency (%)
M	300	0.377 ± 0.017	89.55 ± 8.84
CE		0.373 ± 0.025	
FE		0.317 ± 0.026	

The deposit appearance was visually investigated using an optical microscope. The images were taken at 5 times magnification with the scale bar represents 200 μm . In order to see the position of the deposited feature, the pattern structure on the anode is also presented (Figure 6.6 (a)). The observed original linear feature at the centre of the anode (M) manually fabricated by using kapton tape is presented in Figure 6.6 (b). The original feature dimensions are plotted on the image of the deposited feature by drawing yellow lines with their actual sizes to directly illustrate the degree of broadening. Figure 6.6 shows a feature analysis for the manually fabricated microscale pattern structure 1.

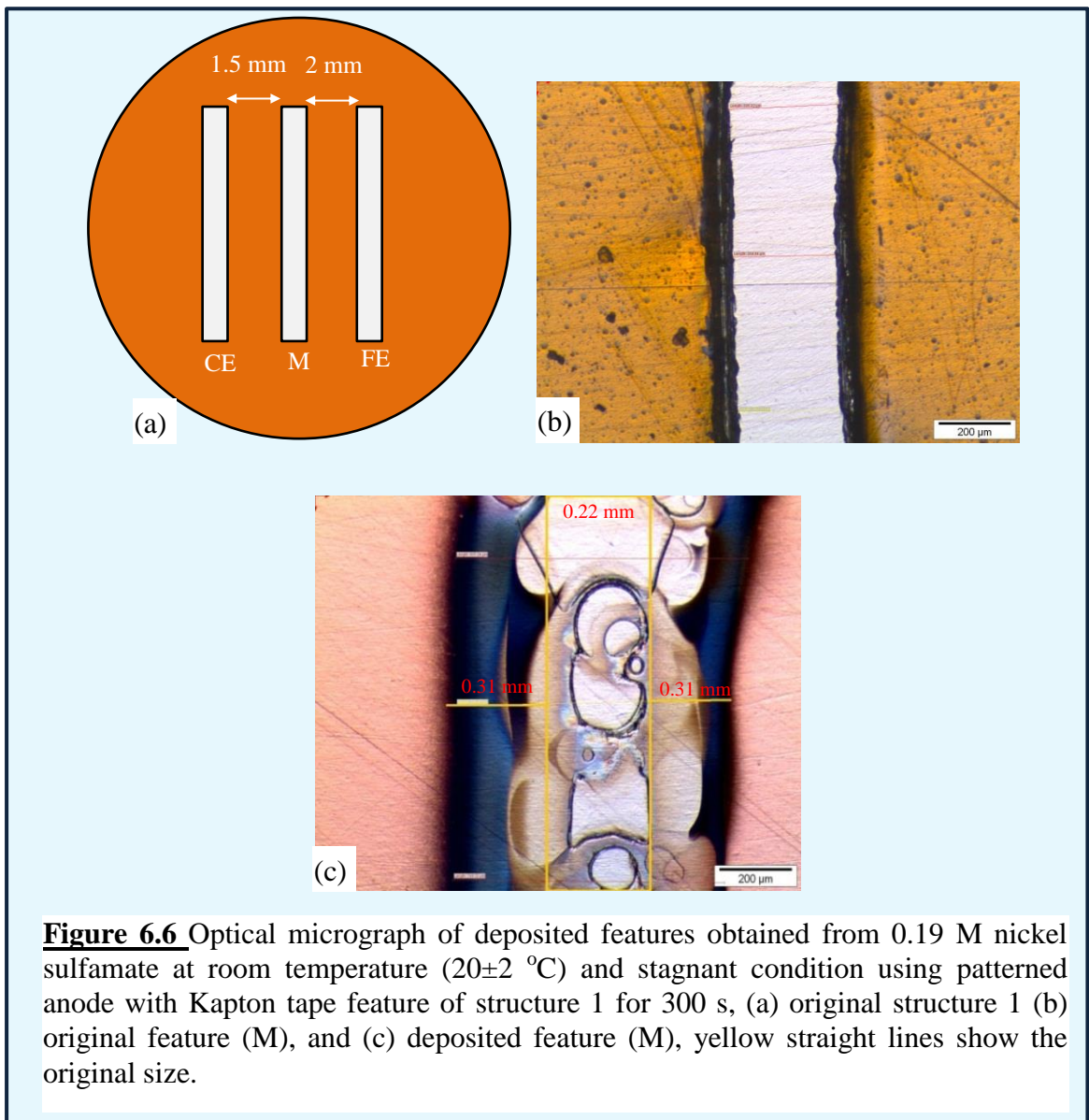


Figure 6.6 Optical micrograph of deposited features obtained from 0.19 M nickel sulfamate at room temperature (20 ± 2 °C) and stagnant condition using patterned anode with Kapton tape feature of structure 1 for 300 s, (a) original structure 1 (b) original feature (M), and (c) deposited feature (M), yellow straight lines show the original size.

As can be seen in Figure 6.6 (c), the deposited nickel exhibits a bright metallic finish. However, a “burnt” deposit indicated by black or grey colour is observed at the edge of the feature which is most probably due to an inclusion of impurities i.e. sulphur

as a result of non-uniform current density. The deposited nickel is observed to be thin as the substrate roughness is visible. The substrate roughness shown in Figure 6.5 has a contribution to the deposit surface roughness. The thinness of the deposited nickel was mainly due to deposition time limitation as the experiment had to be terminated at around 300 s due to the formation of gas bubbles covering the electrode surface. Accordingly, the submicron thickness of the deposited nickel of around $0.377\ \mu\text{m}$ was obtained in the case of this manually fabricated microscale feature of structure 1. Figure 6.6 also clearly shows the broadening of the deposited nickel feature as compared with the original feature. The degree of spreading has been presented in Table 6.4.

6.4.2 Manually fabricated micropattern structure 2

Second attempt to achieve micro scale pattern transfers was carried out with a manually created micro-pattern feature of structure 2 as shown in Figure 4.9 (b). The pattern transfer experiments were performed in unstirred 0.19 M nickel sulfamate solution, at a room temperature ($20 \pm 2\ ^\circ\text{C}$), and at applied current density of $-7.59 \pm 0.92\ \text{mA}/\text{cm}^2$ for 125 s. The deposition time was limited to 125 s as a significant increase of the cell potential suddenly occurred at deposition time beyond 125 s with the excessive H_2 evolution.

Deposited nickel patterns were obtained under this arrangement. Comparison between the deposited features width and the original one is shown in Table 6.6. Each data point is an average of at least 5 repetitions of the pattern transfer experiments to ensure its reproducibility. The variation represents a total error as a combination of systematic and random errors. The degree of broadening is presented as a ratio between the deposited feature width (D) and the original one (O). In the case of micropattern using kapton tape - structure 2, the current spread caused the deposited nickel width to be larger than the original by around 74 to 113 %. Compared with the result for structure 1 (Table 6.4), the feature broadening of structure 2 is smaller. The difference in the degree of spreading may be attributed to the different deposition time and the original feature size. This is in agreement with the result for millimetre scale pattern transfer that the broadening of the deposited feature width tended to increase for a longer deposition time. As also has been discussed that degree of deposited feature spreading increases for smaller pattern feature width.

The thickness of the deposited nickel determined at the centre of the feature based on the surface profile as shown in Figure 6.7 which was measured using optical

profilometry is presented in Table 6.7. The thickness at the centre was used to estimate the volume and the amount of deposited nickel for each feature shape and size using the half ellipsoidal model as has been demonstrated for the previous feature structure. The result of the calculations were added up together to obtain overall volume and amount of the deposited nickel.

Table 6.6 Feature spread of nickel pattern transfer on micropattern feature (structure 2) via galvanostatic plating at -7.59 ± 0.92 mA/cm² for 125 s, with LM-middle line, SRL-small rectangle 2 mm gap from middle line, SRR- small rectangle 1.5 gap from middle line, D = deposited feature width and O=original feature width.

Feature	Original Feature Width (O) (μm)	Deposition Time (s)	Deposit Feature Width (D) (μm)	D/O (%)
LM	353.33 \pm 5.44	125	711.11 \pm 1.70	204.95 \pm 0.46
SRL	578.22 \pm 17.67		997.33 \pm 42.16	173.88 \pm 6.43
SRR	427.22 \pm 12.64		909.56 \pm 11.76	213.25 \pm 7.78

The overall efficiency of the plating process was calculated based on the total estimated amount of the deposited nickel and Faraday's equation. The result of the calculation is shown in Table 6.7. The variation in the deposit thickness and current efficiency is due to a combination of systematic and random error. The error bar for the current efficiency came from the variation in the thickness and feature dimension measurements.

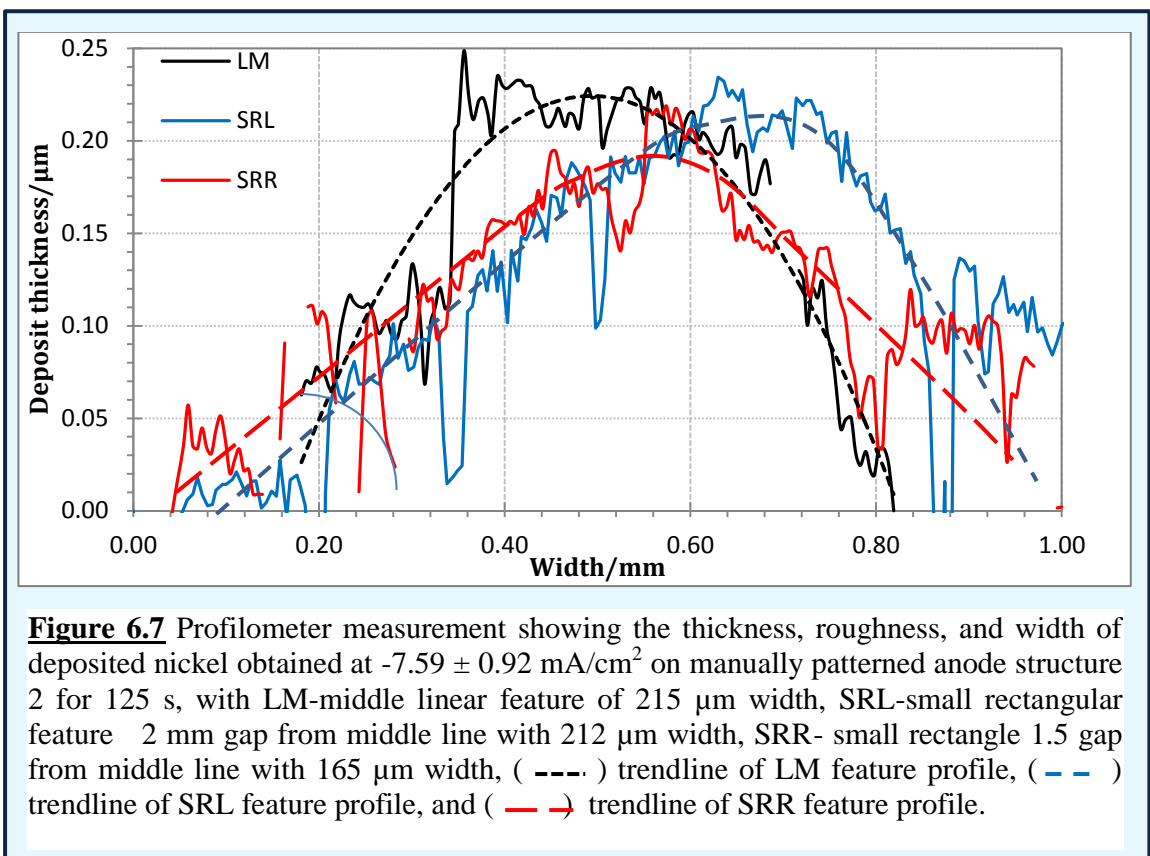
Table 6.7 Current efficiency of nickel pattern transfer on micropattern feature (structure 2) via galvanostatic plating at -7.59 ± 0.92 mA/cm² for 125 s, with LM-middle line, SRL-small rectangle 2 mm gap from middle line, SRR- small rectangle 1.5 gap from middle line.

Feature	Deposition Time (s)	Deposit Thickness (μm)	Current Efficiency (%)
LM	125	0.215 \pm 0.023	90.88 \pm 14.00
SRL		0.212 \pm 0.031	
SRR		0.165 \pm 0.019	

Observing the current efficiency of around 90 % that has been demonstrated in the pattern transfer experiments on manually fabricated microscale feature (Table 6.5

and 6.7), it is in agreement with a typical current efficiency of nickel electrodeposition process reported in literature which is in the range of 90 – 97 % ^[154]. Comparing to the current efficiency achieved in the millimetre scale pattern transfer, the current efficiency in this case is higher which could be associated with the greater applied current density.

The cathodic current efficiency and deposition rate of the process of nickel pattern transfer are comparatively lower than those obtained with a conventional sulfamate process. This is most possibly due to the different operating condition as the experiments were carried out in the electrolyte containing a low concentration of nickel salt, without agitation, and at a room temperature (20 ± 2 °C). On the other hand, the conventional process of nickel electrodeposition normally runs in a higher nickel salt concentration, under appropriate agitation, and at a temperature between 32 – 60 °C. In addition, competing reactions taking place during the nickel pattern transfers process i.e. hydrogen evolution, decomposition of sulfamate and water might also be the reason behind the low current efficiency.



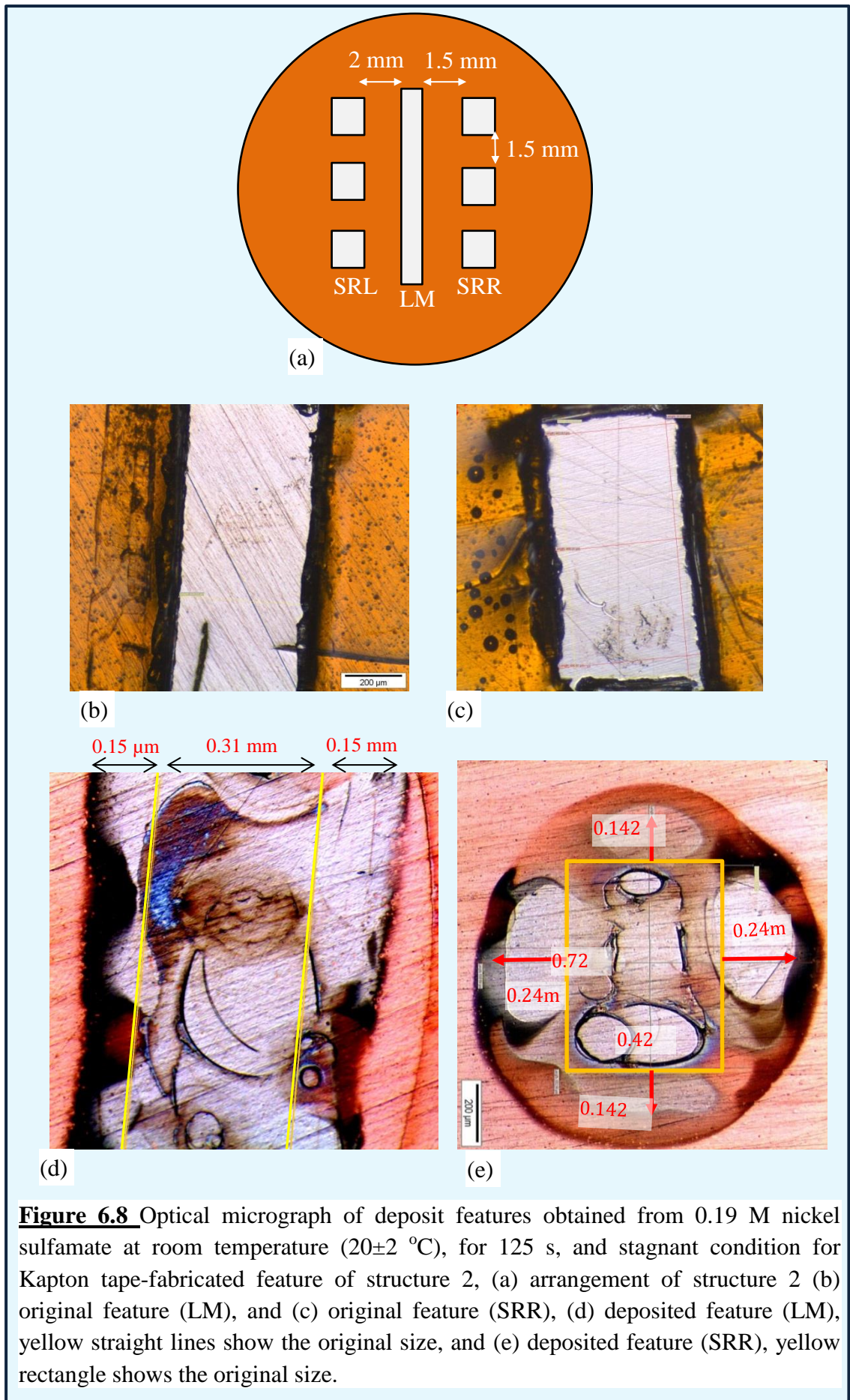
The deposit surface profiles measured across the entire width are shown in Figure 6.7. The Figure shows the thickness, the width, and the shape of the deposited feature which have been discussed and presented in Table 6.6 and 6.7. In addition, Figure 6.7 also suggests the roughness of the deposit surface which has been previously discussed due to the influence of uneven substrate and entrapped gas bubbles.

Observing the surface profiles obtained from the profilometer measurement (Fig. 6.3 (a), 6.5, and 6.7), the deposited feature tended to be bell-shaped curve. This shape was similar to the result obtained from the simulation and modelling of current distribution which showed that the deposit would be bell-shaped. The high level of roughness shown in the surface profile was mainly due to the effect of entrapped gas bubbles. In addition, a significant roughness of the surface profile was possibly also caused the submicron thickness of the deposit that exposes the substrate roughness as a result of mechanical work (polishing).

An analysis of the deposited feature obtained from the manually fabricated micropattern using kapton tape structure 2 is presented in Figure 6.8. The microscale pattern structure is shown in Figure 6.8 (a) in order to illustrate the position of features discussed in this section. The appearance of original linear and rectangular features manually fabricated using kapton tape is presented in Figure 6.8 (b) and (c) respectively. The appearance of a deposited nickel transferred in the experiments for the linear (LM) and rectangular (SRR) features were visually analysed using optical microscope. Optical micrographs of the features are presented in Figure 6.8 (d) and (e) respectively. The images were obtained at 5 times magnification and the scale bar represents 200 μm . The original features represented by yellow straight lines are drawn on the images to see a direct comparison.

It can be seen in Figure 6.8 (d) and (e) that the deposited feature dimensions are greater than the original one indicating a spreading of the deposited nickel. The degree of spreading has been discussed and presented in Table 6.6. In the case of small rectangular feature (Figure 6.8 (e)), the deposited feature clearly shows an elliptical shape as the degree of spreading along the edge is not uniform. The spreading at the centre part along the length of the feature is greater than that towards the edge. One of possible explanations for this is that the non-uniform current density distribution caused the difference of deposited feature spreading at each part along the edge.

In the case of manually fabricated pattern features using kapton tape, the percentage of deposited feature spread compared to its original feature was observed to increase with smaller feature width, as shown by the results of pattern transfer on microscale feature structure 1 and 2 in Table 6.4 and 6.6. For the micropattern structure 2 (Figure 4.9 (b)), with a feature width of 0.35 – 0.58 mm, the current spread were between 73.88 and 113.25 % (Table 6.6), whereas for the micropattern structure 1 (Figure 4.9 (a)), with a pattern width of 0.22 – 0.29 mm, the spread was 178.57 – 266.67 % (Table 6.4).



As can be seen in Figure 6.6 (c) and 6.8 (d, e) which are confirmed by the roughness of the surface shown in Figure 6.5 and 6.7, a non-uniform thickness of the deposit feature is clearly visible. Some local parts without nickel deposit or with less deposit thickness are observed. This was most probably caused by gas bubbles covering some area of the electrode as result of hydrogen evolution. The presence of gas bubbles increases the ohmic drop at the particular area which possibly hinders the nickel deposition reaction.

The thickness of the deposited nickel obtained from the experiments of pattern transfer on the manually created microscale feature structure 2 was around 0.215 μm . As has been discussed, a time limitation (125 s) due to excessive gas bubbles covering the electrode surface leading to early termination of the process is the main reason of achieving such thin deposit. Figure 6.8 (e) shows that some areas on the deposited feature with thinner or even without nickel deposit are visible showing copper substrate. The gas bubbles entrapped within the narrow interelectrode gap increased the electrolyte resistance hindering the electrodeposition process. As a result at an area covered by the gas bubbles very thin or no deposited nickel is observed in the figure.

As shown in Figure 6.8 (d) and (e), the deposited nickel exhibits a metallic appearance at the most part of the features. However, at the edge around the feature, “burnt” deposits indicated by black colour are observed, which have been previously discussed, due to an adsorption of impurities on to the deposited nickel.

6.5 Microscale Pattern Transfer using Photoresist

6.5.1 Photolithographed micropattern structure 1

Further investigation on the capability of Enface system to transfer a micropattern was carried out with a photolithographed micropattern (described in Figure 4.11). In the case of structure 1, the micro scale pattern was fabricated using a negative photoresist with a thickness of 2.4 μm . The galvanostatic pattern transfer experiments were carried out in the same conditions i.e. a stagnant solution and a room temperature (20 ± 2 °C). The applied current density was -0.91 ± 0.07 mA/cm² respected to the exposed active area of the anode. The electrodeposition experiments were performed for two different deposition times of 300 s and 600 s.

As a negative photoresist was used on the pattern feature structure shown in Figure 4.11, the pattern that would be transferred covered most of the anode surface (around 74 %) with dimensions in millimetre scale so that measurements of deposited feature dimensions were not practicable. Therefore, the measurement was focusing on

the inverse of the patterns that have dimensions in micrometre scale as has been described in Table 4.8 which consisted of large squares (793.65 μm x 793.65 μm), small squares (304.6 μm x 304.6 μm), small circles (diameter of 209.65 μm), and some other smaller complex features.

After several pattern transfer experiments were carried out, deposited nickel features were obtained. However, it was apparent that only the inverse pattern of large square shape (793.65 μm x 794.65 μm) was observed to be replicated on the cathode surface. The large square dimensions were measured (D) and as compared with the original size (O), the area of the large square has shrunk due to the deposited nickel spreading. Figure 6.9 shows that the size of large square replica became smaller for a longer deposition time. The comparison is shown in Table 6.8. The thickness of the deposited nickel was also measured by using optical profilometer at the edge of the large square shape which is also presented in Table 6.7. The error was a combination of random and systematic errors calculated based on the variation of the measurement results.

Table 6.8 Large square shrinkage and thickness of deposited nickel obtained from photolith micropattern feature structure 1 at current density of $-0.91 \pm 0.07 \text{ mA/cm}^2$ for 300 s and 600 s.

Original Feature (μm)	Deposition Time (s)	Deposit Feature Width (μm)	D/O (%)	Thickness (μm)
793.65 x 793.65	300	734.00 ± 28.82	92.33 ± 9.83	0.108 ± 0.006
	600	457.10 ± 17.11	57.59 ± 5.27	0.136 ± 0.024

As can be seen in Table 6.8, the duplicated large square area on the substrate became smaller over time as at 300 s its width is approximately 8% smaller than the original one and the size significantly decreased by about 42 % for a deposition time of 600 s. This indicates that the current spreading increased as a function of time which is in agreement with previous result of the millimetre scale and the manually fabricated micro scale pattern transfers. The more spreading of deposited nickel also implied to the low thickness growth rate.

The surface profile across the large square measured using the optical profilometer which also shows the width, thickness, and roughness is presented in Figure 6.9. In this case, the profile in the middle part shows the roughness of the exposed copper substrate with no deposited nickel, whilst the profile towards the edge represents the deposited nickel.

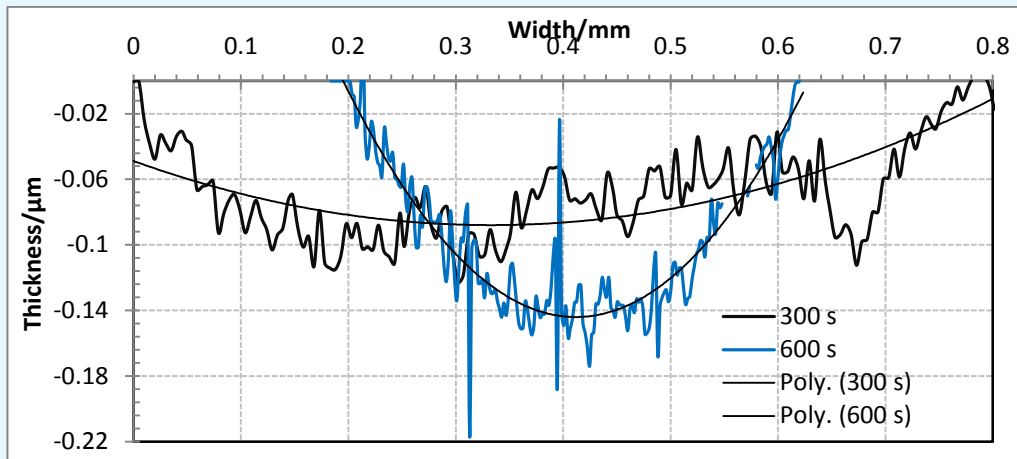
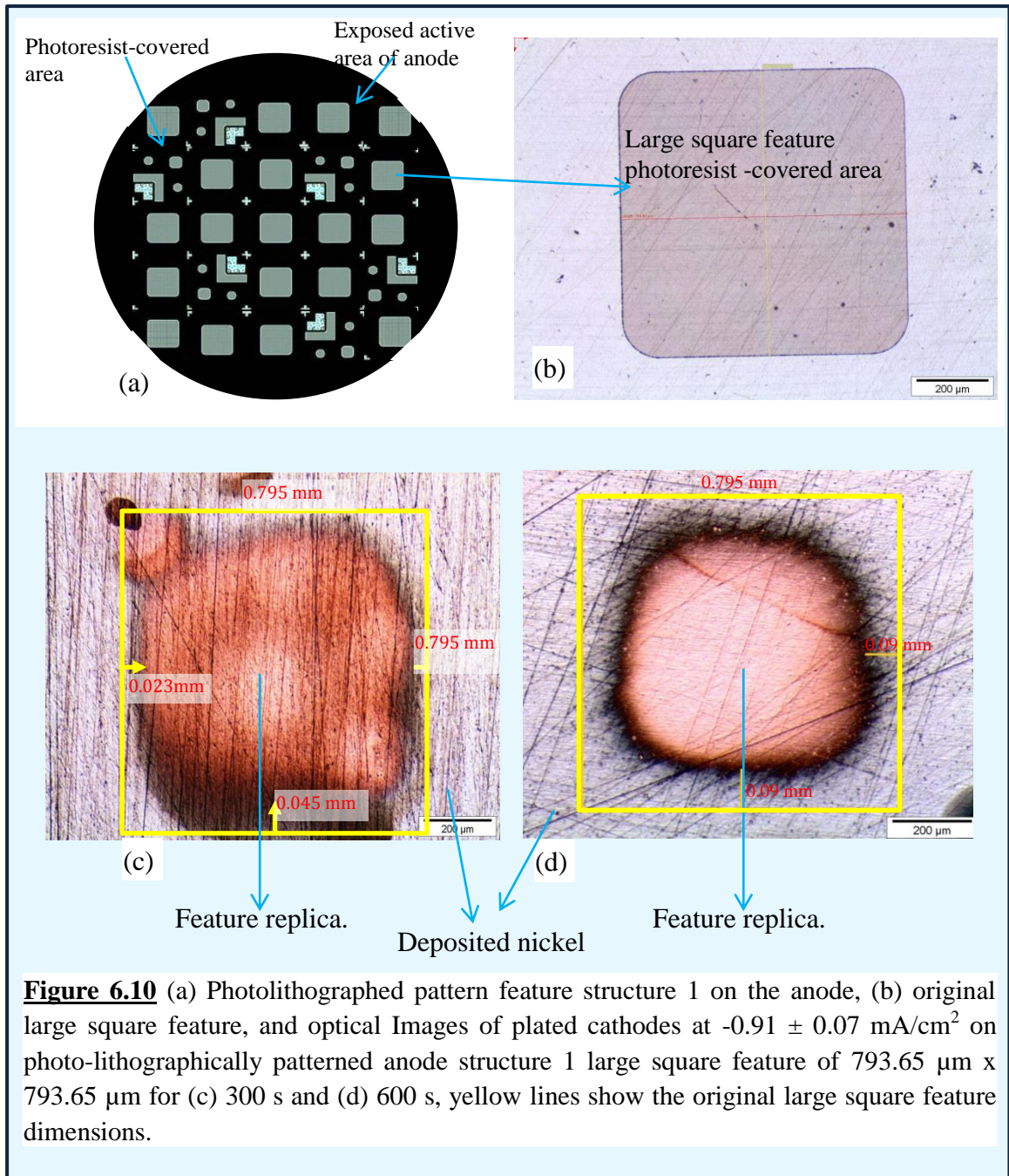


Figure 6.9 Profilometer measurement showing the thickness, roughness, and width of deposited nickel obtained at $-0.91 \pm 0.07 \text{ mA/cm}^2$ on photolithographically patterned anode structure 1 for 300 s and 600 s. the features were large square of $793.65 \mu\text{m} \times 793.65 \mu\text{m}$.

The deposited nickel feature obtained from pattern transfer experiments on the photolithographed anode of microscale pattern structure 1 is visually analysed through its optical micrograph as presented in Figure 6.10. The micrographs were taken at 5 times magnification and the scale bar represents $200 \mu\text{m}$. The structure 1 of microscale pattern feature fabricated through photolithography is shown in Figure 6.10 (a) in order to illustrate the overall arrangement. In order to see a direct comparison of the feature dimension, the original inverse pattern feature of large square and optical micrographs of the deposited nickel with the replicated large square area are shown in Figure 6.10 (b), (c), and (d) respectively.

Comparing the large square dimension as shown in Figure 6.10 (c) and (d), the replicated feature area on the substrate is clearly shown to be smaller than the original one. As has been discussed in Table 6.8, this phenomenon was mainly due to a deposited nickel spreading. The replicated feature is observed to be no longer square as it nearly turns to a circular shape indicating that the spreading of deposited nickel came from any direction along the edge. However, the spreading at each part along the edge was not uniform.



The deposited nickel shows a bright metallic finish appearance with a typical burnt deposit at areas along the edge. A roughness of the substrate is also shown as the thickness of the deposit was in the range of $0.108 - 0.136 \mu\text{m}$ obtained at deposition times of 300 and 600 s. The electrodeposition experiments could not be carried out at longer processing time as the deposited nickel obtained at a deposition time beyond 600 s covered the entire surface of the substrate, therefore no feature replication was obtained. This might be due to the spreading of deposited nickel that increases over time eventually covering the entire surface of the substrate. A gradual degradation of the photoresist leading to a loss of deposition selectivity could be another reason as the photoresist was detached from the anode surface at the end of the experiment.

6.5.2 Photolithographed micropattern structure 2

The photolithographed micropattern structure 2 was fabricated by using a positive photoresist of 0.8 μm thickness. The pattern transfer experiments were carried out at $1.93 \pm 0.46 \text{ mA/cm}^2$ for 300 s. The cell potential was found to be around -2.2 V. Very thin deposited nickels were obtained, however only pattern replications of large square and linear features were obtained. Measurements of feature dimensions carried out using optical microscope to estimate the degree of broadening are presented. The width of deposited nickel patterns (D) obtained from the measurement is compared with the original feature's (O) as shown in Table 6.9. The error is a combination of systematic and random errors from the measurements.

Table 6.9 Feature spread of nickel pattern transfer on photolithographed micropattern feature structure 2 at $1.93 \pm 0.46 \text{ mA/cm}^2$ for 300 s.

Original Feature (μm)	Deposition Time (s)	Deposit Feature Width (μm)	D/O (%)
Large square: 803 x 803	300	933.35 ± 61.60	116.23 ± 7.67
Linewidth: 498	300	669.95 ± 89.31	134.53 ± 17.93

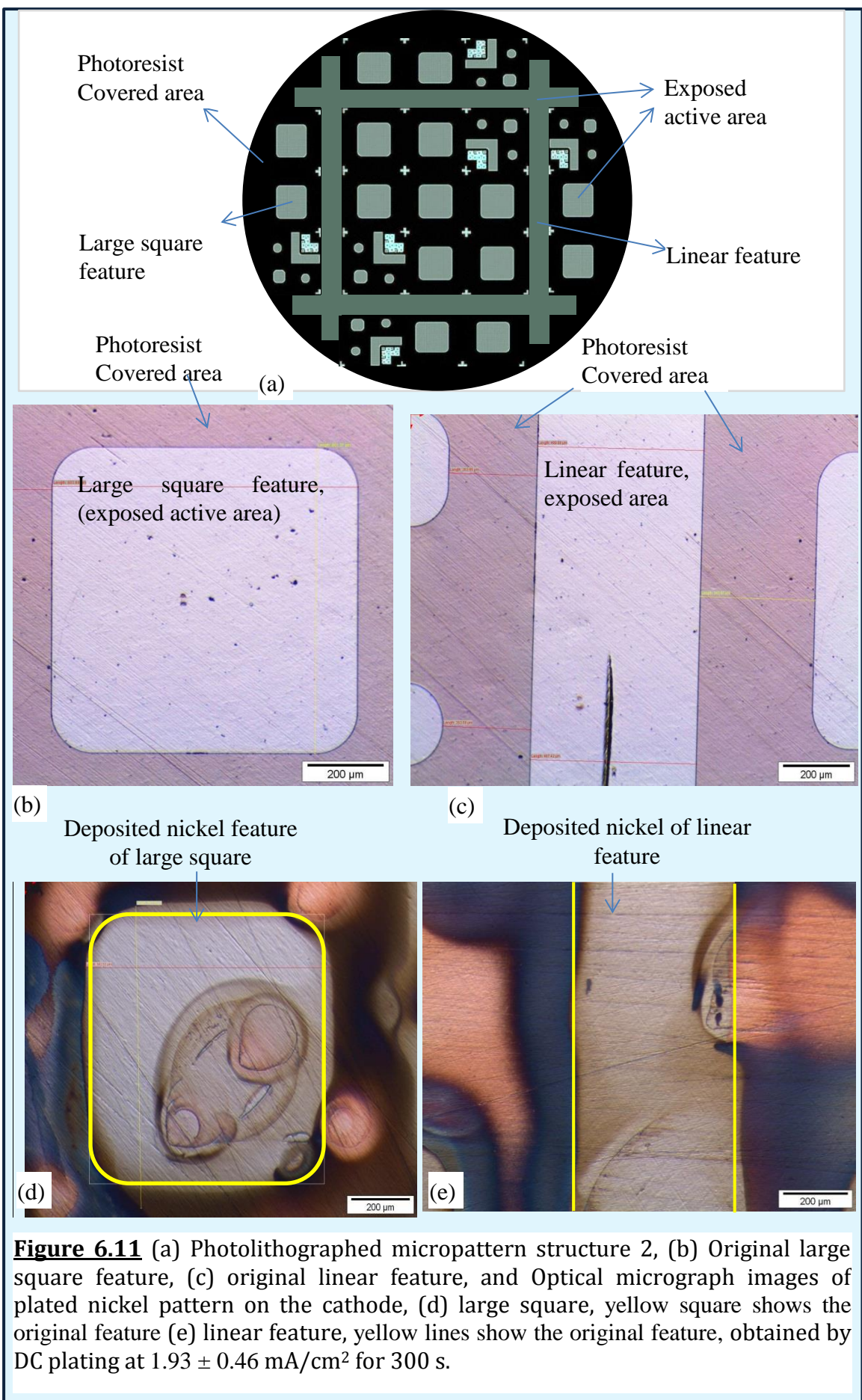
As shown in Table 6.9, the deposited features are greater by 16.23 and 34.53 % than the original one at a deposition time of 300 s. A comparison of the large square and the linear feature indicates that a greater spreading of the deposited nickel was observed on smaller feature dimension. Due to the thinness of the deposited nickel, the thickness could not be measured as it was impeded by the substrate roughness. Electrodeposition experiments at a longer deposition time was attempted to increase the deposit thickness, however as the photoresist quickly degraded during the experiment, a deposited feature was not obtained at deposition time longer than 300 s.

The measurement of deposited feature dimension showed that the pattern on the substrate did not exactly replicate the pattern feature on the anode; it is a clear indication of current spread. For different processing time in the pattern transfer experiments of the feature of 1 mm x 5mm, the feature spread was about 48 – 98 % of the original pattern features (Table.6.2). The deposited feature widened with increasing

deposition time. This was also confirmed by the result of the experiments on the photolithographed micropattern structure as shown in Figure 6.9 and 6.10.

Figure 6.11 shows a deposited feature analysis for microscale pattern feature structure 2. The structure, the original feature of linear and large square, and optical images of the deposited features are shown. Figure 6.11 (d) and (e) shows a direct comparison of the original feature and the deposited feature demonstrating the deposited nickel spreading which has been presented in table 6.8. The deposited nickel appearance shows a dull metallic finish surrounded by burnt deposit along the feature edge which is thought due to an inclusion of impurities as the current density at the middle part and at the edge of the feature was different.

In the case of the pattern transfer of photolithographed micro feature structure 2 with a photoresist thickness of 0.8 μm , it was observed that the photoresist rapidly degraded during the experiment. The photoresist was observed to be completely detached from the anode surface after the first experiment. The rapid degradation of photoresist during the experiment may lead to an increase in an exposed active area on the anode, a loss of deposition selectivity, and a spread of deposited nickel over the cathode surface. Therefore, due to this fact further measurements were not carried out.



6.6 General comparison of deposited features

The burnt deposit with black or grey colour at areas along the edge was always observed on every deposited feature obtained from all pattern feature sizes and structures including the millimetre scale, the manually fabricated microscale, and the photolithographed microscale. It was thought that an inclusion of impurities on to the deposited nickel caused the deposit to be black and burnt as a result of non-uniform current density distribution. Further investigation on the burnt deposit composition carried out by using energy dispersive X-ray (EDX) analysis was necessary to see whether there are impurities adsorbed on to the deposit. The result of the EDX analysis would be presented in the section of material analysis.

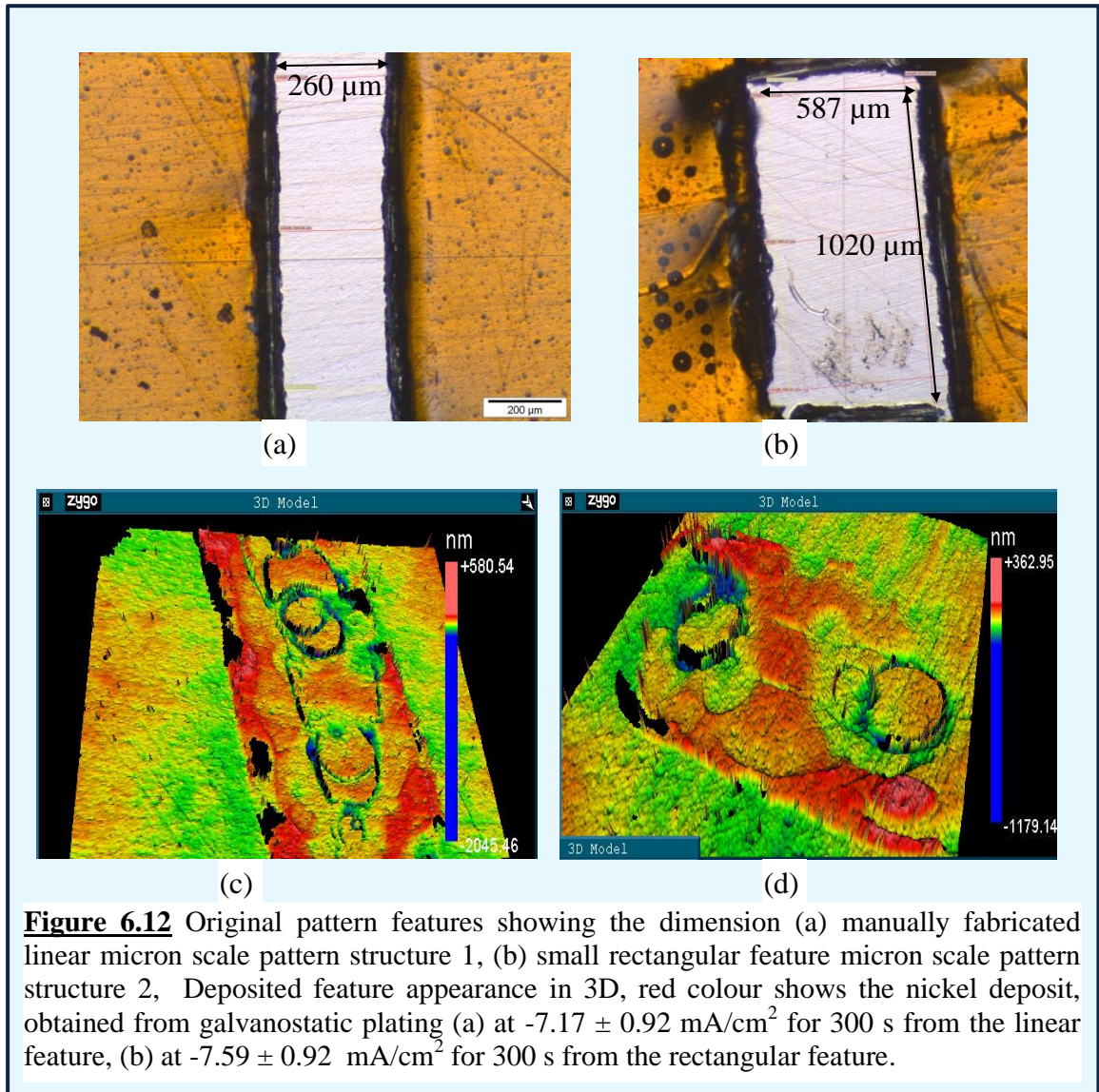
A comparison was carried out between deposited features obtained from manually fabricated features and those fabricated by photolithography. Deposited nickels at the edge obtained from photolithographed feature were found to be sharper and straighter than those obtained from manual feature. This was most probably due to the fact that the edge of manual feature was uneven and rough as result of manual handling limitation which has been described in Figure 4.7.

The degree of deposited feature broadening obtained from the manual features fabricated using kapton tape was observed to be greater than that obtained from the photolithographed features. This could be due to the fact that the kapton tape was thicker than the photoresist. The thickness of kapton tape was around 65 μm , whilst the photoresist was 0.8 – 2.4 μm . In this case, the thickness of the resist played important role in achieving the desirable interelectrode gap as the gap was obtained by inserting a stainless steel shim (250 μm thickness) in between the two electrodes. By turning the electrode holders to clockwise direction, the electrodes were brought to be closer to each other until gently touching the shim. When the shim was taken out from the space, an electrode gap of around 250 – 300 μm was expected to be achieved. However, the thickness of the kapton tape provided an extra space resulting in a further interelectrode distance obtained on manual feature. The greater interelectrode gap led to more deposited feature spreading as more space available for the current line to spread.

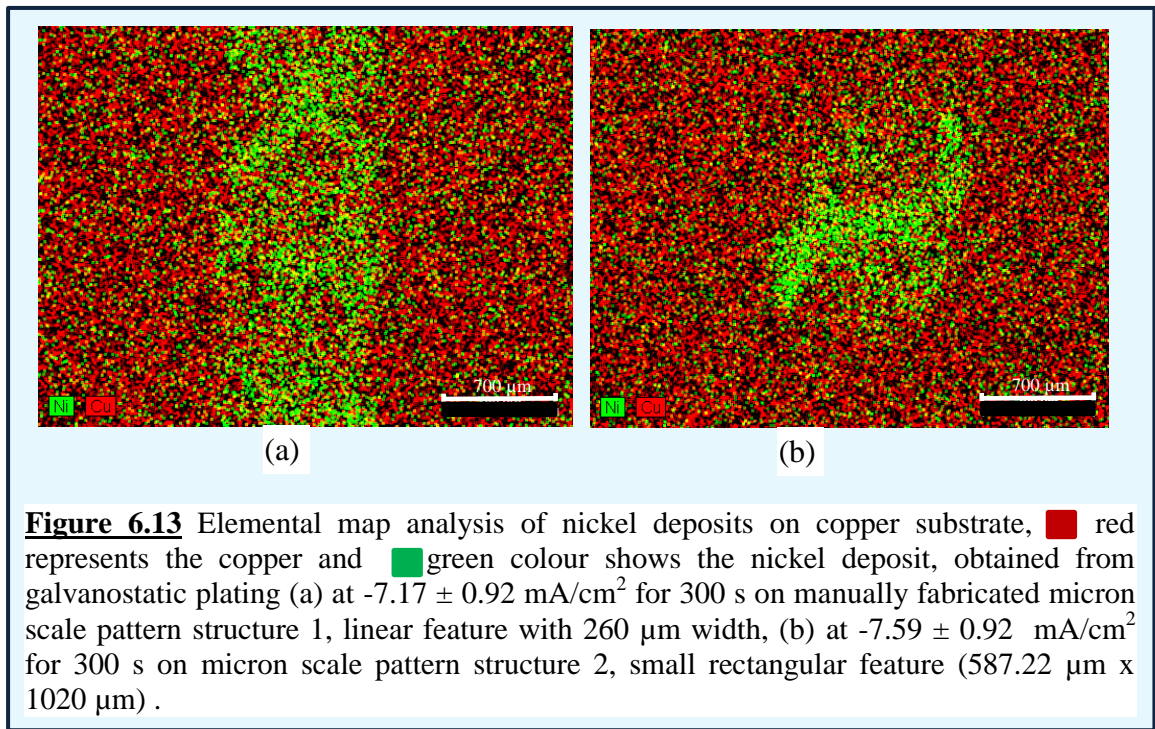
6.7 Surface Analysis

Figure 6.12 shows the typical appearance of the deposited feature in 3D. As shown by colour bar, the variation of colour defines the height level of the area with an order from the highest is pink, red, yellow, green, and blue respectively. The areas with pink, red, or yellow colour represent deposited nickel whilst base surface representing the substrate is

shown on the area with green or blue colour. The deposited feature is clearly visible by the red colour indicating higher level of thickness. However, different colours are observed within the deposited feature area indicating that the thickness of deposited nickel is not uniform. The non-uniformity of the deposited nickel thickness is shown by the red and pink colour represents thicker area, whilst the yellow, green, and blue colour observable inside the feature indicating areas with less thickness or without deposited nickel. In addition, a reddish colour around the feature suggested that nickel nucleation forming nickel nuclei might occur during pattern transfer process at that area due to the current spreading.



This observation is in agreement with the finding of an elemental mapping analysis. Elemental maps shown in Figure 6.13 were obtained by EDX measurement to analyse the distribution of each single element i.e. Ni and Cu on the cathode surface. In Figure 6.13, nickel and copper elements are represented by green and red colour respectively, whilst the scale bar is representing 700 μm.



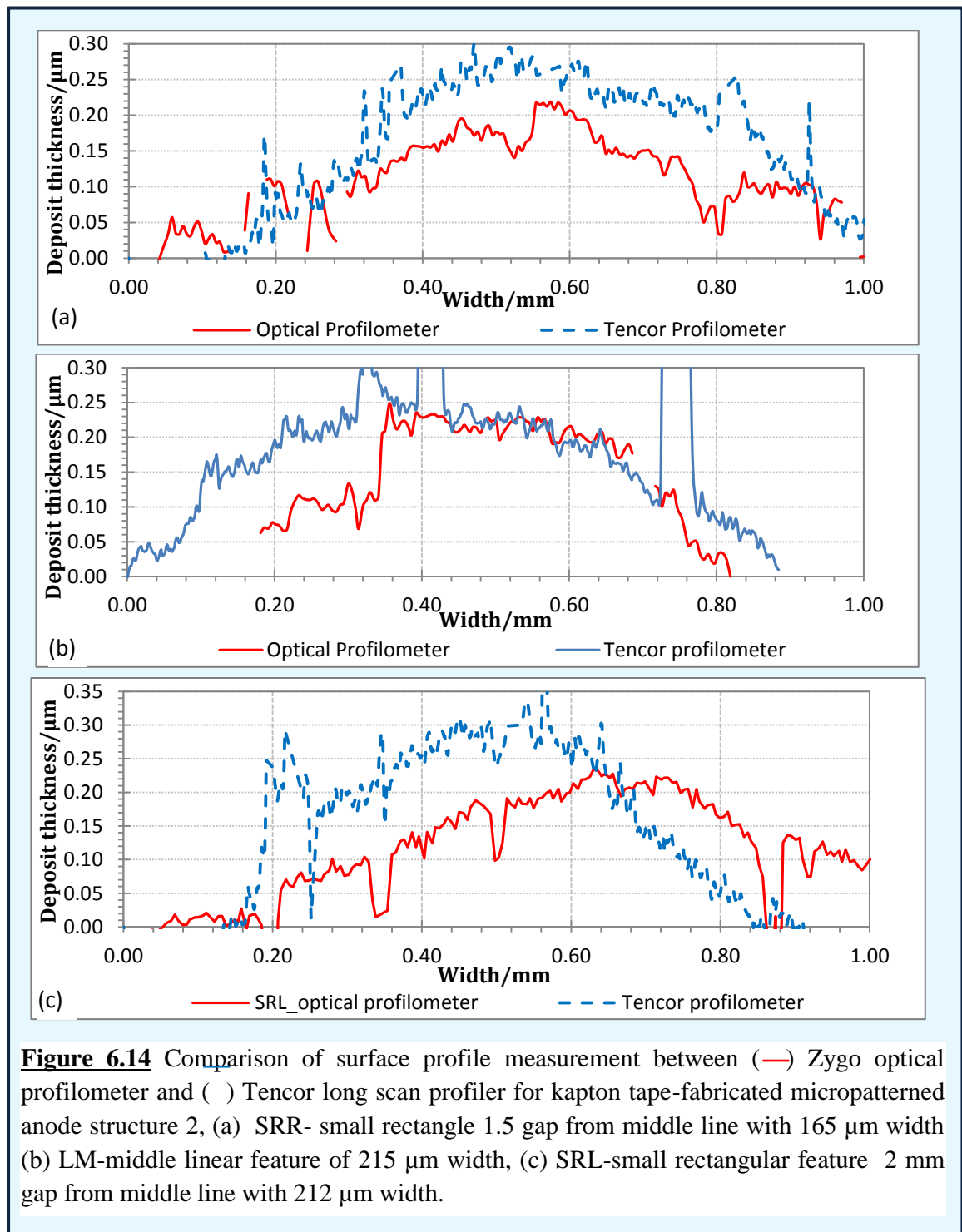
The elemental maps clearly show a band of deposited nickel over the copper substrate demonstrating deposited features of (a) line and (b) rectangle. Red colour representing copper is still visible inside the features indicating either very thin nickel deposit was obtained so that copper was detected or non-uniform thickness of the deposited nickel. Nickel was also observed to be on the area around the features which is most probably due to the nickel nucleation process as has been previously discussed as a result of a current spreading.

6.8 Verification of thickness and surface profile measurements

Two measurement methods for measuring deposited feature profiles, contact and non-contact technique, were used to verify if the measurements were accurate and valid. For non-contact technique, optical based profiler (Zygo) was used in the most measurement; whereas contact method of stylus based profilometer (Tencor P1) was used in the surface profile measurement of particular samples. Results from the two measurements were plotted into graphs in order to directly compare the surface profile, the width, and the thickness of the deposited nickel features.

Figure 6.14 shows the surface profile obtained by using Zygo optical profiler and compared with that obtained by using Tencor P1 long scan profiler for the deposited nickel feature on manually kapton tape-fabricated microstructure 2. As can be seen in the Figure, the two measurement methods produced a similar surface profile in which the thickness on the centre is higher than that is in the edge forming a bell-shape curve. Observing the width of the deposited feature, there is a difference of around

8.0 %. In addition, the thickness measured by using Tencor profiler differs from that obtained by using Zygo profiler by 12.4 %.



A possible explanation for these different results might be that the measurements were taken at different position across the feature width. Due to the non-uniform thickness and roughness, a surface profile was varied from one position to another.

Another possible explanation for the different result is that the different approach in the measurements resulted in the different surface profiles. The non-contact technique Zygo profilometer is based on imaging and microscopy to perform scanning

white-light interferometry. Measurement using this non-contact technique is affected by the quality of surface to be measured such as a surface feature causing diffraction, deep valley which cause scattering, and surface slope^[253]. In the case of measurement of deposited feature surface profile, the quality of surface containing dark/black deposit might affect the result as the area with dark/black deposit did not reflect the light. Accordingly, a surface profile of the area with black/dark deposit was not obtained as can be seen in Figure 6.14 that the surface profile obtained by Zygo optical profiler at some parts across the width are missing.

The contact technique, Tencor stylus profiler measurement, was carried out by direct contact of the stylus to the surface. The stylus was dragged across the surface at a particular rate to detect valleys and peaks on the surface that would be converted to electrical signals producing the surface topography^[253]. According to this, the contact technique directly records the surface profile through the sensitive stylus with less interference^[253].

In this case, the results obtained by using Tencor stylus profiler seem to be more valid than those obtained by Zygo optical profiler. However, the differences are not too significant. The insignificant differences between the two results suggest that the surface profile measurements using the Zygo optical profiler were fairly accurate.

6.9 Material Analysis

6.9.1 EDX Analysis

In order to examine whether the deposited feature was metallic, the samples were investigated by energy dispersive X-ray (EDX) analysis. As the deposit at the middle was metallic in appearance and at the edge of the feature was a burnt deposit with black/grey colour, the analysis was carried out for both parts. The spectra of the EDX analysis of middle part of the deposit are shown in Figure 6.15 (a), whilst Figure 6.15 (b) shows the EDX spectra for the edge of the deposit feature.

The EDX analysis at the middle part the deposit feature shown in Figure 6.15 (a) shows peaks for metallic nickel, and copper which arise from the substrate were detected. The EDX spectra for the edge of the feature which appeared burnt with black/grey colour (Figure 6.15 (b)) revealed that beside nickel and copper, sulphur and oxygen were also present. This is indicative that impurities were adsorbed on to the deposited feature leading to a formation of black/burnt deposit at the feature edge. The non-uniform current density may lead to reactions involving the complexing agent (e.g. sulfamate) and formation of nickel oxide. The sulfamate was probably decomposed resulted in sulphur being adsorbed and was present on the burnt deposit.

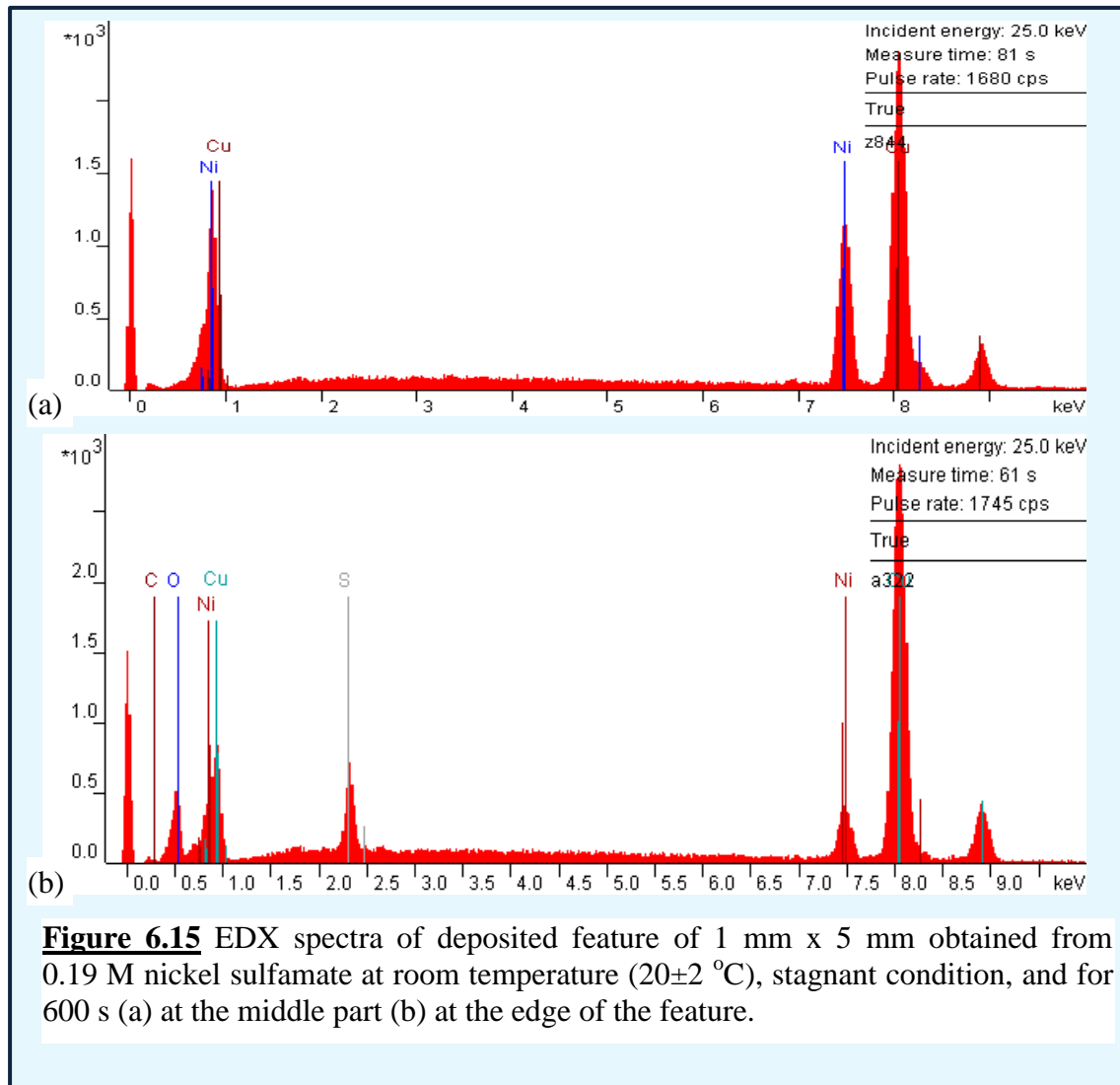


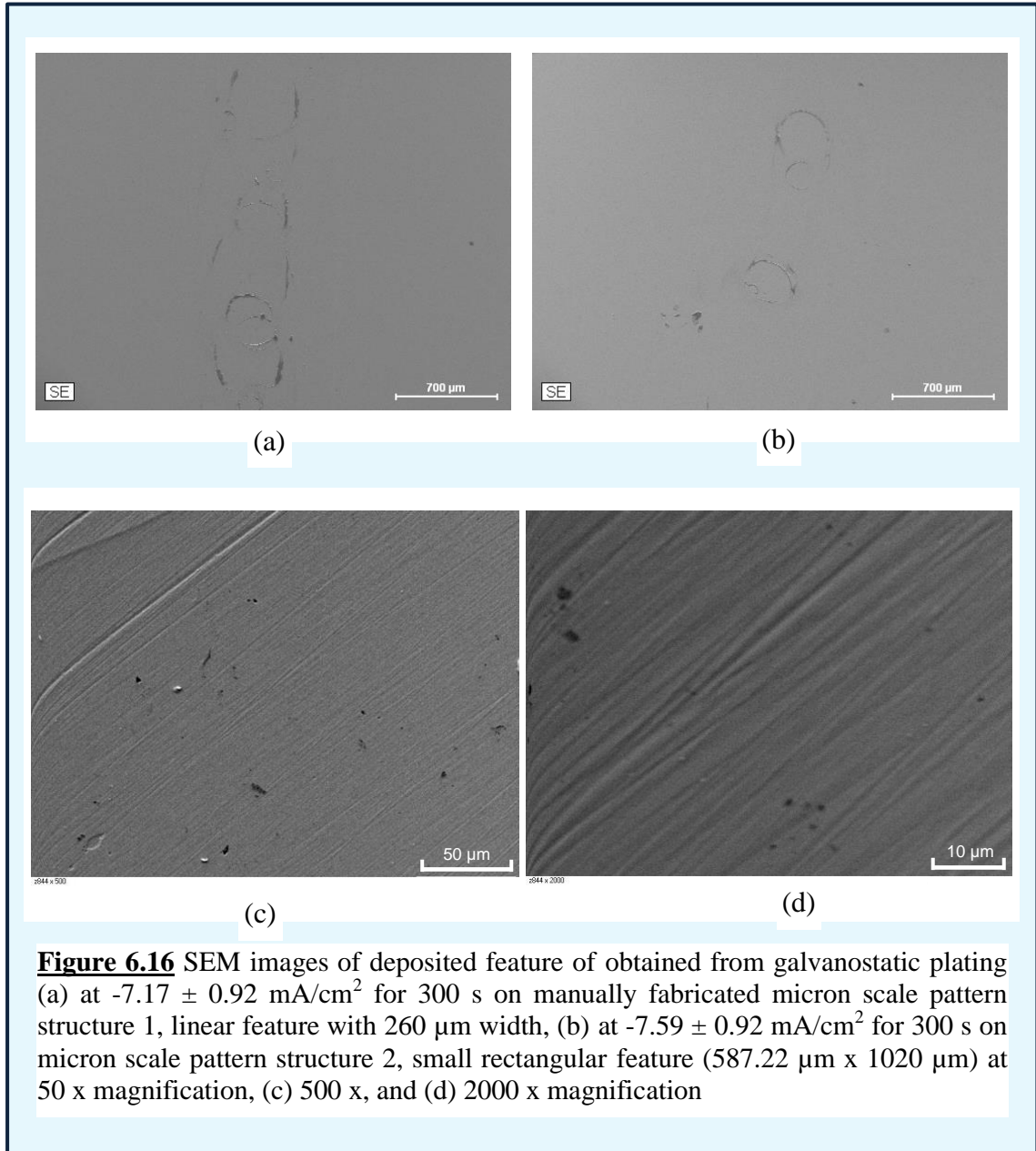
Figure 6.15 EDX spectra of deposited feature of 1 mm x 5 mm obtained from 0.19 M nickel sulfamate at room temperature (20 ± 2 °C), stagnant condition, and for 600 s (a) at the middle part (b) at the edge of the feature.

6.9.2 Scanning Electron Microscopy (SEM)

A further investigation on the deposited feature morphology was carried out using scanning electron microscopy (SEM) method. The measurement was performed on deposited features obtained from galvanostatic plating (a) at -7.17 ± 0.92 mA/cm² for 300 s on linear feature manually fabricated micron scale pattern structure 1, and at -7.59 ± 0.92 mA/cm² for 300 s on small rectangular feature micron scale pattern structure 2 at 50 x magnification. Figure 6.16 shows SEM images of deposited nickel of both features. As can be seen in Figure 6.16, the deposit surface within the features is relatively rough and inhomogeneous. This measurement is in agreement with previous surface analysis using optical microscope.

A closer investigation on the deposited nickel was carried out by using SEM analysis with higher magnifications of 500 x and 2000 x in order to see the density of the deposit. Even though SEM image at low magnification showed the roughness

(Figure 6.16 (a), (b),) SEM images at higher magnification on an area with nickel deposit, as shown in Fig 6.16 (c) and (d), show fine, smooth and dense deposit surface. This suggests that if the gas bubbles issue can be eliminated, macroscopically and microscopically fine, smooth, homogeneous, compact, and dense nickel deposit would be achieved

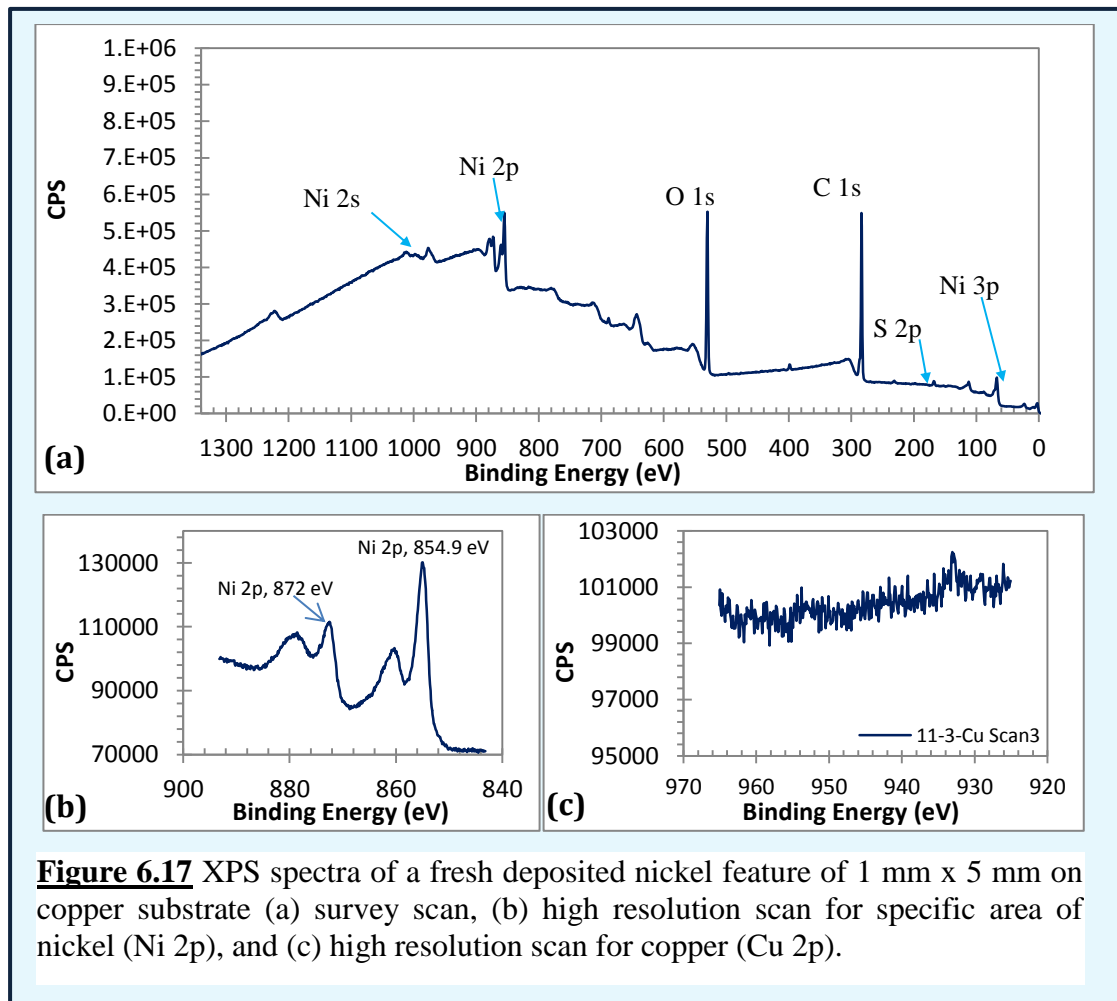


6.9.3 X-ray Photo electron Spectroscopy (XPS) Analysis

Owing to the thinness of the deposited nickel layer, it was necessary to investigate if copper diffused from the substrate passed through the nickel layer. X-ray Photoelectron Spectroscopy (XPS) measurement was carried out to investigate if the diffusion of copper occurs. The analysis was carried out on the deposited nickel surface

up to 10 nm depth to see if the copper was detected indicating copper diffusion occurred along pores or grain boundaries. The XPS analysis was carried out using K-Alpha instrument (Thermo Scientific).

XPS analysis was carried out for four differently conditioned samples. Initially, as a baseline data, a freshly obtained deposited feature was investigated to see whether copper was present on the surface. To investigate the possibility of copper diffusion during a period of the pattern feature storage, XPS was carried out on a deposited feature stored in a room temperature for 2 months. As typical device operation is at higher temperature for a long period, therefore a sample was treated by a temperature of around 90 °C for 100 hours prior to XPS measurement. Finally, copper diffusion may be enhanced during bonding process, to see the possibility; a sample of deposited pattern feature was annealed at temperature of 180 – 200 °C for 5 -10 minutes representing the bonding condition.



During the XPS measurements, the average error in energy position which represents a deviation of the scan value of energy binding for a particular peak from the true value of reference was $\pm 0.14\%$. Figure 6.17 shows XPS spectra for the newly

deposited nickel with 1s, 2s, 2p, and 3p following the detected elements represent energy bands where the ejected electron located which is also called photoelectric lines. The XPS survey in Figure 6.17 indicates the presence of nickel, oxygen, carbon, and sulphur. Two very intense peaks were observed, at binding energy of 531.3 eV was the oxygen (O 1s) and at 284.6 eV which was indicative of the carbon (C 1s). The presence of sulphur (S 2p) was shown by a small peak at 165 eV. The nickel was detected by the appearance of four peaks at 1008.8 eV (Ni 2s), 854.9 eV (Ni 2p), and 68 eV (Ni 3p) as well as 872 eV (Ni 2p) at higher resolution scan.

The peaks for nickel was not as intense as for carbon/ oxygen, whereas a copper peak was not observed, hence a higher resolution scan was performed to further check the presence of nickel and copper as shown in Figure 6.17 (b) and (c) respectively. At higher resolution scan, the peak of nickel is clearly visible, but there is no copper peak. This shows that there was no copper contamination during electrodeposition. It also indicates that the deposited nickel was relatively dense and compact so that the copper diffusion rate could be minimised.

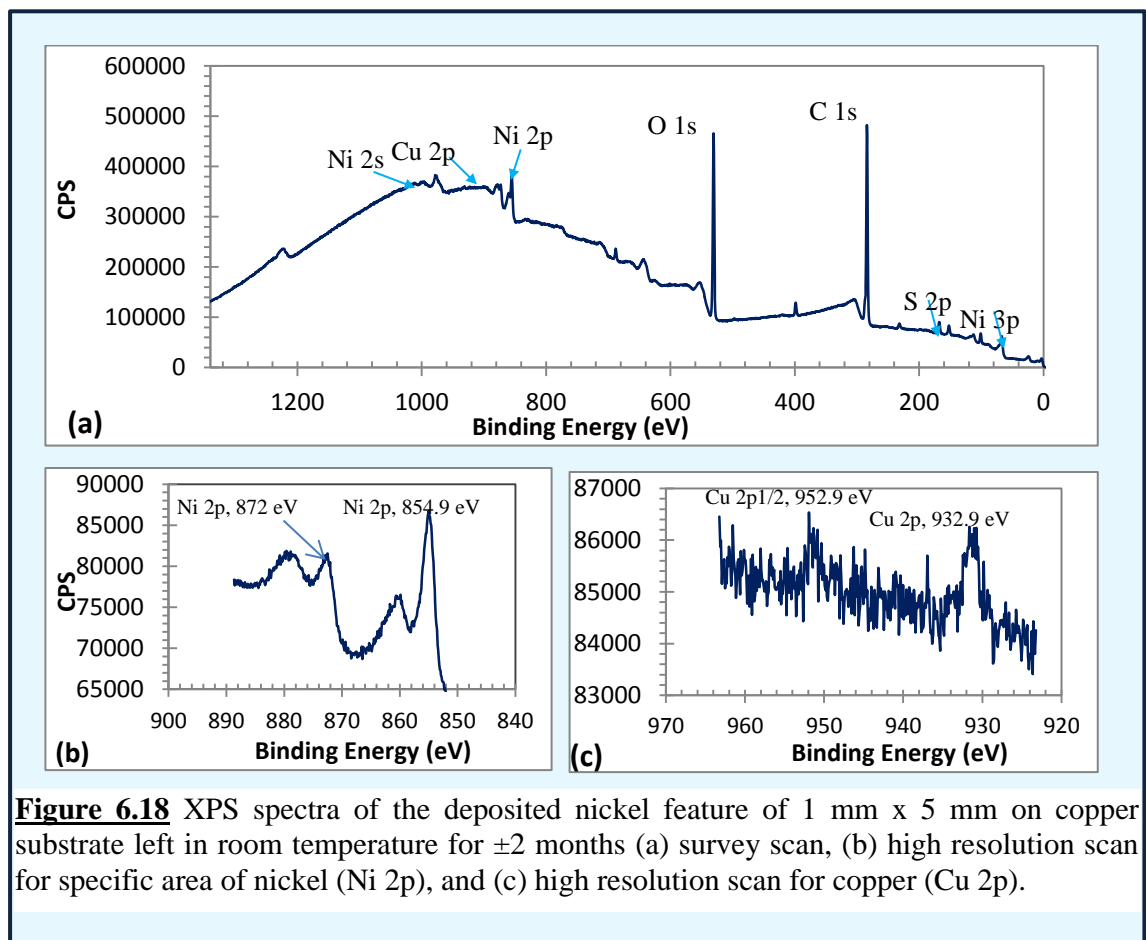


Figure 6.18 XPS spectra of the deposited nickel feature of 1 mm x 5 mm on copper substrate left in room temperature for ± 2 months (a) survey scan, (b) high resolution scan for specific area of nickel (Ni 2p), and (c) high resolution scan for copper (Cu 2p).

Figure 6.18 shows XPS spectra for the deposited nickel feature stored in a room temperature for ± 2 months. As shown in Figure 6.18 oxygen, carbon, and sulphur were

present on the deposited nickel. The presence of copper was also detected in the survey scan indicated by a small peak at binding energy of 932.9 eV. To show the presence of nickel and copper more clearly, a high resolution scan was carried out. The results are presented in Figure 6.18 (b) and (c) showing clear peaks for nickel at binding energies of 854.9 and 872 eV along with those at 68 and 1008.8 eV visible in the survey scan. In addition, copper peaks at binding energies of 932.9 and 952.9 eV are shown. This indicates that copper diffusion occurred during the period of storage in room temperature.

Figure 6.19 shows the XPS spectra for the sample maintained at a constant temperature of 95 ± 5 °C for 100 hours. The survey scan (Figure 6.19 (a)) also shows oxygen, carbon, and sulphur peaks. A slightly more intense peak of copper at binding energy of 932.9 and 952.9 eV was also observed indicating that more copper was present. Nickel peaks are observed at binding energies of 68, 854.9, 872, and 1008.8 eV. The peaks of nickel and copper are more clearly visible at high resolution scan as shown in Figure 6.19 (b) and (c).

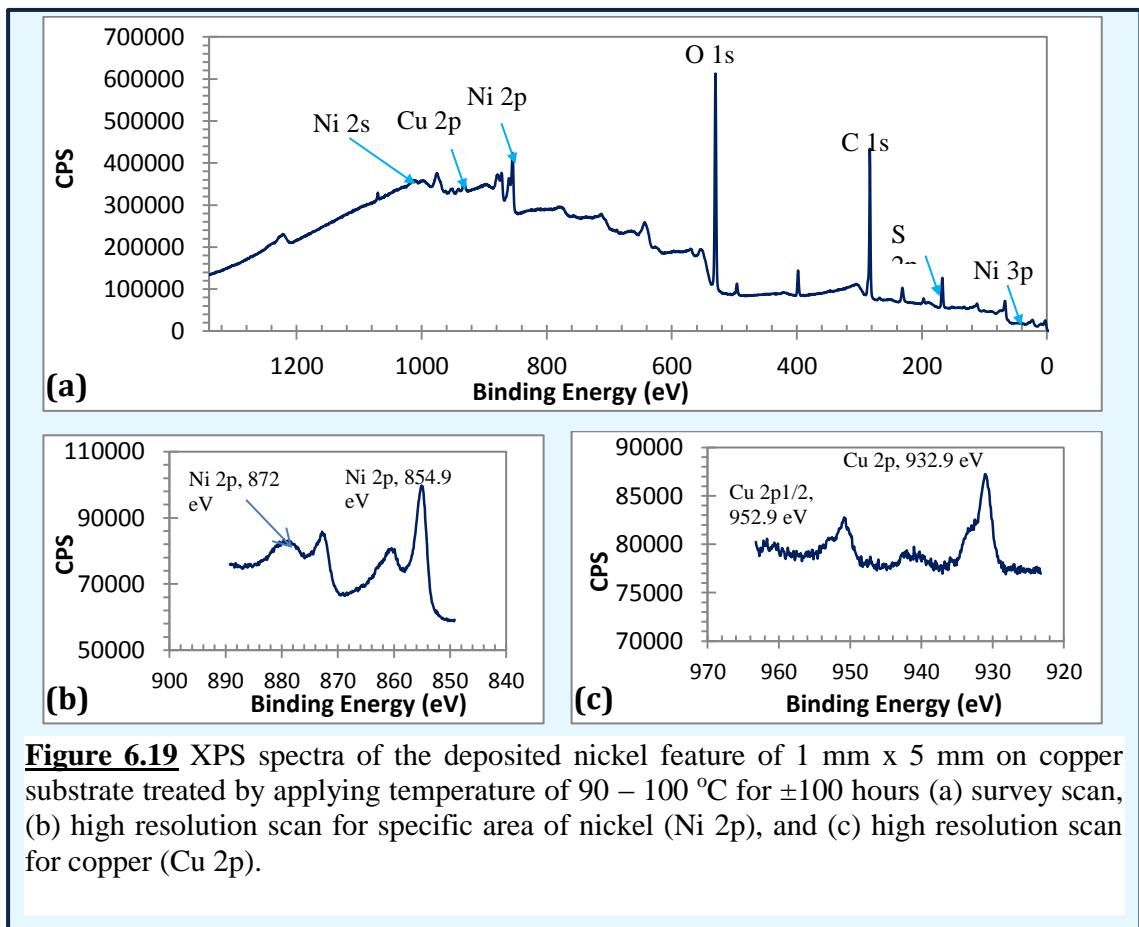
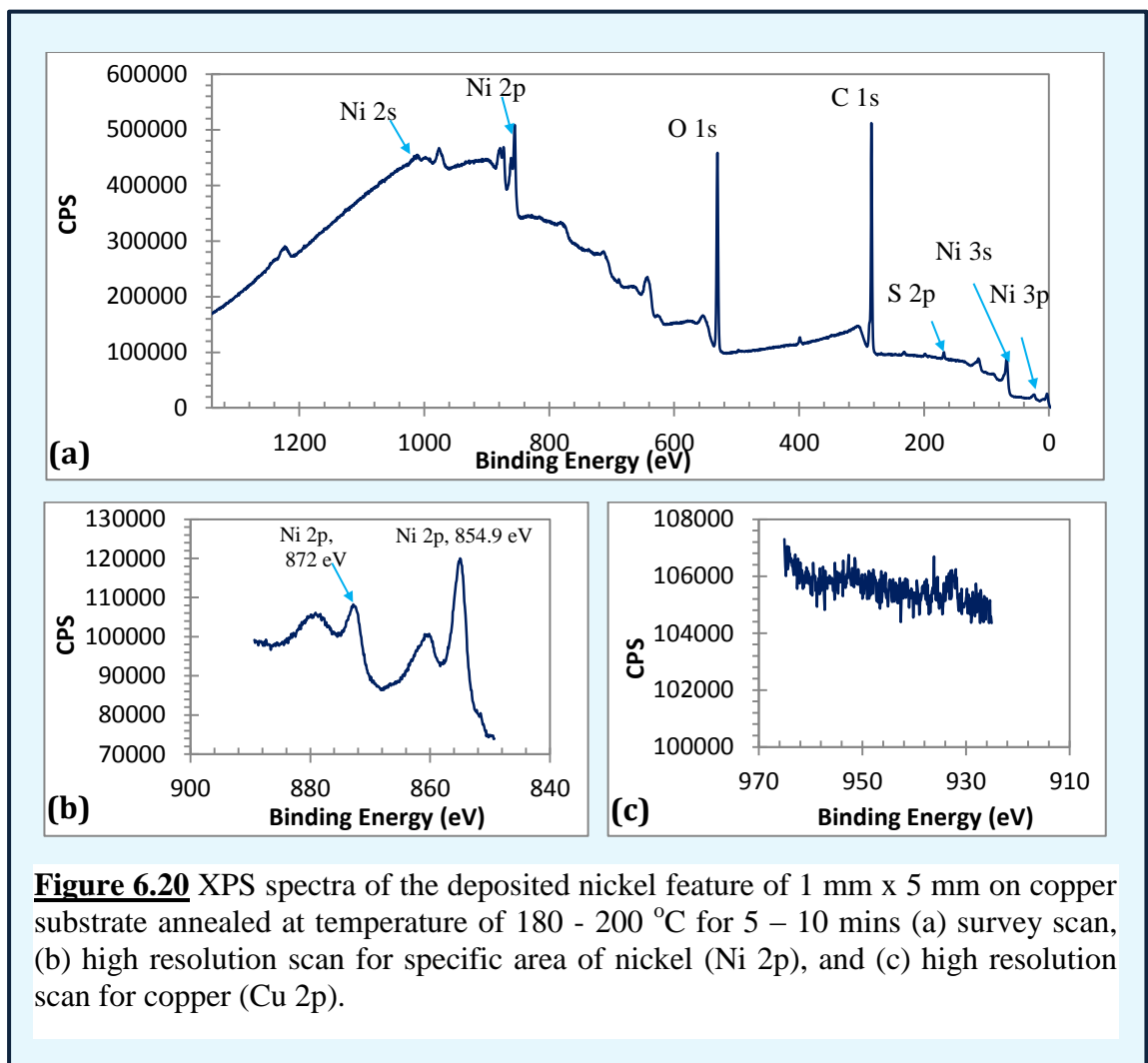


Figure 6.19 XPS spectra of the deposited nickel feature of 1 mm x 5 mm on copper substrate treated by applying temperature of 90 – 100 °C for ± 100 hours (a) survey scan, (b) high resolution scan for specific area of nickel (Ni 2p), and (c) high resolution scan for copper (Cu 2p).

Figure 6.20 shows the XPS spectra for the sample of deposited nickel annealed at temperature of 180 - 200 °C for 5 – 10 mins. The survey scan in Figure 6.20 (a) for the deposited nickel after the treatment did not show any copper peak. Small peaks associated with nickel at binding energies of 68, 112, 854.9, 872, and 1008.8 eV is visible. The high resolution scan as shown in 6.20 (c) also confirmed that the copper was not detected, on the other hand, the high resolution scan at nickel region shown in 6.20 (b), the nickel peaks are more clearly visible. Here, it is a clear indication that high temperature treatment for short time did not accelerate copper diffusion through the deposited nickel.



As similar peaks are observed in Figure 6.17 -6.19, refer to XPS database by The National Institute of Standards and Technology (NIST) ^[254], the chemistry of nickel observed in those figures could be identified based on their peaks and binding energies. Table 6.10 shows the chemistry of nickel associated to the peaks and the binding energies obtained from Figure 6.17 – 6.19.

Table 6.10 A summary of identification of nickel chemistry based on the peaks and binding energy observed from the XPS scan in Figure 6.17- 6.19 for deposited nickel feature of 1 mm x 5 mm on copper substrate.

Peaks	Binding Energies	Associated Chemistry
(Ni 2s)	1008.8 eV	Metallic Nickel
(Ni 2p)	872.0 eV	NiO
(Ni 2p)	854.9 eV	Metallic nickel
(Ni 3p)	68.0 eV	Ni(OH) ₂

Based on the database of NIST ^[254], the chemistry of the nickel peaks shown in Figure 6.20 is identified. Table 6.11 shows the chemistry of nickel associated to the peaks and the binding energies obtained from Figure 6.20. An additional nickel peak (Ni 3s) at a binding energy of 112 eV appeared in the survey scan which is associated with nickel monoxide (NiO) indicates that the high temperature treatment accelerate nickel oxidation.

Table 6.11 Identification of nickel chemistry based on the peaks and binding energy observed from the XPS scan in Figure 6.20 for a deposited nickel feature of 1 mm x 5 mm on copper substrate annealed at temperature of 180 - 200 °C for 5 – 10 min.

Peaks	Binding Energies	Associated Chemistry
(Ni 2s)	1008.8 eV	Metallic Nickel
(Ni 2p)	872.0 eV	NiO
(Ni 2p)	854.9 eV	Metallic nickel
(Ni 3s)	112.0 eV	NiO
(Ni 3p)	68.0 eV	Ni(OH) ₂

Overall investigation on the nickel chemistry for the four different samples indicates that the deposited nickel was mainly in a metallic form. However, nickel oxidation occurred because of a direct contact with an open environment. The oxidation of nickel might be accelerated by a higher temperature annealing as more nickel oxide (NiO) peak was detected on the annealed sample at 180 -200 °C.

As can be seen in figure 6.17 – 6.20, the presence of Cu (I) was confirmed by the peaks of Cu 2p_{3/2} at 932.9 eV and Cu 2p_{1/2} at 952.9 eV ^[254, 255] which are associated

with metallic copper and CuO/Cu₂O respectively. As presented in Table 6.10 and 6.11, oxygen which was evident in the XPS survey scan on all samples might be attributed to oxide and hydroxide compound ^[254, 256, 257]. The O1s peak detected at binding energy 531.3 eV can be associated with Ni(OH)₂ ^[254, 257] and Cu₂O ^[254, 256]. The very intense C 1s peak which was apparent at binding energy of 284.6 eV was most probably caused by a carbon contamination from the XPS instrument due the cracking of vacuum oil during the analysis took place ^[256, 258]. Sulphur peak appeared at a binding energy of 165 eV might be due to an adsorption of sulphur on the deposited nickel surface as a result of electrolyte decomposition during pattern transfer process as has been discussed in section 6.9.1.

The material analysis using EDX and XPS measurement on the deposited feature confirmed that nickel deposits obtained from the pattern transfer experiments was metallic. XPS analysis also aimed to investigate whether the copper from the substrate diffused through the deposited nickel to reach its surface due to porosity. Copper was not detected on the fresh deposited nickel surface indicating that there was no copper contamination during electrodeposition. However, a low amount of copper was observed on the sample stored for 2 months indicating that copper diffused through the nickel layer over time. This indicates that that the copper diffusion rate could be minimised as the deposited nickel was relatively dense and compact. More intense copper peak was observed on the sample that was treated with temperature of 90 – 100 °C for 100 hours. As would be expected, the copper diffusion rate increases when the sample was constantly exposed to a high temperature. In addition, there was a clear indication that high temperature treatment for a short period of time did not accelerate copper diffusion through the deposited nickel.

6.10 Effect of increasing mass transfer

As previously mentioned, the entrapped gas bubbles is one of the main problems on the process of nickel pattern transfer using Enface. This suggests that sufficient agitation was required to remove the gas bubbles from the interelectrode gap. The agitation technique has to be appropriately selected not only for eliminating the bubbles and enhancing mass transfer but also to achieve a good pattern transfer.

Ultrasound is a popular method in an electrochemical system ^[226]. In typical electrodeposition, the ultrasonic agitation could enhance the process by reducing crack formation ^[227] and increasing the rate of mass transfer as well as the electrochemical

reaction^[226]. Therefore, electrodeposition of nickel under the ultrasonic agitation was carried out in order to investigate whether the entrapped gas bubbles could be minimised and to nickel pattern transfer performance could be improved using this agitation technique.

Nickel pattern transfer experiments were carried out under ultrasound agitation for millimetre scale feature of 1 mm x 5 mm at current density of -4.93 mA/cm^2 for deposition times of 1200 s and 1500s. The ultrasonic wave used in the experiments was at 35 % and 45 % of its maximum amplitude corresponding to 18 and 26 W/m^2 power densities. Cell voltage during the pattern transfer experiments was monitored and compared to those recorded during pattern transfer experiment under stagnant solution.

Figure 6.21 shows the cell potential profiles against time recorded during pattern transfer experiments at provided applied current density for Enface process with and without ultrasound agitation. As can be seen, in the stagnant case, the cell potential substantially increased at deposition time between 300 s and 600 s. The deposition time could be significantly extended in the pattern transfer experiment under ultrasound agitation. This indicates that ultrasound has a capability to remove the bubbles and extend deposition time.

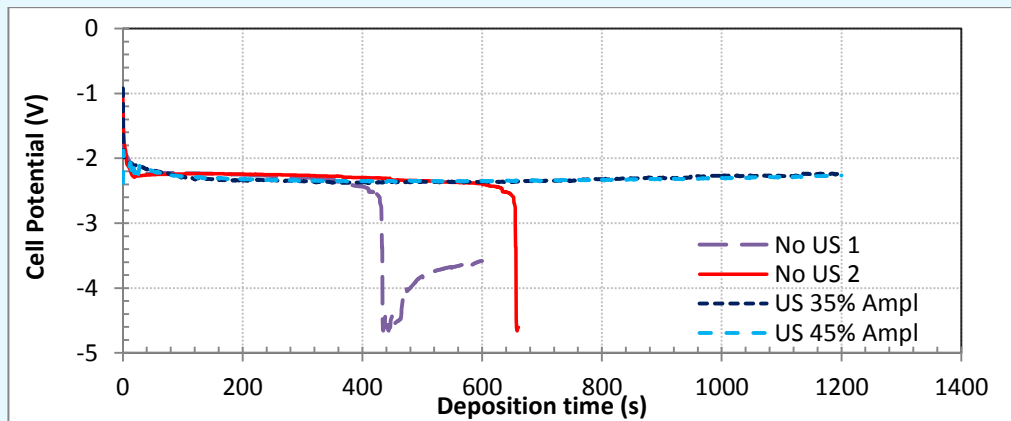


Figure 6.21 Cell potential profile of nickel pattern transfer using Enface under stagnant condition and ultrasound agitation on 1 mm x 5 mm feature.

Deposited nickel features obtained from pattern transfer experiments under ultrasound agitation is characterised using several parameters including the broadening of the feature, the deposit thickness, the surface profile, and the deposit appearance/morphology. The deposit spreading was determined by measuring the feature width which then compared to the original pattern feature. A summary of the measurement is presented in Table 6.12. It can be seen in the table that, the deposited

feature obtained under ultrasound power density of 18 W/m^2 is 116.42 % greater than the original. Moreover, at 45 % of maximum amplitude corresponding to 26 W/m^2 power density, more broadening of the deposited feature is observed.

The deposited features obtained under ultrasound agitation suffered more spreading, compared to those obtained under stagnant conditions as shown in Table 6.2 and Table 6.12. The deposited features spread under the ultrasound agitation were 216.42 – 300.27 %, whilst under stagnant conditions ranged between 148 and 198 %. This is thought to be caused by the longer deposition time and the effect of ultrasonic wave power.

Table 6.12 A summary of feature broadening measurements of the nickel deposit obtained under ultrasound wave of 18 and 26 W/m^2 power densities.

Original Feature		US power density & time	Deposit Feature Width (mm)	Broadening Width (%)
Length (mm)	Width (mm)			
5.15±0.38	1.25±0.7	18 W/m^2 , 1200 s	2.71±0.44	216.42±35.00
		26 W/m^2 , 1500 s	3.76±0.42	300.27±33.19

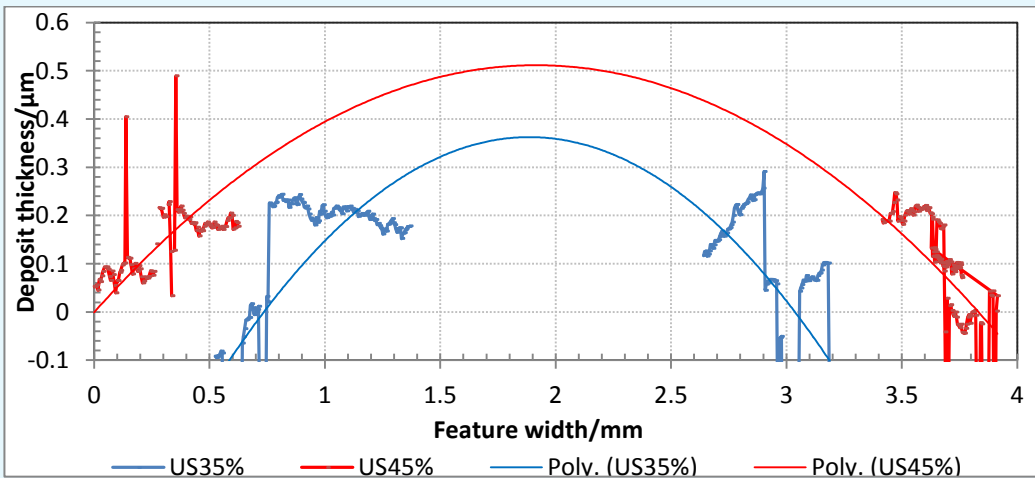


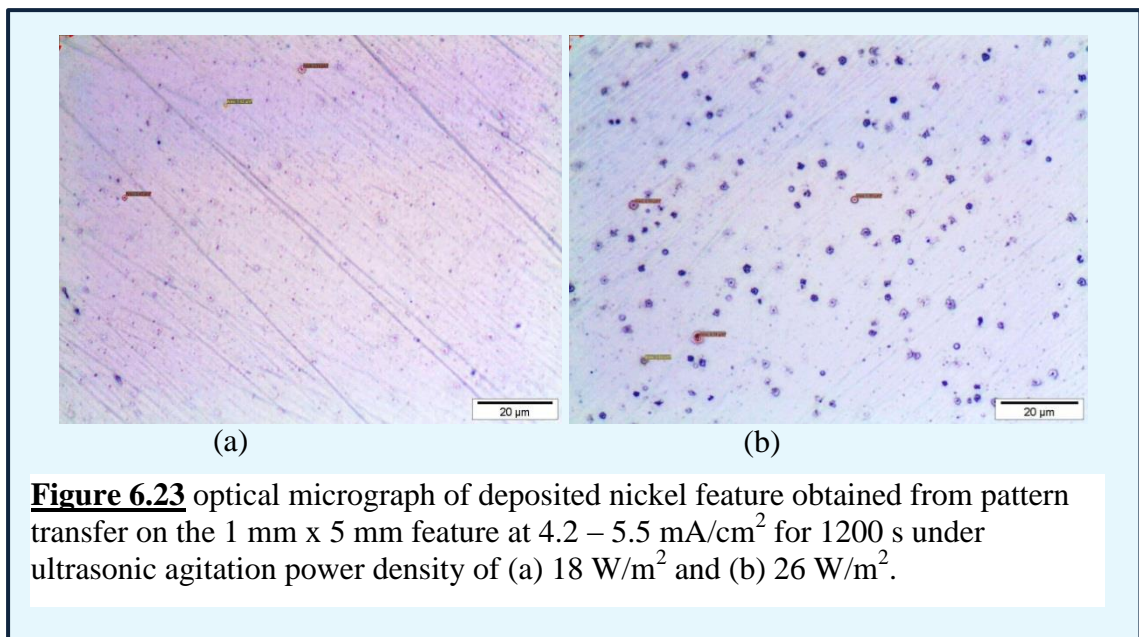
Figure 6.22 Optical profilometer measurements showing the deposit thickness, surface profile and the roughness of the deposited features (— —) 26 W/m^2 ultrasound power density for 1500 s and (— —) 18 W/m^2 power density for 1200 s, with power densities of 18 and 26 W/cm^2 respectively.

The deposited nickel thickness and the surface profile across the width were measured using optical profilometry. The measurement was carried out on the both edges and the entire width profile was approximated using polynomial trendline. Figure 6.22 shows the optical profilometry scan showing the approximated surface profile across the width and thickness for deposited features obtained from 1 mm x 5 mm feature, under ultrasound agitation of 18 and 26 W/m^2 power density.

As can be seen in Figure 6.22, the thickness of the deposited feature grew up with time as the thicknesses were 0.36 and 0.52 μm at 1200 s and 1500 s respectively. However, comparing the deposit thickness to the stagnant data, the thickness obtained under ultrasound agitation was relatively thinner as a deposited nickel thickness of around 0.53 - 0.54 μm was achieved at deposition time of 480 – 600 s under stagnant condition. This was most probably because of the greater deposited feature spread under ultrasound agitation.

The deposit surface morphology was investigated using an optical microscope. Figure 6.23 shows the micrograph of nickel deposit obtained under ultrasound agitation at applied current density of 4.93 mA/cm^2 for 1200 s. Unlike the morphology to those obtained under stagnant conditions, more homogeneous deposit and uniform thickness were obtained indicated by the fact that localised skip plating was not visible. This is an initial indication of the capability of ultrasound to eliminate the bubbles.

However, as shown in Figure 6.23 (a) small pits are barely visible on the deposit obtained at 18 W/m^2 power density of ultrasound agitation. The pits become more apparent on the deposit surface obtained under higher power density of 26 W/m^2 (Figure 6.23 (b)). As visually observed during experiments, the pits were possibly caused by cavitation bubbles produced by ultrasound wave. At higher power density the pits were more apparent indicating that the higher the power density, the more cavitation bubbles were produced.



In the case of photolithographed pattern feature, a pattern replication was not obtained under the ultrasound agitation at both power densities of 18 and 26 W/m^2 . The photoresist pattern features were observed to rapidly degrade due to the cavitation

bubbles and the pressure from ultrasonic wave. The degradation led the photoresist to easily detach from the substrate surface causing a loss of selective electrodeposition.

6.11 Analysis of Electrolyte Stability and Enface Process Sustainability

As a new nickel pattern transfer process using Enface method has been established, it is essential to evaluate the stability of the chosen electrolyte and the process sustainability. Since multiple use of electrochemical tool for pattern transfer is one of the major benefits of Enface process, the electrolyte has to be capable of supporting the process. For this reason, the physicochemical properties of the nickel electrolyte developed for Enface process was investigated before being used for the experimentation and after a number of experiments over a period of time. The pH and conductivity were initially measured being 6.77 and 2.19 S/m respectively. After approximately 50 pattern transfer experiments the pH was 6.70 and the conductivity was 2.26 S/m. The physicochemical properties of the electrolytes before and after being used in the experiments remained within the required range. This indicates that the bath stability could be maintained after a number of pattern transfer experiments (e.g. 50 times). This also shows that the electrolyte is reliable for multiple uses.

To quantitatively analyse the Enface process sustainability, material and energy consumption, cost effectiveness, the electricity consumption, chemical usage, and labour cost during photolithography in a clean room and patterning process were taken into account. The data for photolithographic patterning process were collected through direct interview with clean room staffs at Newcastle University carried out by Roy, S. (2011), the data for Enface process were estimated accordingly with the chemical usage, processing time, and energy consumption were determined based on the experimental results.

However, in this work, only pattern transfer using Enface on manually fabricated micro pattern feature using kapton tape can be used in the analysis, as the photoresist quickly degraded during the experiments. A comparison between photolithographic and the Enface patterning process is shown in Table 6.13. In the pattern transfer experiments using Enface, one single tool could be used to deposit at least 20 substrates which were subsequently used as basis of the assessment.

As can be seen in Table 6.13, the cost effectiveness of Enface process mostly comes from energy consumption and chemical usage. The energy consumption and the

chemical usage are reduced by more than 95 % and around 88 % respectively. The total cost to produce 20 pattern replications could be saved by around 67 %.

Table 6.13 Comparison between photolithographic patterning and Enface process on the assessment of energy consumption, chemical usage, and labour cost

Base: 20 patterned substrate	Photolithographic Patterning Process*	Enface Process
Energy Consumption		
- Clean room usage	17.60 kWh	0.88 kWh
- Patterning process	0.09 kWh	0.07 kWh
- Total	17.69 kWh	0.95 kWh
- Cost	£ 1.407	£ 0.076
Chemical usage		
- Photolithography (resist, developer, and stripper)	10.12 l	0.506 l
- Patterning process (nickel salts and additive))	5.25 kg	0.626 kg
- Cost	£ 773.95	£ 86.43
Labour Cost		
- Photolithography	4.00 man-hours	0.25 man-hours
- Patterning process	3.49 man-hours	4.39 man-hours
- Cost	£ 748.91	£ 458.89
Total Cost	£ 1,524.27	£ 545.39

* Data collected through a direct interview with clean room staffs at Newcastle University by Roy, S (2011)

Chapter 7

Simulation and Modelling of Current Distribution

7.1 Background

Obtaining deposit uniformity, particularly in the thickness and morphology, is a key issue in every application of electrodeposition^[259]. A demand for uniformity is even more crucial when the electrodeposition is used in electronics devices due to its strict requirements^[259]. As the electrodeposited metal morphology is greatly affected by a current distribution^[260, 261], it is important to understand how a deposit is distributed across the cathode surface^[259, 260]. The morphology of the deposit at different points may differ if the local current density is not evenly distributed^[259, 260]. Therefore, the calculation of current density distribution is an important consideration in designing electrochemical systems and analysing electrochemical processes to achieve optimum electrodeposit uniformity^[262, 263]. A highly efficient and low cost process also can be attained if the design of the electrochemical system is optimised^[259, 260].

In general, the current distribution in an electrochemical system is influenced by^[260]: (1) the cell geometry, (2) the conductivity of components, (3) the kinetics of the electrochemical reactions at electrodes, and (4) the mass transfer of reacting species. Current distribution is commonly classified into three different categories: primary, secondary, and tertiary distribution. The primary current distribution only considers the effect of the cell geometry and the electrolyte conductivity. If the effect of kinetics (activation overpotential) is incorporated in the calculation, secondary current distribution is obtained. The current distribution will be tertiary if all parameters are included in the calculation^[264].

The calculation of current distribution involves complex mathematical models and non-linear partial differential equations even for a simple electrochemical system^[260]. The complexity increases when complicated geometry and hydrodynamic parameters are involved^[260]. Empirical^[265] and analytical^[259, 261] methods have been used to determine optimum current distribution. However, more recently, numerical and computational methods are used^[259-265].

In this work, an investigation on current and potential distribution was required to determine electrochemical conditions that allow one to achieve selective deposition required for pattern transfer. A numerical model for simulation of current density of nickel patterns using the Enface system is shown here. The model was developed to investigate the secondary current distribution of nickel pattern transfer process using

Enface technique by assuming the kinetics of the process obeys Butler-Volmer model. The resulting data were used to understand the current distribution during Ni patterns transfer using Enface.

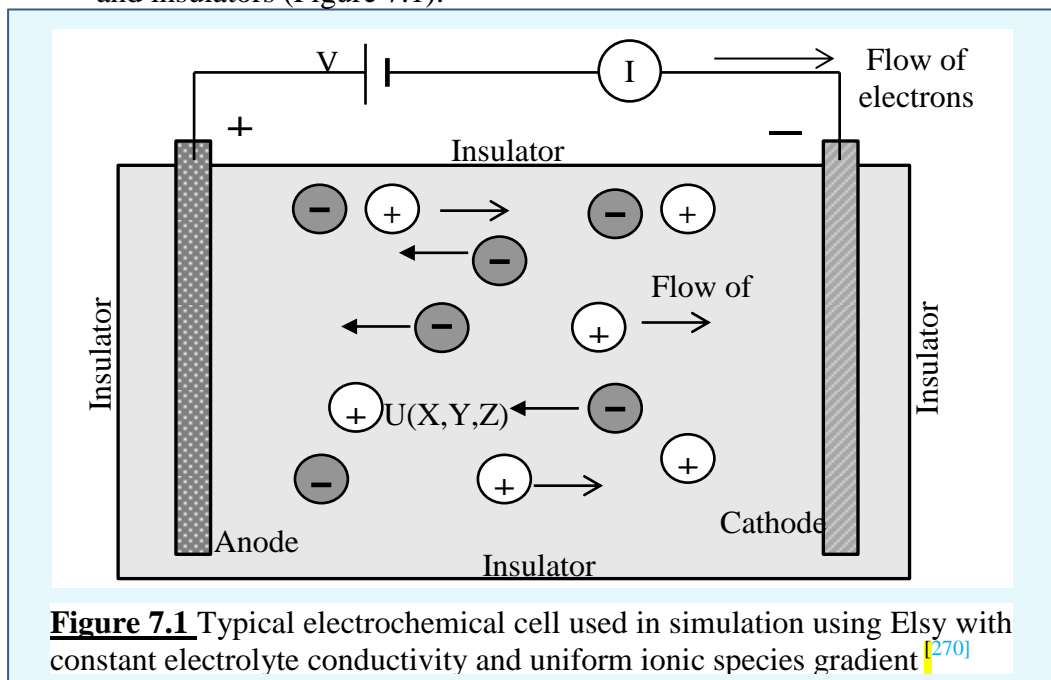
The modelling and simulation was carried out using a commercially available software named Elsy (ELSYCA NV) developed by Johan Deconinck *et al.* (1997) which can be found in a number of publications ^[266-269]. In this software, Laplace's equation in the potential model theory is solved by considering appropriate boundary conditions using the Boundary Element Method ^[266-269].

In the first stage, geometry of the electrochemical cell was designed and defined in the software to determine a cell configuration (either 2D or axy-symmetrical term) that represents the actual cell used in the experiments. Thereafter, modelling of current distribution using patterned anodes with different feature shapes and sizes was carried out. The current density distribution at the cathode and the shape development of the deposit on the cathode surface were studied.

7.2 Basic Principle of the Numerical Calculation using ElSy

In order to calculate the current density distribution in the software, several assumptions are taken into account ^[270, 271]:

1. The electrochemical system comprises an electrolyte surrounded by electrodes and insulators (Figure 7.1).



2. The arrangement allows the electrons flowing from external circuit to pass through the ionic solution which results in a transfer of charge. At the same time, a transfer of material due to the potential and concentration gradient

coupled with fluid mechanics take place. The passage of the current initiates electrochemical reactions to occur at the electrodes.

3. Overall mass transfer between the electrode surface and the solution is described by ionic species mobility, mass balance, current flow, and electro-neutrality.
4. Concentration gradient of the ions in the solution is uniform.
5. The conductivity of the electrolyte and the electrodes are constant.
6. Ions transport equation is developed for an infinitely dilute solution.

All factors influencing the process are taken into consideration in order to solve mass and charge transfer problems.

7.2.1 General Transport Equations for Multi-ion System in Dilute Solutions

7.2.1.1 The flux of an ionised species

Considering an infinitely dilute solution of n ionised species in unionised solvent at a constant temperature and pressure, the flux of an uncharged solute (i) caused by migration, diffusion, and convection can be expressed by ^[218, 270, 271]:

$$N_i = -z_i u_i F c_i \nabla \phi - D_i \nabla c_i + c_i v \quad (7.1)$$

flux migration diffusion convection

Where,

- | | |
|---|--|
| N_i is the flux of species i (mol/cm ² s) | z_i is a number of the charge |
| F is Faraday's constant, 96847 C/mol | c_i is the molar concentration, mol/cm ³ |
| $\nabla \phi$ is potential gradient, Volt | D_i is the diffusion coefficient, cm ² /s |
| v is the solvent velocity, cm/s | |
| u_i is the mechanical mobility of the species, cm ² mol/Js | |

7.2.1.2 Mass Balance for a small volume

A material balance for each species i in a small volume element is simply the accumulation of species i concentration for a time t as result of net input plus production from chemical reactions. The accumulation is given by ^[218, 270, 271]

$$\frac{\partial c_i}{\partial t} = -\nabla \cdot N_i + R_i \quad (7.2)$$

Accumulation Net input Production

Where, R_i is the production rate of species i , and $\nabla \cdot N_i$ is the flux divergence which is the net flux of species i per unit volume. The chemical reaction is usually neglected as

the electrochemical reactions are often restricted to a region in close proximity with the electrode surface.

7.2.1.3 Electroneutrality

In the bulk of electrolytic solution, the condition is electrically neutral; hence the equation of the electroneutrality is given by ^[218, 270, 271]:

$$\sum_i^n z_i c_i = 0 \quad (7.3)$$

Equation (7.4) is derived from Poisson's equation

$$\nabla^2 \phi = -\frac{F}{\epsilon} \sum_i^n z_i c_i \quad (7.4)$$

With ϵ is dielectric constant of the solution or the permittivity (Farad/m)

$\frac{F}{\epsilon}$ is very large (e.g. 1.392×10^{14} Vm/mol in aqueous solution), to separate a charge requires considerably large electric field. It also implies no free charge density is present in the system as being very quickly neutralised or flowing to the solution boundary due to the large electric conductivity. This condition is properly approximated by the electroneutrality term ^[218, 270, 271].

7.2.1.4 The Current Density

The motion of charged particles in an electrolyte results in the current flow. The overall current density is quantitatively defined as a sum of each individual flux multiplied by its charge per mol ^[218, 270, 271].

$$j = F \sum_i^n z_i N_i \quad (7.5)$$

With j is current density, mA/cm²

7.2.1.5 The continuity Equation

For electrochemical systems involving hydrodynamics of the electrolytic solution, the velocity of an incompressible fluid flow can be determined using the Navier-Stokes equation ^[218, 270, 271]

$$\rho \left(\frac{\partial v}{\partial t} + v \cdot \nabla v \right) = -\nabla p + \mu \nabla^2 v + \rho g \quad (7.6)$$

Where, ∇p : Hydrostatic pressure gradient ($kg/m^2 s^2$)

$\mu \nabla^2 v$: The viscous force ($kg/m^2 s^2$)

ρg : The gravity force ($kg/m^2 s^2$)

The density (ρ) and the viscosity (μ) of the electrolytic solution are constant

In a very small volume element of the electrolytic solution, the overall material balance is defined by:

$$\frac{\partial \rho}{\partial t} = -\nabla \cdot (\rho v) \quad (7.7)$$

If the density is assumed to be constant, the equation (7.7) can be shortened to the continuity equation

$$\nabla \cdot v = 0 \quad (7.8)$$

This equation solved together with equation (7.6) results in the velocity (v) at each point [218, 270, 271]

7.2.2 Derivative equations for the ions transport in dilute solution

The current density equation (7.5) can be expressed in terms of diffusion, convection, and migration by substituting equation (7.1) to equation (7.5) [218, 270, 271].

$$j = -F^2 \sum_i^n z_i u_i c_i \nabla \phi - F \sum_i^n z_i D_i \nabla c_i + F v \sum_i^n z_i c_i \quad (7.9)$$

Considering the electroneutrality condition (equation (7.3)), and the electric conductivity (κ , S/m) of the solution ($1/\Omega$), where

$$\kappa = F^2 \sum_i^n z_i u_i c_i \quad (7.10)$$

The current density equation is simplified to

$$j = -\kappa \nabla \phi - F \sum_i^n z_i D_i \nabla c_i \quad (7.11)$$

A combination of equation (7.1) and (7.2) leads to a more comprehensive formula of the material balance. With an assumption of no homogeneous chemical reaction in the bulk of solution, the transport of material and charge in the infinitely diluted solution can be written as:

$$\frac{\partial c_i}{\partial t} + v \cdot \nabla c_i = z_i F \nabla \cdot (u_i c_i \nabla \phi) + \nabla \cdot (D_i \nabla c_i), i = 1 \dots n \quad (7.12)$$

$$\sum_i^n z_i c_i = 0 \quad (7.13)$$

7.2.3 Applications of Potential-Theory Model

In a well agitated electrochemical system runs at steady state condition with an excessive supporting electrolyte for increasing the electrolyte conductivity, several implications can be drawn ^[218, 270, 271]

- The time-dependent term can be excluded from equation (7.12) due to the steady state condition.
- The flux of the electro-active species (i) can be ignored as the electrolyte containing excessive supporting solution.
- When forced convection stirring becomes dominant, then concentration gradient can be excluded.

Therefore, the current density equation can be rewritten as

$$j = -\kappa \nabla \phi \quad (7.14)$$

And equation (7.12) can be simplified to

$$\nabla^2 \phi = 0 \quad (7.15)$$

Equation (7.15) is popular as Laplace's equation.

This simplified potential model is solved by Elsy using the Boundary Element Method (BEM) with boundary conditions described in the following section.

7.2.4 Boundary Conditions

7.2.4.1 Electrodes

An electrochemical reaction takes place on an electrode surface at a particular rate is driven by charge transfer overpotential. The overpotential is expressed by the following equation ^[218, 270, 271]

$$\eta = V - \phi - E_e = f(c_0, j_n) \quad (7.16)$$

With V is metal potential (Volt), ϕ is solution potential at close proximity to the electrode, E_e is equilibrium potential and c_0 is surface concentration of the species.

In the electrochemical kinetics, the overpotential relates to the current density by Butler-Volmer equation ^[218, 271]

$$j = j_0 \left[\exp\left(\frac{\alpha_A n F \eta}{RT}\right) - \exp\left(\frac{-\alpha_C n F \eta}{RT}\right) \right] \quad (7.17)$$

A linear relationship of j - η is obtained for small value of the overpotential, whereas at large value of η , one of the exponential becomes negligible.

7.2.4.2 Deposition at Electrodes

Using Faraday's law, the amount of deposited material on the electrode can be calculated. The thickness of the deposit (h) for a deposition time of Δt is calculated by the following equation [218, 270, 271]

$$h = -\frac{\phi M}{z F \rho} j \Delta t \quad (7.18)$$

Where M is atomic weight of the metal deposited (mol/g) and ϕ is the efficiency of the process or the cathodic current.

7.2.4.3 Insulating walls

The wall of the electrochemical cell including the gas/air above the electrolyte is considered as insulators. As insulating materials, the current cannot pass through them. As consequence, the overall current density at any points on the insulator is equal to zero [218, 270, 271].

$$j_y = j \cdot 1_y = -\kappa \nabla \phi \cdot 1_y = -\kappa \frac{\partial \phi}{\partial y} \quad (7.19)$$

$$\frac{\partial \phi}{\partial y} = 0 \quad (7.20)$$

With y is normal distance from the surface

7.3 Method of Solution

In the Elsy software, the electrochemical cell is visualised as a closed system consisting two electrodes and insulators represented by geometrical points and lines. The lines were divided into a number of elements with a maximum ratio of elements of two adjacent lines was set to be 5. In this simulation, the cathode and the anode were set at 60 and 30 elements respectively as using too high number of elements led to non-convergence calculation due to too small mesh spacing. Even though to some extent, a better result of simulation may be obtained at higher number of elements, the results using > 60 cathode elements differed by $< 1\%$ at all cathodes. Thus 60 elements sufficed for the simulation.

The boundary conditions of the electrochemical cell during electrodeposition process must be defined in order to solve the system of modelling equations. At the walls defined as insulators, the ion flux and the current was set equal to zero. At the cathode surface, where electrochemical reactions take place, the current and ion flux were set to follow Butler-Volmer equation model. This kinetic parameter was

determined experimentally. The conductivity of the solution must be known which was also determined experimentally.

The result of the computation was obtained if a convergence criterion was attained. Convergence was achieved when the input and output current in the calculation of the cell modelling were identical. In this simulation, the convergence of the current density calculation was achieved at a condition where the current residual reached a value of $< 0.001 \text{ mA/cm}^2$. The convergence was achieved within 7 iterations (at maximum number of iterations 20).

7.4 Kinetic parameters

Kinetic parameters of nickel electrodeposition were experimentally determined using the standard three-electrode cell (Figure 4.1) with accompanying apparatus and procedure comprehensively described in chapter 4. The kinetic parameters of the system have been analytically and graphically determined as well as compared to other data in literature as have been discussed in chapter 5 section 5.3.

The parameters used in this simulation listed in Table 7.1 are those obtained by a graphical method as has been thoroughly discussed in chapter 5 section 5.4. The Tafel slope and the exchange current density were obtained from the graph in Figure 5.7; whilst the cathodic charge transfer coefficient was calculated based on the Tafel slope using equation 3.25 (see Chapter 5 section 5.4). The physical properties of the electrolyte including the temperature, the pH, and the conductivity were experimentally measured as has been presented in Table 4.2 Chapter 4 section 4.1.

Table 7.1 Physicochemical properties and kinetic parameters of the electrolyte used in micropattern transfer process simulations. κ is the measured electrolyte conductivity, j_0 is the calculated exchange current density, and α_c is the calculated cathodic transfer coefficient.

Electrolyte and Substrate	T (°C)	pH	κ (S/m)	$D_{Ni^{2+}}$ (cm ² /s)	Tafel Slope (mV/dec)	j_0 (mA/cm ²)	α_c
0.19 M Ni(SO ₃ .NH ₂) ₂ copper	20 ± 2	6.70 ± 0.22	2.19 ± 0.06	7.00E-06	159	3.16E-04	0.37

7.5 Reactor Configuration

In order to simulate our experiments, the geometry of electrochemical reactor in the modelling had to be identical to the reactor used in the experiments. The electrochemical cell configuration used in the nickel electrodeposition experiments is shown in Figure 7.2 (a) equipped with electrode diameter of 10 mm and 20 mm holder diameter. The red dash-line represents the Elsy reaction system. To perform the simulation, the Elsy software provides two possible reactor geometries e.g. 2D and axy-symmetrical models. Figure 7.2 (b) shows the 2D reactor geometry and the reactor shape (b') represented by the geometry. To obtain the axy-symmetrical model, the original cell orientation was rotated by 90° clockwise. The axysymmetrical reactor geometry and the representing shape are shown in Figure 7.2 (c) and (c') respectively. The dimension of the reactor models was proporsionally adjusted.

Considering the actual reactor geometry used in the experimental work, the axy-symmetrical configuration might be the better option as it fits the actual shape and geometry of the original cell. However 2D was preferred due to its practicality for pattern transfer simulation. Therefore, in the first stage of the simulation, the current density distribution in the 2D was compared to the axy-symmetrical to see whether similar current distributions along the electrode were produced. If so, the 2D model sufficed to represent the actual cell geometry and could be used for further simulation.

The reactor geometries (2D and axy-symmetrical model) were defined into the Elsy software using parameters representing their dimensions including the interelectrode gap of 0.3 mm. The simulations were carried out for an electrolyte conductivity of 2.19 S/m corresponding to the conductivity of the electrolyte used in the experimental work i.e. 0.19 M nickel sulfamate. In this stage, a primary current distribution was employed to define the electrode kinetics.

The geometry of the electrochemical reactor in Figure 7.2 (b) and (c) were visualised in the software by geometrical points and lines. Each line was divided into a number of elements. Every line also had to be specified either as an insulator or an electrode in order to declare where Ni deposition could proceed.

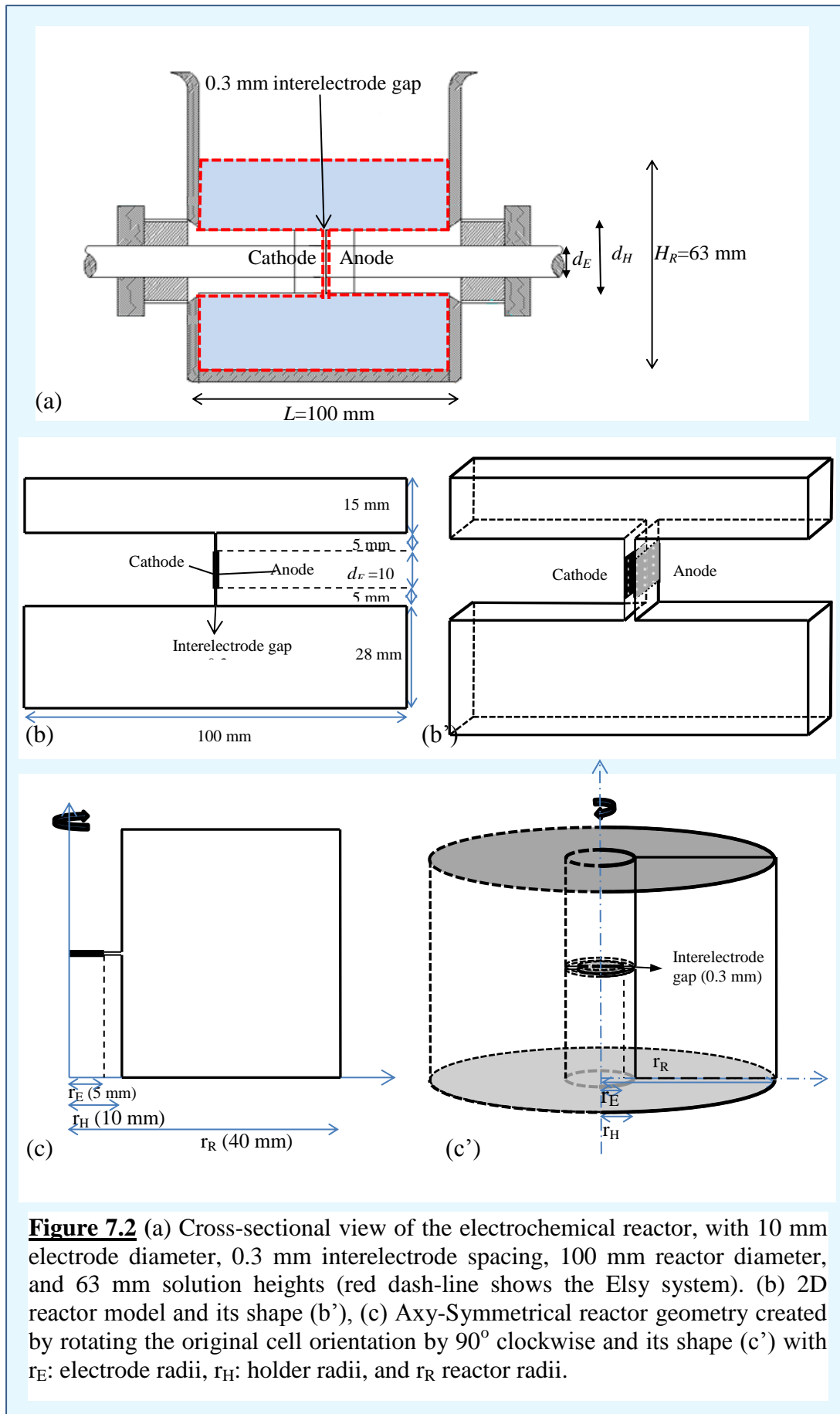


Figure 7.2 (a) Cross-sectional view of the electrochemical reactor, with 10 mm electrode diameter, 0.3 mm interelectrode spacing, 100 mm reactor diameter, and 63 mm solution heights (red dash-line shows the Elsy system). (b) 2D reactor model and its shape (b'), (c) Axy-Symmetrical reactor geometry created by rotating the original cell orientation by 90° clockwise and its shape (c') with r_E : electrode radii, r_H : holder radii, and r_R reactor radii.

In order to thoroughly examine the current density distribution in the 2D configuration, calculations were performed with different sizes of electrode (d_E) with a constant value of electrode holder size (d_H), reactor height (H_R , height of filled section) and length (L). Axy-symmetrical geometry calculations were carried out on various electrode radii (r_E) with a constant value of r_H (radius of holder) and r_R (reactor radius). A summary of the electrode sizes is presented in Table 7.2.

Table 7.2 Electrodes and holders size of electrochemical cell used in the simulation

2D model		Axy-symmetrical model	
Electrode size (d_E , mm)	Holder size (d_H , mm)	electrode radius (r_E , mm)	Holder radius (r_H , mm)
20	20	10	10
10	20	5	10
8	20	4	10
4	20	2	10

A comparison of the current density distribution across the cathode for 2D and axy-symmetrical reactor models is illustrated in Fig. 7.3. The current density is shown against normalized length x/L . It can be seen that the current density is uniform between $0.08 < x/L < 0.92$. It can be seen in Fig. 7.3, as expected in a parallel plane electrode configuration, the current density significantly increases at the edge of the cathode ^[218]. The pattern should be located on the area where uniform current density exists.

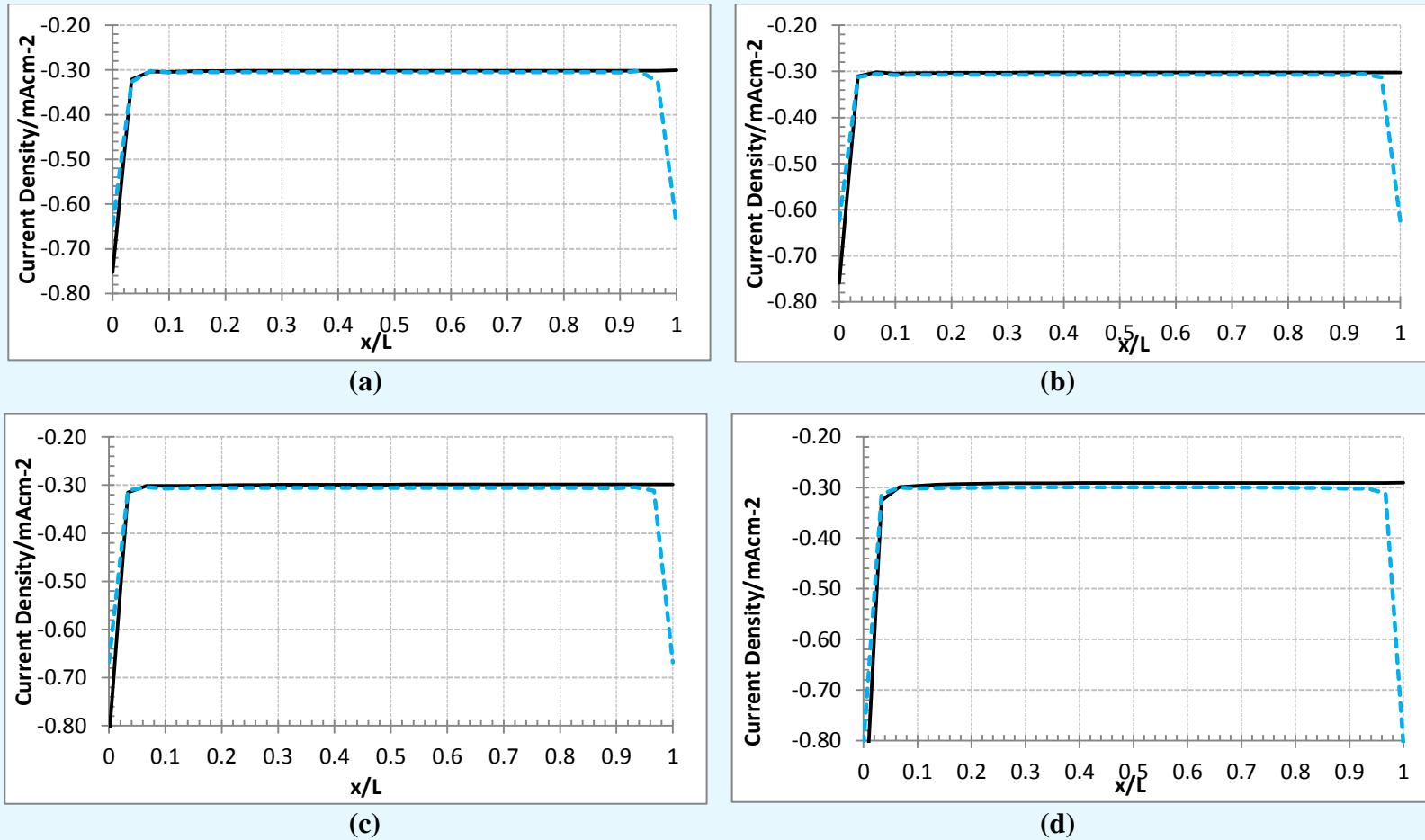


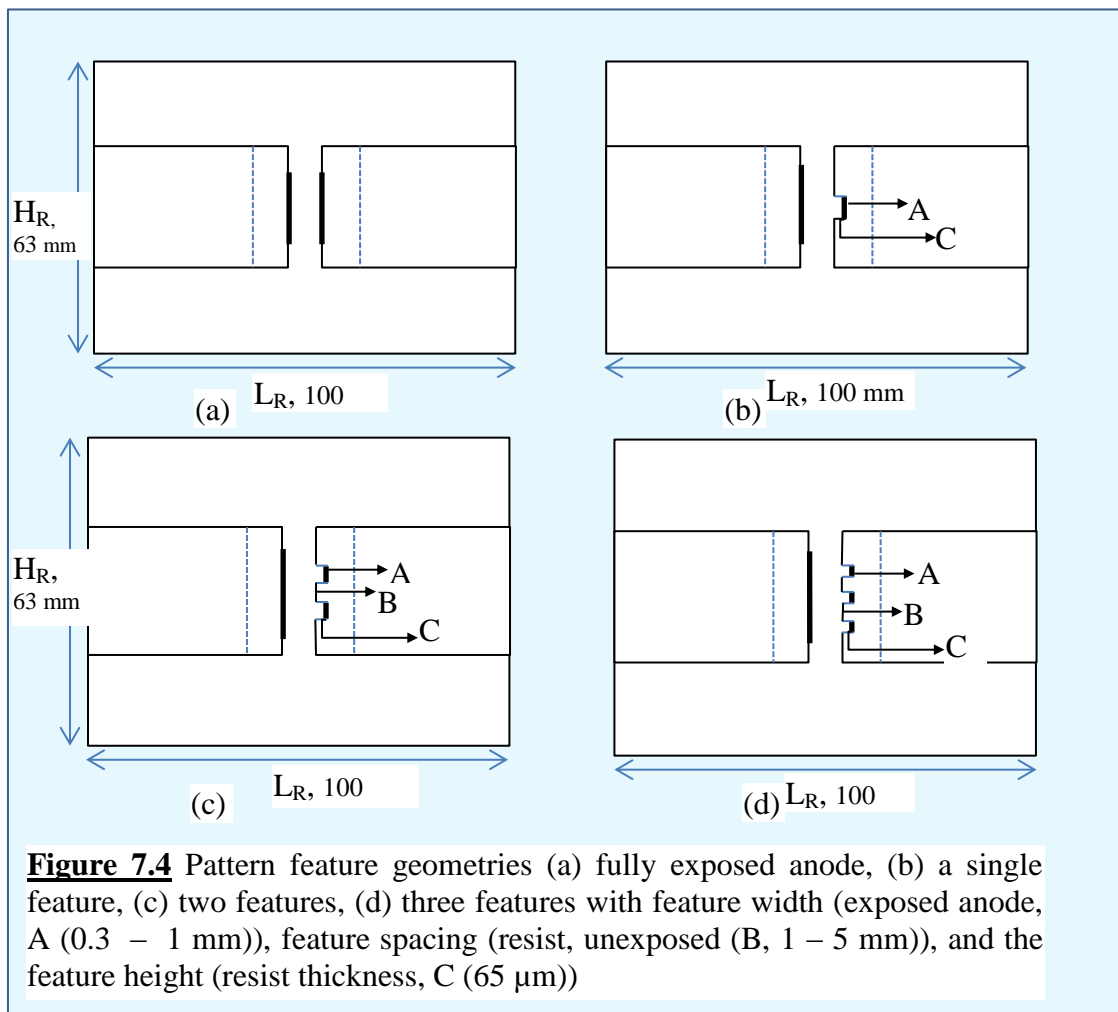
Figure 7.3 Current distributions across the cathode for 2D and axy-symmetrical configuration (a) $d_E=20$, $r_E = 10$, (b) $d_E=10$, $r_E = 5$, (c) $d_E=8$, $r_E = 4$, (d) $d_E=4$, $r_E = 2$, (— Axy-symmetrical, - - - 2D model)

Figure 7.3 shows the location of uniform current density along the electrode for the two different methodologies. The data show that the current is uniform over 80 % of the surface area. Patterns should be located at the middle of the anode for ensuring a uniform deposit thickness was achieved.

As observed in Figure 7.3, the current density using 2D and axy-symmetrical system overlay each other for all electrode sizes. The only different is that at the edge of the electrode, current density in the axy-symmetrical is higher by approximately 19 %. The difference may be due to the extra space around the electrode ^[218]. Based on the results, 2D configuration is sufficient for the pattern transfer simulation representing the actual reactor geometry.

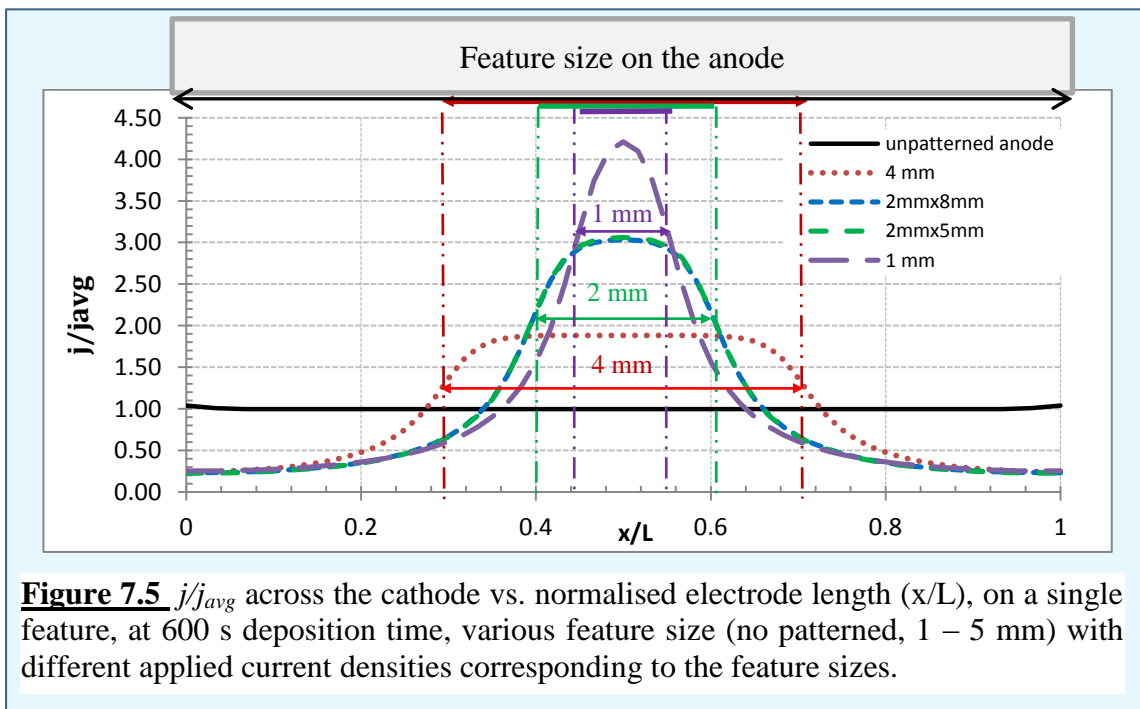
7.6 Pattern Transfer Modelling

Pattern transfer modelling was carried out for 1, 2, and 3 features configuration in 2D reactor geometry. The configurations of pattern features used in the simulation are shown in Figure 7.4. In this case, geometric parameters investigated were the feature width (A) and the feature spacing (B).



7.6.1 Simulation on a single feature

Pattern transfer simulation was initially carried out on anode with no pattern and with a single feature of different sizes i.e. 4 mm x 8 mm, 2 mm x 8 mm, 2 mm x 5 mm, and 1 mm x 5 mm. The simulations were performed for 600 s processing time at applied currents similar to those used in the experiments. Dimensionless current (j/j_{avg}) shown against normalised length (x/L) across the cathode are presented in Figure 7.5. j is the calculated current density and j_{avg} is the average applied current density. As can be seen, the current density across the cathode for an un-patterned anode shows a uniform distribution at 96 % electrode area. However, the uniformity decreases as the feature size of exposed part on the anode was reduced. At a cathode area directly facing to the feature (exposed area of anode), the highest value of the current density was observed. The shape of the current density distribution also changes forming a sharper peak as the feature size decreases. Figure 7.5 also confirms that the current densities on the feature increased with decreasing pattern feature area. As has been explained, the active area on the anode was used as a basis in the current density calculation as the active area of the cathode change over time. Therefore, the smaller active area on the anode due to the feature size increases the current density.



Even though a current spread is clearly visible, Figure 7.5 suggests that a selective deposition of nickel could be achieved, indicated by the difference between high and low current density. Nickel would be deposited on the cathode at a highest rate on the area directly facing the exposed part of the anode. On the other hand, a lower deposition rate was shown on the cathode area facing the covered part. This different

rate of deposition leads to pattern transfer and is expected to produce deposit shapes as illustrated in Figure 7.6. It can be seen that the deposited feature would be thicker at an area facing directly to the uncovered anode. Thinner deposit might be formed on the surrounding area due to the current dispersion. The smaller feature size, the sharper peak of deposit was obtained forming bell-shaped deposited feature.

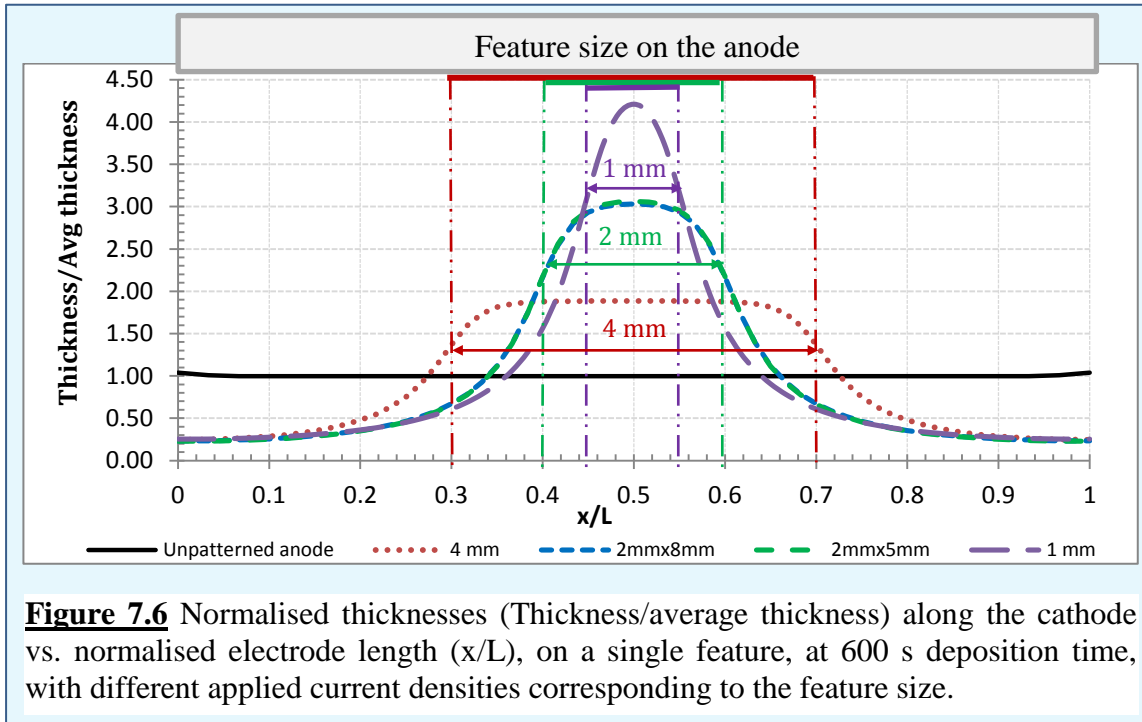


Figure 7.6 Normalised thicknesses (Thickness/average thickness) along the cathode vs. normalised electrode length (x/L), on a single feature, at 600 s deposition time, with different applied current densities corresponding to the feature size.

7.6.2 Simulation on 2 pattern features

Pattern transfer simulation was carried out on an anode with two parallel features of 0.3 mm width.

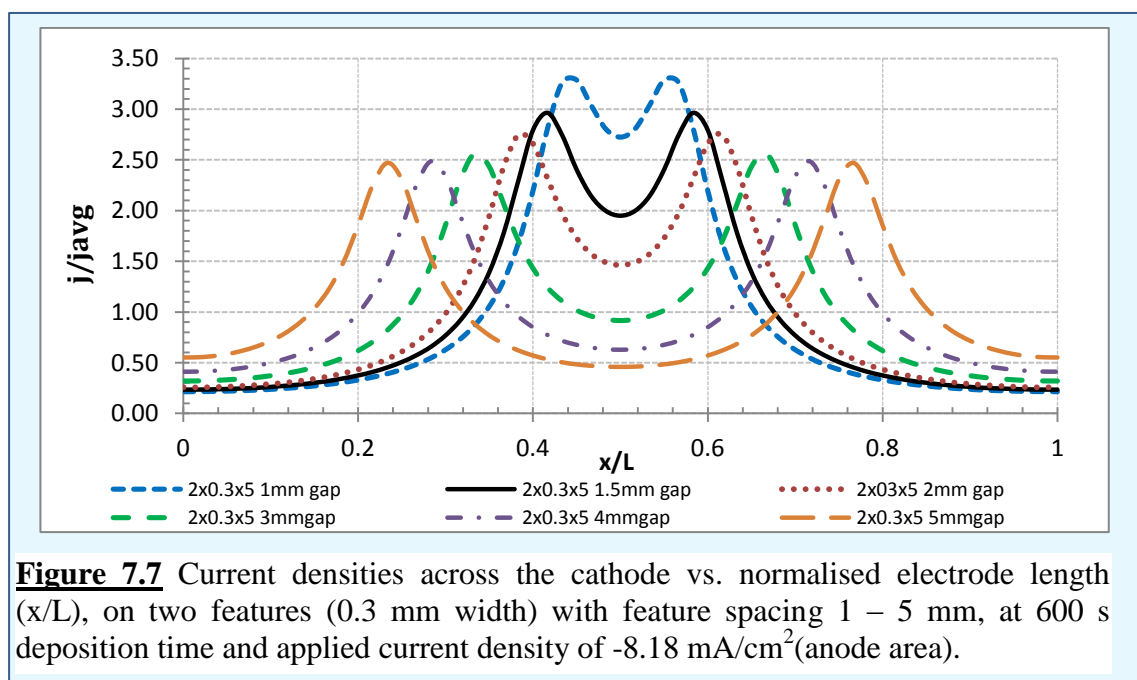


Figure 7.7 Current densities across the cathode vs. normalised electrode length (x/L), on two features (0.3 mm width) with feature spacing 1 – 5 mm, at 600 s deposition time and applied current density of -8.18 mA/cm^2 (anode area).

The features were located on the centre of the anode as described in Figure 7.4 (c). To investigate the effect of a space between the features (B), different spacing ranged between 1 mm and 5 mm were studied. The feature was kept at 0.3 mm width, whilst the distance between the features was increased from 1 mm to 5 mm with an insulator thickness of 65 μm and 0.3 mm interelectrode gap. The insulator thickness was set at 65 μm according to the actual thickness of kapton tape used in the fabrication of pattern features. The current density of -8.18 mA/cm^2 was applied to the system for 600 s deposition time. The cathode width was maintained to be constant at 10 mm. The current density distribution across the cathode for each feature gap is shown in Figure 7.7.

It can be seen from Figure 7.7 that two current density peaks are observed at all feature gaps of 1 – 5 mm indicating the metal could selectively be deposited. In this case, pattern transfer can possibly be achieved but the deposited features may overlap each other when the feature spacing is not sufficient. The selectivity of the deposition process increases with the increase of feature separation indicated by the larger ratio of lower current density with the two current densities peaks.

The results obtained in this works are in agreement with those obtained in previous simulation and modelling on copper etching ^[84, 270]. It was suggested that amongst three feature separation distances of 300, 500, and 700 μm being observed, the best pattern transfer (etching) selectivity was achieved at a feature gap of 700 μm for 100 μm feature width ^[84, 270]. This implied that acceptable feature distance to obtain pattern transfer was approximately 7 times as the feature width. In this work, selective electrodeposition was achieved fairly well at a feature spacing of $> 2 \text{ mm}$ which is about 7 times as the feature width of 0.3 mm as can be seen in Figure 7.7.

To see how the deposited feature shape and thickness grow at the feature separation length of 2 mm and 5 mm, pattern transfer simulations for 0.3 mm x 5 mm feature with these separation length were carried out at a current density of -8.18 mA/cm^2 and at various deposition times i.e. 100 – 600 s. The deposit shape evolution for the two parallel rectangular features of 0.3 mm x 5 mm at different processing times separated by 2 and 5 mm gap is presented in Figure 7.8 (a) and (b) respectively.

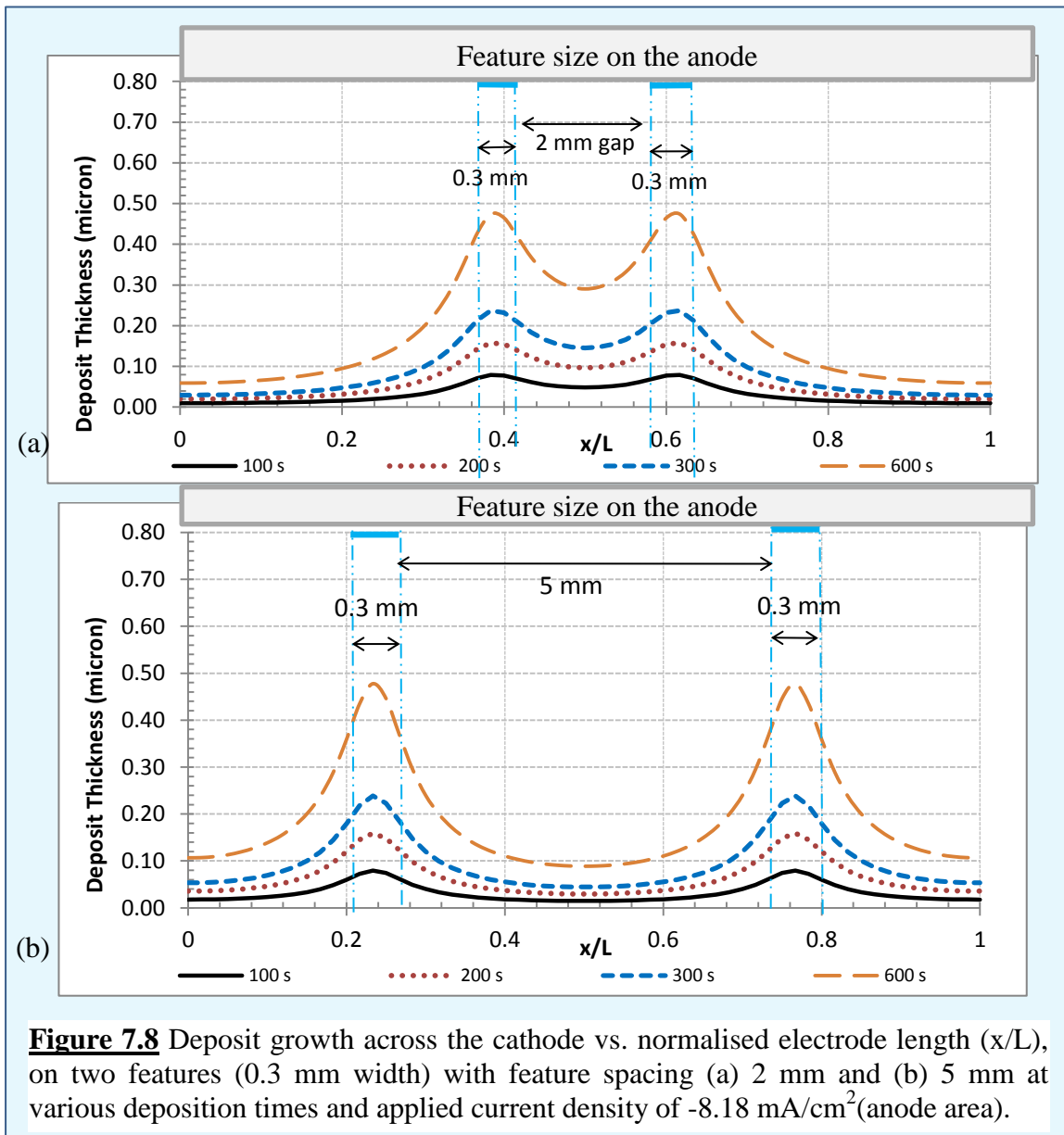


Figure 7.8 Deposit growth across the cathode vs. normalised electrode length (x/L), on two features (0.3 mm width) with feature spacing (a) 2 mm and (b) 5 mm at various deposition times and applied current density of -8.18 mA/cm^2 (anode area).

7.6.3 Simulation on 3 pattern features

The experiments of pattern transfer for three parallel features of 0.3 mm x 5 mm was carried out at feature separation distance of 1.5 mm and 2 mm as described in Figure 4.9 (a) structure 1. Current density distribution for the same configuration was simulated to compare with the experimental result. At first, the current distribution across the cathode was calculated for different deposition time i.e. 100 – 300 s and the result is shown in Figure 7.9

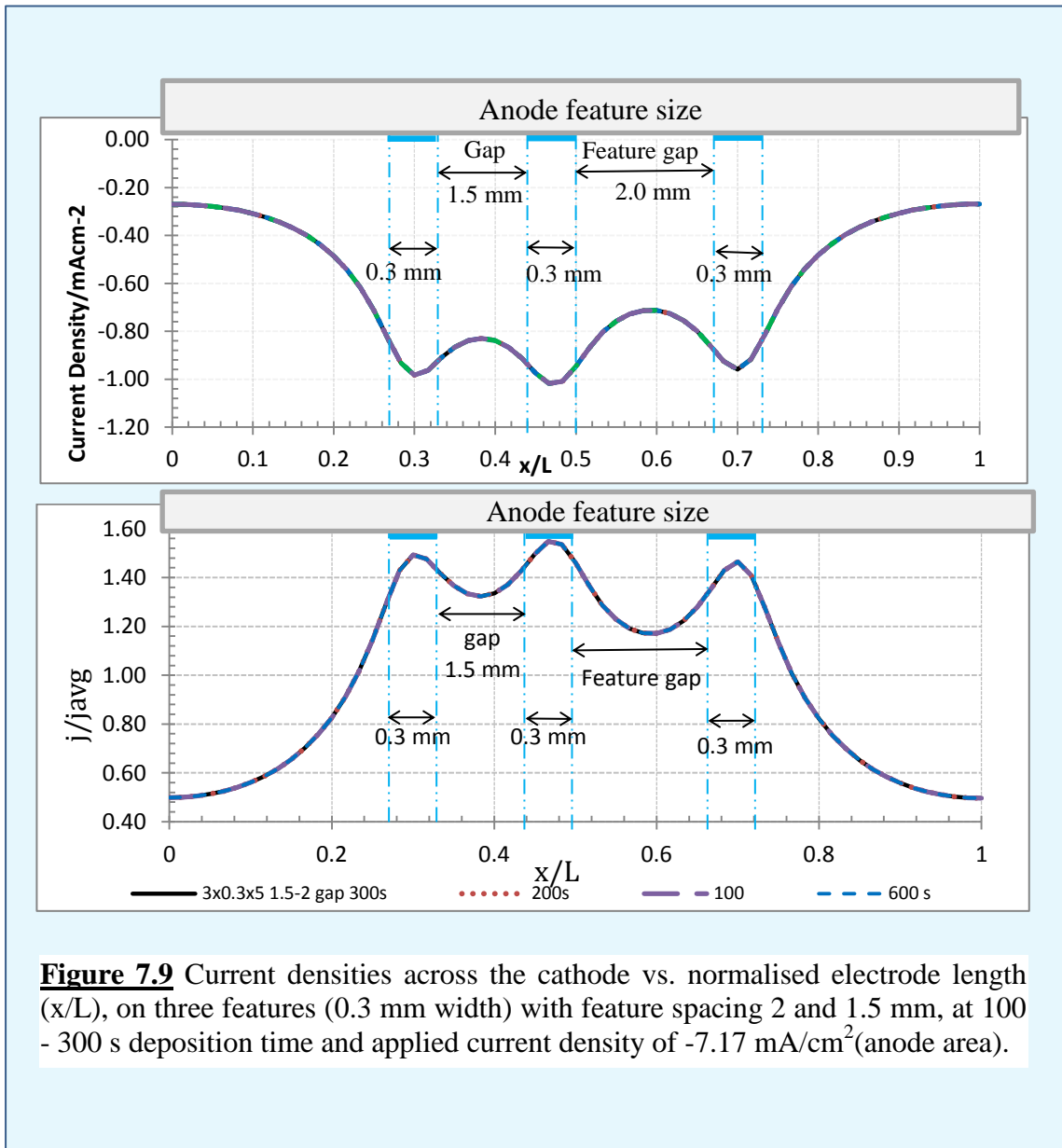
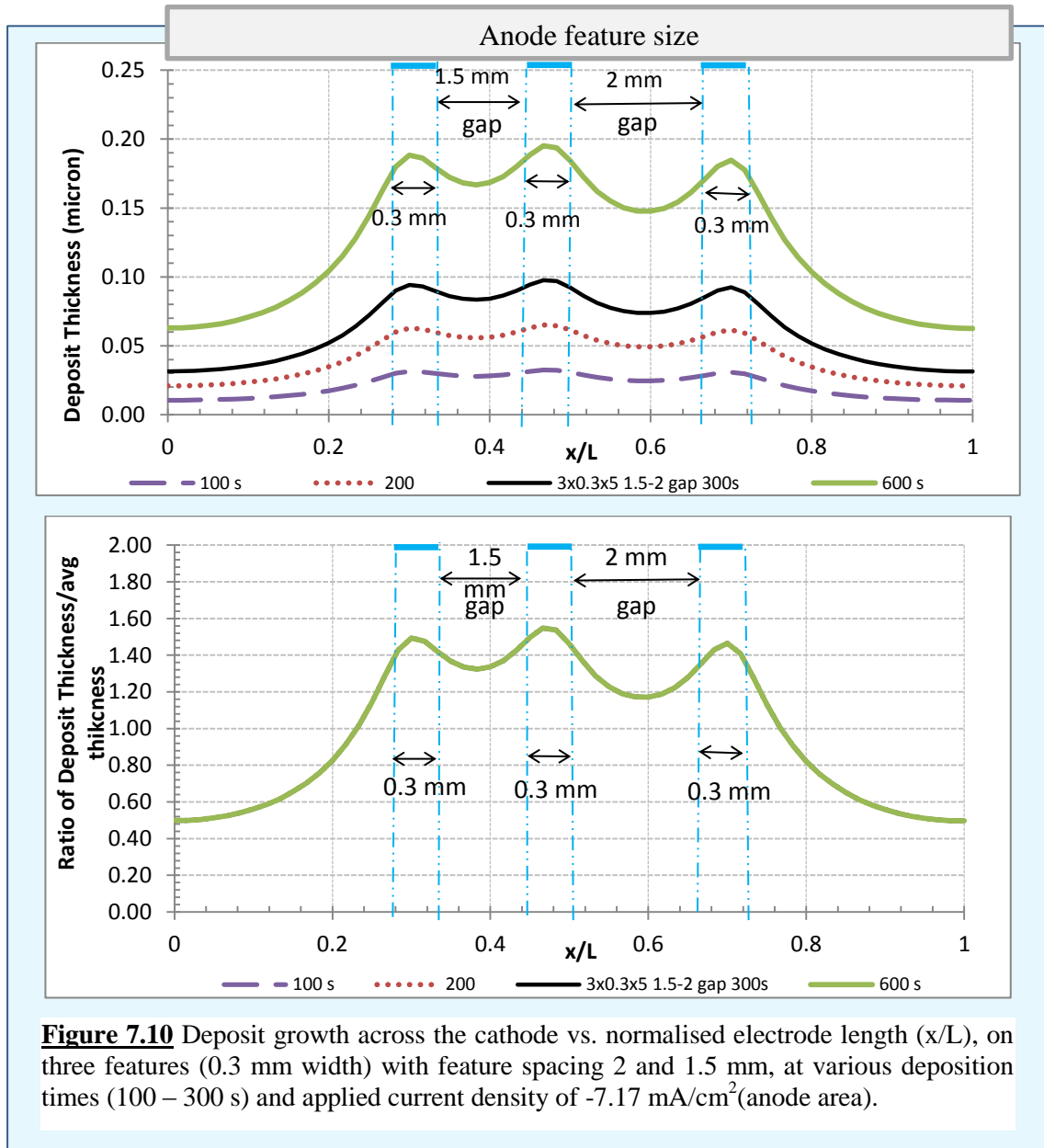


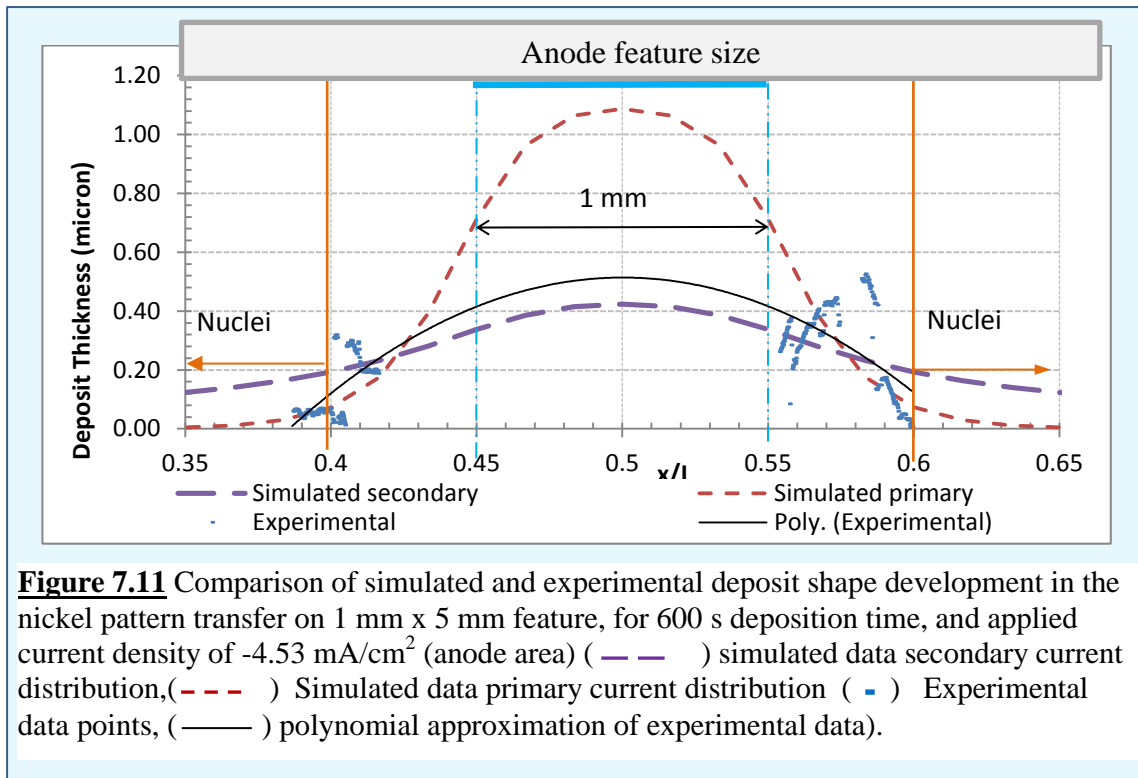
Figure 7.9 Current densities across the cathode vs. normalised electrode length (x/L), on three features (0.3 mm width) with feature spacing 2 and 1.5 mm, at 100 - 300 s deposition time and applied current density of -7.17 mA/cm^2 (anode area).

Small peaks and trough of current densities are observed, however, it is shown that almost the entire deposit grows at the same rate, which would lead to a single feature. Selective deposition is not possible in this case. As also shown in Figure 7.9, the current densities profile did not change with time which may be due to very slow deposit growth rate. As consequence, there was no significant change in inter-electrode gap and ohmic drop. The expected growth rate of the deposit is shown in Figure 7.10.

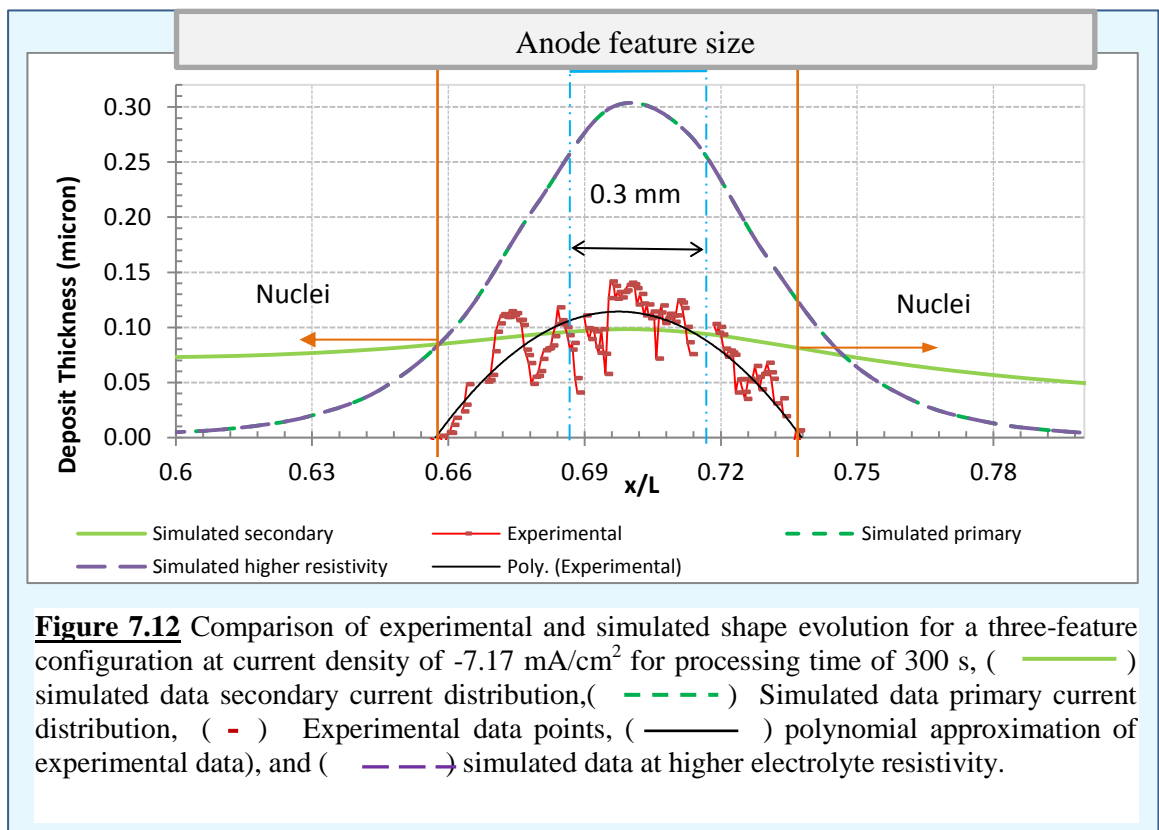


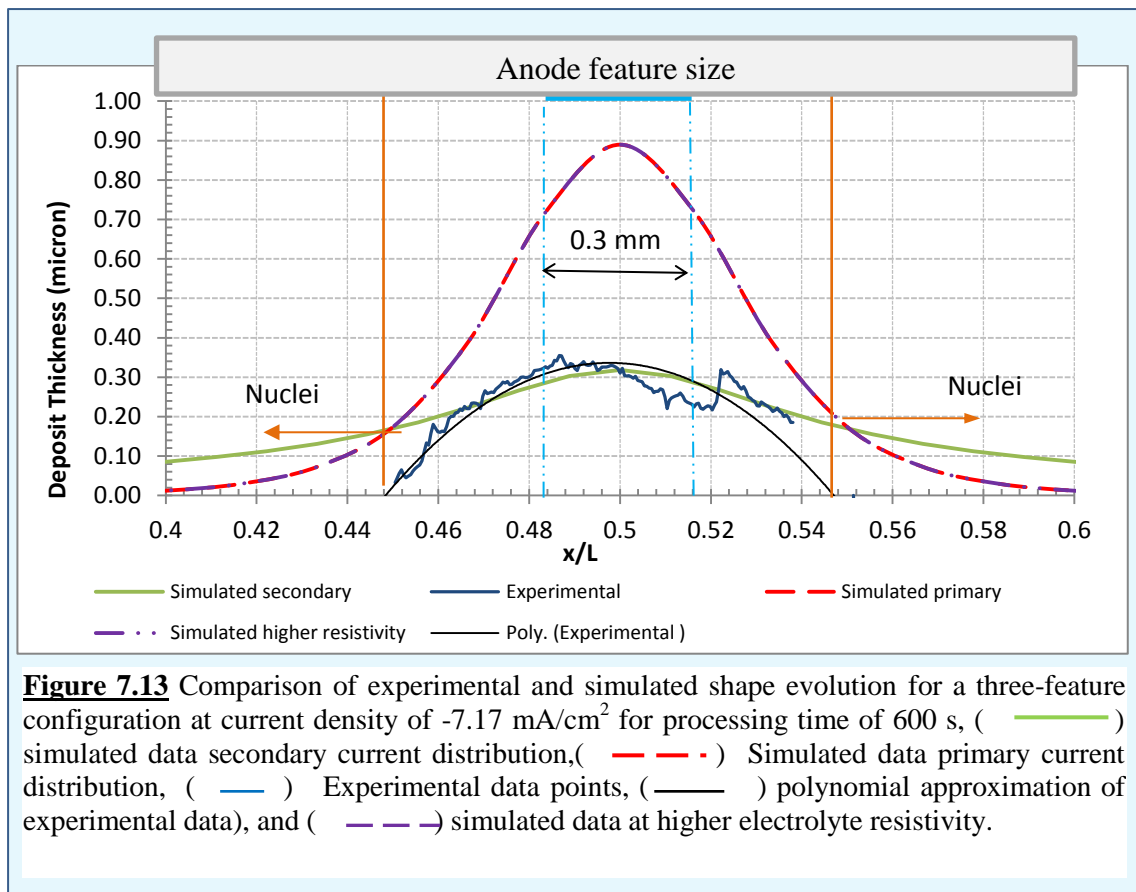
7.6.4 Comparison between Experimental and Simulated Results

The results of the simulation were verified by comparing the shape development of the deposit to the experimentally measured feature. The comparison was performed for a feature of 1 mm x 5 mm and the three-feature configuration. Figure 7.11 shows the comparison of deposit growth of simulated and experimental data for 1 mm x 5 mm feature at current density of -4.53 mA/cm^2 and 600 s processing time. Simulated data on primary current density is also included. As can be seen in Figure 7.11, the thickness and the shape evolution experimentally obtained is much better than that obtained in the simulation with secondary current distribution system. In particular, the experiment shows that the edge of the deposited feature is sharper than that predicted by simulation.



Even though selective deposition, as has been shown in the simulation, is not possible to be achieved in the case of three parallel features, pattern transfers were experimentally obtained. The comparison between simulated and experimental result for three-feature configuration obtained at a current density of -7.17 mA/cm^2 for deposition times of 300 s and 600 s are shown in Figure 7.12 and 7.13 respectively.



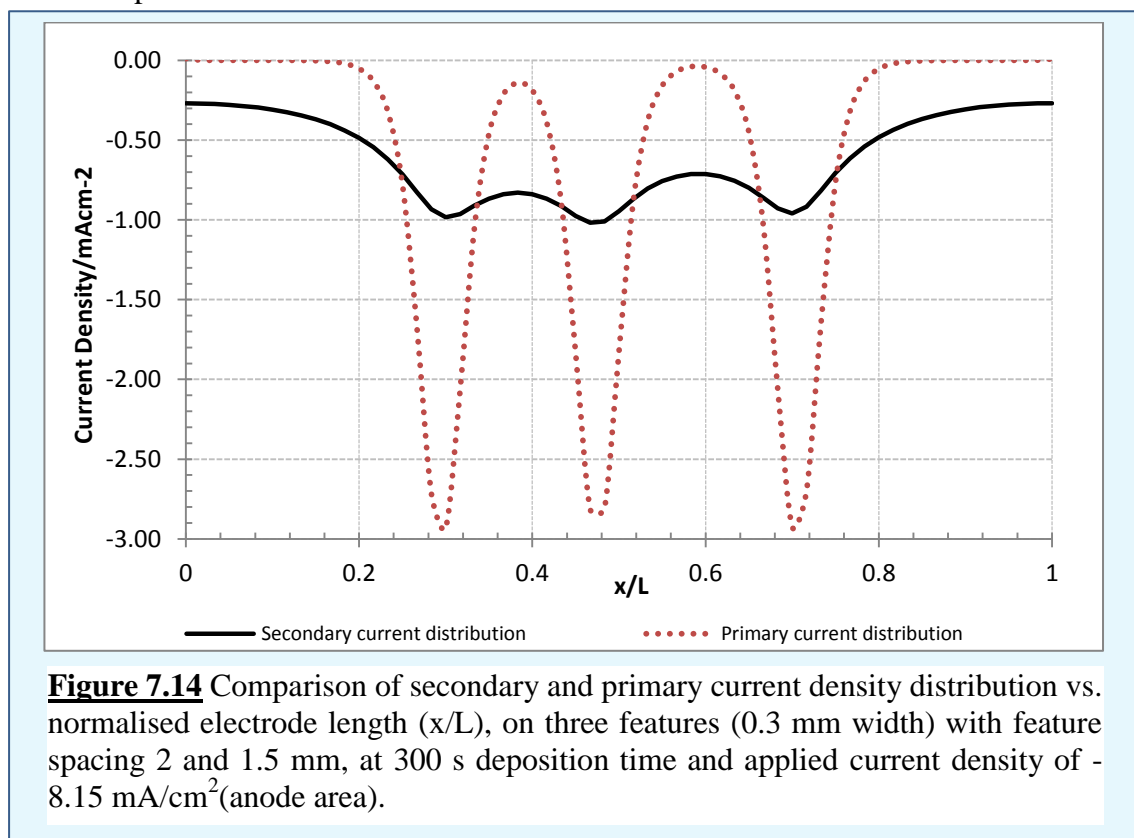


In the case of three parallel feature configuration as shown in Figure 7.12 and 7.13, similar results were obtained. Even though the thickness of simulated and experimental shows reasonable agreement, the shape of the deposit was significantly different. The shape evolution of experimentally deposited features is much better than the calculated as the edge of the deposited feature is sharper.

The comparison implies that the results of the experiments are consistently much better than those obtained in the simulation. One possible explanation for these results is that in the experiments, the low current density at area around the edge of the feature due to the current spread led to an initial nucleation process forming of a low density of nickel nuclei scattered around the feature. The low density nickel nuclei were not visually observed and were not possible to incorporate them in the surface profile measurement. Therefore, the deposited feature obtained from the experiments was sharper. This explanation is supported by the fact that nickel was detected at the area around the deposited feature as has been discussed in Chapter 6 section 6.4.2 illustrated in Figure 6.1.2 and 6.13.

7.7 Effect of Current Distribution

The result of current density distribution modelling and simulation, shown in Figure 7.14, indicates that at a condition when primary current distribution becomes predominant, the current spreading could be minimised leading to a more selective deposition. The primary current distribution occurs if the process is only determined by cell geometry and an electrolyte ohmic drop provided the kinetics of the electrochemical reaction is very fast so that can be neglected. However, in a real electrochemical cell, the kinetics of reaction is finite leading to current limitation. Therefore, the kinetics of the electrochemical reaction is usually used to define a boundary condition at the electrode process.



The primary current density distribution can be achieved at lower solution conductivity and smaller interelectrode gap^[36]. Although the use of pulse current plating can achieve primary current distribution^[272], Qi-Bai Wu *et.al* concluded that the current spreading was not significantly reduced by pulse plating^[36].

In the case of nickel electrodeposition process, the reaction of nickel reduction is well known to have a slow kinetics. Therefore, lowering the electrolyte conductivity and narrowing the interelectrode gap allowed one to achieve pattern transfer, however the deposited feature still significantly widened. This is one of possible explanations for the greater broadening of deposited nickel feature in this work compared to the deposited copper spreading carried out by Qi-Bai Wu *et.al*^[36].

Chapter 8

Conclusions

Since the standard photolithographic patterning method is a multi-step process, requires a clean room, and generates carbonaceous waste, “maskless” pattern transfer has gained more attention recently. Such a “maskless” pattern transfer process, Enface (Electrochemical nano and micro-fabrication by Flow and Chemistry), has been proposed which offers a possibility to achieve more sustainable process. Earlier studies of Enface have focused on the etching and the deposition of copper from dilute copper solutions under forced convection. This present work aimed to study the feasibility of nickel pattern transfer through electrodeposition without photolithography of substrate using Enface technology under stagnant condition. Nickel plating has been chosen due to its popular use in microelectronics, electroforming and other coatings. As nickel is typically plated from electrolytes containing high concentration of Ni(II) ions, it would be advantageous if nickel patterns could be deposited from electrolytes containing much lower concentrations of nickel ions which could also establish Enface as a resource efficient process.. Unlike copper deposition process which is a fast reaction and controlled by mass transfer, nickel plating is a slow reaction and controlled by a combination of mass transfer and kinetics, in conditions where Enface has never been applied before

The nickel pattern transfer using Enface technology has been demonstrated through several stages. Initially, the nickel electrolyte appropriate for Enface process has been developed and selected based on thermodynamics consideration and physicochemical properties recommended by previous studies. Electrochemical behaviour of the selected nickel electrolyte has been investigated by polarisation experiments in a standard three-electrode cell using RDE system. The polarisation experiments were also carried out in a three-electrode cell specifically designed for Enface process to see if the cell geometry affected the electrochemical characteristics of the electrolyte. Using the polarisation data, potential and current density ranges for nickel electrodeposition were identified. Thereafter, applied current densities for nickel pattern transfer were determined accordingly. Nickel pattern transfer experiments on various pattern feature sizes and structures including a manual feature of millimetre scale, manual features of micron scale, and photolithographed micron scale features have been performed. Deposited nickel features were successfully obtained and characterised comprehensively.

The following conclusions can be drawn from the present study:

- A 0.19 M nickel sulfamate ($\text{Ni}(\text{SO}_3\cdot\text{NH}_2)_2$) has been chosen for use in the electrodeposition of nickel pattern on copper substrates using Enface system. It has been shown that the electrolyte of 0.19 M nickel sulfamate can be used in nickel pattern transfer in Enface system, at a room temperature (20 ± 2 °C), and under stagnant condition. The electrolyte has advantages of cost effectiveness, lower metal ion concentration, neutral pH, non acidifying additive requirement, and room temperature operation. In addition, the electrolyte is stable for multiple uses ensuring distinctive advantages of Enface technology can be achieved.
- Polarisation data for the electrolyte of 0.19 M nickel sulfamate obtained from a standard three-electrode cell and RDE system confirmed that the electrodeposition of nickel takes place through multiple steps including a formation and adsorption of an intermediate ($\text{Ni}(\text{OH})^+$) and two consecutive single-electron transfers. The data at various RDE rotation speeds suggested that overall nickel electrodeposition reaction is controlled by a combination of kinetics and mass transfer.
- Based on the steady state polarisation data, kinetic analysis for nickel electrodeposition has been carried out by analytical and graphical methods showing a fairly well agreement results. In addition, the kinetic parameters obtained in this work are in the range of acceptable values in literature. Kinetics parameters of Tafel slope, cathodic charge transfer coefficient, and exchange current density for the nickel electrodeposition process in the electrolyte of 0.19 M nickel sulfamate have been found to be 159 mV/decade, 0.37, and 3.16×10^{-4} mA/cm² respectively.
- Polarisation experiments for the electrolyte carried out in Enface system suggested that potential-current densities behaviour was affected by the pattern feature area. Higher current densities were obtained at smaller feature area. Therefore it is necessary to determine potential and current density ranges where nickel deposition occurs for each pattern feature size by polarisation experiments. Reduction potential of nickel has been found to be in the range of -0.7 to -1.0 V with corresponding current densities are varied according to the feature sizes. These potential and current density ranges have been used to determine optimum applied current densities for each pattern feature size and structure.

- Pattern transfer of nickel using Enface system can be achieved by galvanostatic deposition method using the optimum applied current densities determined by polarisation data. Cell potentials during the galvanostatic pattern transfer processes were monitored. In the case of manual features the cell voltages were found to be in the range of -2.2 to -2.4 V prior to the process termination due to a substantial cell potential increase. The significant increase of cell voltage leading to the termination of the pattern transfer process was caused by hydrogen evolution that simultaneously occurs with nickel deposition forming entrapped gas bubbles within the narrow gap covering the entire electrode surface. In the case of photolithographed features, the cell voltages were monitored to be in the range of -2.15 to -2.4 V with no sudden increase of cell potential and deposition time limitation.
- In the case of manual features, at applied current densities lower than the optimum value, the cell voltages dropped to be below -2.2 V resulting in no pattern replication was obtained. Whilst, At higher applied current densities, the cell potentials were found to be exceeding -2.4 V leading to excessive gas bubbles evolution resulting in a considerable increase in the cell potential and a burnt deposited nickel. This shows potential and time thresholds for nickel pattern deposition with manually fabricated features.
- Nickel pattern transfer using Enface on millimetre scale of 1 mm x 5 mm feature size in the electrolyte of 0.19 M nickel sulfamate and room temperature (20 ± 2 °C) was successfully achieved at a current density of -4.53 ± 0.55 mA/cm². The broadening of deposited feature due to current spread was in the range of 148 ± 0.20 % to 198 ± 0.56 %. The thickness growth rate of nickel deposition was 0.06 µm obtained at cathodic current efficiency between 57.12 % and 83.79 %. \in this case, the deposition time of 480 s has been shown to have highest cathodic current efficiency.
- Nickel pattern transfer using Enface on manually fabricated microscale pattern features was achieved with two different feature structures and area at current densities of -7.17 ± 0.92 mA/cm² (for structure 1) and -7.59 ± 0.92 mA/cm² (structure 2). The deposition time was set to be 480 s, however due to the issue of gas bubbles and the sudden increase of cell potential, the pattern transfer experiment was terminated at 300 s and 125 s respectively. The thickness of the

deposited nickel was in the range of 0.165 to 0.377 μm obtained at current efficiencies of 89.55 – 90.88 %.

- In comparison with their original size, the degree of broadening of deposited features of smaller pattern feature has been found to be greater. For instance, on manual features of millimetre scale the spread of deposited features was about 148.30 – 198.07 %, whereas on micrometre scale features, the broadening was 278.57 – 366.67 % even at shorter deposition time. In addition, the deposited features have also been shown to widen with increasing deposition time as the spread was around 174 -213 % at 125 s and about 279 – 367% at 300 s deposition times.
- Nickel pattern transfer with photolithographed microscale pattern features using a photoresist was achieved. However, further investigations could not be performed as the photoresist was quickly degraded during the experiments due to the entrapped hydrogen gas bubbles leading to the increase of pH in the area near the surface. The photoresist may become soluble in the alkaline environment
- The deposited features have been shown to be elliptical shape showing around their edges, whilst the surface profile across the width is a bell-shaped. The elliptical shape is indicative of non-uniform current distribution along the feature edge, whereas the bell-shaped profile indicates that the current distribution across the width is not uniform too. Therefore, based on the deposited feature dimension of length and width coupled with the thickness determined according the bell-shaped peak, the volume and the amount of deposited nickel can be well estimated using a half ellipsoid model.
- The deposited nickels have been shown to be a bright metallic appearance on most area of the features. However, the deposited feature at the edges of the features exhibit burnt deposited nickels with dark and black colour. This is thought due to non-uniform current distribution across the feature width leading to an inclusion of impurities as at lower current density more impurities are adsorbed. EDX analysis on the edge of the feature which appeared as burnt deposit confirmed that beside nickel and copper, sulphur and oxygen were also present. This is indicative that impurities were adsorbed on to the deposited feature leading to black/burnt deposit at the feature edge.

- The morphology of the deposited nickel investigated by using an optical microscope and a low magnification SEM shows that the deposited nickels were thin and rough due to the deposition time limitation and the entrapped gas bubbles. However, further investigation with higher magnification SEM on an area with nickel deposit indicates that the deposit was relatively dense and homogeneous. So if the problem of entrapped gas bubbles can be overcome, the entire deposited nickel surface would be smooth, dense, and homogeneous with uniform thickness.
- Deposited nickel appearance in 3D obtained by an optical profilometry has revealed that nickel nucleation occurs to form nickel nuclei at the area around the feature during pattern transfer process due to current spreading. As confirmed by EDX elemental mapping analysis, nickel was found at the area around the deposited feature which is thought as nickel nuclei possibly formed due to the current spread.
- EDX and XPS analysis confirmed that the deposited features were metallic nickel, however some impurities i.e. sulphur and oxygen were found to be present on the deposited nickel at the feature edge. XPS scan identified the presence of nickel hydroxide and oxide on the deposit surface. The hydroxide was formed during pattern transfer process and the oxidation of nickel takes place when in contact with oxygen in open air. XPS measurement also confirmed that copper did not diffuse through the nickel layer immediately after the sample was obtained. The diffusion of copper through nickel layer occurs with increasing time and is accelerated at higher temperature. .
- Modelling and simulation of Enface process can be carried out in 2D geometry representing the actual electrochemical cell. The feature has to be located on the centre of the electrode to ensure uniform current distribution is achieved. The simulation confirmed that the calculated current densities increase with decreasing feature size. The current distribution across the feature during nickel pattern transfer experiment has been explained by the result simulation. Non uniform current distribution across the width was observed with the highest current density is at the centre of the feature and the lowest is at the feature edge.

- The simulation showed that selective nickel electrodeposition could be achieved on a single, double, or three parallel features. However, current spread and deposited feature overlapping may occur if the feature spacing is not maintained sufficiently. In this work, the feature gap has to be maintained by about 7 times greater than the feature width to achieve fairly well selective electrodeposition.
- Based on the comparison of thickness and shape evolution, the results of the experiments are consistently much better than those obtained in the simulation as the experimental deposited feature has a sharper edge which may be due to an increase of ohmic drop caused by gas bubbles leading to primary current distribution.
- Ultrasound is a potential agitation method in nickel pattern transfer to eliminate gas bubbles problem, as has been demonstrated in the preliminary experiments. However, small pits were observable on the deposited nickel under ultrasound agitation at 18 and 26 W/m² power density which can be linked to cavitation bubbles from the ultrasonic wave.

Chapter 9

Future work

The most significant problem encountered to nickel pattern transfer process using Enface was excessive hydrogen evolution leading to entrapped gas bubbles. This has been demonstrated to be detrimental to the electrodeposition process, the nickel pattern deposit, and the photoresist. Finding a technique to minimise the effect of the gas bubbles is crucial in order to obtain good pattern deposit and to fully achieve the advantages of Enface process. Based on this, ultrasound has been shown to be able to potentially diminish the effect of the entrapped gas bubbles; however pattern transfer experiments under ultrasound agitation with 18 W/m^2 and 26 W/m^2 power densities showed that the cavitation bubbles and the pressure of the ultrasonic wave were harmful to the nickel deposit and the photoresist. Therefore, an optimisation of ultrasound agitation in term of power density use and time arrangement is vital in order to achieve a condition where the effect of gas bubbles, cavitation bubbles, and ultrasonic wave could be minimised.

The photoresist of AZ-5214E (AZ Electronic Materials) with a $0.8 - 2.4 \mu\text{m}$ thicknesses used in the photolithographed features was observed to rapidly degrade and damage during the process due to the entrapped gas bubbles, cavitation bubbles, and ultrasonic wave. As a result, pattern replications were not possible to obtain and the multiple uses of the tool could not be achieved. Therefore, in order to fully gain Enface distinctive advantages, it is necessary to select the most appropriate photoresist type, to optimise thickness and the reliability of the photoresist.

It has been demonstrated in nickel pattern transfer experiments that the optimum applied current density depends on the feature size as an exposed active area on the anode, as a smaller pattern feature area required a higher applied current density. Polarisation experiments were required to determine the optimum applied current density for every single feature size which is not practical and will impede the application of this technique in wider context. Therefore, further investigation on the relationship between applied current densities and feature size and area to develop a formula is important for determining the optimum applied current densities for every single pattern feature size.

So far, electrodeposition using Enface have been performed for a single layer metal of copper (previous research) and nickel (this work). Study on metal multilayer using Enface has never been carried out. Metal multilayer is commonly used in various applications, for example, nickel is frequently used with palladium as a metal multilayer in microelectronics. In the last two decades, nickel/palladium bilayer has gained increasing attention for industrial application, particularly in microelectronic packaging. Nickel as an under layer of deposited palladium in a Ni/Pd leadframe packaging plays an important role of preventing diffusion of the substrate (copper or copper alloy), protecting the copper leadframe from oxidation and corrosion, and providing solderable and wire bondable surfaces. Therefore, it would be beneficial to explore the capability of Enface in dealing with electrodeposition of metal multilayer, i.e. Pd on deposited Ni.

REFERENCES

- [1] Franssila, S., (2010), Introduction to Microfabrication, 2nd Edition, John Wiley & Sons Ltd, West Sussex, United Kingdom.
- [2] Madou, M. J., (2002), Fundamental of Microfabrication: The Science of Miniaturisation, CRC Press, Boca Raton, FL; London
- [3] Anwar, K., Han, T., and Kim, S. M., (2010), Reversible Sealing Techniques for Microdevice Applications, Sens. Actuators B: Chem., doi:10.1016/j.snb.2010.11.002
- [4] E. Jung, A. Ostmann, D. Wojakowski, C. Landesberger, R. Aschenbrenner, and H. Reichl, (2003), Ultra-thin chips for miniaturized products, Microsystem Technologies, 9, 449–452.
- [5] Krebs, A., Knoll, T., Nußbaum, D., and Velten, T., (2012), Microsystem Technologies, Online First™, 9 April 2012.
- [6] Chen, Q., Li, G., Jin, Q.-H., Zhao, J.-L., Ren, Q.-S., and Xu, Y.-S., (2007) Journal of Microelectromechanical System, Vol. 16, No. 5.
- [7] Franke, T. A., and Achim Wixforth, A., (2008), Microfluidics for Miniaturized Laboratories on a Chip, ChemPhysChem, 9, 2140 – 2156
- [8] O'Donnell-Maloney, M. J. and Little, D.P., (1996), Microfabrication and array technologies for DNA sequencing and Genetic Analysis: Biomolecular Engineering 13 151-157
- [9] Tolfree, D. W. L., (1998), Microfabrication using synchrotron radiation, Rep. Prog. Phys. 61 313–351
- [10] Van Noije, W. A. M., Swart, J. W., Seabra, A. C., Verdonck, P., Zambom, L. S., Diniz, J. A., Doi, I., Zakia, M. B. P., Mansano, R. D., and Moreiral, L., (2001), Initiatives for Promotion of Microelectronics and Micro fabrication at Sao Paulo State Universities – Brazil, IEEE.
- [11] Wong, Hei, Filip, V., Wong, C. K., and Chung, P. S., (2006), Silicon Integrated Photonics for Microelectronics Evolution, Proc. 25th International Conference on Microelectronics (MIEL), IEEE.
- [12] Tennant, D. M., Koch, T. L., Mulgrew, P. P., and Gnall, R. P., Ostermeyer, F., and Verdiell, J-M, (1992) Characterization of near-field holography grating masks for optoelectronics fabricated by electron beam lithography, J. Vac. Sci. Technol. B 10(6).

-
- [13] Raja Jain, J., Ly-Gagnon, D-S., Balram, K. C., White, J. S., Brongersma, M. L., Miller, D. A. B., and Howe, R. T., (2011), Tensile-Strained Germanium-on-Insulator Substrate Fabrication for Silicon-Compatible optoelectronics, *Optical Materials Express* 1(6), 1121--1126
- [14] Xie, D., Jiang, Y., Pan, W., and Li, Y., (2003), A novel microsensor fabricated with charge-flow transistor and a Langmuir–Blodgett organic semiconductor film, *Thin Solid Films* 424 247–252.
- [15] Shim, J. H., Do, H., and Lee, H., (2010), Simple Fabrication of Amperometric Nitric Oxide Microsensors Based on Electropolymerized Membrane Films, *Electroanalysis* 22, No. 3, 359 – 366
- [16] Betancourt, T. and Brannon-Peppas, L., (2006), Micro- and nanofabrication methods in nanotechnological medical and pharmaceutical devices, *International Journal of Nanomedicine*:1(4) 483–495
- [17] Baudoin, R., Corlu, A., Griscom, L., Legallais, C., and Leclerc, E., (2007), Trends in the development of microfluidic cell biochips for in vitro hepatotoxicity, *Toxicology in Vitro* 21 535–544
- [18] Tadigadapa, S. A. and Najafi, N., (2003), Developments in Microelectromechanical Systems (MEMS): A Manufacturing Perspective, *Transactions of the ASME: Journal of Manufacturing Science and Engineering*, Vol. 125, 816-823
- [19] Grayson, A. C. R., Shawgo, R. S., Johnson, A. M., Flynn, N. T., Li, Y., Cima, M. J., and Langer, R., (2004), A BioMEMS Review: MEMS Technology for Physiologically Integrated Devices, *Proceeding of The IEEE*, Vol. 92, No. 1,
- [20] A. Jebens, (2009), Economic Forecast: Facing the Perfect Storm, *Semiconductor International*, Reed Business Information (2009)
- [21] Doe, P. *Global MEMS/Microsystems markets and opportunities*, SEMI Emerging Markets (2007). accessed 30 September 2009, Available online: <http://www.electroiq.com/index/display/nanotech-article-display/341040/s-articles/s-small-times/s-volume-8/s-issue-3/s-columns-and-departments/s-news/s-global-mems-microsystems-markets-and-opportunities.html>,
- [22] Wolfe, D.B., and Whitesides, G.M., (2005), "Rapid Prototyping of Functional Microfabricated Devices by Soft Lithography", *Nanolithography and Patterning Techniques in Microelectronics*, Bucknall, D.G., Eds., Woodhead Publishing Limited.

-
- [23] SchÖnenberger, I. and Roy, S., (2005), Microscale pattern transfer without photolithography of substrates, *Electrochimica Acta* 51 pp. 809 – 819
- [24] Kathuria, Y. P., (2000) Metal rapid prototyping via a laser generating/selective sintering process, *Proceedings of the Institution of Mechanical Engineers, Part B: Journal of Engineering Manufacture* 214: 1
- [25] Frisque, G., R. Tejada, et al. (2000). "Modeling pattern transfer in ion-beam lithography masks." *Microelectronic Engineering* 53(1–4): 623-626.
- [26] Stengl, G. and Glavish, H. f., Ion beam lithography, US Patent No 4985634
- [27] Tandon, U. S. (1992). "An overview of ion beam lithography for nanofabrication." *Vacuum* 43(3): 241-251.
- [28] Brown, W. L., T. Venkatesan, et al. (1981). "Ion beam lithography." *Nuclear Instruments and Methods in Physics Research* 191(1–3): 157-168.
- [29] Vieu, C., F. Carcenac, et al. (2000). "Electron beam lithography: resolution limits and applications." *Applied Surface Science* 164(1–4): 111-117.
- [30] Chang, T. H. P. (1975). "Proximity effect in electron-beam lithography." *Journal of Vacuum Science and Technology* 12(6): 1271-1275.
- [31] Fujita, J., Y. Ohnishi, et al. (1996). "Ultrahigh resolution of calixarene negative resist in electron beam lithography." *Applied Physics Letters* 68(9): 1297-1299.
- [32] Doniavit, A., A.R. Mileham, and L.B. Newnes, (2000), *A systems approach to photolithography process optimization in an electronics manufacturing environment*. *International Journal of Production Research*, **38**(11): p. 2515-2528.
- [33] May, G. S. and Spanos, C. J., (2006) *Fundamentals of Semiconductor Manufacturing and Process Control*, pp. 34 -39, John Wiley & Sons, Inc. New Jersey
- [34] Pease, R.F. and Chou, S. Y., (2008), lithography and other patterning techniques for future electronics, *Proceedings of the IEEE*, 96 (2): 248 – 270
- [35] Leslie, T., W. Arden, et al. (1994). "Photolithography overview for 64 megabit production." *Microelectronic Engineering* **25**(1): 67-74.
- [36] Wu, Q.-B., T. A. Green, et al. (2011). "Electrodeposition of microstructures using a patterned anode." *Electrochemistry Communications* 13(11): 1229-1232.
- [37] Roy, S., (2007), Fabrication of micro- and nano-structured materials using mask-less processes, *journal of Physics D: Applied Physics*, 40 p. 413-416
- [38] S. Wolf and R. Tauber, (2000), "Silicon processing for the VLSI era", Vol. 1 2nd ed., Lattice Press

- [39] J. Helbert, (2001) "Handbook of VLSI microlithography", 2nd ed., Noyes Publications
- [40] Gates, B. D., Q. Xu, et al. (2005). "New Approaches to Nanofabrication: Molding, Printing, and Other Techniques." Chemical Reviews **105**(4): 1171-1196.
- [41] Rothschild, M. et al. (2003), Recent Trends in Optical Lithography Recent Trends in Optical, Lincoln Laboratory Journal, 14 (2): 221-236
- [42] Bhat, S. and Seshan, K.,(2001), Chapter 7: Contamination Control, Defect Detection, and Yield Enhancement in Gigabit Manufacturing, From Handbook of Thin Film Deposition Processes and Techniques: Principles, Methods, Equipment and Applications, Second Edition, William Andrew Inc.
- [43] Roy, D., Basu, P. K., and Eswaran, S. V. (2002), Photoresist for Microlithography, Resonance (July 2002)
- [44] Pimpin, A. and Srituravanich, W., (2012), Review on Mico- and Nanolithography Techniques and their Application, ENGINEERING JOURNAL , 16 (1): 37 – 55
- [45] Qin, D., Y. Xia, et al. (1998). "Photolithography with transparent reflective photomasks." Journal of Vacuum Science & Technology B: Microelectronics and Nanometer Structures **16**(1): 98-103.
- [46] Bhushan, B., (2007), Springer Handbook of Nanotechnology, 2nd Edition, Springer, New York
- [47] Craven, D. (1996), Photolithography Challenges for the Micromachining Industry, BACUS Symposium
- [48] L.T. Romankiw, E.J.M. O'Sullivan, in: P. Rai-Choudhury (Ed.), (1997), Handbook of Microlithography, Micromachining and Microfabrication, Vol. 2, SPIE Optical Engineering Press, Bellingham,.
- [49] Nguyen, N-T. and Wereley, S. T., (2002), Fundamentals and Applications of Microfluidics (Artech House microelectromechanical systems series) Artech House Inc. 80-82
- [50] Mattox, D. M., (2010), Handbook of Physical Vapour Deposition (PVD) Processing (Second Edition), Elsevier Inc., Oxford, UK
- [51] Mattox, D. M., (1973), Fundamental of Ion Plating, Journal of Vacuum Science and Technology, vol. 10, issue 1, p. 47
- [52] Teer, D. G., (1976), The energies of ions and neutrals in ion plating, J. Phys. D: Appl. Phys., Vol. 9, L187
- [53] Auciello, O. and A. I. Kingon (1992). A critical review of physical vapor deposition techniques for the synthesis of ferroelectric thin films. Applications of

- Ferroelectrics, 1992. ISAF '92., Proceedings of the Eighth IEEE International Symposium on Applications of Ferroelectrics.
- [54] Prodi-Schwab, A., T. L uthge, et al. (2008). "Modified procedure for the sol–gel processing of indium–tin oxide (ITO) films." *Journal of Sol-Gel Science and Technology* 47(1): 68-73.
- [55] Choy, K.L., (2003), Chemical vapour deposition of coatings, *Progress in Materials Science* 48 57–170
- [56] Yan, Xiu-Tian and Xu, Yongdong, (2010), *Chemical Vapour Deposition: An Integrated Engineering Design for Advanced Materials* 1st Edition, XIV, 327 p. 1-28. Springer-Verlag London Limited.
- [57] Creighton, J.R. and Ho, P., (2001), Introduction to Chemical Vapor Deposition (CVD), in *Surface Engineering Series Vol. 2: Chemical Vapour Deposition* edited by Park, J-H. and Sudarshan, T. S., ASM International USA,
- [58] Datta, M. and L. T. Romankiw (1989). "Application of Chemical and Electrochemical Micromachining in the Electronics Industry." *Journal of The Electrochemical Society* **136**(6): 285C-292C.
- [59] Tang, P. T., (2008), Utilising Electrochemical Deposition for Micro Manufacturing, in *Multi-Material Micro Manufacture* edited by S. Dimov and W. Menz, Whittles Publishing Ltd. Cardiff University, Cardiff, UK
- [60] Gamburg, Y. D. and Zangari, G., (2011), *Theory and Practice of Metal Deposition*, Springer science + Business Media, LLC, 291-292
- [61] Djokić, S. S. and Cavallotti, P. L., (2010), Electroless Deposition: Theory and Applications, in *Electrodeposition: Theory and Practice*, edited by Djokić, S.S., *Modern Aspects of Electrochemistry* 48, Springer Science+Business Media, LLC
- [62] Paunovic, M. and Schlesinger, M., (1998) *Fundamentals of Electrochemical Fabrication*, John Wiley & Sons, Inc. New York.
- [63] Bard, A. J. and Faulkner, L. R., (2001) *Electrochemical Methods: Fundamentals and Applications*, 2nd edition, 22 – 43, John Wiley and Sons, Inc.
- [64] Kuleshova, J., E. Koukharenko, et al. (2010). "Optimization of the electrodeposition process of high-performance bismuth antimony telluride compounds for thermoelectric applications." *Langmuir* 26(22): 16980-16985.
- [65] Osaka, T., N. Takano, et al. (2003). "Microfabrication of electro- and electroless-deposition and its application in the electronic field." *Surface and Coatings Technology* 169–170(0): 1-7.

- [66] Datta, M. and D. Landolt (2000). "Fundamental aspects and applications of electrochemical microfabrication." *Electrochimica Acta* 45(15–16): 2535-2558.
- [67] Haberkorn, N., M. Ahlers, et al. (2009). "Tuning of the martensitic transformation temperature in Cu–Zn thin films by control of zinc vapor pressure during annealing." *Scripta Materialia* 61(8): 821-824.
- [68] Cui, Z., (2008), *Nanofabrication*, DOI: 10.1007/978-0-387-75577-9_6, Pp. 234 - 262 Springer Science & Business Media, LLC
- [69] Baca, A. G. and Ashby, C. I. H., (2005), *Fabrication of GaAs devices*, The Institution of Engineering and Technology, London: 117 - 118
- [70] Sutikno, M., U. Hashim, et al. (2007). "A systematic dry etching process for profile control of quantum dots and nanoconstrictions." *Microelectronics Journal* 38(8–9): 823-827.
- [71] Anenden, M.P., Svehla, M., Lovell, N. H., and Suaning, G. J., (2011), Process development for dry etching polydimethylsiloxane for neural electrodes, *Conf Proc IEEE Eng Med Biol Soc.* 2011:2977-80.
- [72] Burns, D. W., (2011) *MEMS Wet-Etch Processes and Procedures*, in R. Ghodssi, P. Lin (eds.), *MEMS Materials and Processes Handbook*, DOI 10.1007/978-0-387-47318-5_8, Springer Science+Business Media, LLC
- [73] Mahendran, S., Devarajan, R., Nagarajan, T., and Majdi, A., (2010), A Review of Micro-EDM, *Proceeding of the International Multiconference of Engineers and Computers Scientists (IMECS) Vol 2*, Hongkong.
- [74] Teimouri, R and Baseri, H., (2012). "Study of Tool Wear and Overcut in EDM Process with Rotary Tool and Magnetic Field." *Advances in Tribology* **2012**. Article ID 895918, 8 pages, doi:10.1155/2012/895918, Hindawi Publishing Corporation
- [75] McGeough, J. A., (1988), *Advanced Methods of Machining*, Chapman and Hall Ltd, London
- [76] Meijer, J. (2004). "Laser beam machining (LBM), state of the art and new opportunities." *Journal of Materials Processing Technology* 149(1–3): 2-17.
- [77] Dubey, A. K. and V. Yadava (2008). "Laser beam machining—A review." *International Journal of Machine Tools and Manufacture* 48(6): 609-628.
- [78] Park, D. S., T. I. Seo, et al. (2005). "Mechanical etching of micro pockets by powder blasting." *The International Journal of Advanced Manufacturing Technology* 25(11): 1098-1104.

- [79] Song, W., Kim, Y-H., Kim, M-S., Ahn, S-H., and Lee, C. S., (2010), Fine-Sized Etching of Flexible Substrates Using Nano Particle Deposition System (NPDS), *Materials Transactions*, Vol. 51, No. 11 pp. 2099 to 2103
- [80] Slikkerveer, P. J., P. C. P. Bouten, et al. (2000). "High quality mechanical etching of brittle materials by powder blasting." *Sensors and Actuators A: Physical* 85(1–3): 296-303.
- [81] Roy, S., (2009), EnFACE: A Mask Less Process for Circuit Fabrication, *Circuit World* 35/3 8-11
- [82] Datta, M. and D. Landolt (2000). "Fundamental aspects and applications of electrochemical microfabrication." *Electrochimica Acta* 45(15–16): 2535-2558.
- [83] SchÖnenberger, I., (2004), Electrochemical microfabrication without photolithography : copper substrates, MPhil Thesis, School of Chemical Engineering and Advanced Materials, Newcastle University.
- [84] Nouraei, S. and Roy, S., (2008), Electrochemical Process for Micropattern Transfer without Photolithography: A Modeling Analysis, *Journal of The Electrochemical Society*, Vol. 155 No. 2 Pp. D97-D103
- [85] Hayden, C. J. and C. Dalton (2010). "Direct patterning of microelectrode arrays using femtosecond laser micromachining." *Applied Surface Science* 256(12): 3761-3766.
- [86] Hayden, C. J. and Dalton, C., (2010). "Direct patterning of microelectrode arrays using femtosecond laser micromachining." *Applied Surface Science* 256(12): 3761-3766.
- [87] Roy, S., (2010), Electrochemical Microfabrication without Photolithography – a Sustainable Manufacturing Process, Innovative electronics Manufacturing Research Centre (IeMRC), 5th Annual Conference, Loughborough University. Available online at (accessed 23rd June 2011):
<http://www.lboro.ac.uk/research/iemrc/documents/EventsDocuments/5th%20Annual%20Conference%202010/Presentations/Roy-Micro%20Pattern%20Transfer%20for%20IeMRC.pdf>
- [88] Hartman, R. L. and Jensen K. F. (2009). "Microchemical systems for continuous-flow synthesis." *Lab on a Chip* 9(17): 2495-2507.
- [89] Sugiyama, S., Amaya, S. and Viet Dao, D., (2012), Development of polymer MEMS process technology as an approach to a sustainable production system, *Adv. Nat. Sci.: Nanosci. Nanotechnol.* 3 015009 (7pp)

- [90] Malek, C. K., F. T. Hartley, et al. (2003). "Fast prototyping of high-aspect ratio, high-resolution X-ray masks by gas-assisted focused ion beam." *Microsystem Technologies* 9(6): 409-412.
- [91] Hessel, V., D. Kralisch, et al. (2008). "Sustainability through green processing - novel process windows intensify micro and milli process technologies." *Energy & Environmental Science* 1(4): 467-478.
- [92] Dario, P., Carrozza, M. C., Benvenuto, A., and Menciassi, A., (2000), *Microsystems in biomedical applications*, J. Micromech. Microeng. 10 235–244
- [93] Wehrmeyer, H., Clayton, A., and Lum, K., (2002), *Foresighting for Development*, GMI Theme Issue, GMI 37 Spring 2002, Greenleaf Publishing
- [94] Becker, H. and C. Gärtner (2008). "Polymer microfabrication technologies for microfluidic systems." *Analytical and Bioanalytical Chemistry* 390(1): 89-111.
- [95] Yamada, S., T. Mrozek, et al. (2003). "Toward Environmentally Friendly Photolithographic Materials: A New Class of Water-Soluble Photoresists." *Macromolecules* 37(2): 377-384.
- [96] Ionov, L. and S. Diez (2009). "Environment-Friendly Photolithography Using Poly(N-isopropylacrylamide)-Based Thermoresponsive Photoresists." *Journal of the American Chemical Society* 131(37): 13315-13319.
- [97] Lin, C. H., Yang, H. et al. (2008). "Fast patterning microstructures using inkjet printing conformal masks." *Microsystem Technologies* 14(9): 1263-1267.
- [98] B. F. Barclay, What designers should know about LDI: not just a tool for fine lines, laser direct imaging eliminates phototools and tightens design tolerances. Aspects to consider when designing for LDI. (Design Rules For LDI), *Printed Circuit Design & Manufacture*, (2004). Available online at: http://www.accessmylibrary.com/coms2/summary_0286-3552212_ITM (accessed 10 /06/2010)
- [99] Zaidi, S. H., Chu, A., and Brueck, S. R. J., (1995), *Scalable Fabrication and Optical Characterisation of nm Si Structures*. Soc. Symp. Proc. Vol. 358 pp. 957-968
- [100] Yoo, H., et al. (2009). "Parallelized laser-direct patterning of nanocrystalline metal thin films by use of a pulsed laser-induced thermo-elastic force." *Nanotechnology* 20(24): 245301.
- [101] Burt, J., Goater, A., Hayden, C., Morris, D., Rizvi, N., and Talary, M., *Developments In The Microfabrication Of Biochips Using Laser Micromachining*, Institute of Bioelectronic and Molecular Microsystems, University of Wales, available online at:

- http://www.lasermicromachining.com/downloads/AILU_Developments_In_The_Microfabrication_Of_Biochips_Using_Laser_Micromachining.pdf
(Accessed 10/06/2010)
- [102] Williams, G. L., et al. (2004). "The patterning of fine-pitch electrical interconnections on non-planar substrates: a comparison between methods utilising laser ablation and electro-deposited photoresist." *Sensors and Actuators A: Physical* 112(2–3): 360-367.
- [103] Solà, M. D., (2010), Study of the Laser Forward Transfer for the preparation of miniaturised Biosensors, PhD Thesis, Department De Física Aplicada i òptica, Universitat De Barcelona, Spain.
- [104] Liu, T.-C., et al. (2006). "Development of an artificial neural network to predict lead frame dimensions in an etching process." *The International Journal of Advanced Manufacturing Technology* 27(11-12): 1211-1216.
- [105] Conde, O. and Silvestre, A. J., (2004), Laser-assisted deposition of thin films from photoexcited vapour phases, *Appl. Phys. A* 79, 489–497
- [106] Santos, M.J., Silvestre, A.J., and Conde, O., (2002), Laser Assisted Deposition of r-B4C Coatings using Ethylene as Carbon Precursor, *Surface and Coatings Technology* 151-152 160
- [107] Bondi, S.N., Lackey, W.J., Johnson, R.W., Wang, X., and Wang, Z.L., (2006) Laser assisted chemical vapor deposition synthesis of carbon nanotubes and their characterization, *Carbon* 44 1393–1403
- [108] Manshina, A., et al. (2007). "Laser-assisted metal deposition from CuSO₄-based electrolyte solution." *Laser Physics Letters* 4(2): 163-167.
- [109] Santschi, C., et al. (2009). "Focused Ion Beam: A Versatile Technique for the Fabrication of Nano-Devices." *Praktische Metallographie-Practical Metallography* 46(3): 154-156.
- [110] Wang, Y., Bokor, J., and Lee, A., (2004), Maskless Lithography Using Drop-On-Demand Inkjet Printing Method, *Emerging Lithographic Technologies VIII*, edited by R. Scott Mackay, *Proceedings of SPIE Vol. 5374 SPIE*, Bellingham, WA,
- [111] Hayes, D. J., Cox, W. R., and Grove, M. E., (1999) *Low-Cost Display Assembly and Interconnect Using Ink-Jet Printing Technology*, MicroFab Technologies, Inc., Display Works.
- [112] Al-Chami H. and Cretu, E., (2009), Inkjet Printing of Microsensors, *IEEE 15th International Mixed-Signals, Sensors, and Systems Test Workshop*.

- [113] Doraiswamy, A., Dunaway, T. M., Wilker, J. J., and Narayan, R. J., (2009), Inkjet Printing of Bioadhesives, *Journal of Biomedical Materials Research Part B: Applied Biomaterials J Biomed Mater Res Part B: Appl Biomater* 89B: 28–35
- [114] Bagheri-Tar, F., Sahimi, M., and Tsotsis, T. T., (2007), Preparation of Polyetherimide Nanoparticles by an Electrospray Technique, *Ind. Eng. Chem. Res.*, 46, 3348-3357.
- [115] Suksamran, T., Opanasopit, P., Rojanarata, T., Ngawhirunpat, T., Ruktanonchai, U., and Supaphol, P., (2009), Biodegradable alginate microparticles developed by electrohydrodynamic spraying techniques for oral delivery of protein, *Journal of Microencapsulation*; 26(7): 563–570
- [116] Wang, D., Rocks, S.A., and Dorey, R.A., (2009), Micromoulding of PZT film structures using electrohydrodynamic atomization mould filling, *Journal of the European Ceramic Society* 29 1147–1155.
- [117] Said, R. A., (2003), Microfabrication by localized electrochemical deposition: experimental investigation and theoretical modelling, *Nanotechnology* 14 523
- [118] Seol, S. K., A. R. Pyun, et al. (2005). "Localized Electrochemical Deposition of Copper Monitored Using Real-Time X-ray Microradiography." *Advanced Functional Materials* 15(6): 934-937.
- [119] Pellicer, E., Pané, S., Panagiotopoulou, V., Fusco, S., Sivaraman, K. M., Suriñach, S., Baró, M. D., Nelson, B. J., and Sort, J., (2012), Localized Electrochemical Deposition of Porous Cu-Ni Microcolumns: Insights into the Growth Mechanisms and the Mechanical Performance, *Int. J. Electrochem. Sci.*, 7 4014 – 4029
- [120] Madden, J. D. and Hunter, I. W., (1996), Three-Dimensional Microfabrication by Localised Electrochemical Deposition, *Journal of Microelectromechanical Systems*, vol. 5, no. 1
- [121] Lin, J. C., T. K. Chang, et al. (2010). "Localized electrochemical deposition of micrometer copper columns by pulse plating." *Electrochimica Acta* 55(6): 1888-1894.
- [122] Lee, C-Y., Lin, C-S., and Lin, B-R., (2008), Localized electrochemical deposition process improvement by using different anodes and deposition directions *J. Micromech. Microeng.* 18 105008
- [123] Nelson, J. B., Wisecarver, Z., and Schwartz, D. T., (2007), Electrochemical printing: mass transfer effects, *J. Micromech. Microeng.* 17 1192–1199

- [124] Whitaker, J. D., Nelson, J. B., and Schwartz, D. T., Electrochemical printing: software reconfigurable electrochemical microfabrication, *J. Micromech. Microeng.* 15 (2005) 1498–1503
- [125] Hoepfner, S., R. Maoz, et al. (2003). "Constructive Microlithography: Electrochemical Printing of Monolayer Template Patterns Extends Constructive Nanolithography to the Micrometer–Millimeter Dimension Range." *Nano Letters* 3(6): 761-767.
- [126] Nelson, J. B. and Schwartz, D. T., (2005), Electrochemical printing: in situ characterization using an electrochemical quartz crystal microbalance, *J. Micromech. Microeng.* 15 2479–2484
- [127] Bhattacharyya, B., J. Munda, et al. (2004). "Advancement in electrochemical micro-machining." *International Journal of Machine Tools and Manufacture* 44(15): 1577-1589.
- [128] Maurer, J. J., J. J. Mallett, et al. (2010). "Electrochemical micromachining of Hastelloy B-2 with ultrashort voltage pulses." *Electrochimica Acta* 55(3): 952-958.
- [129] Zhu, D., N. S. Qu, et al. (2009). "Electrochemical micromachining of microstructures of micro hole and dimple array." *CIRP Annals - Manufacturing Technology* 58(1): 177-180
- [130] Ma, X.-Z., L. Zhang, et al. (2007). "Electrochemical micromachining of nitinol by confined-etchant-layer technique." *Electrochimica Acta* 52(12): 4191-4196.
- [131] Allongue, P., P. Jiang, et al. (2004). "Electrochemical Micromachining of p-Type Silicon†." *The Journal of Physical Chemistry B* 108(38): 14434-14439.
- [132] Bhattacharyya, B., M. Malapati, et al. (2005). "Experimental study on electrochemical micromachining." *Journal of Materials Processing Technology* 169(3): 485-492.
- [133] Mutlu, S., Basu, A. S., and Gianchandani, Y. B., (2005), Maskless Electrochemical Patterning of Gold Films for Biosensors using Micromachined Polyimide Probes, *IEEE Sensors 2005 Conference*, Irvine, California, USA.
- [134] Hon, K. K. B., L. Li, et al. (2008). "Direct writing technology—Advances and developments." *CIRP Annals - Manufacturing Technology* 57(2): 601-620.
- [135] Roy, S., Process for Manufacturing Micro- and Nano-devices, US Patent No. 7776227 B2
- [136] Habib, M.A., Gan, S.W., and M. Rahman, (2009), Fabrication of complex shape electrodes by localized electrochemical deposition, *Journal of Materials Processing Technology* 209 4453–4458.

- [137] Muller, A.D., Muller, F., and M. Hietschold, (2000), Localized electrochemical deposition of metals using micropipettes, *Thin Solid Films* 366 32±36
- [138] Nouraei, S. and S. Roy (2009). "Design of experiments in electrochemical microfabrication." *Electrochimica Acta* **54**(9): 2444-2449.
- [139] Gabrielli, C., P. Moçotéguy, et al. (2004). "Mechanism of copper deposition in a sulphate bath containing chlorides." *Journal of Electroanalytical Chemistry* **572**(2): 367-375.
- [140] Grujicic, D. and B. Pesic (2006). "Electrochemical and AFM study of nickel nucleation mechanisms on vitreous carbon from ammonium sulfate solutions." *Electrochimica Acta* **51**(13): 2678-2690.
- [141] Saraby-Reintjes, A. and M. Fleischmann (1984). "Kinetics of electrodeposition of nickel from watts baths." *Electrochimica Acta* **29**(4): 557-566.
- [142] Shina, S. G., (2008), *Green Electronics Design and Manufacturing: Implementing Lead-Free and RoHS-Compliant Global Products*, p. 301-304, McGraw-Hill, Inc. New York, NY, USA.
- [143] Harper, C. A., (2004), *Electronic Materials and Processes Handbook*, 3rd Edition, p. 6.12-14, McGraw-Hill Inc. New York.
- [144] Strandjord, A. J. G., Popelar, S., and Jauernig, C., (2002), Interconnecting to aluminium - and copper-based semiconductors (electroless-nickel/gold for solder bumping and wire bonding), *Microelectronics Reliability* 42 p. 265–283
- [145] Zhao, P., Pecht, M., Kang, S., and Park, S., (2006), Assessment of Ni/Pd/Au-Pd and Ni/Pd/Au-Ag Pre-Plated Leadframe Packages Subject to Electrochemical Migration and Mixed Flowing Gas Tests, *IEEE Transactions on Components and Packaging Technologies*, Vol. 29, No.4 p. 818-826
- [146] Wang, R., Kuder, R., Wu, B., Emmerson, G.T., Seeley, G.j., and Lee, J., (2002), Understanding Leadframe Surface Treatment and Its Impact on Package Reliability, 2002 Electronic Components and Technology Conference.
- [147] Nugent, D., (2009), A Technical and Commercial Survey of the Leadframe Industry, Private Report, Unpublished.
- [148] Heong, T. K. and Harun, F., (2010), Challenges in Copper 2nd Bond Quality on Nickel Palladium Leadframe, 34th International Electronic Manufacturing Technology Conference
- [149] Chinda, A., Akino, H., and Koizumi, R., (1998), Environment Protecting Palladium-Plated Leadframe, *Hitachi Cable Review*, No. 17, Article No. 9

- [150] Fan, C., A. Blair and J. A. Abys, (2000), Nickel/Palladium Surface Finish for Semiconductor Packaging Application, Surface Finishes Forum Conference Proceedings
- [151] Tsuru, Y., M. Nomura, et al. (2000). "Effects of chloride, bromide and iodide ions on internal stress in films deposited during high speed nickel electroplating from a nickel sulfamate bath." Journal of Applied Electrochemistry **30**(2): 231-238
- [152] Luo, J.K., Pritschow, M., Flewitt, A.J., Spearing, S.M., Fleck, N.A. and Milne, W.I. (2006) Effects of process conditions on properties of electroplated Ni thin films for microsystem applications. *Journal of the Electrochemical Society*, **153**, (10), D155-D161.
- [153] Kelly, J. J., Goods, S. H., Talin, A. A., and Hachman, J. T., (2006), Electrodeposition of Ni from Low-Temperature Sulfamate Electrolytes, I. Electrochemistry and Film Stress, *Journal of The Electrochemical Society*, **153** (5) p. C318-C324.
- [154] Schlesinger, M. and Paunovic, M., (2000), *Modern Electroplating*, 4th Edition, p. 139-199, Electrochemical Society Series, John Wiley and Sons, Inc. New York
- [155] Allen, D.M., Duclos, N., Garbutt, I., Saumer, M., Dhum, Ch., Schmitt, M., and Hoffmann, J.E., (2006), The Effects of Additives on the Physical Properties of Electroformed Nickel and on the Stretch of Photoelectroformed Nickel Components, Dans Symposium on Design, Test, Integration and Packaging of MEMS/MOEMS - DTIP 2006, Stresa, Lago Maggiore : Italie
- [156] Davis, J. R., (2000), *Nickel, Cobalt and Their Alloys: 8 (ASM Specialty Handbook)*, ASM International, Pp. 1 - 123
- [157] Badarulzaman, N., A. Mohamad, et al. (2010). "The evaluation of nickel deposit obtained via Watts electrolyte at ambient temperature." Journal of Coatings Technology and Research **7**(6): 815-820
- [158] Sadiku-Agboola, O., Sadiku, E.R., and Biotidara, O.F., (2012), The properties and the effect of operating parameters on nickel plating (review), *International Journal of the Physical Sciences* Vol. **7**(3), pp. 349 - 360
- [159] Saitou, M., S. Oshiro, et al. (2008). "Effect of temperature on nickel electrodeposition from a nickel sulfamate electrolyte." Journal of Applied Electrochemistry **38**(3): 309-313
- [160] Pourbaix, M., (1974), *Atlas of Electrochemical Equilibria in Aqueous Solution*, 2nd English Edition, Houston Tech. National Association of Corrosion Engineering, p. 331-341.

- [161] Nasirpouri, F., Bending, S. J., Peter, L. M., and Fangohr, H., (2011), Electrodeposition and magnetic properties of three-dimensional bulk and shell nickel mesostructures, *Thin Solid Films* 519 (2011) 8320–8325
- [162] Dini J. W., (1993) Electrodeposition: the materials science of coatings and substrates, Noyes Publication, New Jersey, Pp. 2-5.
- [163] Bhatt, D. P., (1997), Electroplating and Metal Finishing, P. 32.12, Shipra Publications
- [164] Li, C.-q., X.-h. Li, et al. (2007). "Nickel electrodeposition from novel citrate bath." *Transactions of Nonferrous Metals Society of China* **17**(6): 1300-1306.
- [165] Xu, Q., Y.-l. Qiao, et al. (2009). "Electro-deposition and characterizations of nickel coatings on the carbon–polythene composite." *Journal of Applied Electrochemistry* 39(12): 2513-2519.
- [166] Karmakar, S., S. Kumar, et al. (2011). "Nano-electronics and spintronics with nanoparticles." *Journal of Physics: Conference Series* 292(1): 012002.
- [167] Lins, V. F. C., E. Ceconello, et al. (2008). "Effect of the Current Density on Morphology, Porosity, and Tribological Properties of Electrodeposited Nickel on Copper." *Journal of Materials Engineering and Performance* **17**(5): 741-745.
- [168] Tripathy, B. C., P. Singh, et al. (2001). "Effect of organic extractants on the electrocrystallization of nickel from aqueous sulphate solutions." *Journal of Applied Electrochemistry* **31**(3): 301-305.
- [169] Sakamoto, T., K. Azumi, et al. (2010). "Effects of 2-buthyne-1,4-diol additive on electrodeposited Ni films from a Watts-type bath." *Electrochimica Acta* **55**(28): 8570-8578.
- [170] Dolgikh, O., N. Sotskaya, et al. (2009). "Electroplating of catalytically active nickel coatings from baths of various anionic compositions." *Protection of Metals and Physical Chemistry of Surfaces* **45**(6): 718-723.
- [171] Vincenzo, A. and Cavallotti, P. L., (2008), Structure and Electrokinetic Study of Nickel Electrodeposition, *Russian Journal of Electrochemistry*, Vol. 44, No. 6, pp. 716–727.
- [172] Wesley, W.A., (1939) 75th General Meeting E.M Baker Presiding
- [173] Godon, A., J. Creus, et al. (2011). "Characterization of electrodeposited nickel coatings from sulphamate electrolyte without additive." *Materials Characterization* **62**(2): 164-173.

- [174] Tsuru, Y., M. Nomura, et al. (2002). "Effects of boric acid on hydrogen evolution and internal stress in films deposited from a nickel sulfamate bath." Journal of Applied Electrochemistry **32**(6): 629-634.
- [175] Chung, C.-K., W. Chang, et al. (2010). "Electroplating of nickel films at ultra low electrolytic temperature." Microsystem Technologies **16**(8): 1353-1359
- [176] Singh, V. B. and R. S. Sarabi (1994). "Study of some physical properties and structure of nickel electrodeposits from sulphamate-mixed organic solvents." Materials Chemistry and Physics **39**(2): 124-128
- [177] Saito, F. et al. (2007) Technically Speaking Metal Finishing 34
- [178] Li, J.-d., P. Zhang, et al. (2009). "Uniformity study of nickel thin-film microstructure deposited by electroplating." Microsystem Technologies **15**(4): 505-510.
- [179] Gomes, C. R., and Kieling, V. C. (1998) Effect of Solution Composition in Nickel Electrodeposition on Silicon Surfaces, Metal Finishing Pp. 49 – 51
- [180] Wesley, W. A. and Carey. J. W., The Electrodeposition of Nickel from Chloride Solutions, the Seventy-fifth General Meeting, held at Columbus, Ohio, April 28, 1939, B. M. Baker presiding.
- [181] R. Oriňáková, A. Turoňová, D. Kladeková, M. Gálová and R. M. Smith, Recent developments in the electrodeposition of nickel and some nickel-based alloys, Journal of Applied Electrochemistry 36:957–972 (2006)
- [182] Oriňáková, R., L. Trnková, et al. (2004). "Application of elimination voltammetry in the study of electroplating processes on the graphite electrode." Electrochimica Acta 49(21): 3587-3594
- [183] Bockris, J. O. M., D. Drazic, et al. (1961). "The electrode kinetics of the deposition and dissolution of iron." Electrochimica Acta **4**(2–4): 325-361.
- [184] Sasaki, K. Y. and J. B. Talbot (2000). "Electrodeposition of Iron-Group Metals and Binary Alloys from Sulfate Baths. II. Modeling." Journal of The Electrochemical Society 147(1): 189-197
- [185] Hessami, S. and C. W. Tobias (1989). "A Mathematical Model for Anomalous Codeposition of Nickel-Iron on a Rotating Disk Electrode." Journal of The Electrochemical Society **136**(12): 3611-3616.
- [186] Matlosz, M. (1993). "Competitive Adsorption Effects in the Electrodeposition of Iron-Nickel Alloys." Journal of The Electrochemical Society **140**(8): 2272-2279
- [187] Lantelme, F., A. Seghioer, et al. (1998). "Model of nickel electrodeposition from acidic medium." Journal of Applied Electrochemistry **28**(9): 907-913

- [188] Nielsen, C. B., A. Horsewell, et al. (1997). "On texture formation of nickel electrodeposits." Journal of Applied Electrochemistry **27**(7): 839-845
- [189] Šupicová, M., R. Rozik, et al. (2006). "Influence of boric acid on the electrochemical deposition of Ni." Journal of Solid State Electrochemistry **10**(2): 61-68.
- [190] Ji, J. and W. C. Cooper (1996). "Nickel speciation in aqueous chloride solutions." Electrochimica Acta **41**(9): 1549-1560.
- [191] Chassaing, E., M. Jousselein, et al. (1983). "The kinetics of nickel electrodeposition: Inhibition by adsorbed hydrogen and anions." Journal of Electroanalytical Chemistry and Interfacial Electrochemistry **157**(1): 75-88.
- [192] Epelboin, I., M. Jousselein, et al. (1981). "Impedance measurements for nickel deposition in sulfate and chloride electrolytes." Journal of Electroanalytical Chemistry and Interfacial Electrochemistry **119**(1): 61-71
- [193] Wiart, R. (1990). "Elementary steps of electrodeposition analysed by means of impedance spectroscopy." Electrochimica Acta **35**(10): 1587-1593.
- [194] Hart, A. C. (2011), Substitution issues related to the use of nickel in electrolytic and electroless surface engineering processes, Transactions of the Institute of Metal Finishing 89 (4), pp. 181-186
- [195] Gabe, D.R. and Chen, L., (2009), Optimisation of nickel electrodeposition solutions for power usage, Transactions of the Institute of Metal Finishing, 87 (1), pp. 8-10.
- [196] Davis, J.R. (2000) Corrosion: understanding the basics, ASM International, pp. 42-44
- [197] Watson, S. J., Smallwood, R. H., Brown, B. H., Cherian, P., and Bardhan, K. D. (1996) *Physiol. Meas.* 17 21–27
- [198] Atkins, P. and De Paula, J., (2009), *Atkins' Physical Chemistry*, 9th edition OUP Oxford.
- [199] Vanyšek, P. (1998-1999), Electrochemical Series, in *CRC Handbook of Chemistry and Physics: A Ready-Reference Book of Chemical and Physical Data*, David R. Lide, ed., 79th Edition, pp. 5.93 – 5.94, CRC Press, Washington DC, USA
- [200] Beier, S. P. and Hede, P. D., (2010), *Chemistry*, 2nd Edition, Pp. 113 – 119, Ventus Publishing ApS.
- [201] Whitten, K. W., Davis, R. E., and Peck, M. L. (2009), *Chemistry*, 9 edition, Thomson Brooks/Cole, P. 756

- [202] Dzyazko, Y. S., (2006), "Purification of a diluted solution containing nickel using electrodeionization." *Desalination* **198** (1–3): 47-55.
- [203] Palana, O. G., (2009) Electroplating, in Engineering Chemistry Book, Pp. 151 – 165, Tata McGraw Hill Education Pvt. Ltd. New Delhi.
- [204] Rai-Choudhury, P. (Ed.), (1997), Handbook of Microlithography, Micromachining and Microfabrication, Vol. 2, P. 206, SPIE Optical Engineering Press, Bellingham,
- [205] Scholz, F., (2010), Electroanalytical methods: Guide to experiments and applications, 2nd ed, Pp. 11- 31, Springer Heidelberg Dordrecht London
- [206] Revie, R. W., (2011), Uhlig's Corrosion Handbook, 3rd Edition, Pp. 93 – 100, John Wiley & Sons Inc. New Jersey
- [207] Buckle, R. (2007), The Recovery of Metals from Waste Solutions by Electrochemical Method, Thesis, Newcastle University, United Kingdom
- [208] Walsh, F. C. and Herron, M. E., (1991), Electrocrystallization and electrochemical control of crystal growth: fundamental considerations and electrodeposition of metals, *J. Phys. D: Appl. Phys.* 24 217
- [209] Landolt, D., (1994), Electrochemical and materials science aspects of alloy deposition, *Electrochimica Acta* **39** (8–9): 1075-1090.
- [210] Li, J., Zhong, T-K, and Wadsworth, M. E., (1992), Application of mixed potential theory in hydrometallurgy, *Hydrometallurgy* 29 (1–3): 47-60.
- [211] Noel, M. and Vasu, K. I., (1990), Cyclic voltammetry and the frontiers of electrochemistry, Pp. Chapter 4 164 -170, Oxford & IBH Publishing Co. Pvt. Ltd., New Delhi
- [212] Lavine, G. L., (2012) Chapter 19: Electrochemical Kinetics, available online at: http://docencia.izt.uam.mx/gtll/procesamiento_acuoso/index.htm, accessed 02/12/2012.
- [213] Bagotsky, V. S., (2005), Fundamental of Electrochemistry, John Wiley & Sons Inc, New Jersey, Pp. 219 -235
- [214] Prasad, S. K., (2004) Advanced Wirebond Interconnection Technology, Springer; 1 edition, Pp. 235
- [215] Lew, L. F. and A. N. L. Lau (2010). Influence of copper contamination on contact quality between gold wire and Nickel-Palladium bond pad through X-ray photoelectron spectroscopy. Physical and Failure Analysis of Integrated Circuits (IPFA), 2010 17th IEEE International Symposium on the

- [216] Durbha, M. and M. E. Orazem (1998). "Current Distribution on a Rotating Disk Electrode below the Mass-Transfer-Limited Current: Correction for Finite Schmidt Number and Determination of Surface Charge Distribution." *Journal of The Electrochemical Society* 145(6): 1940-1949.
- [217] Navarrete, R. and Venkataramani, S., (2010) Determining the Behaviour of The Rotating Disk Electrode System, accessed on 16/06/2010, available online at: math.arizona.edu/~shankar/projects/Raymundo.pdf
- [218] Newman, J. and Thomas-Alyea, K. E., (2004), *Electrochemical System*, 3rd Edition, Prentice-Hall Pp. 373 - 448.
- [219] Selman, J. R. and Tobias, C. W., (1978), *Advances in Chemical Engineering: Mass Transfer Measurements by the Limiting Current Technique*. Vol. 10. Academic Press.
- [220] Schlichting, H., Gersten, K., (2000), *Boundary-Layer Theory*, 8th ed. P. 328 New York: Springer
- [221] Levich, V. G., (1942). *Acta Physiochim. URSS*. 17, 257.
- [222] Crow, D. R., (1994), *Principles and applications of electrochemistry*, 4th edition, pp. 214, Stanley Thornes LTD. Cheltenham, UK
- [223] Compton, R. G. and Banks, C. E., (2007), *Understanding Voltammetry*, pp. 288-304, World Scientific Publishing, Singapore.
- [224] Inzelt, G. (2013). Pseudo-reference Electrodes. *Handbook of Reference Electrodes*. G. Inzelt, A. Lewenstam and F. Scholz, Springer Berlin Heidelberg: 331-332.
- [225] Kasem, K. K. and Jones, S., (2008), Platinum as Reference Electrode in Electrochemical Measurement, *Platinum Metals Rev.*, 2008, 52, (2), 100–106
- [226] Mason, T.J., Lorimer, J.P. (2002), *Applied Sonochemistry: Uses of Power Ultrasound in Chemistry and Processing*, Wiley.
- [227] Ohsaka, T., Goto, Y., Sakamoto, K., Isaka, M., Imabayashi, S., and Hirano, K. (2010), Effect of intensities of ultrasound sonication on reduction of crack formation and surface roughness in iridium electrodeposits. *Transactions of the institute of metal finishing*. 88, 4.

-
- [228] Sonics, (2013), ULTRASONIC PROCESSORS FOR SMALL AND MEDIUM VOLUME APPLICATIONS, accessed 18 June 2013, Available online at: <http://www.sonics.biz/liquid-new-sheet/VC505-750.pdf>
- [229] Plieith, W., (2008), *Electrochemistry for material sciences*, 2nd Edition, 118 - 154, Elsevier Science
- [230] Myland, J. C. and K. B. Oldham (2000). "Uncompensated Resistance. 1. The Effect of Cell Geometry." *Analytical Chemistry* **72**(17): 3972-3980.
- [231] Oldham, K. B., and N. P. C. Stevens, (2000), Uncompensated Resistance. 1. The Effect of reference electrode non-ideality, *Analytical Chemistry* **72**(17): 3981-3988.
- [232] Scribner, L. L. and Taylor, S. R., (1990), *The Measurement and Correction of Electrolyte Resistance in Electrochemical Tests*, Astm Special Technical Publication, ASTM International. Pp. 95 - 108
- [233] Oelßner, W., et al. (2006). "The iR drop – well-known but often underestimated in electrochemical polarization measurements and corrosion testing." *Materials and Corrosion* **57**(6): 455-466.
- [234] Coleman, S. (2011), PhD First Year Report, School of Chemical Engineering and Advanced Materials, Newcastle University.
- [235] Mittemeijer, E. J. and Scardi, P. (2004), *Diffraction Analysis of the Microstructure of Materials*, Springer, New York, Pp. 420 – 421.
- [236] Cui, C. Q. and J. Y. Lee (1995). "Nickel deposition from unbuffered neutral chloride solutions in the presence of oxygen." *Electrochimica Acta* **40**(11): 1653-1662
- [237] Zoski, C. G. (2007), *Handbook of Electrochemistry*, Pp. 453, 840, Elsevier, Oxford, UK.
- [238] Seo, M. H., et al. (2005). "The effects of pH and temperature on Ni–Fe–P alloy electrodeposition from a sulfamate bath and the material properties of the deposits." *Thin Solid Films* **489**(1–2): 122-129.
- [239] Albalat, R., et al. (1991). "Electrochemical nucleation of nickel on vitreous carbon electrodes: the influence of organic additives." *Journal of Applied Electrochemistry* **21**(8): 709-715.
- [240] Njau, K. N. and L. J. J. Janssen (1995). "Electrochemical reduction of nickel ions from dilute solutions." *Journal of Applied Electrochemistry* **25**(10): 982-986.

- [241] Vasilache, T., Gutt, S., Vasilache, F., and Gutt, G. (2010), Studies Regarding Nickel Electrodeposition from Watts bath with addition of Polyvinylpyrrolidone and Sodium Lauryl Sulfate, METAL, Roznov pod Radhostem, Czech Republic, EU
- [242] Muñoz, A. G., et al. (2003). "First stages of Ni deposition onto vitreous carbon from sulfate solutions." *Thin Solid Films* 429(1–2): 119-128.
- [243] Cui, C. Q. and J. Y. Lee (1994). "Effects of Oxygen Reduction on Nickel Deposition from Unbuffered Aqueous Solutions: I. Deposition Process and Deposit Structure." *Journal of The Electrochemical Society* 141(8): 2030-2035.
- [244] Panda, A. (2003), PhD Thesis, The Louisiana State University, available online accessed 10 June 2013 at: http://etd.lsu.edu/docs/available/etd-0404103-141239/unrestricted/Panda_dis.pdf.
- [245] Bockris, J. O'M., (1953) Parameters of Electrode Kinetics, Electrochemical Constants, NBS Circular 524, U. S. Government Printing Office, Washington, D. C., pp.243-262, available at <http://faculty.kfupm.edu.sa/ME/hussaini/Corrosion%20Engineering/02.05.05.htm>.
- [246] Mohanty, U. S., et al. (2001). "Effect of pyridine and its derivatives on the electrodeposition of nickel from aqueous sulfate solutions. Part II: Polarization behaviour." *Journal of Applied Electrochemistry* 31(9): 969-972.
- [247] Davison, W. and J. A. Harrison (1973). "The deposition of Ni from aqueous sulphate and sulphamate solutions." *Journal of Electroanalytical Chemistry and Interfacial Electrochemistry* 44(3): 431-443.
- [248] Ibrahim, M. M. (2006). "Black nickel electrodeposition from a modified Watts bath." *Journal of Applied Electrochemistry* 36(3): 295-301.
- [249] Mamantov, G., Jenkins, H. W. Manning, D, L., Exchange Current Measurements on the Nickel-Nickel(II) Couple in Molten Fluorides, available online at http://web.anl.gov/PCS/acsfuel/preprint%20archive/Files/11_1_MIAMI_04-67_0147.pdf
- [250] Thakar, R., J. P. Wilburn, et al. (2011). "Studies of Edge Effects with Shroud-Modified Electrodes." *Electroanalysis* 23(7): 1543-1547.
- [251] Ju, H., H. Chen, et al. (1993). "Investigation of microelectrodes: IX: Study of the edge effects at a microdisk electrode." *Journal of Electroanalytical Chemistry* 361(1–2): 251-256.

- [252] Ferapontova, E. E., J. G. Terry, et al. (2007). "Electrochemical deposition of Zn on TiN microelectrode arrays for microanodes." *Electrochemistry Communications* 9(2): 303-309
- [253] Vorburger, T. V., et al. (2007). "Comparison of optical and stylus methods for measurement of surface texture." *The International Journal of Advanced Manufacturing Technology* 33(1-2): 110-118.
- [254] Naumkin, A. V., Kraut-Vass, A., Gaarenstroom, S. W., and Powell, C. J., (2013), NIST X-ray Photoelectron Spectroscopy Database, NIST Standard Reference Database 20, Version 4.1, Available online at : <http://srdata.nist.gov/xps/EnergyTypeValSrch.aspx> (Accessed 7 Feb 2013)
- [255] McIntyre, N. S. and M. G. Cook (1975). "X-ray photoelectron studies on some oxides and hydroxides of cobalt, nickel, and copper." *Analytical Chemistry* 47(13): 2208-2213.
- [256] Boyapati, V. A. R. and C. K. Kanukula (2013). "Corrosion Inhibition of Cu-Ni (90/10) Alloy in Seawater and Sulphide-Polluted Seawater Environments by 1,2,3-Benzotriazole." *ISRN Corrosion* 2013: 22.
- [257] Payne, B. P., et al. (2011). "X-ray photoelectron spectroscopy studies of reactions on chromium metal and chromium oxide surfaces." *Journal of Electron Spectroscopy and Related Phenomena* 184(1-2): 29-37.
- [258] Cicileo, G. P., et al. (1999). "Comparative study of organic inhibitors of copper corrosion." *Corrosion Science* 41(7): 1359-1375.
- [259] Dukovic, J. O. (1990). "Computation of current distribution in electrodeposition, a review." *IBM Journal of Research and Development* 34(5): 693-705.
- [260] Popov, K. I., Živković, P. M., and Nikolić, N. D., (2011), A mathematical model of the current density distribution in electrochemical cells, *J. Serb. Chem. Soc.* 76 (6) 805–822
- [261] Landau, U. (2009), Current Distribution in Electrochemical Cells: Analytical and Numerical Modeling, in Schlesinger, M. (ed.), *Modelling and Numerical Simulations II, Modern Aspects of Electrochemistry* 44, Springer Science+Business Media LLC.
- [262] Georgiadou, M. (2003). "Modeling current density distribution in electrochemical systems." *Electrochimica Acta* 48(27): 4089-4095.

- [263] Kawamoto, H. (1992). "Numerical calculation of secondary current distribution in a two-dimensional electrochemical cell with a resistive electrode." Journal of Applied Electrochemistry **22**(11): 1113-1116.
- [264] Yang, S., Yang, W., Sun, G., and Knickle, H., (2006), Secondary current density distribution analysis of an aluminum–air cell, *Journal of Power Sources* **161** (2006) 1412–1419
- [265] Jagush, F. A., et al. (1990). "Predicted Secondary Current Distributions for Linear Kinetics in a Modified Three-Dimensional Hull Cell." Journal of The Electrochemical Society **137**(6): 1848-1851.
- [266] Van Den Bossche, B., et al. (1995). "Quasi-one-dimensional steady-state analysis of multi-ion electrochemical systems at a rotating disc electrode controlled by diffusion, migration, convection and homogeneous reactions." Journal of Electroanalytical Chemistry **397**(1): 35-44.
- [267] Van Den Bossche, B., et al. (1996). "Numerical steady state analysis of current density distributions in axisymmetrical systems for multi-ion electrolytes: application to the rotating disc electrode." Journal of Electroanalytical Chemistry **411**(1–2): 129-143.
- [268] Dan, C., et al. (2001). "Numerical simulation of transient current responses in diluted electrochemical ionic systems." Journal of Electroanalytical Chemistry **505**(1–2): 12-23.
- [269] Bortels, L., et al. (1996). "The multi-dimensional upwinding method as a new simulation tool for the analysis of multi-ion electrolytes controlled by diffusion, convection and migration. Part 1. Steady state analysis of a parallel plane flow channel." Journal of Electroanalytical Chemistry **404**(1): 15-26.
- [270] Nouraei, S. (2008), Mask-less micron scale structuring of metals and alloys: principles and applications, Thesis, Newcastle University
- [271] Elsy v6.0 Manual, (2006), Elsyca Software Documentation, ElsyCa NV, Belgium
- [272] Chandrasekar, M. S. and M. Pushpavanam (2008). "Pulse and pulse reverse plating—Conceptual, advantages and applications." Electrochimica Acta **53**(8): 3313-3322.

Appendices

Appendix A: Calculation of Electrolytes Conductivity

The molar conductivity of dissolved substance (Λ_m) is given by equation (1)

$$\Lambda_m = \nu_+ \lambda_+ + \nu_- \lambda_- \quad (1)$$

Where $\lambda = (\text{mSm}^2\text{mol}^{-1})$ and the number of moles of cations ν_+ and anions ν_- are from 1 mole dissolved electrolyte.

The conductivity of an electrolyte $\kappa = (\text{s/m})$ is the product of the molar conductivity Λ_m multiplied by the electrolyte concentration $c = \text{mol/m}^3$

$$\kappa = c_+ \nu_+ \lambda_+ + c_- \nu_- \lambda_- \quad (2)$$

$$\kappa = c(\nu_+ \lambda_+ + \nu_- \lambda_-) \quad (3)$$

$$\kappa = c * \Lambda_m \quad (4)$$

Table App. 1 the ionic conductivities of chemical ions used in this work

Cation	λ_+ ($\text{mSm}^2\text{mol}^{-1}$)	Anion	λ_- ($\text{mSm}^2\text{mol}^{-1}$)
Hydronium (H_3O^+)	34.97	Sulfamate ($\text{SO}_3\cdot\text{NH}_2$) ⁻	4.83
Nickel (Ni^{2+})	4.96	chloride (Cl^-)	7.63
Pd^{2+} *)	5.95		
NH_4^+	7.35		

The conductivity of a 0.19 M Ni ($\text{SO}_3\cdot\text{NH}_2$)₂ + 0.01 NiCl₂ can be calculated using the equations (1) and (4) as follow:

$$\Lambda_{\text{Ni}(\text{SO}_3\cdot\text{NH}_2)_2} = 1 * 4.96 \text{ mSm}^2\text{mol}^{-1} + 2 * 4.83 \text{ mSm}^2\text{mol}^{-1} = 14.62 \text{ mSm}^2\text{mol}^{-1}$$

$$\Lambda_{\text{NiCl}_2} = 1 * 4.96 \text{ mSm}^2\text{mol}^{-1} + 2 * 7.63 \text{ mSm}^2\text{mol}^{-1} = 20.22 \text{ mSm}^2\text{mol}^{-1}$$

$$\begin{aligned} \kappa_{\text{Ni}(\text{SO}_3\cdot\text{NH}_2)_2} &= 14.62 \text{ mSm}^2\text{mol}^{-1} * 190 \text{ mol m}^{-3} = 2777.8 \text{ mS m}^{-1} \\ &= 2.7778 \text{ Sm}^{-1} \end{aligned}$$

$$\begin{aligned} \kappa_{\text{NiCl}_2} &= 20.22 \text{ mSm}^2\text{mol}^{-1} * 10 \text{ mol m}^{-3} = 202.2 \text{ mS m}^{-1} \\ &= 0.2022 \text{ Sm}^{-1} \end{aligned}$$

$$\kappa_{\text{Ni}(\text{SO}_3\cdot\text{NH}_2)_2} + \kappa_{\text{NiCl}_2} = 2.98 \text{ Sm}^{-1}$$

The presence of hydrogen/hydronium ions was also incorporated in the calculation of conductivity. The concentration of hydronium was quantified by the solution pH. pH of the solution of 0.19 M Ni (SO₃.NH₂)₂ + 0.01 NiCl₂ was 6.45. The contribution of pH to the conductivity was calculated as follows:

$$\begin{aligned} \text{pH} &= 6.45 \\ [\text{H}^+] &= 3.55 \times 10^{-7} \text{M} = 3.55 \times 10^{-4} \text{ mol/m}^3 \\ \kappa_{\text{H}^+} &= 34.97 \text{ mSm}^2\text{mol}^{-1} \times 3.55 \times 10^{-4} \text{ mol m}^{-3} = 1.24 \times 10^{-2} \text{ mSm}^{-1} \\ \kappa_{\text{H}^+} &= 1.24 \times 10^{-5} \text{ Sm}^{-1} \end{aligned}$$

The contribution of the presence of hydrogen ions to the conductivity was very small which can be neglected.

$$\kappa_{\text{H}^+} \lll \kappa_{\text{Ni}(\text{SO}_3.\text{NH}_2)_2} + \kappa_{\text{NiCl}_2} \rightarrow 1.24 \times 10^{-5} \text{ Sm}^{-1} \lll 2.98 \text{ Sm}^{-1}$$

Appendix B

Estimation of Ni^{2+} Depletion with the Electrode gap

It was thought that the current density decreasing after the first peak observed at a potential around -0.4 V was possibly caused by a lack of nickel ions within the narrow gap. The first electron transfer consumed the nickel ions leading to the limited amount of nickel within the gap. Therefore, it was necessary to estimate the reaction rate to see how much nickel that has been consumed.

Table Appendix B Data used in the calculation

No		
1	Diameter of the electrode	1 cm
2	Diameter of the electrode + Holder	2 cm
3	Interelectrode gap	0.03 cm
4	Concentration of the solution ($C_{Ni^{2+}}^{bulk}$)	0.19 M
5	Applied current density	-0.035 mA/cm ²
6	Applied current (up to the first wave)	-0.028 mA
7	Time (up to the first current density wave)	200 s
8	Diffusion coefficient ($-D_{Ni^{2+}}$)	7.00E-06 cm ² /s
9	Diffusion layer thickness (δ)	53.5 μ m

A. Volume of the solution within the narrow gap : 0.047 cm³ = 4.71E-05 litre

B. The amount of nickel ions within the gap : 8.96E-06 mol

Before the reaction begin to occur, the surface concentration of nickel ions (Ni^{2+}) would be similar to its concentration in the solution bulk which is 0.19 M. So the amount of Ni^{2+} at the cathode surface would be : 8.96E-06 mol = 5.26E-04 gram

C. The amount of Ni^{2+} consumed due to the application of a current of -0.035 mA/cm² for 200 s

$$m = It \frac{M}{nF} \quad (\text{Faraday's law})$$

$$m = (-0.28E-04 \text{ A} \times 200 \text{ s}) / (1 \times 96500) = 5.7E-08 \text{ mol} = 3.35E-06 \text{ gram}$$

$$\text{The rate of depletion would be} = 7.1E-07 \text{ mol/s}$$

Comparison between the result and the total $Ni(OH)^+$ available at the electrode surface would be:

= $5.7E-08$ mol/ $8.96E-06$ mol
= 0.0064
= 0.64 %